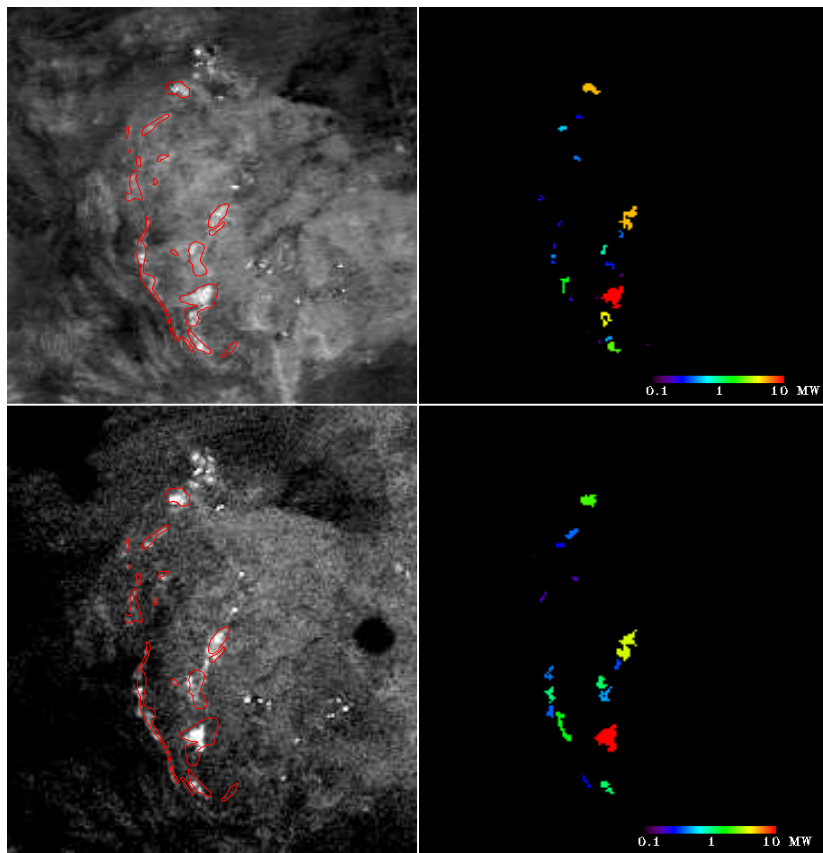

COAL FIRE QUANTIFICATION USING ASTER, ETM AND BIRD SATELLITE INSTRUMENT DATA

Anke Tetzlaff



Munich 2004

Cover: *Night-time thermal images of the Wuda coalfield in China with corresponding energy images, taken with the ETM satellite instrument. Red outlines mark coal fire induced surface anomaly zones mapped during the field campaign in September 2002. The energy values reflect coal fire related surface radiative energy releases [MW] of the entire investigated coal fire zones. The energy retrievals were computed via a new satellite based coal fire quantification approach that is presented in the following thesis. Upper left) ETM TIR channel, 28th September 2002 (night-time); upper right) energy image 28th September 2002 (night-time); lower left) ETM TIR channel 25th September 2001 (night-time); lower right) energy image 25th September 2001 (night-time).*

Coal fire quantification using ASTER, ETM and BIRD satellite instrument data

Anke Tetzlaff

Dissertation
Faculty of Geosciences
Ludwig-Maximilians-University
Munich

Anke Tetzlaff

Munich, September 2004

First referee:

Prof. Dr. W. Altermann

Second referee:

Dr. F. Wieneke

Oral examination:

22nd December 2004

LIST OF CONTENT

| | |
|--|-------------|
| Acknowledgements | v |
| Abstract | vii |
| List of figures | xi |
| List of tables | xv |
| List of acronyms | xvii |
| | |
| 1 INTRODUCTION | 2 |
| 1.1 Aims and objectives | 2 |
| 1.2 Previous works | 3 |
| 1.3 Research approach | 5 |
| 1.4 Available satellite data | 6 |
| 2 THEORETICAL BACKGROUND OF COAL FIRES | 10 |
| 2.1 Coal ignition and combustion | 10 |
| 2.2 Classification of coal fires | 11 |
| 2.3 The thermal surface anomaly of coal fires | 12 |
| 2.4 Environmental impacts and hazards of coal fires in China | 13 |
| 3 THEORETICAL BACKGROUND THERMAL REMOTE SENSING | 14 |
| 3.1 General background | 14 |
| 3.1.1 <i>Emissivity, Planck's law, Wien's displacement law, Stefan-Boltzmann's law</i> | 14 |
| 3.1.2 <i>Solar and terrestrial radiation</i> | 16 |
| 3.2 Correction and calibration of thermal satellite data | 17 |
| 3.2.1 <i>Conversion of digital number to at-sensor radiance</i> | 17 |
| 3.2.2 <i>Atmospheric correction</i> | 18 |
| 3.2.3 <i>Conversion of sensor radiance to brightness temperature</i> | 18 |
| 3.3 Fire quantification via satellite analysis | 19 |
| 3.3.1 <i>The bi-spectral technique</i> | 20 |
| 3.3.2 <i>The MODIS method</i> | 22 |
| 3.3.3 <i>The MIR method</i> | 23 |
| 4 GEOGRAPHIC AND GEOLOGIC OVERVIEW OF THE RUQIGOU, GULABEN AND WUDA COALFIELDS | 26 |
| 4.1 General geological and geographical description of the Helan Mountain area | 27 |
| 4.2 Ruqigou and Gulaben coalfield | 28 |

| | | |
|------------|---|-----------|
| 4.2.1 | <i>Geological situation</i> | 29 |
| 4.2.2 | <i>Mining situation and coal properties</i> | 29 |
| 4.2.3 | <i>Coal fires</i> | 31 |
| 4.3 | Wuda coalfield | 32 |
| 4.3.1 | <i>Geologic situation</i> | 32 |
| 4.3.2 | <i>Mining situation and coal properties</i> | 33 |
| 4.3.3 | <i>Coal fires</i> | 34 |
| 5 | FIELD OBSERVATIONS OF THE RUQIGOU, GULABEN AND WUDA COALFIELDS | 36 |
| 5.1 | Coal fire mapping | 36 |
| 5.2 | Temperatures and sizes of coal fire induced surface anomalies in the study areas | 38 |
| 5.3 | Detailed investigation of a subsurface and a near surface coal fire in the Wuda coalfield | 40 |
| 5.4 | Intraday variations of background and coal fire temperatures | 46 |
| 5.5 | Temperature measurements of the Yellow River water surface | 49 |
| 5.6 | Conclusions | 50 |
| 6 | THE POTENTIAL OF THE ETM, ASTER AND BIRD INSTRUMENT TO REGISTER SPECTRAL COAL FIRE RADIANCES | 54 |
| 6.1 | Methods | 54 |
| 6.1.1 | <i>Simulated coal fire and background conditions</i> | 54 |
| 6.1.2 | <i>Sensitivity criteria</i> | 55 |
| 6.1.3 | <i>Sensitivity calculations</i> | 56 |
| 6.2 | ETM sensitivity study | 57 |
| 6.2.1 | <i>Satellite and instrument characteristics</i> | 57 |
| 6.2.2 | <i>Sensitivity study</i> | 59 |
| 6.2.3 | <i>Conclusions</i> | 68 |
| 6.3 | ASTER sensitivity study | 69 |
| 6.3.1 | <i>Satellite and instrument characteristics</i> | 69 |
| 6.3.2 | <i>Sensitivity study</i> | 70 |
| 6.3.3 | <i>Conclusions</i> | 77 |
| 6.4 | BIRD sensitivity study | 78 |
| 6.4.1 | <i>Satellite and instrument characteristics</i> | 78 |
| 6.4.2 | <i>Sensitivity study</i> | 79 |
| 6.4.3 | <i>Conclusions</i> | 85 |

| | | |
|------------|--|------------|
| 7 | CONCEPTUAL APPROACH: THE DERIVATION OF COAL FIRE RADIATIVE ENERGY VIA TIR RADIANCES | 86 |
| 7.1 | Methods | 86 |
| 7.2 | Derivation of CFRE via ASTER and ETM TIR radiances | 87 |
| 7.2.1 | <i>ETM channel 6</i> | 87 |
| 7.2.2 | <i>ASTER channel 10, ASTER channel 12, ASTER channel 14</i> | 89 |
| 7.3 | Discussion of limitations of the TIR approach | 92 |
| 8 | CASE STUDY I: THE ESTIMATION OF COAL FIRE RELATED, SURFACE RADIATIVE ENERGY RELEASES OF THE RUQIGOU, GULABEN AND WUDA COALFIELDS USING ETM, ASTER AND BIRD DATA | 96 |
| 8.1 | Analysis of ETM data | 96 |
| 8.1.1 | <i>Methods</i> | 96 |
| 8.1.2 | <i>Interpretations</i> | 97 |
| 8.1.3 | <i>Conclusions</i> | 105 |
| 8.2 | Analysis of BIRD data | 106 |
| 8.2.1 | <i>Methods</i> | 106 |
| 8.2.2 | <i>Interpretations</i> | 108 |
| 8.2.3 | <i>Conclusions</i> | 109 |
| 8.3 | Analysis of ASTER DATA | 114 |
| 8.3.1 | <i>Methods</i> | 114 |
| 8.3.2 | <i>Interpretations</i> | 115 |
| 8.3.3 | <i>Conclusions</i> | 118 |
| 8.4 | General conclusions | 118 |
| 9 | CASE STUDY II: THE POTENTIAL OF ETM AND BIRD DATA TO QUANTIFY MOVEMENTS AND ACTIVITY CHANGES IN COAL FIRE RELATED, SURFACE ANOMALIES | 119 |
| 9.1 | Comparison of ETM brightness temperatures and field observations | 119 |
| 9.1.1 | <i>Methods</i> | 119 |
| 9.1.2 | <i>Interpretations</i> | 124 |
| 9.1.3 | <i>Conclusions</i> | 126 |
| 9.2 | Analysis of multi-temporal BIRD and ETM night-time data | 127 |
| 9.2.1 | <i>Methods</i> | 127 |
| 9.2.2 | <i>Interpretations and conclusions regarding a multi-temporal ETM analysis</i> | 128 |
| 9.2.3 | <i>Interpretation and conclusion regarding a multi-temporal BIRD data analysis</i> | 131 |

| | | |
|-------------|---|------------|
| 9.3 | General conclusions | 135 |
| 10 | AN ASTER AND ETM SATELLITE DATA BASED, AUTOMATED, COAL FIRE QUANTIFICATION (CFQ) ALGORITHM | 138 |
| 10.1 | The aim of the CFQ algorithm | 138 |
| 10.2 | CFQ algorithm description | 139 |
| 10.2.1 | <i>Algorithm outline</i> | 139 |
| 10.2.2 | <i>Module 1: Calibration and atmospheric correction</i> | 140 |
| 10.2.3 | <i>Module 2: Clustering of adjacent coal fire pixels and computation of CFRE</i> | 141 |
| 10.2.4 | <i>Module 3: Preparation of output</i> | 141 |
| 10.3 | Quality assessment | 142 |
| 10.4 | Description of required input for the CFQ algorithm, and its output products | 142 |
| 10.4.1 | <i>Inputs to the CFQ algorithm</i> | 142 |
| 10.4.2 | <i>CFQ algorithm output products</i> | 143 |
| 10.5 | Limitations and transferability of the CFQ algorithm | 144 |
| 11 | CONCLUSIONS | 148 |
| 12 | REFERENCES | 151 |

ACKNOWLEDGEMENTS

The research was carried out at the German Aerospace Center (DLR). This work was accomplished as a part of a German Ministry of Education and Science (BMBF) funded project, begun in 2001 at the DLR.

First of all I would like to thank my supervisor Priv. Doz. Dr. Wladyslaw Altermann for accepting this thesis, and for his guidance and constant support during the last three years. I am equally indebted to the DLR team, led by Dr. Harald Mehl, for allowing me to realise this project within Dr. Stefan Voigt's working group and for providing me with financial and logistical support throughout this period.

Secondly, I would like to thank the various international partners who supported the field activities in China during September 2002 and 2003. Special thanks also go to colleagues at the International Institute for Geo-Information Science and Earth Observation (ITC, Holland), including amongst others Dr. Paul van Dijk, Dr. Xiangmin Zhang, Dr. Ben Maathuis and Christoph Hecker for their support and advice during the fieldwork. In addition, I am very grateful to the Beijing Remote Sensing Corporation (BRSC) for organising and supporting the field activities. I am indebted to Y. Jia (Wuda Mining Bureau, Shenhua Group) for his guidance during the fieldwork. Acknowledgements also go to the Ruqigou Mining Company (Ningxia Industry Bureau of Coal), the Gulaben Mining Company (Taixi Group) and the Wuda Mining Bureau (Shenhua Group) for the provision of geological, geographical, mining maps, and for logistical support.

I am very grateful to the various colleagues at the DLR who intensively supported this research. Special thanks go to the DLR coal fire team, including Dr. Boris Zhukov, Dr. Stefan Voigt, Dr. Jianzhong Zhang, Claudia Kuenzer and Dr. Andreas Hirner for the valuable discussions and constant help given in connection with many aspects of the research. Dr. Rudolf Richter generously supported the atmospheric correction of the satellite data, and his constant advice with regard to any question concerning the thermal calibration of the satellite data was invaluable. Thanks also to Dr. Andrea Petrocchi and Niels Ringelmann for patiently helping me to solve programming problems.

I am also grateful to the DLR BIRD team for providing BIRD satellite data, including data synchronised with the ground campaign measurements in 2002 and 2003. In addition, I would like to thank the ITC for the ASTER data acquisition request and for performing the level 1b data processing.

Thanks go to the various project partners from the German coal fire initiative, including colleagues from the German Montan Technology (DMT), Federal Institute for Geosciences and Natural Resources

(BGR, Germany), Institute for Materials Research and Testing (BAM, Germany), Leibniz Institute for Applied Geosciences (GGA, Germany), HD (HarbourDom GmbH) and Technical University of Freiberg (Germany) for their constructive comments, which helped to improve this research.

Finally, I very much appreciate the help of the various persons who carefully read the manuscript of this work, including Boris Zhukov (DLR), Dieter Oertel (DLR), Claudia Kuenzer (DLR), Rudolf Richter (DLR), Stefan Voigt (DLR), Andreas Hirner (DLR), Hartwig Gielisch (DMT), Martin Schmidt (BAM), Paul Parker and Martial Duguay.

ABSTRACT

Coal fires cause severe environmental and economic problems. Although satellite remote sensing has been used successfully to detect coal fires, a satellite data based concept that can quantify the majority of the detected coal fires is still missing. Recently, the determination of fire radiative energy (FRE) has been introduced as a new remote sensing tool to quantify forest and grassland fires. This thesis tests the concept of remotely measured FRE, with a view to ascertaining its potential applicability to coal fires. It contains an investigation of a new generation of satellite instruments, including the operational Enhanced Thematic Mapper (ETM) instrument, the experimental Bi-spectral InfraRed Detection (BIRD) satellite sensor and the experimental Advanced Spaceborne Thermal Emission and Reflection Radiometer (ASTER), which explores the potential of these sensors to determine coal fire radiative energy (CFRE). Additionally, based on the results of this analysis, the thesis presents a new, automated ETM and ASTER data based algorithm, adapted to quantify coal fires in semi-arid to arid regions in northern China.

Field observations carried out in September 2002 and 2003 in three coalfields in northern China (the Wuda, Gulaben and Ruqigou coalfields) demonstrate that coal fire related, surface anomalies are significantly cooler than forest and grassland fires. The theoretical investigation of the ASTER, ETM and BIRD instruments outlines the fact that the thermal infrared (TIR) or mid infrared (MIR) spectral channels of the ASTER, ETM and BIRD instrument are particularly effective in registering these 'warm spots', whilst the short wave infrared (SWIR) spectral range is, however, insufficiently sensitive to be able to register spectral coal fire radiances. The commonly used bi-spectral fire quantification method (Dozier, 1981) can be applied to BIRD data in order to quantify relatively large and / or hot coal fires. However, existing FRE retrieval approaches fail to quantify coal fires via ASTER and ETM instrument data. In this thesis, a new CFRE retrieval method is presented, which links the fire and background TIR spectral radiances to the CFRE through an empirical relationship.

This newly developed TIR method is applied to visually detected fire clusters from night-time ASTER data, and from both day- and night-time ETM data, taken from the three study coalfields in northern China. The ASTER and ETM CFRE values, calculated via the TIR method, are compared to CFRE estimates from BIRD data, calculated via the existing bi-spectral method. Despite the different spatial resolution and spectral properties of the ETM, ASTER and BIRD instruments, CFRE computed from ASTER, ETM and BIRD data show good correlations with one another. However, CFRE retrievals from daytime data appear to be very undependable to background temperature variations, while CFRE, estimated from night-time data, appears to be relatively stable. A comparison between night-time ETM-derived CFRE and the figures given by local mining authorities for total coal fire induced, coal loss estimates in the Wuda coalfield gives a clear indication that the overall dimension of the coal fire

problematic can in fact be approximated via satellite data CFRE retrievals. It is thus expected that CFRE derived from night-time satellite data will become a crucial tool in obtaining reliable, quantitative information for coal fires.

A multi-temporal comparison of CFRE retrievals from night-time BIRD and ETM data, covering the Ruqigou and Wuda coalfields, indicates that only major shifts or activity changes in coal fire induced, surface anomalies can be observed by means of these data. These results, which could only partially be verified by field observations, indicate that ETM or BIRD data can be used to monitor major changes in coal fire related, surface anomalies. These data however cannot entirely replace detailed field observations, especially in case of smaller and / or cooler coal fire related, surface anomalies.

ZUSAMMENFASSUNG

Kohlefeuer verursachen gravierende ökologische und wirtschaftliche Probleme. In der Vergangenheit wurden Kohlefeuer erfolgreich mit Hilfe von Satellitenbilddaten detektiert, allerdings fehlt ein Fernerkundungskonzept, das eine Quantifizierung der Mehrzahl der anhand der Satellitenbilddaten detektierten Kohlefeuer ermöglicht. Vor kurzem wurde ein neues Fernerkundungskonzept für die Quantifizierung von Wald- und Steppenfeuern vorgestellt, das auf der Abschätzung der Strahlungsenergie eines Feuers (FRE) beruht. In der vorliegenden Arbeit wird geprüft, inwiefern dieses Konzept auf Kohlefeuer übertragen werden kann. Eine neue Generation von Satelliteninstrumenten, die das operationelle „Enhanced Thematic Mapper“ (ETM) Instrument, den experimentellen „Bi-spectral InfraRed Detection“ (BIRD) Sensor und das „Advanced Spaceborne Thermal Emission and Reflection“ (ASTER) Radiometer einschließt, wird analysiert um zu prüfen, inwieweit mit Hilfe dieser Sensoren die Strahlungsenergie von Kohlefeuern (CFRE) abgeschätzt werden kann. Zusätzlich wird, basierend auf den Ergebnissen dieser Analyse, ein automatischer ASTER und ETM Daten Algorithmus zur Quantifizierung von Kohlefeuern vorgestellt, der für semi-aride bis aride Gebiete in Nordchina angepasst ist.

Geländearbeiten, die im September 2002 und 2003 in drei Kohleabbaugebieten in Nordchina (Wuda, Gulaben und Ruqigou) durchgeführt wurden, zeigen, dass Oberflächenanomalien von Kohlefeuern wesentlich kälter als Wald- und Steppenfeuer sind. Die theoretische Analyse der ASTER, ETM und BIRD Sensoren zeigt, dass die thermalen (TIR) oder mittleren Infrarot Kanäle (MIR) der untersuchten Sensoren besonders geeignet sind, diese „warmen Stellen“ aufzuzeichnen. Im Gegensatz hierzu sind die kurzwelligen Infrarot Kanäle (SWIR) nicht ausreichend empfindlich, um spektrale Kohlefeuerstrahlung zu registrieren. Die theoretische Studie legt dar, dass die häufig eingesetzte Zweikanalmethode zur Quantifizierung von Feuern (Dozier, 1981) nur angewandt werden kann, um relative heiße und große Kohlefeuer mit Hilfe von BIRD Daten zu quantifizieren. Für ASTER und ETM Daten können existierende Quantifizierungskonzepte für die Analyse von Kohlefeuern nicht eingesetzt werden. In dieser Arbeit wird für ASTER und ETM Daten eine neue Methode zur Bestimmung der Strahlungsenergie eines Kohlefeuers vorgestellt. Hierbei wird die aufgezeichnete TIR Strahlung des Hintergrundes und des Feuers über einen empirischen Ansatz zu der Strahlungsenergie des Kohlefeuers in Bezug gesetzt.

Diese neu entwickelte TIR Methode wird in einer Fallstudie für Gruppen von Bildelementen von visuell detektierten Kohlefeuern der untersuchten Sensoren angewandt. Die potentiellen „Kohlefeuerbildelemente“ stammen hierbei von ETM Tagdaten, sowie ASTER Nacht- und Tagdaten von den drei untersuchten Kohlegebieten in Nordchina. Die über die TIR Methode berechneten ASTER und ETM CFRE Werte werden mit CFRE-Abschätzungen von BIRD Daten verglichen, die

über die Zweikanalmethode (Dozier, 1981) bestimmt wurden. Trotz der verschiedenen räumlichen und spektralen Eigenschaften der BIRD, ASTER und ETM Instrumente, zeigen die berechneten CFRE-Werte gute Übereinstimmungen. Allerdings sind die aus den Tagesdaten abgeleiteten CFRE-Abschätzungen sehr instabil gegenüber ermittelten Schwankungen der Hintergrundtemperatur, wohingegen CFRE-Abschätzungen von Nachtdaten wesentlich stabiler sind. Ein Vergleich der aus ETM Nachtdaten abgeleiteten CFRE des Kohlegebietes Wuda mit Angaben der lokalen Minenbehörden über Kohlefeuer bedingte Kohleverluste zeigt an, dass die allgemeine Dimension der Kohlefeuerproblematik über CFRE-Abschätzungen gut angenähert werden kann. CFRE von Satellitenbilddaten könnten deshalb ein wichtiges und verlässliches Werkzeug zum Sammeln von quantitativen Daten von Kohlefeuern werden.

Ein multi-temporaler Vergleich von CFRE, die anhand von BIRD und ETM Nachtdaten der untersuchten Kohleabbaugebiete berechnet wurde, legt dar, dass nur wesentliche Verlagerungen oder Veränderungen der Aktivität von Oberflächenanomalien eines Kohlefeuers mit Hilfe von Satellitenbilddaten überwacht werden können. Diese Ergebnisse konnten nur zum Teil über Feldbeobachtungen verifiziert werden. Trotzdem deuten sie an, dass ETM und BIRD Nachtdaten dazu verwendet werden können, um wesentliche Veränderungen von Oberflächenanomalien eines Kohlefeuers zu überwachen. Allerdings können sie besonders im Fall von kleinen und kalten Oberflächenanomalien gründliche Felduntersuchungen nicht ersetzen.

LIST OF FIGURES

| | | |
|--------------------|---|----|
| Figure 1-1: | Coal fire distribution in China. | 2 |
| Figure 3-1: | Planck radiance versus wavelength for different temperatures. | 15 |
| Figure 3-2: | Solar and earth spectral radiance. | 16 |
| Figure 4-1: | Location of the Wuda, Ruqigou and Gulaben coalfield. | 26 |
| Figure 4-2: | Optical images of the Ruqigou and Gulaben coalfield. | 28 |
| Figure 4-3: | Fire fighting activities in the Ruqigou and Gulaben coalfield. | 31 |
| Figure 4-4: | Optical images of the Wuda coalfield. | 34 |
| Figure 5-1: | Coal fire related surface anomalies mapped during the field campaign in September 2002 on top of the panchromatic channel of the ETM scene from 29 th September 2002 | 37 |
| Figure 5-2: | Detailed maps of the coal fire 7 and 8 of the Wuda coalfield. | 41 |
| Figure 5-3: | Thermal and optical images taken in September 2003 of the Wuda coal fire number 7. | 42 |
| Figure 5-4: | Infrared images and optical photos of a sub-surface coal fire at the Wuda coalfield. | 43 |
| Figure 5-5: | Infrared images and optical photos of a near surface coal fire at the Wuda coalfield. | 45 |
| Figure 5-6: | Intraday temperature measurements of a horizontal black shale surface, a horizontal sandstone surface, a horizontal vegetation surface and a fire crack. | 46 |
| Figure 5-7: | Intraday temperature measurements of an approximately eastern (10° dip) and western (25° dip) facing slope. | 47 |
| Figure 5-8: | Temperature distribution on a fire crack. | 48 |
| Figure 5-9: | Temperature distribution on a fire crack. | 49 |
| Figure 6-1: | Spectral radiance recorded by the ETM channel 5 of an image pixel corresponding ground segment containing a sub-pixel fire component at various fire temperatures, fire sizes and background conditions (homogeneous background). | 60 |
| Figure 6-2: | Spectral radiance recorded by the ETM channel 5 of an image pixel corresponding ground segment containing a sub-pixel fire component at various fire temperatures, fire sizes and background conditions (inhomogeneous background). | 61 |
| Figure 6-3: | Spectral radiance recorded by the ETM channel 7 of an image pixel corresponding ground segment containing a sub-pixel fire component at various fire temperatures, fire sizes and background conditions (homogeneous | 62 |

| | | |
|---------------------|--|-----------|
| | background). | |
| Figure 6-4: | Spectral radiance recorded by the ETM channel 7 of an image pixel corresponding ground segment containing a sub-pixel fire component at various fire temperatures, fire sizes and background conditions (inhomogeneous background). | 63 |
| Figure 6-5: | Spectral radiance recorded by the ETM channel 6 of an image pixel corresponding ground segment containing a sub-pixel fire component at various fire temperatures, fire sizes and background conditions (homogeneous background). | 64 |
| Figure 6-6: | Spectral radiance recorded by the ETM channel 6 of an image pixel corresponding ground segment containing a sub-pixel fire component at various fire temperatures, fire sizes and background conditions (inhomogeneous background). | 65 |
| Figure 6-7: | Spectral radiance recorded by the ASTER channel 10 of an image pixel corresponding ground segment containing a sub-pixel fire component at various fire temperatures, fire sizes and background conditions (homogeneous background). | 71 |
| Figure 6-8: | Spectral radiance recorded by the ASTER channel 10 of an image pixel corresponding ground segment containing a sub-pixel fire component at various fire temperatures, fire sizes and background conditions (inhomogeneous background). | 72 |
| Figure 6-9: | Spectral radiance recorded by the ASTER channel 14 of an image pixel corresponding ground segment containing a sub-pixel fire component at various fire temperatures, fire sizes and background conditions (homogeneous background). | 73 |
| Figure 6-10: | Spectral radiance recorded by the ASTER channel 14 of an image pixel corresponding ground segment containing a sub-pixel fire component at various fire temperatures, fire sizes and background conditions (inhomogeneous background). | 74 |
| Figure 6-11: | Band-averaged Planck's function for the ASTER TIR channels. Due to the fact that the ASTER TIR channels have an upper saturation limit, the band-averaged Planck's function is only given in the sensibility range of the corresponding TIR bands. | 77 |
| Figure 6-12: | Spectral radiance recorded by the BIRD MIR channel of an image pixel corresponding ground segment containing a sub-pixel fire component at various fire temperatures, fire sizes and background conditions (homogeneous | 79 |

| | | |
|---------------------|---|------------|
| | background). | |
| Figure 6-13: | Spectral radiance recorded by the BIRD MIR channel of an image pixel corresponding ground segment containing a sub-pixel fire component at various fire temperatures, fire sizes and background conditions (inhomogeneous background). | 80 |
| Figure 6-14: | Spectral radiance recorded by the BIRD TIR channel of an image pixel corresponding ground segment containing a sub-pixel fire component at various fire temperatures, fire sizes and background conditions (homogeneous background). | 81 |
| Figure 6-15: | Spectral radiance recorded by the BIRD TIR channel of an image pixel corresponding ground segment containing a sub-pixel fire component at various fire temperatures, fire sizes and background conditions (inhomogeneous background). | 82 |
| Figure 6-16: | Band-averaged Planck's function for the BIRD MIR (blue) and TIR (green) channels. | 84 |
| Figure 7-1: | Surface temperature plotted against the ratio of the total fire energy emitted by a unit area surface to its corresponding spectral radiance recorded in the spectral range of the ETM band 6. | 87 |
| Figure 7-2: | Relationship between the spectral radiance observed by the ETM TIR sensor and the fire total emitted energy release. | 88 |
| Figure 7-3: | Surface temperature plotted against the ratio of the total fire energy emitted by a unit area surface to its corresponding spectral radiance recorded in the spectral range of ASTER bands. | 90 |
| Figure 7-4: | Relationship between the spectral radiance observed by the ASTER TIR sensor and the fire total emitted energy release. Data are from 1000 modelled fire scenarios with a fire area ranging between 1 m to 1100 m, a fire temperature ranging between 350K to 600K and a background temperature ranging between 273K to 300 K. | 91 |
| Figure 8-1: | ETM SWIR and TIR channels with superimposed coal fire related, surface anomalies. | 98 |
| Figure 8-2: | ETM TIR bands with superimposed coal fire related, surface anomalies in the Wuda coalfield and corresponding radiative energy release images of detected coal fire clusters. | 101 |
| Figure 8-3: | ETM TIR bands with superimposed coal fire related surface anomalies of the Ruqigou / Gulaben coalfields and corresponding radiative energy release images of detected coal fire clusters. | 102 |

| | | |
|---------------------|--|------------|
| Figure 8-4: | BIRD MIR bands with superimposed coal fire related, surface anomalies of the Wuda coalfield and corresponding radiative energy release images of detected coal fire clusters. | 110 |
| Figure 8-5: | BIRD MIR bands with superimposed coal fire related, surface anomalies of the Ruqigou / Gulaben coalfields and corresponding radiative energy release images of detected coal fire clusters. | 111 |
| Figure 8-6: | ASTER and ETM TIR bands with superimposed coal fire related, surface anomalies of the Wuda coalfield and radiative energy release images of detected coal fire clusters. | 116 |
| Figure 9-1: | ETM channel 6 (daytime, 21.09.02) brightness temperatures, superimposed with a detailed surface map of the sub-surface coal fire 7 of the Wuda coalfield. | 121 |
| Figure 9-2: | ETM channel 6 (night-time, 28.09.02) brightness temperatures, superimposed with a detailed surface map of the sub-surface coal fire 7 of the Wuda coalfield. | 122 |
| Figure 9-3: | ETM channel 6 brightness temperatures (daytime, 21.09.02), superimposed with a detailed surface map of the near-surface coal fire 8 of the Wuda coalfield. | 123 |
| Figure 9-4: | ETM channel 6 brightness temperatures (night-time, 28.09.02), superimposed with a detailed surface map of the near-surface coal fire 8 of the Wuda coalfield. | 124 |
| Figure 9-5: | ETM night-time TIR channels of the Wuda coalfield with corresponding CFRE images. The CFRE images were computed via the TIR method. | 129 |
| Figure 9-6: | BIRD night-time MIR channels of the Ruqigou coalfield with corresponding CFRE images The CFRE images were computed via the bi-spectral technique using BIRD MIR and TIR channel as input data. | 133 |
| Figure 10-1: | Outline of the coal fire quantification (QFC) algorithm. | 139 |
| Figure 10-2: | An example of the CFQ algorithm main output: CFRE images from the Ruqigou and Gulaben coalfields, derived from ETM night-time TIR data. | 143 |

LIST OF TABLES

| | | |
|--------------------|--|-----------|
| Table 1-1: | Listing of satellite data used in this study. | 6 |
| Table 2-1: | Coal fire classification according to Zhang et al. (2004). | 11 |
| Table 3-1: | Spectral ranges and corresponding radiation sources. | 17 |
| Table 4-1: | Content of carbon, hydrogen and nitrogen in coal samples of the Ruqigou and Gulaben coalfields. | 30 |
| Table 4-2: | Water content, ash content and calorific value of coal samples of the Ruqigou and Gulaben coalfields. | 30 |
| Table 4-3: | Content of carbon, hydrogen and nitrogen in coal samples of the Wuda coalfield. | 33 |
| Table 4-4: | Water content, ash content and calorific value of coal samples of the Wuda coalfield. | 33 |
| Table 5-1: | Technical characteristics of the radiant thermometer used during the field campaigns in September 2002 and September 2003. | 38 |
| Table 5-2: | Technical characteristics of the thermal camera used during the field campaign in September 2003. | 38 |
| Table 5-3: | Temperatures of coal fire related surface anomalies of representative coal fires of the study areas measured during the field campaign in 2002 and 2003. | 40 |
| Table 5-4: | Temperature measurements of the Yellow River during cloud free ASTER, ETM and BIRD satellite overpasses in September 2002. | 50 |
| Table 6-1: | Atmospheric parameters used to model MIR and TIR atmospheric effects. | 57 |
| Table 6-2: | Atmospheric parameters used to model SWIR atmospheric effects. | 57 |
| Table 6-3: | Spectral characteristics of the ETM instrument. | 58 |
| Table 6-4: | Minimum and maximum coal fire size which can be registered by the ETM channel 5 and 7 at a certain fire temperature and background condition. | 66 |
| Table 6-5: | Minimum and maximum coal fire size which can be registered by the ETM channel 6 at a certain fire temperature and background condition. | 66 |
| Table 6-6: | ASTER instrument characteristics. | 69 |
| Table 6-7: | Minimum and maximum coal fire size which can be registered by the ASTER channel 10 at a certain fire temperature and background condition. | 75 |
| Table 6-8: | Minimum and maximum coal fire size which can be registered by the ASTER channel 14 at a certain fire temperature and background condition. | 75 |
| Table 6-9: | Technical characteristics of the two BIRD imaging instruments. | 78 |
| Table 6-10: | Minimum coal fire size which can be registered by the BIRD MIR channel at a certain fire temperature and background condition. | 83 |
| Table 6-11: | Minimum coal fire size which can be registered by the BIRD TIR channel at a | 83 |

certain fire temperature and background condition.

| | | |
|--------------------|---|------------|
| Table 8-1: | Coal fire related, surface radiative energy releases, derived from recognised anomaly pixels in the ETM TIR bands, for mapped Wuda coalfield anomaly zones. | 103 |
| Table 8-2: | Coal fire related, surface radiative energy releases derived from recognised anomaly pixels in the ETM TIR bands for mapped Ruqigou / Gulaben coalfield anomaly zones. | 104 |
| Table 8-3: | Path radiance, atmospheric ground-to-sensor transmittance, and downwelling flux of atmosphere used for atmospheric corrections of the BIRD MIR and TIR data. | 106 |
| Table 8-4: | Coal fire related, surface-radiative energy releases, equivalent fire temperatures and equivalent fire sizes, derived from recognised anomaly pixels in the BIRD MIR bands, for each mapped anomaly zone of the Wuda coalfield. | 112 |
| Table 8-5: | Coal fire related, surface-radiative energy releases, equivalent fire temperatures and equivalent fire sizes, derived from recognised anomaly pixels in the BIRD MIR bands, for each mapped anomaly zone of the Wuda coalfield. | 113 |
| Table 8-6: | Coal fire related, surface-radiative energy releases, derived from recognised anomaly pixels in the ETM and ASTER TIR bands, for mapped anomaly zone of the Wuda coalfield. | 117 |
| Table 9-1: | Coal fire related, surface energy releases derived from two ETM channel 6 night-time data sets at different temporal settings. | 130 |
| Table 9-2: | Coal fire related, surface radiative energy releases, equivalent fire temperatures and equivalent fire sizes, derived from two BIRD data sets (MIR + TIR channels) at different temporal settings. | 134 |
| Table 10-1: | Radiances at the maximum and minimum digital number of the ETM TIR channel, used to transform ETM level 1b DN values to spectral radiances. | 140 |
| Table 10-2: | Radiances at the maximum and minimum digital number of the ASTER TIR channel, used to transform ETM level 1b DN values to spectral radiances. | 140 |
| Table 10-3: | Path radiance, atmospheric ground-to-sensor transmittance and downwelling flux of atmosphere used for the atmospheric correction of the ETM channel 6. | 141 |
| Table 10-4: | Path radiance, atmospheric ground-to-sensor transmittance and downwelling flux of atmosphere used for the atmospheric correction of the ASTER channel 10. | 141 |
| Table 10-5: | An example of the CFQ output ASCII file. | 144 |

LIST OF ACRONYMS

| | |
|-------------------------|--|
| ASTER | Advanced Spaceborne Thermal Emission and Reflection Radiometer |
| AVHRR | Advanced Very High Resolution Radiometer |
| BAM | German Federal Institute for Materials Research and Testing |
| BIRD | Bi-spectral InfraRed Detection |
| BMBF | German Ministry of Education and Science |
| CFRE | coal fire radiative energy |
| DLR | German Aerospace Centre |
| DMT | German Montan Technology |
| DN | digital number |
| EOS | Earth Observing System Data Gateway |
| ETM | Enhanced Thematic Mapper |
| ERSDAC | US Earth Remote Sensing Data Analysis Center |
| ESA | European Space Agency |
| GTZ | Deutsche Gesellschaft für technische Zusammenarbeit (The GTZ is an German international cooperation enterprise for sustainable development with worldwide operations.) |
| GMES OC | Global Monitoring for Environment and Security Earth Observation Component |
| HSRS | Hot Spot Recognition System |
| IFOV | instantaneous field of view |
| ITC | International Institute for Geo-Information Science and Earth Observation |
| LD | lower registration limit |
| L_{max} | radiance at the maximum calibrated digital number |
| L_{min} | radiance at the minimum calibrated digital number |
| L_{path} | atmospheric path radiance |
| METI | Japans Ministry of Economy, Trade and Industry |
| MIR | mid infrared spectral region |
| MODIS | Moderate Resolution Imaging Spectro-radiometer |
| NASA | US National Aeronautics and Space Administration |
| NIR | near infrared spectral region |
| NOAA | US National Oceanic and Atmospheric Administration |
| R I | background model (detailed description in chapter 6.1.1): night-time, no reflectance |
| R II | background model (detailed description in chapter 6.1.1): daytime, |

| | |
|----------------|---|
| | homogeneous coal surface |
| R III | background model (detailed description in chapter 6.1.1): daytime, homogeneous sandstone surface |
| R IV | background model (detailed description in chapter 6.1.1): daytime, heterogeneous coal surface |
| R IV | background model (detailed description in chapter 6.1.1): daytime, heterogeneous sandstone surface |
| SWIR | short wave infrared spectral region |
| Th I | background model (detailed description in chapter 6.1.1): winter, homogeneous background |
| Th II | background model (detailed description in chapter 6.1.1): summer, homogeneous background |
| Th III | background model (detailed description in chapter 6.1.1): winter, heterogeneous background |
| Th IV | background model (detailed description in chapter 6.1.1): summer, heterogeneous background |
| TM | Thematic Mapper |
| trans | atmospheric transmissivity |
| UD | upper registration limit |
| USGS | US Geological Survey |
| VAS | Visible Infrared Spin Scan Radiometer and Atmospheric Sounder |
| VIS | visible spectral range |
| WAOSS-B | Wide Angle Optoelectronic Stereo Scanner |

INTRODUCTION

1 INTRODUCTION

1.1 Aims and objectives

Coal fires cause severe environmental and economic problems worldwide. They result in a reduction of the coal reserve, lead to atmospheric pollution through the emission of greenhouse related gases, cause land subsidence and negatively impact human health in nearby areas.

China is the worlds' largest coal producer and faces the world's biggest coal fire problem (Kuenzer et al., submitted). Although coal basins are widely distributed in China, coal fires occur mainly in the northern part of the country where semi-arid to arid conditions prevail and where most Chinese mining activity occurs (Rosema et al., 1999). Major coal fire areas stretch out in a 5000 km long belt from the Xinjiang province in the west, to the Pacific in the east (Zhang, 1998; figure 1-1). There is geological evidence, as well as historical documentation, that coal fires existed in northern China more than 1000 years ago, although it is assumed that the number of coal fires increased drastically since large-scale mining activities began (Gielisch, 2002; Rosema et al., 1999).

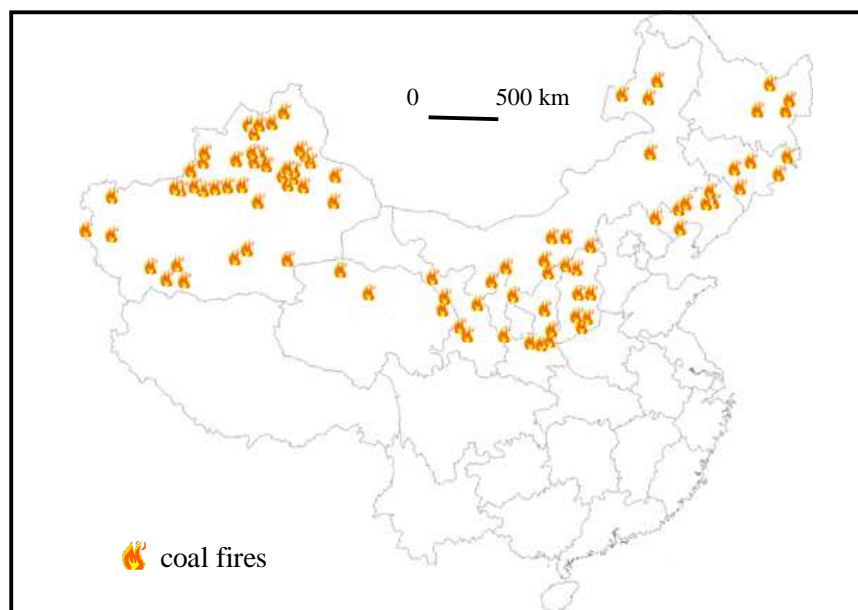


Figure 1-1: Coal fire distribution in China. Major coal fire areas in China are located in a 5000 km long east-west mining belt (adapted from: <http://www.gi.alaska.edu/~prakash/coalfires/china.html>).

Due to the enormous coal fire induced economic and environmental threat, the Chinese government is putting heavy emphasis on the coal fire problem. In 1994 the coal fire problem was mentioned as one of the five most serious geological hazards in the ' 21st Century Agenda' (Guan et al., 1996; Zhang, 1998). A geo-scientific Sino-German Coal Fire Research Initiative has, since 2003, been investigating the coal fire problem in China. The project includes various partners from different geo-scientific fields and focuses on developing innovative technologies for exploration, extinction and monitoring of coal fires in China. The German Ministry of Education and Science (BMBF) founded a remote sensing

1 Introduction

project in 2001, at the German Aerospace Centre (DLR), as part of a preliminary engagement in the issue. One of its main objectives is to set up an automated, satellite image based coal fire detection and quantification algorithm, that can be used to detect and quantify coal fires in large regions in northern China.

Satellite remote sensing has already been used successfully to detect coal fires in the past (e.g. Chen, 1992; Mansor et al., 1994; Prakash et al., 1995; Prakash et al., 1997; Zhang et al., 1997; Zhang, 1998; Prakash et al., 1999; Vekerdy et al., 1999). In 2004 Voigt et al. presented an integrated, remote sensing approach to the delineation of coal fires in large regions. Zhang et al. (submitted) have recently developed an automated (i.e. non-interactive) coal fire detection algorithm, which has been proven to detect coal fires in unknown areas on Enhanced Thematic Mapper (ETM) imagery. However, a remote sensing technique, effective in quantifying coal fires in large regions is still missing. Existing coal fire quantification approaches have focused on the determination of coal fire size and temperature, have been restricted to a few selected coal fire related hot spots (e.g. Zhang et al., 1997; Cassells et al., 1996; Prakash et al., 1997) and are not capable of quantifying coal fires on a regional scale.

In this thesis the concept of remotely measured coal fire radiative energy (CFRE) is introduced as a powerful tool to quantify coal fires on a regional scale. A new generation of satellite instruments is theoretically investigated, examining the instruments' capability to register spectral coal fire radiance, including the operational ETM instrument, the experimental Bi-spectral InfraRed Detection (BIRD) satellite sensor and the experimental Advanced Spaceborne Thermal Emission and Reflection Radiometer (ASTER). In detailed case studies CFRE are computed from ASTER, ETM and BIRD data, for entire coalfields in central China and by comparing these numbers with given numbers of coal fire induced coal loss, the possibilities and limitations of a satellite data based coal fire quantification approach are outlined. In addition, a comparison is made between CFRE computed from multi-temporal BIRD and ETM, with the aim of determining if thermal satellite data can be used to map movements, or activity changes, of coal fire related surface anomalies. Finally, an automated coal fire quantification algorithm, adapted to quantify coal fires in northern China using ASTER and ETM data, is presented.

1.2 Previous works

Airborne and space-borne remote sensing has long been used to quantify forest and grassland fires. A few studies, such as Kaufman et al. (1990), directly observed smoke emissions via satellite observations, but most research concentrated on deriving thermal properties of vegetation fires via the analysis of infrared satellite sensor data. Within the last two decades automated fire detection and quantification algorithms have been developed for Advanced Very High Resolution Radiometer (AVHRR), Visible Infrared Spin Scan Radiometer and Atmospheric Sounder (VAS), and Moderate

1 Introduction

Resolution Imaging Spectro-radiometer (MODIS) data (e.g. Prins and Menzel, 1994; Lee and Tag 1990; Kaufman et al., 1998). The potential of these algorithms to quantify vegetation fires has been demonstrated in large number of case studies (e.g. Matson and Holben, 1987; Setzer and Pereira, 1991).

A common and widely applied fire quantification method is the so-called bi-spectral technique (Dozier, 1981). This quantification approach uses the radiant energy difference of two thermal channels to compute the equivalent temperature and size of a sub-pixel fire component (description in chapter 4, section 4.3.1). Giglio and Kendall (2001) recently investigated the bi-spectral method and found large errors, unless careful consideration of the accuracy of the inter-channel registration and the background temperature characteristics is taken. A major limitation of the bi-spectral technique is the requirement of fire induced enhanced pixel values in at least two infrared channels.

In the coal fire context, coal fire related enhanced pixel values in two infrared channels are only reported from Landsat-5 Thematic Mapper (TM) data. Zhang et al. (1997) calculated temperatures of two sub-pixel coal fires in NE China from TM band 6 data using the bi-spectral approach. Cassells et al. (1996) applied the bi-spectral technique on Landsat-5 TM short wave infrared data to compute the equivalent fire temperature and area of three surface coal fires in NE China. Prakash and Gupta (1999) and Prakash et al. (1997) estimated temperature and area extent of coal fires in the Jharia coalfield (India). They derived pixel-integrated temperatures of potential surface and sub-surface coal fires from TM band 5, 6 or 7 data and applied the bi-spectral technique on coal fire related anomaly pixels that showed enhanced and unsaturated brightness values in both TM channel 5 and 7. Approximately 15 % of the detected surface 'coal fire pixels' could be quantified in these studies using the bi-spectral approach.

To address the requirement of a remote sensing tool, effective in estimating vegetation fire related emissions on a global scale, Kaufman et al. (1996) introduced the concept of remotely measured fire radiative energy (FRE). They estimated FRE of vegetation fires from MODIS data via the analysis of a single infrared channel, using a semi-empirical relationship between the spectral fire radiance and the total emitted fire radiative energy (so-called MODIS method). Recently, Wooster et al. (2003) presented an alternative approach (the so-called MIR method) to calculate FRE directly via the analysis of 'fire pixels' radiances of the BIRD middle infrared (MIR) channel. They computed FRE from forest fires in Australia using BIRD and near-simultaneous MODIS data according to the MIR and MODIS method. They compared their results to retrievals of FRE based on derived fire temperature and area computed via the bi-spectral method and found a good correspondence of derived FRE values. Although the concept of remotely measured FRE has been proven to have a high potential to quantify

1 Introduction

vegetation fires (e.g. Wooster, 2002; Kaufman et al., 1998) it has yet not been applied in the coal fire context.

Saraf et al. (1995) and Prakash et al. (1995) evaluated the possibilities and limitations of remote sensing data to estimate the depth of sub-surface coal fires. Both used TM thermal infrared data to pinpoint sub-surface fire locations and located coal outcrops on TM visible and near infrared channels. The depth of the coal fires was computed using field-derived information on the strike and dip of coal layers and the location of coal outcrops and coal fires in the satellite data.

1.3 Research approach

Two field campaigns were carried out between the 5th and the 29th of September 2002 and between the 10th and the 24th of September 2003, in three coalfields in central China. The three investigated coalfields are located in Ningxia Autonomous Region (Ruqigou coalfield) and Inner Mongolia Autonomous Region (Gulaben and Wuda coalfields). They include all types of coal fires, have different geological and morphological settings and are, like most of the coal fire locations in China, sparsely covered by vegetation. During the two field campaigns the coal fire related surface anomalies in the study areas were mapped and the surface temperatures of the active coal fires were measured (description in chapter 5). These field data are used as ground truth data for the remote sensing analysis.

Taking into consideration the sensor specific, spectral response functions, and the thermal coal fire properties observed during the field campaign, the potential of the ASTER, ETM and BIRD to register coal fire related spectral radiative energy releases is theoretically analysed (description in chapter 6). In addition, existing FRE retrieval methods are evaluated towards their potential to estimate coal fire related surface energy (CFRE) and a new method to compute CFRE via the analysis of TIR spectral radiances is presented (description in chapter 7).

The potential of this new approach to quantify coal fire related surface anomalies is evaluated in two case studies. ETM, ASTER and BIRD satellite data covering the test areas were acquired at different temporal settings including field campaign simultaneous observations. The satellite data are calibrated, geometrically corrected and ‘coal fire pixels’¹⁻¹⁾ are visually detected. In the first case study (description in chapter 8) the potential of ETM, ASTER and BIRD data to quantify coal fires on a regional scale is analysed. The newly developed CFRE retrieval method is applied on visually detected ETM and ASTER fire clusters, including winter and field campaign simultaneous daytime summer

¹⁻¹⁾ The term ‘coal fire pixels’ is used in this thesis to describe a satellite data pixel which can be related to a coal fire.

1 Introduction

data from the year 2002 and 2003. In addition, CFRE are computed via an existing FRE retrieval concept using near simultaneous BIRD data. BIRD derived CFRE are compared to ASTER and ETM CFRE retrievals. For each investigated satellite scene the total CFRE is computed for the Wuda, Ruqigou and Gulaben coalfield and compared to coal fire induced coal loss reported from the corresponding mining companies, outlining both the possibilities and limitations of each sensor to quantify coal fires on a regional scale. In the second case study (description in chapter 9) the potential of BIRD and ETM data to quantify detailed shifts or activity changes of coal fires is evaluated. Two detailed coal fire maps from the Wuda coalfield, as well as ground temperatures observed during an ETM night-time and daytime overpass, are carefully compared to the corresponding satellite data. In addition, CFRE derived from two BIRD night-time data sets as well as two ETM night-time data sets are compared to each other to analyse if multi-temporal thermal satellite data can be used to observe shifts or activity changes of coal fire related surface anomalies.

Finally, the results of the theoretical investigations and of the case studies are combined and an automated ASTER and ETM data based coal fire quantification algorithm suitable to quantify coal fires in northern China (description in chapter 10) is presented.

1.4 Available satellite data

| sensor | path / row | acquisition date |
|--------|-------------|-------------------------|
| ETM | 129 / 33 | 2001/09/25 (nigh-time) |
| | 129 / 33 | 2002/09/21 (daytime) |
| | 226 / 221 | 2002/09/28 (night-time) |
| | 129 / 33 | 2003/02/12 (daytime) |
| ASTER | 35 / 41 | 2002/09/21 (night-time) |
| BIRD | not defined | 2002/02/04 (daytime) |
| | | 2002/09/21 (daytime) |
| | | 2003/01/16 (night-time) |
| | | 2003/09/27 (night-time) |

Table 1-1: *Listing of satellite data used in this study.*

In this study level 1b¹⁻²⁾ satellite data sets from the ETM, ASTER and BIRD sensor were investigated. A detailed listing of the investigated data sets is provided in table 1-1.

¹⁻²⁾ The term level 1b data refers to systematically corrected satellite data sets, i.e. the data is already corrected for scan direction and band alignment as well as radiometry.

1 Introduction

The ETM data sets were either requested as level 1b data directly from the Earth Observing System Data Gateway (EOS) or acquired during a DLR acquisition campaign at the mobile ground receiving station in Ulan Bator. The level 1b data processing of the Ulan Bator ETM data was performed at the DLR. The ASTER data acquisition was requested by the International Institute for Geo-Information Science and Earth Observation (ITC, Holland). The raw ASTER data sets were processed to level 1b data sets at the ITC. The BIRD data were acquired and processed to level 1b data sets by the DLR BIRD team.

THEORETICAL BACKGROUND

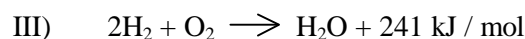
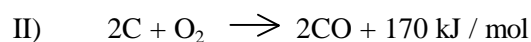
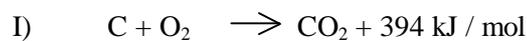
2 THEORETICAL BACKGROUND OF COAL FIRES

The term 'coal fire' refers to combustion in a coal seam, coal storage pile or coal waste pile. In this chapter a short introduction to the coal fire problematic is given, including a description of the coal ignition and combustion process, a presentation of different coal fire types, a description of coal fire related thermal anomalies and an introduction to coal fire induced hazards in China.

2.1 Coal ignition and combustion

Coal is a highly combustible material, and, in addition to a capacity for ignition by external sources, many coals are prone to self ignition. External ignition sources, capable of igniting coal fires, are lightning (Guan et al., 1996), forest fires (Bustin and Mathews, 1985) and man-made fires caused by mining accident or careless human interactions (Kuenzer, submitted). In Indonesia coal fires ignited by forest fires are a serious hazard. It is known that outcropping coal seams ignited by forest fires continue to burn, and can cause forest fires to restart several months after the forest fire was extinguished (Zhang et al., 2004).

Self ignition of coal is, according to recent publications, the second greatest cause of coal fires of large extent, second only to man-made external fire ignitions (Walker, 1999; Van Genderen and Guan, 1997; Kuenzer, submitted). Self-ignition of materials, also referred to as spontaneous combustion, refers to the onset of exothermic chemical reaction and a subsequent temperature rise within a combustible material, without the action of an additional ignition source (Ackersberg, 2003). The self-ignition of coal originates at the interface of coal and atmosphere and occurs when the heat evolved by coal oxidation exceeds the amount of heat dissipated by conduction, convection or self-radiation (Ackersberg, 2003). The low temperature oxidation of coal can be described by the following process equations:



The critical temperature above in which the oxidation and self-heating processes become self-sustaining is about 50 °C for lignites and 70 – 80 °C for bituminous coals (Ackersberg, 2003). The risk of spontaneous combustion strongly depends on a number of external factors as well as on coal specific parameters. Coal specific parameters include, e.g. coal rank (degree of coalification), petrographic composition, methane content, moisture content, as well as particle size and surface area. High coal rank, high content of original oxidised plant material, a relatively large particle size and low specific internal surface decreases the coal' s selfheating capacity (Ackersberg, 2003).

2 Theoretical background of coal fires

External factors such as climate, geology and geomorphology that might influence the self heating process are not yet fully understood and are part of an ongoing research project within the Sino-German Coal Fire Initiative. A dry desert-like climate and high crack frequency are assumed to positively support the self-ignition process (Rosema et al., 1999).

Once a coal fire has started in a coal seam it has a high potential to burn for a long time by spreading along the strike and dip of the coal seam. A coal fire that, for example, started at the surface of an outcropping, dipping coal seam, can cause overlying bedrocks to collapse, resulting in sufficient oxygen supply for the combustion of underground coal. Underground coal fires are known to burn in a depth of several hundred meters in north China (Gielisch, 2002). In most Chinese coalfields underground coal fires are far more frequent than surface coal fires (Rosema et al., 1999). In addition, coal fires can burn for decades, and once a coal fire has started, the problems of extinguishing it are remarkable. The oldest known continuously burning coal fire started to burn 2000 years ago in New South Wales, Australia (Zhang et al., 2004).

2.2 Classification of coal fires

A variety of coal fire classification schemes have been applied by different researchers, for example, Van Genderen and Guan, 1997; Yang, 1995. Zhang et al. (2004) recently recommended a coal fire classification, here illustrated in table 2-1.

| first class | second class | attributes |
|----------------|---------------------|------------------------------------|
| coal seam fire | nature coal fire | surface/underground or sub-surface |
| | coal mine fire | paleo/recent |
| coal heap fire | coal waste fire | extinct/dormant /active |
| | coal stockpile fire | |

Table 2-1: Coal fire classification according to Zhang et. al. (2004).

Coal fires can occur in-situ directly on coal seams as well as on anthropogenic coal heaps (coal waste piles and stockpiles) and consequently, are given a primary classification into coal seam and coal heap fires. Zhang et al. (2004) subdivide the coal fires further according to ignition process, into mining related coal fires and natural coal fires. In addition, attributes are given for each coal fire, as to whether it is surface or sub-surface, paleo (fire was burning in the paleo-time) or recent (fire was burning in recent time), extinct (extinct coal fire and incapable of further burning), dormant (fire is not spreading, but probably capable of re-burning) or active (fire is burning and spreading).

2 Theoretical background of coal fires

2.3 The thermal surface anomaly of coal fires

A coal fire induced thermal surface anomaly (CFSA) is an imported fire characteristic that can be investigated by ground as well as by airborne and satellite based surveys. Due to the fact that coal fires are not restricted to the surface but also occur underground, the CFSA pattern can be rather complex.

The combustion heat of coal is in the order of 30 MJ / kg for standard hard coal to 34 MJ / kg for anthracite coal. The combustion energy dissipates into the environment by a variety of processes such as direct radiation, convection of the air mass above the fire and conduction into the ground. Convection is the physical term used to describe the heat transport by the movements of gases, while conduction refers to the heat transport from solid to solid materials. In the absence of solid matter heat can be transported by radiation.

During the combustion of outcropping coal layers energy is mainly lost by radiation. According to Rosema et al. (1999) conductive heat transports only result in a small, heated rock margin in the vicinity of the surface coal fire, not exceeding a width of a few meters. However, the combusted energy of surface coal fires is also lost by convection of the air mass above the coal fire. The thermal surface pattern of sub-surface coal fires is caused by radiation, conduction and convection. Heat is transported to the surface through the overburdened rocks, by means of the transport of exhausted gases in cracks, as well as through conduction in the coal fire overlying bedrock. In contrast to surface coal fires, sub-surface coal fires spread at such a low speed that the conductive heat transport is significant (Rosema et al., 1999). The convective heat transport is relatively fast, resulting in a significant CFSA along crack zones soon after the fire developed (Rosema et al., 1999).

Zhang (1998) investigated surface temperatures of coal fires in Xinjiang (China) and classified the thermal coal fire induced anomalies into low-amplitude thermal anomalies (surface temperature of up to 293 K above the background temperature), medium-amplitude thermal anomalies (surface temperature between 293 K to 393 K above the background temperature) and high-amplitude thermal anomalies (surface temperature from 393 K to over 573 K above the background temperature). According to his observation most investigated, coal fire induced, CFSA in Xinjiang can be classified as low-amplitude thermal anomalies. Goerlich (2004, pers. communication) investigated coal fires in the framework of a German GTZ ²⁻¹⁾ project at various coalfields in Xinjiang and reported that the overall majority of the investigated coal fires had surface temperatures below 600 K.

²⁻¹⁾ The GTZ is an international cooperation enterprise for sustainable development with worldwide operations. Bodo Goerlich is a coal fire expert of this GTZ coal fire project.

2.4 Environmental impacts and hazards of coal fires in China

Environmental impact and hazards of coal fires in China have been investigated by Feng et al. (1973), Guan et al. (1996), Cassells and Genderen (1995) and Kuenzer et al. (submitted). Major threats include:

- reduction of the coal reserve
- atmospheric pollution through the emission of toxic and green house related gases
- land subsidence

Estimates of annual coal fire related coal losses in China range from 10-20 Mt (Guan et al., 1996) to 200 Mt (Cassells and Genderen, 1995) per year. Taking into consideration that China is the biggest coal producer in the world, with an annual production of 1000 Mt of raw coal, the enormous economic coal fire threat becomes obvious. It is important to note here that coal fires not only burn out coal resources, but also lead to blockage and devaluation of coal resources proximal to the burning coal seam (Zhang, 2004).

Coal fire related gaseous emissions have both local and global consequences. They include green house related gases like carbon monoxide (CO), carbon-dioxide (CO₂), methane (CH₄), sulphur-dioxide (SO₂) as well as toxic gases like hydrogen sulphide (H₂S) and nitrous oxide (N₂O). The gaseous emissions are a long-term health threat for the local population and contribute to the problem of global warming. CO₂ emissions of coal fires in China are currently under evaluation. First estimates range from 0.1 % (Kuenzer et al., submitted) to 2 % (Cassells and Genderen, 1995) of the amount of the total annual man-made CO₂ emission.

In addition, the volume loss caused by burned out coal seams often leads to land subsidence, land slides and the development of cracks or burned pits, posing a threat to local infrastructures and buildings. Burned pits of up to 10 m in diameter and cracks up to 2.5 m width are reported from coalfields in Xinjiang, China (Zhang et al., 2004). According to Zhang et al. (2004) land subsidence is mainly restricted to large coal fire areas, whilst significant subsidence rates are most probably caused by combined effects of both coal fires and coal mining.

3 THEORETICAL BACKGROUND THERMAL REMOTE SENSING

This chapter consists of an introduction to thermal remote sensing, with a short explanation of general principles and an account of thermal correction and calibration techniques. It also contains a brief review of existing fire quantification techniques. For a detailed introduction to thermal remote sensing, see e.g. Lillesand and Kiefer (1994).

3.1 General background

3.1.1 Emissivity, Planck's law, Wien's displacement law, Stefan-Boltzmann's law

All materials above zero K in temperature emit radiation. A perfect emitter, the so-called 'blackbody', emits the maximum amount of radiation at each wavelength. No real material is a perfect emitter and the emissivity (ϵ) of a real material describes how closely its emittance approximates a blackbody:

$$\epsilon_{\lambda,T} = \frac{L_{gb,\lambda}(T)}{L_{bb,\lambda}(T)} \quad (3-1)$$

where:

$$\begin{aligned} \epsilon_{\lambda,T} &= \text{emissivity at a certain wavelength and temperature} \\ L_{bb,\lambda}(T) &= \text{blackbody radiance at a certain wavelength and temperature} \\ L_{gb,\lambda}(T) &= \text{real radiance at a certain wavelength and temperature} \end{aligned}$$

The emissivity is a function of both temperature and wavelength.

The spectral radiance emitted by a blackbody, at a temperature (T), is given by the Planck Function as:

$$L_{bb} = \frac{c_1}{\lambda^5 \pi [e^{c_2/\lambda T} - 1]} \quad (3-2)$$

where:

$$\begin{aligned} L_{bb} &= \text{blackbody radiance} && [\text{W m}^{-2} \text{sr}^{-1} \mu\text{m}^{-1}] \\ \lambda &= \text{wavelength} && [\text{m}] \\ T &= \text{temperature} && [\text{K}] \\ c_1 &= \text{first radiation constant: } 3.742 \times 10^{-22} && [\text{W m}^3 \mu\text{m}^{-1}] \\ c_2 &= \text{second radiation constant: } 0.014 && [\text{m K}] \end{aligned}$$

3 Theoretical background thermal remote sensing

For each temperature the Planck Function has a single maximum at a certain wavelength:

$$\lambda_m = \frac{2897.9}{T} \quad (3-3)$$

where:

$$\lambda_m = \text{wavelength of maximum emission for a blackbody} \quad [\mu\text{m}]$$

Equation (3-3) is known as Wien's displacement law and it indicates that the wavelength of maximum emission shifts toward lower wavelengths at higher temperatures. Figure 3-1 shows Planck radiances plotted versus wavelength and temperature.

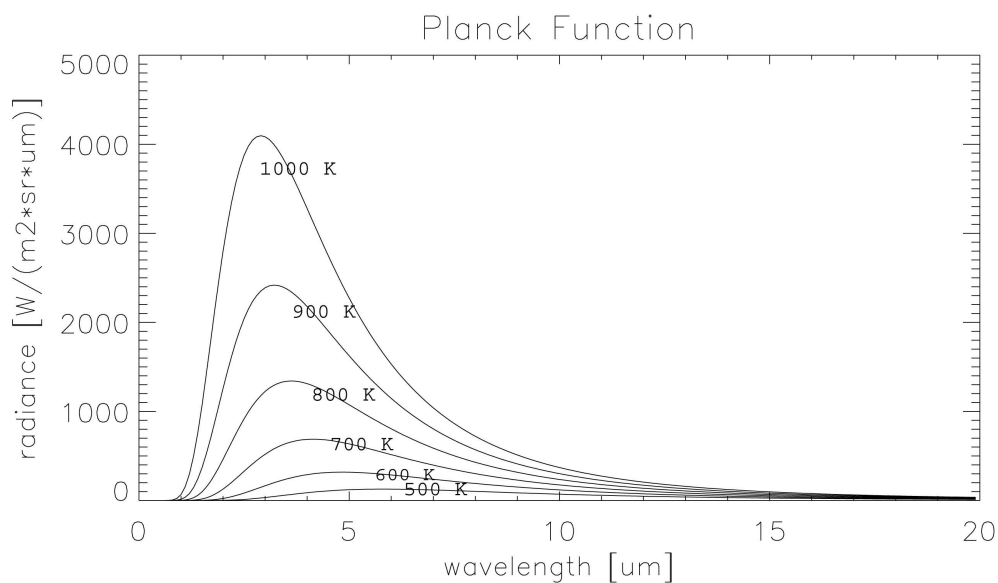


Figure 3-1: Planck radiance versus wavelength for different temperatures. It is important to note that the wavelength of maximum emission shifts toward lower wavelengths at higher temperatures.

Thermal satellite sensors do not register radiances at a discrete spectral wavelength, but rather at a wavelength interval defined by the sensor-specific, spectral response functions. Thus, the Planck function has to be integrated over an instrument response function to calculate the radiance that corresponds to a brightness temperature for a particular instrument channel:

$$L_s = \frac{\int \psi(\lambda) L_{bb}(T, \lambda) d\lambda}{\int \psi(\lambda) d\lambda} \quad (3-4)$$

3 Theoretical background thermal remote sensing

where:

$$\begin{aligned} L_s &= \text{radiance observed by the sensor} \\ \psi &= \text{instrument spectral response} \end{aligned}$$

The total radiative energy emitted from a blackbody is given by the Stefan-Boltzmann law as:

$$M_{bb} = \sigma T^4 \quad (3-5)$$

where:

$$\begin{aligned} \sigma &= \text{Stefan-Boltzmann constant: } 5.67 \times 10^{-8} && [\text{W m}^{-2} \text{K}^{-4}] \\ M_{bb} &= \text{total radiative energy emitted from a blackbody} && [\text{W m}^{-2}] \end{aligned}$$

3.1.2 Solar and terrestrial radiation

The solar radiation reaching the earth is very close to that of a 6000 K blackbody. The wavelength of maximum emission for a blackbody of 6000 K is near 0.5 μm (Wien's displacement law equation 3-3, see also figure 3-2). Temperatures on the earth's surface usually range between 250 K and 330 K, and thus, the radiation emitted by the earth's surface peaks, according to the Wien's displacement law, near 10 μm .

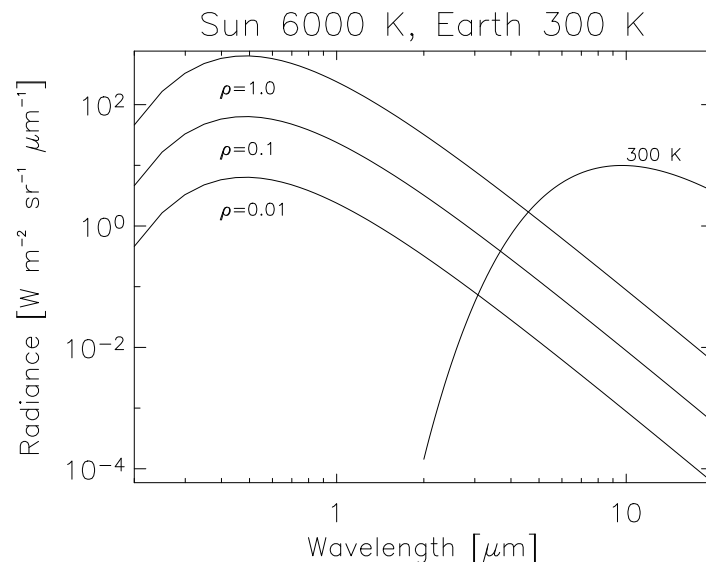


Figure 3-2: Solar and Earth spectral radiance. The solar radiance is plotted for different surface reflectances ρ . The plot indicates that the solar radiance peaks near 0.5 μm , while the radiance emitted by the earth peaks near 10 μm .

3 Theoretical background thermal remote sensing

In the visible spectral range (VIS, 0.4 to 0.7 μm), the near infrared spectral region (NIR, 0.7 to 1.1 μm) and the short wave infrared spectral region (SWIR, 1.1 to 2.5 μm) solar radiation dominates and the earth's self-emitted radiation is insignificant. Hot spots like vegetation fires, industrial chimneys or volcanoes with temperatures higher than 600 K emit significant amounts of terrestrial radiation in the SWIR range and can thus be regarded as exceptions. In the mid infrared spectral region (MIR, 3 to 5 μm) the earth's self-emitted radiation becomes significant. During daytime both solar radiation and terrestrial emission are present in the MIR spectral range. Figure 3-2 indicates that if we assume a surface reflectance or emissivity of 1 the terrestrial radiation is about one tenth solar radiation at about 4.5 μm , at about 5.7 μm solar and terrestrial radiation are equal in magnitude and at about 7.7 μm solar radiation is one tenth terrestrial radiation. In the thermal infrared spectral range (TIR, 8 to 14 μm) the earth's self-emitted radiation dominates and solar radiation is insignificant. Table 3-1 summarizes the above-mentioned spectral ranges and corresponding radiation sources.

| name | wavelength range | radiation source | surface property of interest |
|---|---------------------------|--------------------|------------------------------|
| VIS visible spectral range | 0.4 to 0.7 μm | solar | reflectance |
| NIR near infrared spectral region | 0.7 to 1.1 μm | solar | reflectance |
| SWIR short wave infrared spectral region | 1.1 to 2.5 μm | solar | reflectance |
| MIR mid infrared spectral region | 3.0 to 5.0 μm | solar, terrestrial | reflectance, temperature |
| TIR thermal infrared spectral range | 8.0 to 14.0 μm | terrestrial | temperature |

Table 3-1: Spectral ranges and corresponding radiation sources.

3.2 Correction and calibration of thermal satellite data

3.2.1 Conversion of digital number to at-sensor radiance

Pixel values in satellite data are usually provided as digital numbers (DN) that can be transferred to at-sensor radiances as:

$$L_{s,\lambda} = L_{\min,\lambda} + (L_{\max,\lambda} - L_{\min,\lambda}) * DN / DN_{\max} \quad (3-6)$$

where:

$$L_{s,\lambda} = \text{spectral radiance received by sensor}$$

$$L_{\min,\lambda} = \text{radiance at the minimum calibrated data digital number}$$

3 Theoretical background thermal remote sensing

$$\begin{aligned} L_{\max, \lambda} &= \text{radiance at the maximum calibrated data digital number} \\ DN_{\max} &= \text{maximum digital number} \end{aligned}$$

3.2.2 Atmospheric correction

The radiance measured by an infrared sensor includes emission, absorption and scattering by several components of the earth's atmosphere. Atmospheric corrections are necessary to remove these effects, thus providing only reflected and / or emitted components of the earth surface.

The radiance leaving the surface in the thermal spectral region can be related to the at-sensor radiances as:

$$L_s = L_{\text{path}} + \tau \epsilon_{\text{surf}} L_{\text{surf}} + \tau (1 - \epsilon_{\text{GS}}) F / \pi \quad (3-7)$$

where:

$$\begin{aligned} L_s &= \text{at-sensor radiance} \\ L_{\text{surf}} &= \text{blackbody radiance at the ground surface} \\ L_{\text{path}} &= \text{path radiance} \\ \tau &= \text{ground-to-sensor atmospheric transmittance} \\ \epsilon_{\text{GS}} &= \text{ground surface emissivity} \\ F &= \text{thermal downwelling flux on the ground} \end{aligned}$$

The second term, on the right-hand side of the above given equation, refers to the emitted surface radiance reaching the sensor, while the third term is the atmospheric radiance reflected at the surface and attenuated by the surface-to-sensor path (Richter and Schlaepfer, 2002). In the MIR spectral range the path radiance (L_{path}) consists, during daytime, of a reflective and thermal part. For the TIR range, and for the MIR range during night-time, only the thermal component, i.e. the emitted radiance of different air layers between the ground and the sensor, influences the total at-sensor signal.

The path radiance (L_{path}), ground-to-sensor atmospheric transmittance (τ) and the thermal down-welling flux on the ground (F) can be derived by direct measurements during satellite overpasses, or by using a radiation transfer model for standard atmospheres, such as for example, the common and widely used MODTRAN code (Berk et al., 1998).

3.2.3 Conversion of sensor radiance to brightness temperature

The computation of the brightness temperature as a function of the at-sensor radiance is an inversion of equations 3-2 and 3-4. Unfortunately, equation 3-4 cannot be converted analitically and thus, the

3 Theoretical background thermal remote sensing

solution of the inversion of equation 3-4 can only be calculated numerically. A straightforward approximation is to use the central wavelength of the specific sensor instead of the spectral response function and to invert equation 3-2 as:

$$T_c = \frac{c_2}{\lambda_c \ln [c_1 / (\lambda_c^5 \pi L_s) + 1]} \quad (3-8)$$

where:

$$\begin{aligned} \lambda_c &= \text{central wavelength of sensor} && [\text{m}] \\ T_c &= \text{brightness temperature calculated from central wavelength} && [\text{K}] \end{aligned}$$

Alternatively, an iterative method can be established that uses the result of the of the equation 3-8 as a first guess at the solution of:

$$L_c = \frac{\sum \psi_i L_{bb}(T_c, \lambda_i) \Delta\lambda}{\sum \psi_i \Delta\lambda} \quad (3-9)$$

where:

$$L_c = \text{radiance calculated from an iterative approach}$$

The disadvantage of the iteration is that it is, although being quite accurate, relatively computer time demanding.

Rather than inverting equation 3-2 and 3-3, the equations can be solved numerically by computing an expected sensor radiance for each assumed brightness temperature. As a result a lookup table can be provided that contains a corresponding sensor radiance value for each brightness temperature. This table can be computed for every desired degree of precision by simply enlarging the number of input brightness temperature grid points. Instead of inverting equation 3-2 and 3-3, the lookup table can be inverted, and thus an exact brightness temperature can be given for each registered sensor radiance. Radiance values can be converted to brightness temperatures by simply substituting the registered radiance value by the corresponding brightness temperature value.

3.3 Fire quantification via satellite analysis

Space-borne remote sensing has been widely used to quantify vegetation fires (e.g. Matson and Dozier, 1981; Flannigan and Vonder Haar, 1986; Lee and Tag, 1990; Setzer and Pereira, 1991; Kaufman et al., 1998). Infrared spectro-radiometers can be used directly to measure the radiative energy released by a

3 Theoretical background thermal remote sensing

fire source. It is important to note here though, that satellite sensors can only register that part of the total fire energy emission that is released as radiation.

When observing fires from space, the pixel that corresponds to a ground segment that includes a fire (in the following referred to as a 'fire pixel') will usually not be homogeneous and will contain both fire and other background information. A ground segment that corresponds to a fire pixel will thus consist of a background and a fire-related, thermal component covering different portions of an image pixel. Taking into consideration equation 3-5 (Stefan-Boltzmann law) the total radiative energy release of the sub-pixel fire component can be described as:

$$M_{\text{fire}} = A_{\text{sampl}} \sigma \varepsilon_f \sum q_{\text{fn}} T_{\text{fn}}^4 \quad (3-10)$$

where:

| | | | |
|--------------------|---|--|--------------------------------------|
| M_{fire} | = | radiative energy release of the fire (FRE) | [W] |
| A_{sampl} | = | ground sampling area | [m ²] |
| σ | = | Stefan-Boltzmann constant: 5.67×10^{-8} | [W m ⁻² K ⁻⁴] |
| ε_f | = | fire emissivity | |
| q_{fn} | = | fractional area of the n th fire thermal component within the ground pixel | |
| T_{fn} | = | temperature of the n th fire thermal component | [K] |

Several remote sensing techniques were developed to derive sub-pixel fire information from a heterogeneous image pixel. A common and widely used technique is the so-called bi-spectral method (Dozier, 1981), whereby two measurements of thermal radiances at different wavelength intervals are used to calculate the fire temperature and fire area. Wooster et al. (2003) have recently demonstrated that the bi-spectral fire temperature and area retrievals can be used to estimate the total amount of energy that is emitted as radiation from a fire (the so-called fire radiative energy or FRE). Kaufman et al. (1998) and Wooster et al. (2003) have presented two different approaches, the so-called MODIS and MIR method, to derive FRE of a sub-pixel fire component directly via the analysis of a single infrared measurement. For a detailed review of remote sensing techniques used to compute radiative energy releases of vegetation fires see Wooster et al. (2003).

3.3.1 The bi-spectral technique

The bi-spectral technique is based on the assumption that a hot portion within an image pixel will contribute more to the total energy emitted in the short wave infrared range than in the long wave infrared range (figure 3-1). So, the equivalent fire temperature (T_f) and equivalent proportion of a fire in a pixel (q_f) can be computed by solving the system of two equations:

3 Theoretical background thermal remote sensing

$$L_{s1} = q_f L_{bb,s1}(T_f) + (1 - q_f) L_{bg,s1} \quad (3-11)$$

$$L_{s2} = q_f L_{bb,s2}(T_f) + (1 - q_f) L_{bg,s2} \quad (3-12)$$

where:

$$L_{s1} = \text{atmospherically-corrected pixel radiance of first infrared channel} \\ [\text{W m}^{-2} \text{sr}^{-1} \mu\text{m}^{-1}]$$

$$L_{s2} = \text{atmospherically-corrected pixel radiance of a second infrared channel} \\ [\text{W m}^{-2} \text{sr}^{-1} \mu\text{m}^{-1}]$$

$$L_{bb,s1} = \text{band-integrated Planck Function first infrared channel} [\text{Wm}^{-2}\text{sr}^{-1}\mu\text{m}^{-1}]$$

$$L_{bb,s2} = \text{band-integrated Planck Function second infrared channel} \\ [\text{W m}^{-2} \text{sr}^{-1} \mu\text{m}^{-1}]$$

$$L_{bg,s1} = \text{atmospherically-corrected mean background radiances of first infrared} \\ \text{channel} [\text{W m}^{-2} \text{sr}^{-1} \mu\text{m}^{-1}]$$

$$L_{bg,s2} = \text{atmospherically-corrected mean pixel radiances of second infrared} \\ \text{channel} [\text{W m}^{-2} \text{sr}^{-1} \mu\text{m}^{-1}]$$

The equivalent fire temperature and fire area are the temperature and area of a fire component that would produce the same signal observed in the investigated spectral regions. Thus, the values of fire temperature and size returned by the bi-spectral technique are a clear simplification owing to the fact that real fires will have many different thermal components. The mean pixel radiances of the background ($L_{bg,s1}$, $L_{bg,s2}$) are estimated as the mean radiances of neighbouring non-fire pixels in the vicinity of the anomaly pixel. The band-integrated Planck Function is given by equations 3-2 and 3-4.

The energy release of a sub-pixel fire ($M_{\text{fire, bi-spectral}}$) can be estimated using the temperature (T_f) and area (A_f) provided by the bi-spectral technique according to equation 3-5 (Stefan-Boltzmann law) as:

$$M_{\text{fire, bi-spectral}} = \sigma (T_f^4 - T_{bg}^4) A_f \quad (3-13)$$

where:

$$M_{\text{fire, bi-spectral}} = \text{radiative energy release of the fire derived via the bi-spectral} \\ \text{technique} \quad [\text{W}]$$

$$T_{bg} = \text{background temperature that is assumed to be equal to the} \\ \text{mean temperature in the vicinity of the investigated fire pixel} \\ [\text{K}]$$

$$A_f = q_f A_{\text{sampl}} = \text{equivalent fire area} \quad [\text{m}^2]$$

The bi-spectral method is a common tool used to calculate the temperature and area of a sub-pixel hot spot (e.g. Prins et al., 1998; Robinson, 1991). Nevertheless, Giglio and Kendall (2001) reviewed the bi-

3 Theoretical background thermal remote sensing

spectral method and found large errors if careful consideration is not taken with respect to the accuracy of the inter-channel co-registration of the two input channels and of background characteristics (Wooster et al., 2003).

A further disadvantage of the bi-spectral technique is the fact that it is restricted to image pixels that show anomalous and unsaturated pixel values in at least two input channels, at well-separated wavelength intervals. In addition, the bi-spectral retrievals are very sensitive to background temperature variations, resulting in for example a temperature retrieval error of a few hundreds of Kelvin for small fires ($q_f < 0.005$ % of the pixel area), if the background temperatures varies about +/- 5 K (Wooster et al., 2003). Due to these error sources, Giglio and Kendall (2001) suggest that reliable bi-spectral estimates can only be derived if the fire size q_f exceeds 0.005 % of the pixel area. According to Wooster et al. (2003) the error induced by background temperature variations can be reduced, if the bi-spectral technique is applied to hot pixel clusters rather than to individual single pixels. In addition, a clustering of anomaly pixels reduces the potentially large bi-spectral retrieval errors due to interchannel geometric co-registration errors (Wooster et al., 2003).

3.3.2 The MODIS method

Kaufman et al. (1996, 1998) first introduced the concept of FRE derivation via the analysis of a single infrared measurement. The so-called MODIS method is based on semi-empirical relationships between the fire spectral radiances measured in the 3.9 μm MIR channel of the MODIS instrument and the total FRE emitted over all wavelengths. The 3.9 μm channel was selected as the input channel for the fire analysis, since this spectral range is very sensitive to 600 K to 1000 K hot vegetation fire (see figure 3-1, Planck Function of a 600 K and 1000 K blackbody).

Kaufman et al. (1998) carried out simulations of vegetation fire scenarios each containing different thermal fire and thermal background components within a potential MODIS 4.0 μm fire pixel. They plotted brightness and temperature differences between simulated fire and neighbouring background pixel, against the total FRE release and found, within the limits of the MODIS sensor saturation, very good linear correlations. Thus, a constant factor could be computed that relates the brightness temperature difference of a detected fire and neighbouring background pixel directly to the fire total radiative energy release:

$$M_{\text{fire, MODIS}} = a A_{\text{sampl}} (T_{\text{MIR,p}}^8 - T_{\text{MIR,bg}}^8) \quad (3-14)$$

where:

$$M_{\text{fire, MODIS}} = \text{radiative energy release of the coal fire derived via the}$$

3 Theoretical background thermal remote sensing

| | | |
|--------------|---|--|
| | | MODIS method (W) |
| $T_{MIR,p}$ | = | brightness temperature of potential fire pixel [K] |
| $T_{MIR,bg}$ | = | mean brightness temperature of neighbouring non-fire image pixels (K) |
| a | = | constant factor derived through a best-fit relationship of simulated fire scenarios between the FRE and the composite-fire spectral radiance recorded in the MODIS 3.9 μm channel |

Wooster et al. (2003) adapted the MODIS method to the BIRD MIR channel, where it was seen to have large errors in cases where fire temperature is below 600 K.

3.3.3 The MIR method

Wooster et al. (2003) recently presented an alternative technique, the so-called MIR method, to compute FRE directly from spectral radiances recorded in the BIRD MIR channel. The MIR radiance method is based on the assumption that the total FRE is linearly proportional to the fire pixel radiance recorded in the MIR spectral range:

$$M_{\text{fire, MIR}} = b A_{\text{sampl}} (L_{\text{MIR,P}} - L_{\text{MIR,BG}}) \quad (3-15)$$

where:

| | | |
|------------------------|---|--|
| $M_{\text{fire, MIR}}$ | = | radiative energy release of the coal fire derived via the MIR method [W] |
| b | = | constant derived through a best-fit relationship between blackbody temperature and emitted spectral radiance in the BIRD MIR range |
| $L_{\text{MIR,P}}$ | = | atmospherically-corrected MIR radiance of image pixel [$\text{W m}^{-2} \text{sr}^{-1} \mu\text{m}^{-1}$] |
| $L_{\text{MIR,BG}}$ | = | atmospherically-corrected mean radiance of neighbouring non-fire image pixel [$\text{W m}^{-2} \text{sr}^{-1} \mu\text{m}^{-1}$] |

It is important to note that in contrast to the MODIS method the constant factor b is derived through a best-fit relationship, between blackbody temperature and emitted spectral radiance in the BIRD MIR range, and not through a semi-empirical relationship. Analogous to the MODIS method, the MIR method is only applicable in the case where fire temperature is higher than ~600 K (Wooster et al., 2003). A major advantage of single-band fire quantification methods (MODIS and MIR methods) is the fact that they do not rely on an exact geometric co-registration of different instrument channels.

**GENERAL OVERVIEW AND FIELD INVESTIGATIONS
OF THE RUQIGOU, GULABEN AND WUDA
COALFIELDS**

4 GEOGRAPHIC AND GEOLOGICAL OVERVIEW OF THE RUQIGOU, GULABEN AND WUDA COALFIELDS

In China, the formation of coal on a geological scale occurred in seven periods: Late Carboniferous to Lower Permian, Late Permian, Late Triassic, Early to Middle Jurassic, Late Jurassic to Early Cretaceous, Eogene and Neogene. Carboniferous and Middle Permian coal basins are situated in northern China, Late Permian and Late Triassic coals occur in southern China, Early to Middle Jurassic basins lie in the north-western and northern China, Late Jurassic to Early Cretaceous and Eogene basins are located in north-eastern China, while Neogene coal basins are formed in south-western China (Ren et al., 1999). Nowadays, the Late Carboniferous to Lower Permian coal bearing strata in China are classified as being of Middle to Upper Permian age by many international geologists. The classification follows the results of Diaz et al. (1983) and Jones (1995) which consider the former Late Carboniferous to Lower Permian to be part of the Cathaysia floral province that developed after a Lower Permian transgression.

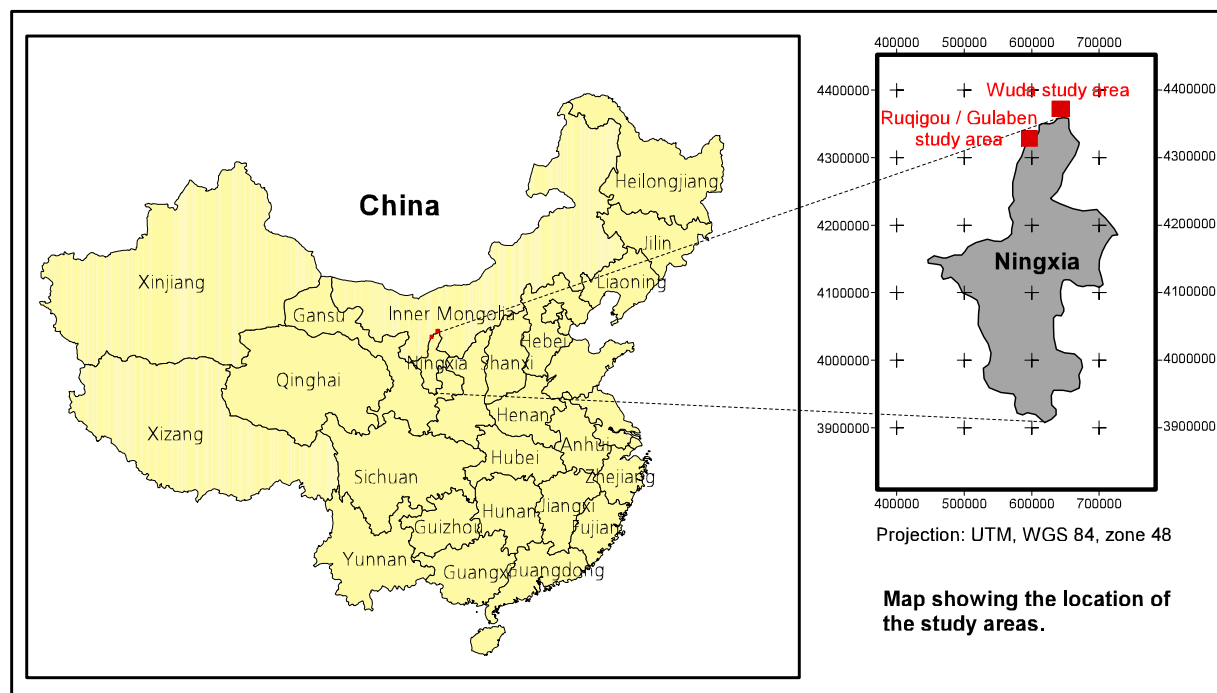


Figure 4-1: Location of the Wuda, Ruqigou and Gulaben coalfields.

The three coalfields Wuda, Ruqigou and Gulaben investigated in this study are situated in northern China (figure 4-1), in the Helan Mountain area and consist of coal-bearing strata of Middle to Late Permian (former Permo-Carboniferous) or Middle Jurassic age.

4.1 General geological and geographical description of the Helan Mountain area

The following geological and geographical description mainly follows the description of Halik et al. (2003) and Gielisch and Kahlen (2003). The two papers are internal project reports, which summarize scientific papers and field reports which are mainly written in Chinese.

The Helan Mountains (Helan Shan) are located in the Ningxia Hui Autonomous Region and the Inner Mongolia Autonomous Region in north China. The 300 km long mountain range stretches approximately 30° north-east, from the town Wuda in the north to the town Zhongwei in the south. The mountains show average altitudes of about 2000 m above sea level.

The Gobi desert, with its wide and open plains, is located west and north of the Helan Mountains, while the alluvial plain of the Yellow River (Huang He) is directly connected to the east. The Helan Shan belongs to the central Asian desert region and has a continental desert climate with long cold winters and very hot summers (Halik et al., 2003).

The Helan Shan is located in the western margin of the North China platform. Oldest rocks belong to the Precambrian and are followed by Cambrian and Ordovician platform limestones and dolomites. A wide hiatus separates Ordovician from Middle Permian (former Permo-Carboniferous) sediments. During the Middle Permian a transgression took place on the North China Platform, which continued during the Late Permian and lead to the development of a paralic environment in the Helan Shan area. The Permian in North China ranged successively from upland, through alluvial and fluvial plain, paralic delta and tidal flat to shallow marine. Upper Permian marine carbonates represent the last marine influence in the Helan Shan. In the Uppermost Permian a major regression resulted in an alluvial-fluvial facies that is documented by conglomerates, sandstones and shales.

During the Triassic a fluvio-lacustrine environment prevailed in the Helan Shan area. Lower Jurassic is missing, while during Middle Jurassic coal bearing sequences of the Ruqigou Formation reveal an environment dominated by rivers and swamps. In the Upper Jurassic the area was uplifted and a lacustrine environment developed. Lower Cretaceous coarse grained sandstones and conglomerates eroded from older Helan Shan formations reflect the uplift of the area during the Yanshan 'Orogeny'. In Tertiary, the Himalaya Orogeny caused repeated uplifting and incision of the older strata and fluvial sandstones and conglomerates were deposited in intra-mountainous basins. Precambrian to Tertiary rocks in the Helan Shan are partly overlaid by quaternary Yellow River deposits and Gobi sands (Gielisch and Kahlen, 2003; Dai et al., 2002).

The Helan Mountains are a typical fault-block that is mainly controlled by an extensional stress field (Chen, 1997). The northern and central part of the Helan Shan can be tectonically subdivided into a northern Palaeozoic Fold Belt, an archaic basement attached to the Fold Belt in the south, a Palaeozoic

4 Geographic and geological overview of the Ruqigou, Gulaben and Wuda coalfields

to Mesozoic Fold Belt of the central Helan Shan and an Archean to Lower Paleozoic region in the south (Gielisch and Kahlen, 2003).

4.2 Ruqigou and Gulaben coalfields

The Ruqigou and Gulaben coalfields (figure 4-2) are situated at the border between the Ningxia Autonomous Region and the Inner Mongolia Autonomous Region, in the central Helan Mountains, at elevations between 1,800 m and 2,500 m above sea level. The Ruqigou coalfield is under administration of Ningxia, while the Gulaben coalfield belongs to Inner Mongolia. The Gulaben coalfield lies approximately 10 km west of Ruqigou coalfield and the area covered by both coalfields stretches between latitudes 39°00' N to 39°01' N and longitude 106°03' E to 106°11' E and covers about 80 km² in total. The coalfields include the mining towns Ruqigou, Baijigou, Dafeng and Gulaben. Chen (1997) reports an annual precipitation of 238 mm for the Ruqigou and Gulaben area with a maximum annual potential evaporation of 2720 mm. As the geological situation and many mining aspects are identical in Gulaben and Ruqigou, the following subsections cover both coalfields.



Figure 4-2: *Ruqigou and Gulaben coalfields. a) Coal town in the Ruqigou coalfield; b) burning mountain in the Ruqigou coalfield; c) outcropping coal layers and small scale mining activities in the Gulaben coalfield.*

4 Geographic and geological overview of the Ruqigou, Gulaben and Wuda coalfields

4.2.1 Geological situation

The Ruqigou and Gulaben coalfields are part of the Palaeozoic to Mesozoic Fold Belt of the central Helan Shan. The Fold Belt is gently folded and shows a general strike from north-east to south-west. Both coalfields are part of a wide, synclinal structure following the general strike of the Fold Belt and including the Chutangou Syncline in the north-west, the Houlugou Anticline (Gulaben coalfield) and the Ruqigou Syncline (Ruqigou coalfield) in the south-east. The flanks of the Ruqigou Syncline have low dip angles (5° to 30°), while the western flank of the Houlugou Anticline is rather steep (35° to 75°) (Gielisch and Kahlen, 2003; DMT, 2001).

The coal seams in both coalfields belong to the Middle Jurassic Ruqigou Formation, which consists of alternating sandstone, siltstone, shale and coal layer. The deposition environment was lacustrine-fluvial including swamps and fluvial channels. Zhang (1998) reports a total formation thickness of 349 m, while the total average coal seam thickness is about 41 m (Chen, 1997). More than ten coal seams are described in the Ruqigou Formation, but only three are regionally distributed in the coalfields (Chen, 1997). Mining operations mainly focus on coal seam No. 2 which has an average cumulative thickness of 19 m and can reach a thickness of up to 40 m in some locations (Chen, 1997).

4.2.2 Mining situation and coal properties

Mining operations have been carried out in both coalfields since the 1960's. The seven mines in the Gulaben coalfield are mainly operated by the Inner Mongolia Tai Xi Anthracite Group, owned by the local government of the Alasag County. The three major mines in the Ruqigou coalfield all belong to the Ruqigou Mining Company (Ningxia Industry Bureau of Coal). Next to the major mines, about 50 privately owned, small-scale mines are still in operation in both coalfields (figure 4-2), although attempts were carried out in recent years to close these mines. The annual coal production in the year 2000 reported from the major mines is about 4 Mt for the Ruqigou coalfield and about 1 Mt for the Gulaben coalfield (Kuenzer et al., submitted; DMT, 2001).

With the exception of the Dafeng Mine (Ruqigou coalfield) and the small-scale private mines, coal is produced underground in both coalfields. Due to the steeper dip in the Gulaben coalfield the degree of mechanisation of the underground mines is limited. The underground mining in the Ruqigou coalfield is mainly restricted to coal seam No. 2 and is carried out by means of mechanized longwall techniques at various levels (DMT, 2001).

The coal quality is very wide ranging, from low volatile bituminous to anthracite coal. The Federal Institute for Materials Research and Testing (BAM, Germany) has recently carried out laboratory investigations on coal from the Gulaben and Ruqigou coalfields. The laboratory experiments were carried out for only a few coal samples from the Wuda, Gulaben and Ruqigou coalfields and are thus

4 Geographic and geological overview of the Ruqigou, Gulaben and Wuda coalfields

not necessarily representative for natural coal properties. A detailed description of the method and results of this primary analysis is given by Krause (2003). The samples from the Gulaben coalfield, taken in a depth of 45 m, were given a rank of 2.5 to 3.0, while the Ruqigou coal samples, taken in a depth of 70 m, were ranked as 2.0 to 3.5. The results of the element analysis as well as the determined water content, ash content and calorific value are listed in table 4-1 and 4-2.

| | C in % | H in % | N in % |
|---------|----------------|---------------|---------------|
| Gulaben | 85.720 ± 2.414 | 3.242 ± 0.042 | 0.683 ± 0.052 |
| Ruqigou | 74.972 ± 4.586 | 2.904 ± 0.045 | 0.653 ± 0.033 |

Table 4-1: Content of carbon, hydrogen and nitrogen in coal samples of the Ruqigou and Gulaben coalfields (elemental analysis performed at BAM; Krause, 2003).

| | Gulaben | Ruqigou |
|----------------------------|-------------|-------------|
| Water content in % of mass | 0.97 ± 0.02 | 2.62 ± 0.11 |
| Ash content in % of mass | 5.1 | 14.9 |
| Calorific value in kJ / kg | 33661 | 29226 |

Table 4-2: Water content, ash content and calorific value of coal samples of the Ruqigou and Gulaben coalfields (elemental analysis performed at BAM; Krause, 2003).

Self-ignition experiments were conducted by the BAM (Krause, 2003) for coal samples from the Gulaben coalfield by a so-called hot storage experiment. Here, coal samples are stored in a laboratory oven under isothermal conditions. Due to the fact that the self-ignition temperature depends on the specific internal surface (description in chapter 2), the experiment was carried out for coal samples of different volume and shape. Cubical coal pieces with edge lengths of 1 cm, 4 cm and 6 cm showed self-ignition temperatures of 578 K, 568 K and 562 K, respectively. Self-ignition temperatures measured for crushed coal of 100 ml, 200 ml and 300 ml were 567 K, 562 K and 552 K, respectively.

In addition, coal samples from the Wuda coalfield were tested for their capacity for ignition from an external ignition source. The Wuda coal has a lower coal rank than the Ruqigou and Gulaben coal (see next sections) and is thus considered to be more easily ignitable than the Ruqigou and Gulaben coal. Using a heated coil, with surface temperatures between 973 K and 1173 K, that was kept in contact with the unmodified Wuda coal sample for about 34 hours, it appeared that it was not possible to ignite the Wuda coal. Hence, these primary experiments indicate that an external ignition source capable of igniting solid coal with a high coal rank from the Gulaben and Ruqigou coalfields needs to be very hot and in long direct contact with the coal. Nevertheless, Krause (2003) demonstrated that crushed Wuda

4 Geographic and geological overview of the Ruqigou, Gulaben and Wuda coalfields

coal samples could be externally ignited in a similar experiment. It is important to note here that these are only preliminary results and that a more detailed investigation of coal samples from the Ruqigou and Gulaben coalfields is to be carried out in the coming years within the Sino-German Coal Fire Initiative.

4.2.3 Coal fires

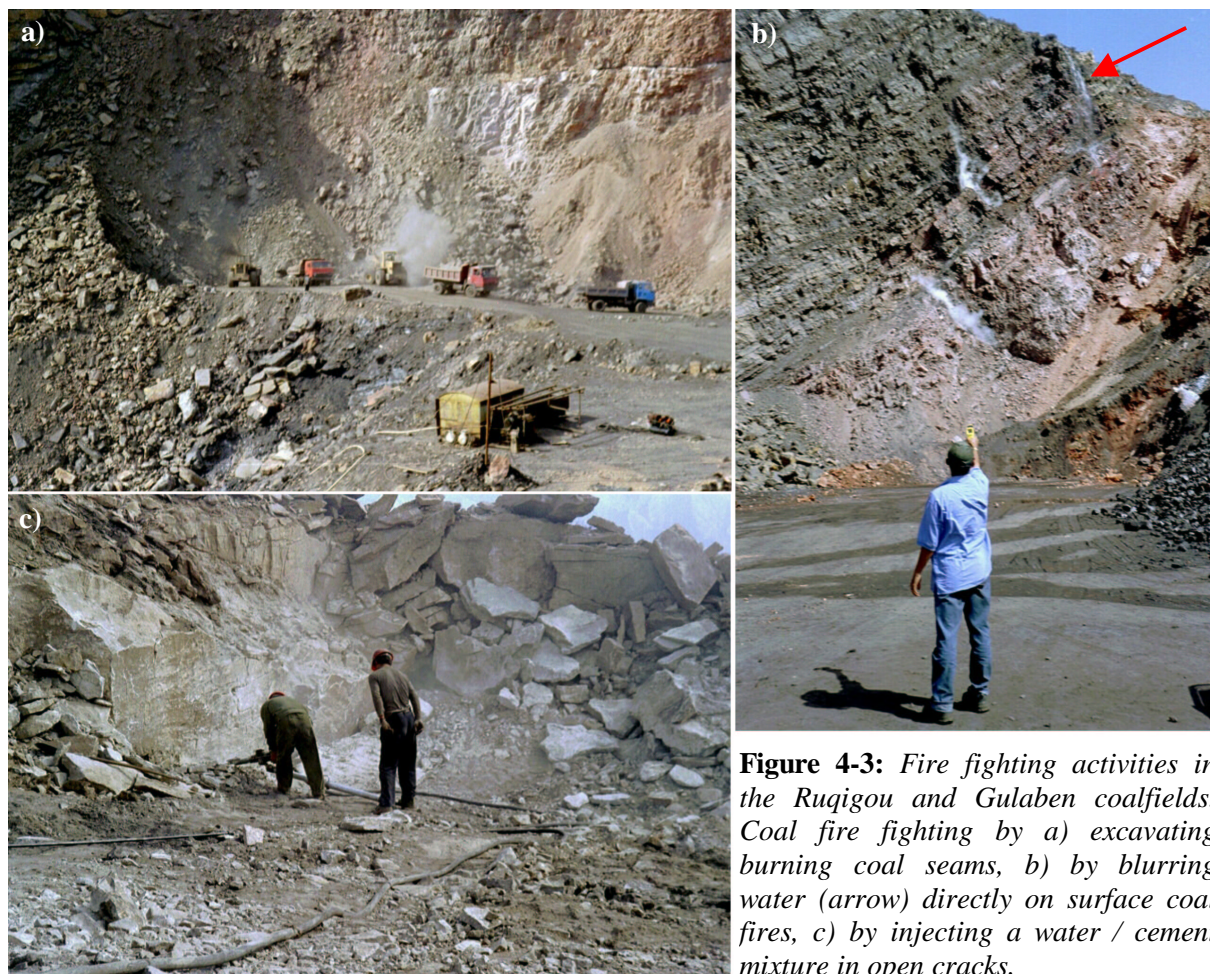


Figure 4-3: Fire fighting activities in the Ruqigou and Gulaben coalfields. Coal fire fighting by a) excavating burning coal seams, b) by blurring burning water (arrow) directly on surface coal fires, c) by injecting a water / cement mixture in open cracks.

Coal fires in the Gulaben coalfields cover an area of about 960000 m² affecting about 10 Mt of coal reserve. In 2002 and 2003 seven active coal fires were reported by the local mining management, stretching in a row along the strike direction of coal seam No. 2. Single fires extend more than 1 km in the strike direction of the coal seam, with a maximum depth of 200 m in dip direction. Beside sub-surface coal fires, surface coal fires burning directly on the outcropping coal seam can be observed at different locations. According to the Tai Xi Anthracite Group, all coal fires in the Gulaben coalfield are strongly linked to mining activities exclusively related to former private mining operations. Fire fighting activities were undertaken in recent years in the Gulaben coalfield, mainly by means of the injection of water-clay or a special mixture of cement and water clay in open cracks. This method's

4 Geographic and geological overview of the Ruqigou, Gulaben and Wuda coalfields

primary aim is to isolate coal fires from non fire areas, and was successfully applied to cease a coal fire close to mining operations (DMT, 2001).

Nineteen active coal seam fires (e.g. figure 4-2) were reported from the Ruqigou coalfield, affecting an area of more than 2000000 m². The coal fires are widespread along the Ruqigou syncline and are in most cases caused by mining activities. The Ningxia Administration Bureau for Safety Inspection for Coal has, since the late 1970's, undertaken intensive fire fighting activities in the Ruqigou coalfield. In total, around 80 million CNY (~ 8 million Euro) has already been spent on fire fighting activities, with an additional 30 million CNY allocated for the near future. About 80 % of the active coal fires are currently covered by extinction activities, resulting in a nearly complete absence of surface coal fires. Active fire fighting is commonly undertaken by either covering the fire with a loess blanket, by injecting a water-clay-cement mixture in open cracks or by directly excavating the fire (figure 4-3). The fire excavation is often carried out by private companies which gain the right to sell the excavated 'fire coal' (DMT, 2001).

4.3 Wuda coalfield

The Wuda coalfield (figure 4-4) is located at the northern tip of the Helan Shan Mountains in a relatively flat topography region, with elevations ranging between 1100 m and 1300 m above sea level. It belongs to the Inner Mongolia Autonomous Region, stretches between latitude 39°26' N to 39°38' N and longitude 106°36' E to 106°46' E and is situated west of the coal-town Wuda. In total the Wuda coalfield has a spatial extension of 35 km². The Gobi Dessert and the Helan Shan Mountains surround the coalfield in northern, southern and eastern direction, while the Yellow River in the east supplies enough water to allow agriculture close to the coalfield. Average annual temperatures in the Wuda area vary around 9 °C with temperature minimum and maximum of -26 °C and 40 °C. The average annual potential evaporation of 3500 mm exceeds vastly the annual average precipitation of 168 mm and indicates very dry climatic conditions (Halik et al., 2003).

4.3.1 Geological situation

The Wuda coalfield is an isolated outcrop of Late Palaeozoic strata and belongs tectonically to the northern Palaeozoic Fold Belt of the Helan Shan. The Late Palaeozoic strata are exposed in a 10 km wide north-south striking syncline with gently (6° to 10°) dipping western flanks and a north plunging fold axis, and the eastern flank of the syncline is cut by a major north-south striking thrust fold (DMT, 2001).

The coal-bearing strata in the Wuda coalfield are of Middle to Late Permian age (former Permo-Carboniferous) and include the Benxi Formation, the Taiyuan Formation, the Shanxi Formation, the

4 Geographic and geological overview of the Ruqigou, Gulaben and Wuda coalfields

Xiashihezi Formation and the Shangshihezi Formation.⁴⁻¹⁾ The major coal bearing formation is the Taiyuan Formation, which consists of 5 coal layers (No. 9, No. 10, No. 12, No. 13 and No. 15) interbedded in a sequence of alternating sandstone, limestone and mudstone layers. The thickness of this formation varies between 70 m and 140 m. In total, 24 coal seams with a various thickness and lateral continuity are reported from the Wuda coalfield, including 14 that are presently mined. The coal seam thickness ranges between 0.2 m and 6 m (Dai et al., 2002; DMT, 2001).

4.3.2 Mining situation and coal properties

Mining operations in the Wuda coalfield include three major underground mines (Wuhushan, Huangbaici, Suhai-Tu), managed by the Wuda Mining Bureau (Shenhua Group). 27 Mt of mineable coal reserves are stated for the Wuda coalfield. The underground mines commonly operate at a depth of 100 m and mechanized longwall methods are applied to extract coal. In addition, small-scale mines occur within the whole Wuda syncline, although major attempts were undertaken in recent years to close these private mines.

The Wuda coalfield is one of the major coking coal mining areas in north China (Dai et al., 2002). Besides coking coal, fat and steam coal is extracted from the coal seams. Coal samples, taken in depth of 80 m, were determined by the BAM to rank between 1.5 and 2.0 (Krause, 2003). The coal properties of these samples are listed in table 4-3 and 4-4.

| | C in wt % | H in wt % | N in wt % |
|------|---------------|---------------|---------------|
| Wuda | 53.818 ± 1.81 | 3.611 ± 0.088 | 0.897 ± 0.054 |

Table 4-3: Content of carbon, hydrogen and nitrogen in coal samples of the Wuda coalfield (elemental analysis performed at BAM; Krause, 2003).

| Wuda | |
|----------------------------|--|
| Water content in % of mass | 1.57 ± 0.015 (“dry”) 4.4 ± 0.09 (“wet”) |
| Ash content in % of mass | 36.1 |
| Calorific value in kJ / kg | 21063 |

Table 4-4: Water content, ash content and calorific value of coal samples of the Wuda coalfield (elemental analysis performed at BAM; Krause, 2003).

⁴⁻¹⁾ The name convention follows the former classification system and, to avoid confusion, is not adapted to the new stratigraphic classification of Diaz et al. (1983) and Jones (1995).



Figure 4-4: Wuda coalfield. a) Wuda coal factory; b) fire fighting by covering near surface coal fires with a water / colloid mixture; c) near surface coal fires with heavy smoke development.

Self-ignition experiments had not yet been conducted by the BAM for the Wuda coal samples, but the significantly lower coal rank of the Wuda coal indicates lower self-ignition temperatures, cf. self-ignition temperatures listed in section 4.2.2 for the Gulaben coal samples (see also chapter 2, section 2.1). As already mentioned in section 4.2.2 a heated coil with surface temperatures between 973 K and 1173 K could not ignite the unmodified Wuda coal sample, while the crushed coal sample could be ignited (Krause, 2003).

4.3.3 Coal fires

Nowadays, an area of 3700000 m² is affected by a coal fires in the Wuda syncline resulting in an estimated annual direct coal loss of 200000 t during the last years. It is estimated that since the 1960s about 10 Mt of coal are directly or indirectly destroyed. The first underground coal seam fire started in the 1960's only a few years after the mining operations started (DMT, 2001). In general, it is stated by the Wuda Mining Bureau that most coal fires are directly linked to small-scale mining activities. Two coal seams are said to be particularly prone to spontaneous combustion (No. 9 and No. 10) and coal

4 Geographical and geological overview of the Ruqigou, Gulaben and Wuda coalfield

stockpiles in the Wuda coalfield ignite due to spontaneous combustion after three to six months (Kuenzer et al. submitted; DMT, 2001).

Nowadays, around twenty coal fires in the Wuda coalfield occur underground or near surface and are widespread along the western flank of the syncline. Recent fire fighting activities have been restricted to coal fires that directly affected large-scale mining operations, resulting in an acceleration of the coal fire problem from year to year. Due to the lack of systematic fire fighting activities, near surface coal fires with heavy smoke development are widely scattered within the syncline (figure 4-4). In addition to coal seam fires, burning stockpiles can be observed in the northern and eastern part of the coalfield.

5 FIELD OBSERVATIONS OF THE RUQIGOU, GULABEN AND WUDA COALFIELDS

The coal fires of the Wuda, Ruqigou and Gulaben coalfield were investigated during two field campaigns in September 2002 and September 2003. The main task of this field activity was to measure surface temperatures of coal fires, in order to determine typical temperatures of coal fire induced surface anomalies. In addition, coal fire surface anomalies of the Gulaben, Ruqigou and Wuda coalfields were mapped to delineate exact coal fire locations. Because an accurate calibration of the satellite data is crucial for satellite-based coal fire quantification, measurements were taken of the temperature of the most suitable calibration targets situated close to the study areas (Yellow River), synchronous with ASTER, ETM and BIRD overpasses. Finally, temperatures of non-fire areas were investigated for typical surface materials at different temporal settings, in order to analyse background temperature variations.

5.1 Coal fire mapping

The investigation focussed on coal fire related, surface anomaly zones. The term coal fire related surface anomaly (CFSA) refers to coal fire induced anomaly pattern that are developed at the surface of an under-ground or surface coal fire. During the investigation in September 2002 the CFSA zones in the Wuda, Ruqigou and Gulaben coalfields were mapped at a scale of 1:25000 (figure 5-1). The CFSA zones of the Wuda coalfield are numbered according to local coal fire maps, while the CFSA of the Ruqigou and Gulaben coalfields are labelled with the author's own indices. Note that during the field investigations only coal seam fires were mapped, while burning stock piles, widespread in the eastern and northern part of the Wuda syncline, were not considered.⁵⁻¹⁾

Since the Wuda coalfield is easy to access, and the local mining companies strongly supported the field activities, all coal fires in this coalfield could be investigated and mapped. Since the Ruqigou and Gulaben coalfields are difficult to access and parts of the coalfields are additionally inaccessible because of restrictions from the local authorities, not all coal fire areas could be investigated. If a particular coal fire could not be mapped, the coal fire delineation was based on information from local fire fighting teams, rather than on the author's own field observations. In order to clearly differentiate between CFSA and abnormal high background temperatures caused by strong sun heating, only temperature anomalies that exceeded the maximum background temperature by at least 5 K and showed non-thermal burning indicators (e.g. smoke, mineral crystallisation), were mapped. The CFSA of sub-surface coal fires are distinctly heterogeneous and the separation of single CFSA (e.g. single fire cracks or fire holes) of one coal fire area was, with respect to the mapping scale, often not possible. Therefore, all CFSA that belong to one sub-surface coal fire were mapped as one continuous polygon.

⁵⁻¹⁾ The term coal fires refers in the following thesis to coal seam fires.

5 Field observations of the Ruqigou, Gulaben and Wuda coalfields

Consequently the mapped fire anomalies have to be regarded as zones, each containing a certain number of CFSA, rather than as continuous anomaly areas.

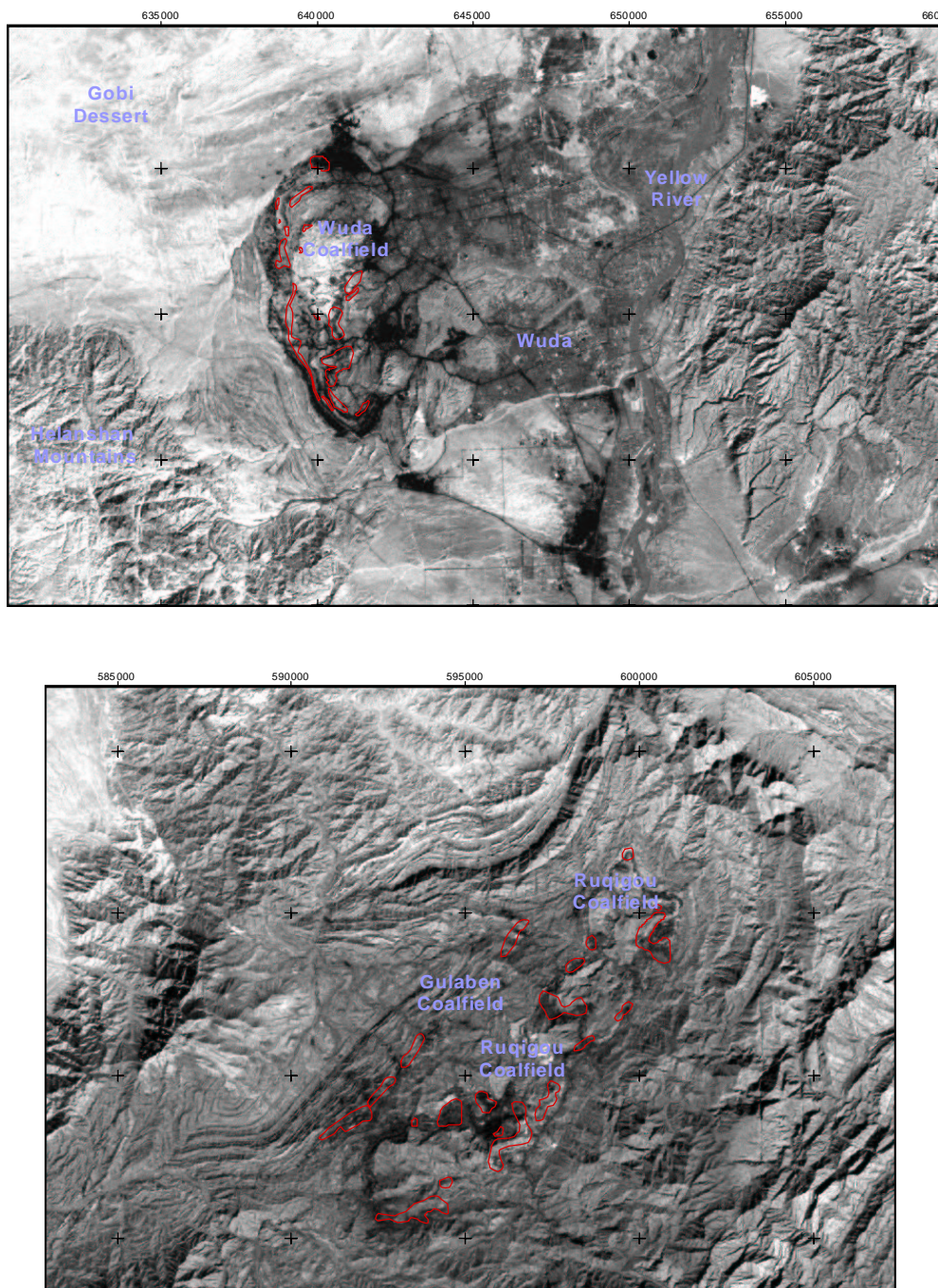


Figure 5-1: Coal fire related surface anomalies (CFSA) mapped during the field campaign in September 2002 (red outline) on top of the panchromatic channel of the ETM scene from 29th September 2002. The red outlined areas should be regarded as zones each containing a certain number of CFSA rather than as continuous anomaly areas. The CFSA zones of the Wuda coalfield are numbered according to local fire maps, whilst the CFSA of the Ruqigou coalfield are labelled with the author's own indices. Top) CFSA zones in the Wuda coalfield; bottom) CFSA zones in the Ruqigou and Gulaben coalfields.

5 Field observations of the Ruqigou, Gulaben and Wuda coalfields

5.2 Temperatures and sizes of coal fire induced surface anomalies in the study areas

Approximately 800 surface temperature measurements were carried out on representative underground fires and surface coal fires in the three study areas. These took place during September 2002 and September 2003, using a radiant thermometer and / or a handheld thermal infrared camera. The technical characteristics of the radiant thermometer and the thermal camera used for the measurements are listed in table 5-1 and table 5-2.

| | type | temperature range | temperature resolution | opening angle |
|---------------------|------------|-------------------|---------------------------|-----------------|
| radiant thermometer | Raytec MX2 | -30 °C to 900 °C | 0.1 K / 1 % of absolute T | 19 mm at 1.15 m |

Table 5-1: Technical characteristics of the radiant thermometer used during the field campaigns in September 2002 and September 2003.

| | type | temperature range | temperature resolution | opening angle | spectral range | size of thermal image |
|----------------|----------|-------------------|---------------------------|---------------|-----------------|-----------------------|
| thermal camera | CAM/TM E | -20 °C to 250 °C | 0.1 K / 2 % of absolute T | 25 ° / 0.3 m | 7.5 μm to 13 μm | 160 x 120 pixel |

Table 5-2: Technical characteristics of the thermal camera used during the field campaign in September 2003.

The temperature measurements were conducted under similar meteorological conditions (blue-sky conditions) with air temperatures ranging between 298 K and 311 K. As in the case of the coal fire mapping, only CFSA that exceeded the maximum background value of at least 5 K, and that additionally showed non-thermal burning indicators (e.g. smoke, mineral crystallisation), were taken into account.

Average and maximum radiant temperatures determined for investigated coal fire areas are listed in table 5-3. All observed coal fire areas showed heterogeneous surface temperatures. CFSA on sub-surface coal fires were mainly restricted to several centimetres and up to two metre wide cracks or holes, with a maximum diameter of four metres. Observed burning zones on outcropping coal seams (surface coal fires) were mostly in a smouldering stage, and always included non-burning coal or burned-out coal ashes. The percentage of CFSA in an ETM pixel, with a corresponding area of 60 m² x 60 m², was, in all cases, relatively small, and did not exceed 30 %. Mean surface radiant temperatures of investigated coal fires range between 339 K and 459 K, while high average temperatures mainly correlate with surface coal fires or strongly collapsed near sub-surface fire zones.

5 Field observations of the Ruqigou, Gulaben and Wuda coalfields

| coal fire ID | date of investigation | fire characteristics | Σ measurements | T background [K] | T mean [K] | T max [K] |
|--------------|-----------------------|--|-----------------------|------------------|---------------------------------------|---------------------------------------|
| Wuda 2 | 09 / 2003 | sub-surface coal fire, partly covered by sand | 38 | 301 to 312 | 339 | 407 |
| Wuda 3 | 09 / 2003 | near surface and sub-surface coal fire, area strongly collapsed, sandstone or shale surface | 64 | 302 to 320 | 358 | 810 |
| Wuda 5 | 09 / 2003 | sub-surface coal fire, cracks and fire holes with max. diameter 5 m | 57 | 301 to 312 | 355 | 519 |
| Wuda 6 | 09 / 2003 | sub-surface coal fire, partly collapsed, shale and sandstone surface, fire holes with max. diameter 3 m and cracks | 51 | 301 to 320 | 404 | 683 |
| Wuda 7 | 09 / 2003 | sub-surface coal fire, parts strongly collapsed, homogenous sandstone plateau | 110 | 306 to 330 | collapse zone: 396 crack zone: 375 | collapse zone: 638 crack zone: 588 |
| Wuda 8 | 09 / 2003 | near surface sub-surface coal fire, collapse and crack zone, sandstone and shale surface | 80 | 303 to 333 | collapse zone: 459 crack zone: 359 | collapse zone: 798 crack zone: 863 |
| Wuda 11 | 09 / 2003 | sub-surface coal fire, surface anomalies mainly along cracks | 96 | 301 to 322 | 388 | 698 |
| Wuda 12 | 09 / 2003 | sub-surface and surface coal fire, cracks and fire holes | 58 | 298 to 315 | 419 | 879 |
| Wuda 16 | 09 / 2003 | sub-surface and surface coal fire, surface anomalies are mainly restricted to outcropping coal seam | 31 | 304 to 324 | 371 | 474 |
| Ruqigou 7 | 09 / 2003 | surface coal fire along outcropping coal seam | 62 | 298 to 326 | 377 | 874 |
| Ruqigou 11 | 09 / 2002 | surface coal fire along outcropping coal seam | 32 | 303 to 316 | 410 | 690 |
| Gulaben 9 | 09 / 2002 | surface coal fire along steeply dipping coal seam | 28 | 307 to 324 | 422 | 713 |

5 Field observations of the Ruqigou, Gulaben and Wuda coalfields

| coal fire ID | date of investigation | fire characteristics | Σ measurements | T background [K] | T mean [K] | T max [K] |
|--------------|-----------------------|---|-----------------------|------------------|------------|-----------|
| Gulaben 12 | 09 / 2002 | surface coal fire along a steeply dipping coal seam | 34 | 305 to 326 | 395 | 658 |

Table 5-3: Temperatures of CFSA of representative coal fires taken in the study areas, measured during the field campaign in 2002 and 2003. Temperature investigations were performed using a radiant thermometer with $\varepsilon = 1$.

Maximum radiant temperatures measured on the surface of investigated coal fires depend strongly on the particular fire characteristics ranging from 407 K to 879 K. Although average anomaly temperatures are below 460 K, 460 K to 600 K CFSA components occur in most of the observed CFSA. Nevertheless, these relatively hot zones are locally limited and usually cover less than 20 % of the CFSA. Hot spots with temperatures of 600 K or higher can be regarded as an absolute exception. They only occur along cracks of near-surface coal fires, or directly on surface coal fires, and are always restricted to small areas within the investigated coal fire zone, never exceeding more than 15 m² within an ETM pixel equivalent area.

5.3 Detailed investigation of a sub-surface and a near-surface coal fire in the Wuda coalfield

Two coal fires in the Wuda coalfield were investigated in detail: a sub-surface (fire 7) and a near-surface coal fire (fire 8). Both fires were mapped at a scale of approximately 1: 5000 (figure 5-2) in September 2002 and different temperature measurements were undertaken during both field campaigns.

An optical image, as well as thermal images of the sub-surface coal fire 7, can be seen in figure 5-3. The images were taken along the southernmost edge of the investigated coal fire area. The sub-surface coal fire is entirely covered by a nearly horizontal, several metre thick sandstone layer. Parts of this sandstone layer are in a state of extreme collapse (dotted and dashed areas in figure 5-2) and several metre wide cracks and fire holes, with relatively intensive surface temperature anomalies, are developed in this zone. In addition, up to 1 metre wide cracks (red lines figure 5-2) can be observed approximately parallel or perpendicular to former mining channels. The CFSA along the coal fire cracks were relatively weak during the two field observation campaigns.

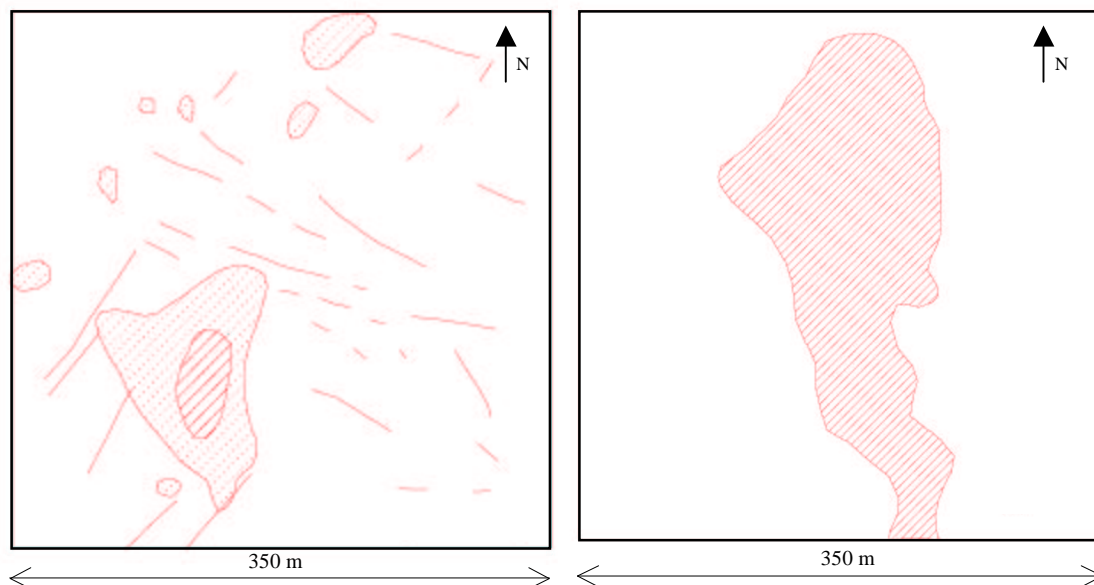


Figure 5-2: Detailed maps of the coal fires 7 and 8 of the Wuda coalfield. Red lines = coal fire cracks with a maximum width of 1 m, red dotted area = strongly collapsed bedrock with active but weak coal fire activity, red dashed area = strongly collapsed zone with intensive coal fire activity (fire 7) or a near-surface coal fire (fire 8). Left) Sub-surface coal fire 7, upper left corner 4376400 / 641000 (UTM, WGS 84); right) near-surface coal fire 8, upper left corner 4374850 / 638900 (UTM, WGS 84).

About 110 temperature measurements were performed with the radiant thermometer, at the site of the sub-surface coal fire, and several thermal images were taken in September 2003. In September 2002 brightness temperatures were measured along two profiles synchronous with Landsat ETM night and daytime satellite overpasses. The temperature profiles are shown in figures 9-1 and 9-2. The local extent, and the thermal properties of the CFSA, had not changed significantly from September 2002 to September 2003.

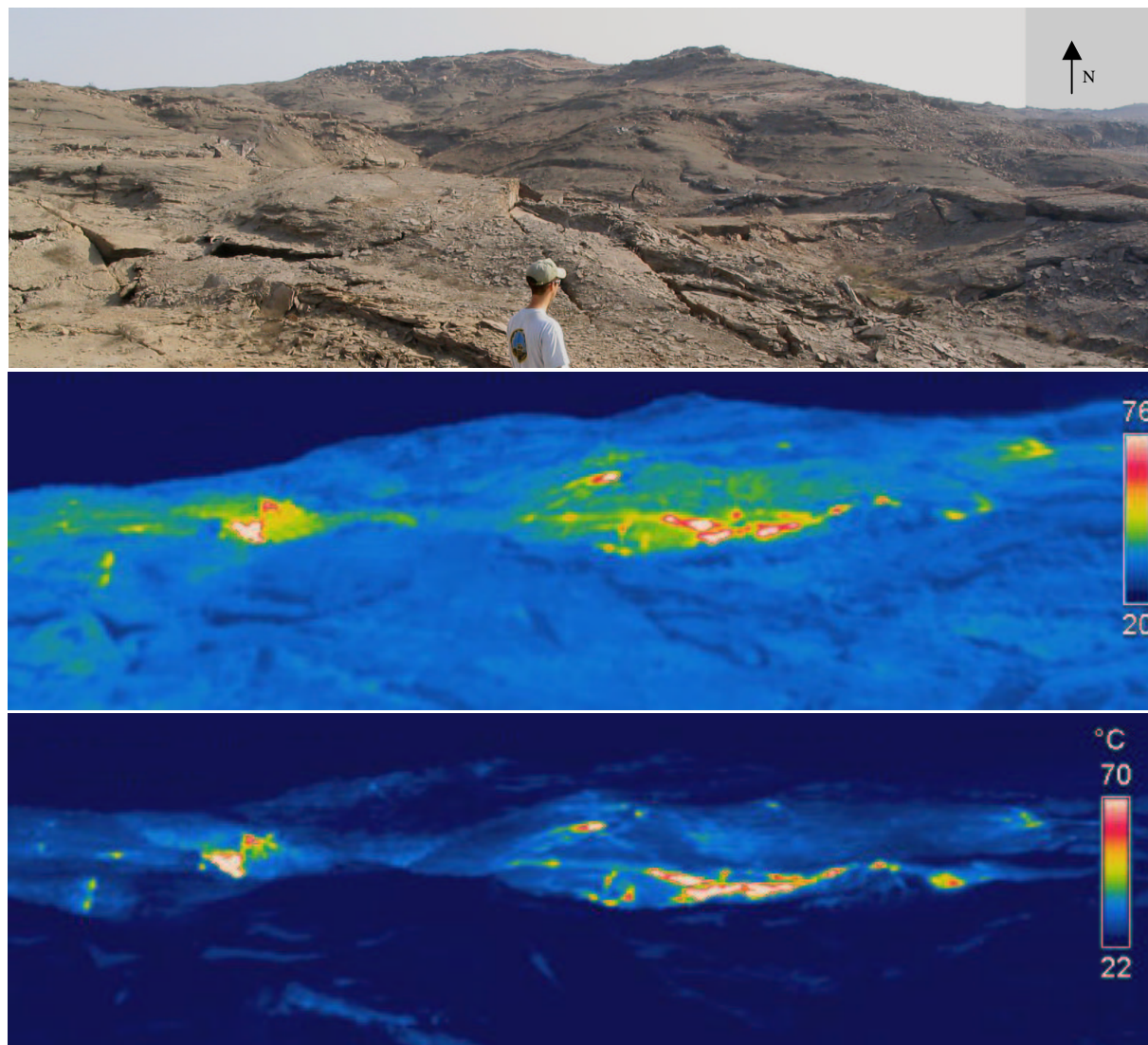


Figure 5-3: Thermal and optical images taken in September 2003 of the Wuda coal fire number 7. Top) Optical image of the coal fire area; middle) thermal image at 11:30 am; bottom) thermal image at 11:30 pm. Each image is a mosaic of 4 thermal camera pictures. The images clearly indicate that relatively hot coal fire related surface temperatures only occur along a few, locally very limited spots.

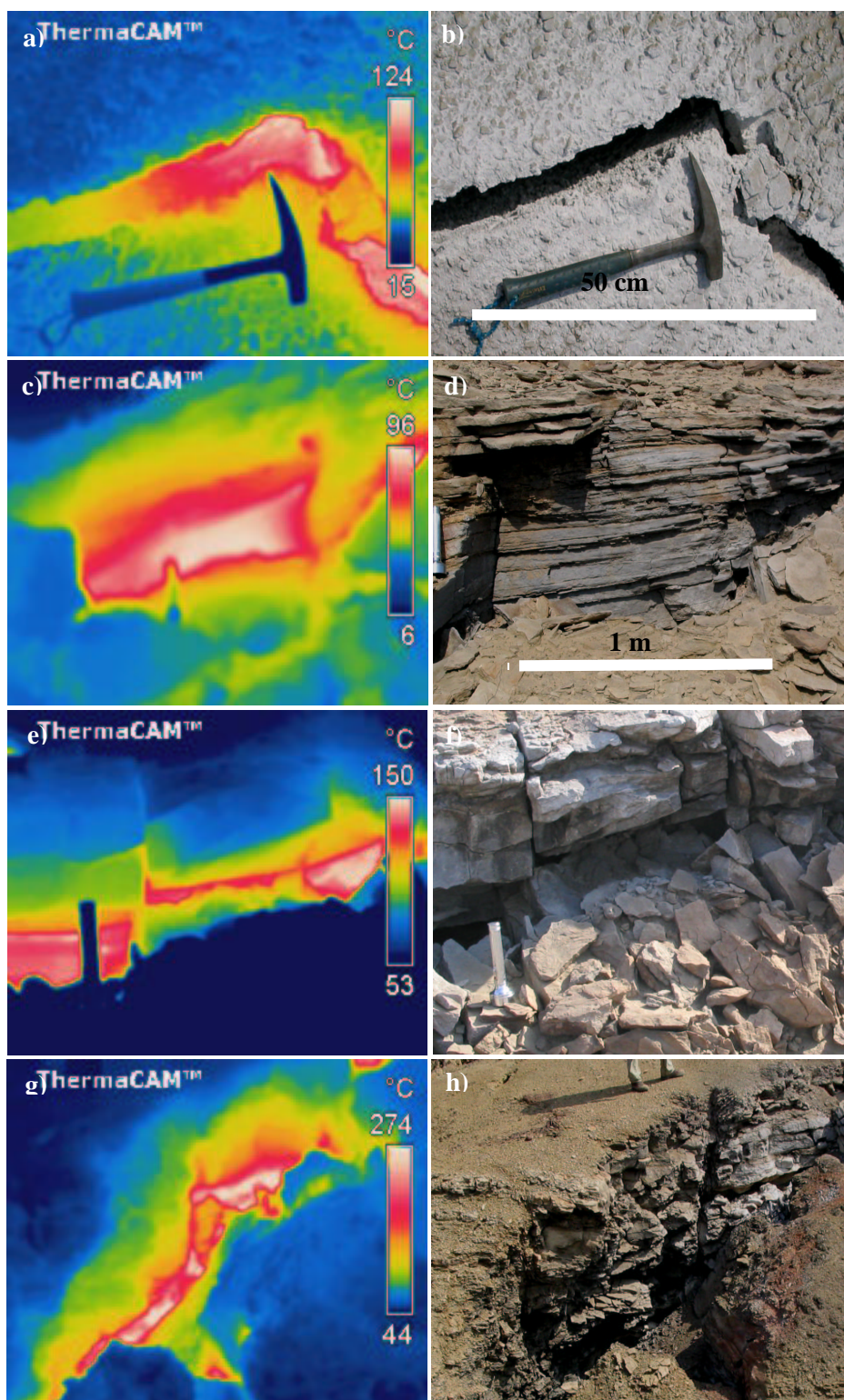


Figure 5-4: Infrared images (left) and optical photos of corresponding area (right) of crack zones along a sub-surface coal fire (coal fire number 7) at the Wuda coalfield. The temperature pattern in a, c and e can be regarded as representative for coal fire cracks in the Wuda coalfield, while the temperature pattern in g, with temperatures exceeding 500 K, are abnormal high.

5 Field observations of the Ruqigou, Gulaben and Wuda coalfields

The radiant temperatures of the CFSA on the investigated sub-surface coal fire ranged between 325 K and 638 K in September 2003. Typical temperature pattern of fire cracks and holes of the Wuda coal fire 7 are shown in figure 5-4. The average temperature of CFSA measured along fire cracks was 375 K in September 2003, while the average temperature of CFSA in the collapsed zone was, at 396 K, slightly higher. The thermal images in figure 5-3, and the temperature profiles in figures 9-1 and 9-2, clearly indicate that the temperatures are not evenly distributed within the mapped CFSA, and that CFSA exceeding 400 K are locally very limited. A conductive heat transport could only be observed in the direct environment of fire cracks or holes of the investigated coal fire, resulting in a thermal aureole of less than 3 m.

Approximately 80 radiant-temperature measurements were carried out at the Wuda near-surface coal fire 8, and additionally, thermal images were taken during the second field campaign. Two temperature profiles were taken synchronously with a daytime ETM overpass in September 2002 (chapter 9, figure 9-3). Night-time temperature profiles could not be measured because, this fire area was not accessible during night-time. Thermal and optical images of the near-surface coal fire zones are displayed in figure 5-5. The map of the CFSA is displayed in figure 5-2.

The burning coal layer of the investigated fire zone is steeply dipping, and CFSA are restricted to an approximately 200 m wide zone along the coal seam, including several fire cracks and holes, as well as near-surface coal fires. The geological strata in this area are roughly N-S striking, and change from white sandstone layers and black shale in the West, to outcropping coal seams and yellow sandstone layers in the East. Maximum surface temperatures reached up to 863 K in September 2002, but the size of these hot spots with temperatures of more than 600 K was locally very limited, and did not exceed 5 m².

Intensive fire activities were observed in the northern and southern part of this CFSA zone, while the centre part of this coal fire was relatively inactive. Average temperatures of CFSA of this near-surface coal fire were with 459 K higher than average temperatures of the investigated zone of the coal fire number 7. The thermal images in figure 5-5 clearly indicate that the temperatures in the CFSA zone were rather heterogeneous. High radiant surface temperatures could be observed locally along crack zones (figure 5-4, a-d), but as in the case of coal fire number 7 the overall temperatures (figure 5-4, g-j) were rather low.

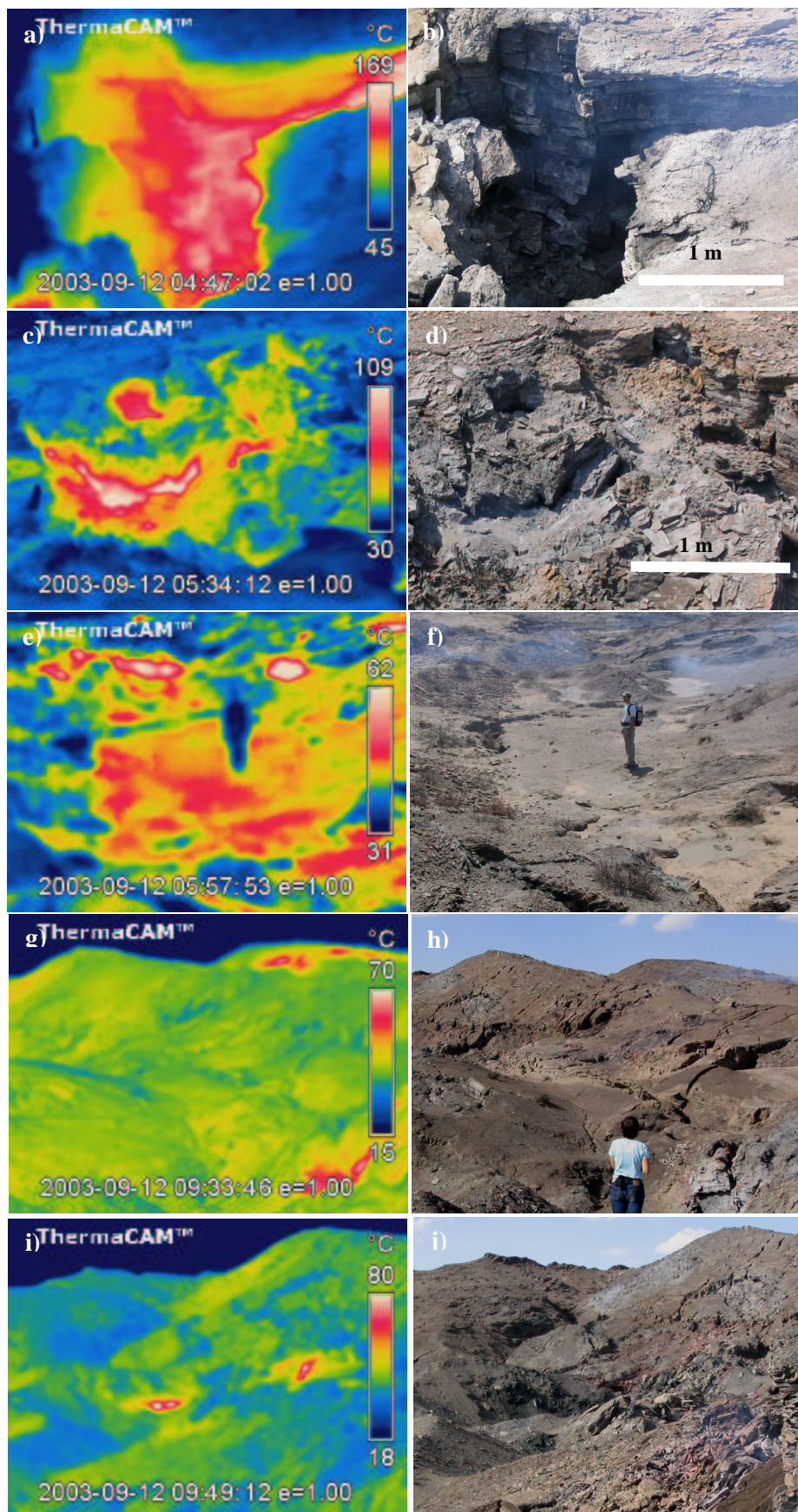


Figure 5-5: Infrared images (left), and optical photos of the corresponding area (right), of a near-surface coal fire (coal fire number 8) at the Wuda coalfield. Temperatures of hot cracks (a – d) exceed locally 380 K, while the overall temperatures measured over large areas (e – j) is remarkably lower. The infrared pictures were taken with a handheld thermal camera.

5.4 Intraday variations of background and coal fire temperatures

In order to examine temperature variations of different background materials and different sun facing slopes, temperature measurements of typical surface materials (vegetation, sandstone and black shale surfaces) and of a representative hill slope were performed with the radiant thermometer. In addition intraday temperature measurements of two fire cracks were carried out with the hand-held thermal camera. All measurements were undertaken on the 23rd September 2002 and the 18th September 2003, under blue-sky conditions, with maximum air temperatures of 311 K.

Intraday temperature plots of a horizontal black shale surface, a horizontal sandstone surface, a horizontal vegetation surface and a fire crack are shown in figure 5-6. The plots clearly indicate that at the time of the ASTER, ETM and BIRD overpasses (approx. 10:30 am and 12:00 am) the radiant-temperature difference between surfaces covered with vegetation, and a black shale surface, is significant, showing an approx. 15 K difference. Temperature variations of different surface materials therefore must be considered as significant during summer daytime satellite acquisition. At 7:30 pm all investigated surfaces show relatively similar radiant temperatures, indicating that background variations are rather low after sunset. The temperature of the investigated fire crack varies during the day, but the variation is not clearly linked to the sun intensity.

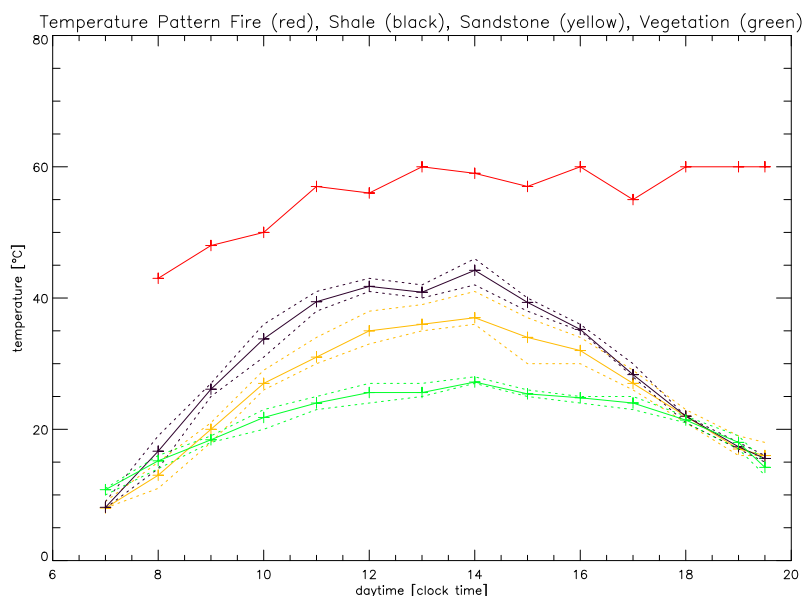


Figure 5-6: Intraday temperature measurements of a horizontal black shale surface (black), a horizontal sandstone surface (yellow), a horizontal vegetation surface (green) and a fire crack (red). Ten different measurements were performed on each investigated surface. Dotted lines mark minimum and maximum temperatures, while solid lines mark corresponding mean temperatures. The graph clearly indicates that background temperature (surfaces including no fire) are significant during daytime overpasses (~ 10:30 to 12 am), but are relatively low after sunset (sun set ~ 6 pm).

Figure 5-7 shows intraday, radiant-temperature measurements of an east- and west-facing slope of a sandstone hill. The flanks of the investigated hill are gently dipping with a slope of about 25° for the

5 Field observations of the Ruqigou, Gulaben and Wuda coalfields

western flank, and a slope of about 10° for the eastern flank. The hill can be considered as representative for the topography of the Wuda coalfield, while the relief energy is significantly higher in the Ruqigou and Gulaben coalfield. The average temperature difference between the eastern and western facing mountain side is maximally 7 K at the time of the satellite overpass ($\sim 10:30$ to 12 am), and therefore significant temperature variations, due to uneven solar heating, can be expected on daytime summer data.

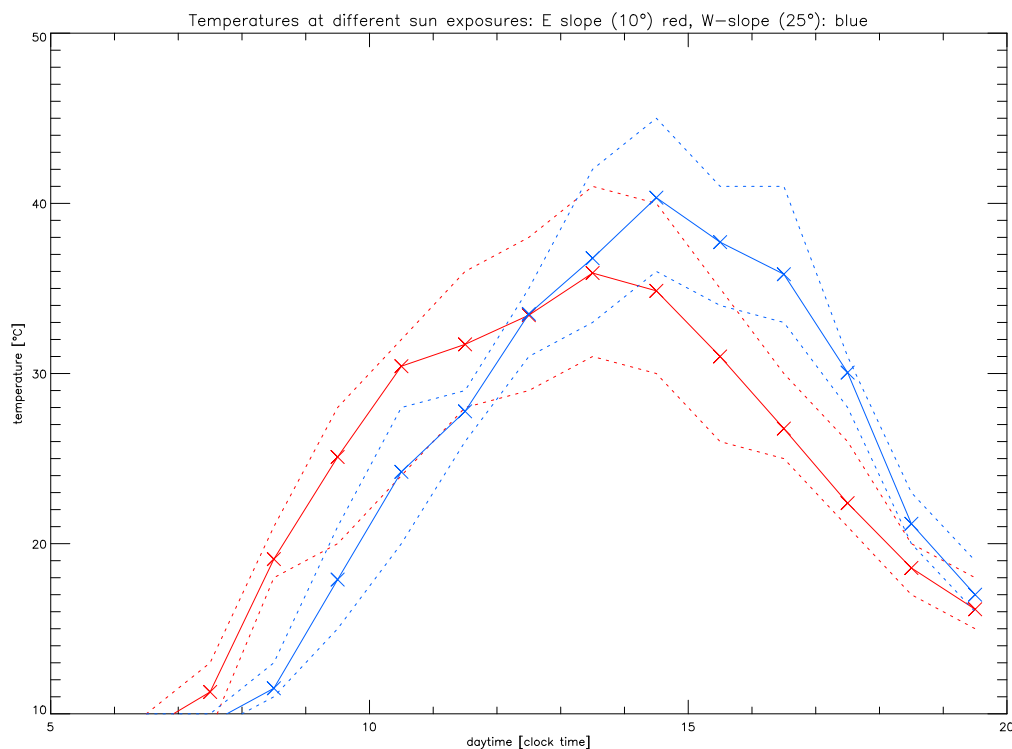


Figure 5-7: Intraday temperature measurements of an approximately east- (10° dip, red) and west-facing (25° dip, blue) slope. Dotted lines mark minimum and maximum temperatures, while solid lines mark corresponding mean temperatures. The graph clearly indicates that temperature variations, due to uneven sun heating, can be significant during daytime summer satellite overpasses ($\sim 10:30$ to 12 am), even in a relatively flat topography.

Thermal images of two fire cracks taken from sunrise to noon are illustrated in figures 5-8 and 5-9. The images were taken on relatively homogeneous surfaces. Both figures clearly indicate that the coal fire induced, temperature anomalies can be clearly detected shortly after sunrise. Although the surface material close to the two fire cracks is relatively homogeneous, background variations become significant at about 10 am, and the CFSA are then much more difficult to discern than early after sunrise. In addition, a CFSA appears along the fire crack 2 (red arrow, figure 5-9) at 10 am which cannot be related to the coal fire crack. At 1 pm the temperature anomalies are spread along the crack and are difficult to discern, at least along fire crack 2. Nevertheless it is important to note here, that the anomalies are significantly stronger around noon and are superimposed on the relatively warm background. The intraday measurements of the two fire cracks clearly indicate that temperature

5 Field observations of the Ruqigou, Gulaben and Wuda coalfields

variations during summer daytime definitely limit the recognition of CFSA. However the temperature anomalies do not disappear, but are superimposed on the background.

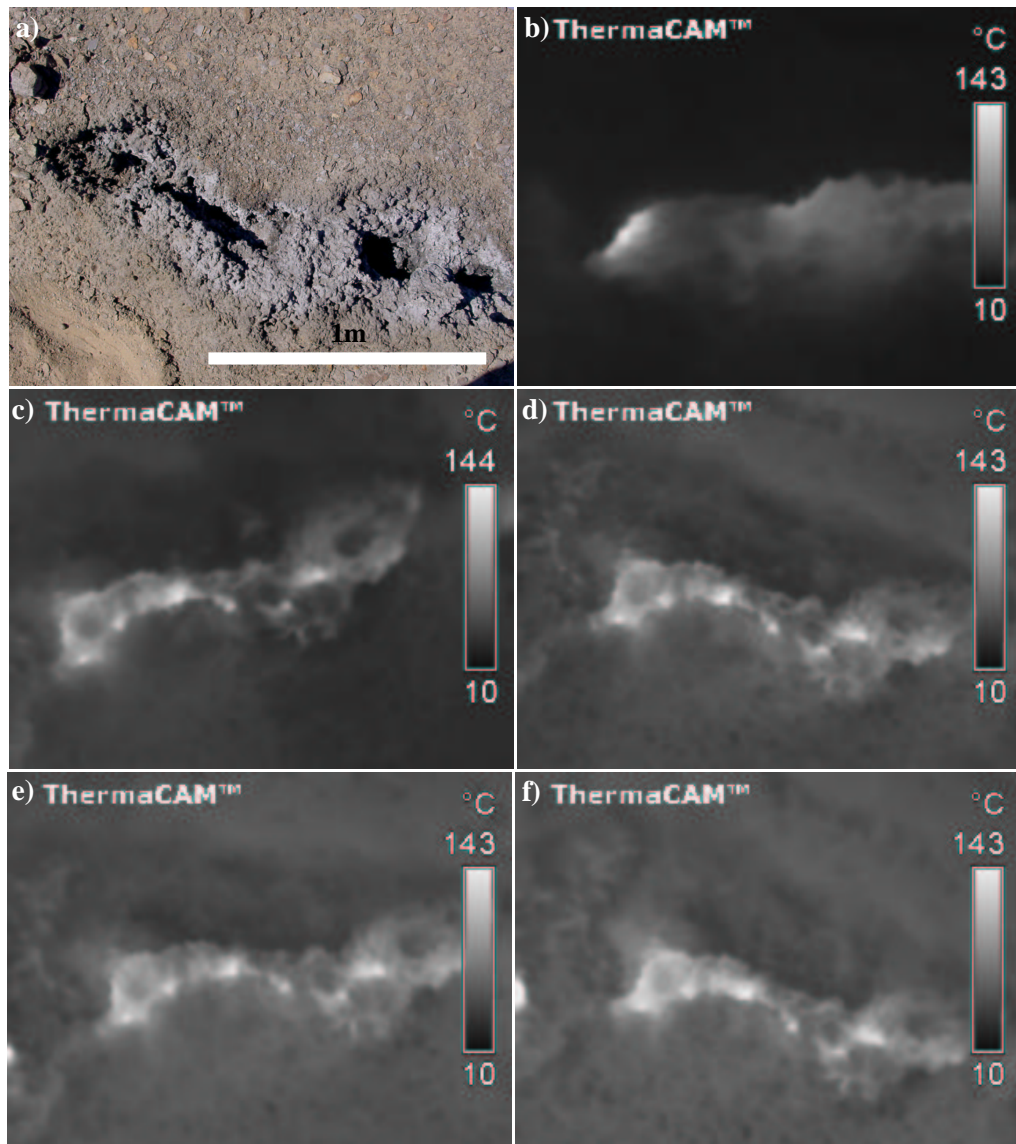


Figure 5-8: Temperature distribution on fire crack. a) Optical image; b) thermal image 7:00 am; c) thermal image 8:30 am; d) thermal image 10:00 am; e) thermal image 11:30 am; f) thermal image 1 pm.

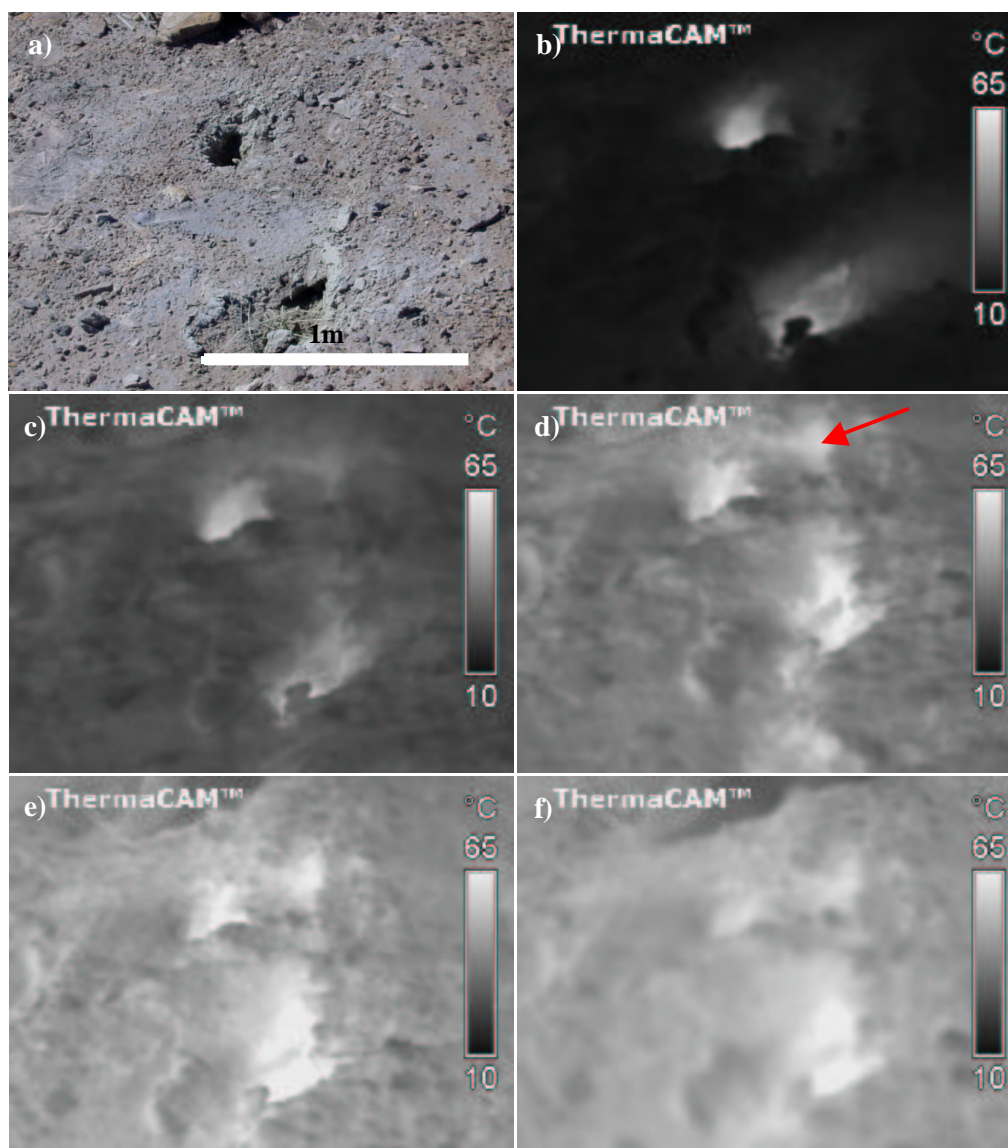


Figure 5-9: Temperature distribution on fire crack 2. a) Optical image; b) thermal image 7:00 am; c) thermal image 8:30 am; d) thermal image 10:00 am; e) thermal image 11:30 am; f) thermal image 1:00 pm. The red arrow marks a CFSA that is not linked to the coal fire, but appears from the 10:00 am image onward due to imbalanced sun heating.

5.5 Temperature measurements of the Yellow River water surface

Temperatures of the Yellow River water surface were measured at one location, synchronous with satellite overpasses to provide a reliable calibration target. The measured radiant temperatures are listed in table 5-4.

5 Field observations of the Ruqigou, Gulaben and Wuda coalfields

| time | T mean [°C] | T min [°C] | T max [°C] | number of measurements |
|---------------------|------------------------|-----------------------|-----------------------|---------------------------------------|
| 2002/09/21 10:30 am | 16.1 | 16.0 | 16.3 | 4 |
| 2002/09/21 12:00 am | 17.1 | 16.5 | 17.3 | 5 |
| 2002/09/21 10:30 pm | 13.7 | 13.5 | 13.9 | 3 |
| 2003/09/28 10:30 pm | 15.3 | 14.7 | 15.9 | 4 |

Table 5-4: *Temperature measurements of the Yellow River water surface during cloud free ASTER, ETM and BIRD satellite overpasses in September 2002.*

5.6 Conclusions

With respect to satellite image based, coal fire quantification, the field observations allow for the following conclusions:

- CFSA in all three study areas have average temperatures ranging from 339 K to 459 K. CFSA with temperatures of more than 600 K occur very seldom and are locally limited. The measured temperatures are similar to typical coal fire related temperatures reported by Zhang (1998) from coalfields in Xinjiang (description in chapter 2, section 2.3). The observed maximum temperature limit of 600 K, reported from Goerlich (2004, pers. communication) for the majority of the coal fires in Xinjiang, is also valid for the three investigated coalfields in central China. Thus, a satellite data based coal fire quantification concept has to target ‘warm’ spots rather than ‘hot spots’ with average temperatures of less than 600 K.
- The area of CFSA in our study area is rather small, not exceeding 30 % of ground segments corresponding to an ETM pixel. Because BIRD and ASTER pixels are larger than an ETM pixel (description in chapter 6), an image pixel that corresponds with a coal fire will always contain both fire and background information. A satellite based coal fire quantification concept therefore has to be based on a sub-pixel concept.

5 Field observations of the Ruqigou, Gulaben and Wuda coalfields

- Background variations due to different surface materials and sun exposure can be significant during summer daytime and can distinctly limit the recognition of CFSA. Thus, optimal temporal conditions, for satellite observation of coal fires, are those periods that have low, or no sun reflectance (i.e. night-time or winter data).

THEORETICAL INVESTIGATIONS

6 THE POTENTIAL OF THE ETM, ASTER AND BIRD INSTRUMENT TO REGISTER SPECTRAL COAL FIRE RADIANCES

This chapter consists of an investigation of the thermal channels of the ETM, ASTER and BIRD instruments. The investigation is aimed at ascertaining each instrument's sensitivity to the registration of spectral coal fire radiances, and takes into consideration the sensor-specific, spectral response functions and the thermal properties of coal fires observed during the field campaigns. The theoretical investigations are performed for different background and coal fire scenarios. In addition, the potential of each instrument to observe spectral coal fire radiances in two unsaturated and spectral well-separated channels is analysed.

6.1 Methods

6.1.1 Simulated coal fire and background conditions

Simulated fire temperatures range between 300 K and 900 K, while simulated fire sizes for ASTER and ETM simulations range between 1 % and 100 % pixel coverage (max. 3600 m² ETM, max 8100 m² ASTER). For the BIRD sensitivity studies a maximum fire size of 10000 m² was assumed. The scenarios include typical temperatures and sizes of investigated coal fire induced, surface anomalies (CFSA).

Simulated background scenarios represent typical temperatures or surface reflectances of coal-bearing strata in the study areas. In the SWIR spectral range the background radiances consist only of reflected sunlight (description chapter 3, section 3.1.2). Five different background conditions are assumed for SWIR simulations:

- Night-time: no reflectance (**R I**)
- Daytime homogeneous coal surface: 10 % reflectance (**R II**)
- Daytime homogeneous sandstone surface: 27 % reflectance (**R III**)
- Daytime heterogeneous coal surface: 10 % reflectance (background variation 20 % reflectance) (**R IV**)
- Daytime heterogeneous sandstone surface: 27 % reflectance (background variation 20 % reflectance) (**R V**)

The assumed SWIR background reflectances are averages measured by Claudia Kuenzer (DLR) on coal and sandstone surfaces during the field campaign in September 2002 at the Wuda coalfield (Kuenzer, 2003, pers. communication).

6 The potential of the ETM, ASTER and BIRD instrument to register spectral coal fire radiances

In the TIR range the sun reflectance is absent (description in chapter 3, section 3.1.2). Consequently, the TIR background conditions are considered here to be exclusively emissive. In the MIR spectral region the self-emitted terrestrial radiation becomes significant (description in chapter 3, section 3.1.2). Nevertheless, due to the need for simplification the reflected sun radiation is neglected in this study.

Four different background winter and summer conditions are assumed for MIR and TIR channel simulations:

- Winter homogeneous background: temperature 273 K (**Th I**)
- Summer homogeneous background: temperature 298 K (**Th II**)
- Winter heterogeneous background: temperature 273 K (background variation +/- 5 K, **Th III**)
- Summer heterogeneous background: temperature 298 K (background variation +/- 10 K, **Th IV**)

Background radiance variations are significantly lower during the night-time than during the daytime due to absence of direct sun heating. The homogeneous TIR background simulations are thus representative for night-time conditions, while the heterogeneous TIR simulations reflect daytime conditions. Due to the fact that the MIR reflectance is neglected in this study, MIR simulations are only fully representative for night-time conditions. Summer background variations approximately reflect the 10:30 am background variation measured during the field campaign (description in chapter 5, section 5.4), while winter background variations are typical, average background temperature variations, observed in ETM or ASTER winter thermal data.

6.1.2 Sensitivity criteria

Within this study a specific channel of the ASTER, ETM and BIRD instrument is considered to be sensitive to the registration of spectral coal fire radiances if:

- the investigated channel has a spectral response function in the SWIR, MIR or TIR spectral range. Our field observations revealed that most coal fire related surface temperatures lie within the temperature range of 350 K to 600 K. According to Planck' s Law (equation 3.2, figure 3-1) 350 K to 600 K blackbodies make no significant emissions in the NIR spectral range, but emit in the TIR, MIR or SWIR spectral range. Thus, only SWIR, MIR or TIR spectral channels have a potential to register spectral coal fire radiances.
- the spectral radiance of most of the representative coal fire scenarios exceeds the background radiance / reflectance and the sensor related errors. The background radiance is

considered to represent the atmospherically corrected, band-integrated Planck function at the background temperature in case of a homogeneous background. For a heterogeneous background the background radiance is considered to be the atmospherically corrected, band-integrated Planck function at the background temperature plus the maximum background variation. These criteria are referred to in the following study as the lower registration limit (LD).

- the spectral radiance of at least one representative coal fire scenario is lower than the saturation limit of the investigated instrument channel (= upper registration limit: UD). In the case where a coal fire corresponding image pixel is saturated, the absolute magnitude of emitted spectral coal fire radiance cannot be determined.

6.1.3 Sensitivity calculations

In order to study the sensitivity of the specific instrument channels to the registration of spectral coal fire radiances, simulated coal fire sizes and temperatures are plotted against pixel integrated spectral radiances, recorded in the investigated BIRD, ASTER and ETM spectral channels (figure 6-1 to 6-15). The data of each plot in figures 6-1 to 6-10 and 6-12 to 6-15 are model simulations of image pixel corresponding ground segments, each containing a fire component of the indicated temperature and size, superimposed on a constant background temperature or reflectance. Different plots are performed for the different background scenarios described in section 6.1.1. Horizontal dashed lines in figures 6-1 to 6-10 and 6-12 to 6-15 indicate the ASTER, ETM and BIRD lower registration limit (LD), or the ASTER and ETM saturation limit (UD).

Owing to the fact that CFSA in all three investigated study areas are significantly smaller than an ASTER, ETM or BIRD pixel (description in chapter 5, section 5.2), a sub-pixel concept was applied to compute the channel-integrated, spectral radiances. The sub-pixel computation was performed using equation 3-11. Band integrated fire and background blackbody radiances ($L_{bb,s1}$ and $L_{bg,s1}$ in equation 3-11) were calculated via equations 3-2 and 3-4. An atmospheric correction was performed, to compute corresponding at-sensor radiances, using atmospheric parameters listed in tables 6-1 and 6-2. The atmospheric parameters were computed via the MODTRAN radiative transfer model (Berk et al., 1998) and adapted to dry desert conditions, with an assumed ground height of 1000 m above sea level.

6 The potential of the ETM, ASTER and BIRD instrument to register spectral coal fire radiances

| | h [km] | Lpath [MW / m ² sr μm] | trans | Flux [MW / m ² μm] |
|---|------------------|---|--------------|---|
| ETM channel 6 (TIR) | 1.0 | 1891.7 | 0.7557 | 5141.4 |
| BIRD MIR channel (visibility 20 km, no reflectance) | 1.0 | 32.4 | 0.7445 | 304.9 |
| BIRD TIR channel (visibility 20 km) | 1.0 | 1854.1 | 0.7107 | 5206.4 |
| ASTER channel 10 (TIR, visibility 20 km) | 1.0 | 980.3 | 0.8341 | 4396.1 |
| ASTER channel 13 (TIR, visibility 20 km) | 1.0 | 317.8 | 0.9538 | 1460.0 |

Table 6-1: Atmospheric parameters used to model MIR and TIR atmospheric effects. *Lpath* = path radiance, *trans* = transmissivity, *h* = height above sea level.

| | h [km] | Lpath [MW / m ² sr μm] | Edir * trans [MW / cm ² μm] | Ediff * trans [MW / cm ² μm] | trans |
|--|------------------|---|--|---|--------------|
| ETM channel 5 (SWIR, visibility 20 km, solar zenith 40°) | 1.0 | 0.0398382 | 16.3147 | 3.41728 | 0.9569 |
| ETM channel 7 (SWIR, visibility 20 km, solar zenith 40°) | 1.0 | 0.0121439 | 5.68096 | 1.12056 | 0.9343 |

Table 6-2: Atmospheric parameters used to model SWIR atmospheric effects. *Lpath* = path radiance, *trans* = transmissivity, *Edir * trans* = direct flux * transmissivity, *Ediff * trans* = diffuse flux * transmissivity, *h* = height above sea level.

6.2 ETM sensitivity study

6.2.1 Satellite and instrument characteristics

The Enhanced Thematic Mapper (ETM) scanning radiometer, on the Landsat 7 satellite, is the latest of a series of earth observation instruments dating back to 1972. The Landsat Program is managed cooperatively by the National Aeronautics and Space Administration (NASA, US), the National Oceanic and Atmospheric Administration (NOAA, US) and the US Geological Survey (USGS). Landsat 7 was launched in 1999, into a sun-synchronous, near polar orbit. The spacecraft crosses the Equator between 10:00 am and 10:15 am on a descending north to south path, completes over 14 orbits per day and covers the entire earth every 16 days.

6 The potential of the ETM, ASTER and BIRD instrument to register spectral coal fire radiances

The ETM instrument scans the earth with a swath width of 185 km and replicates the capabilities of the Thematic Mapper on Landsat 4 and 5. Unlike its predecessors the ETM includes new features, like a panchromatic band with a 15 m spatial resolution, an improved radiometric calibration and a TIR channel with a 60 m spatial resolution. The spectral characteristics of the ETM instrument are listed in table 6-3.

| band number | spectral range [μm] | ground resolution [m] |
|----------------|----------------------------------|-----------------------|
| 1 (VIS) | 0.45 to 0.515 | 30 |
| 2 (VIS) | 0.525 to 0.605 | 30 |
| 3 (VIS) | 0.63 to 0.69 | 30 |
| 4 (NIR) | 0.75 to 0.90 | 30 |
| 5 (SWIR) | 1.55 to 1.75 | 30 |
| 6 (TIR) | 10.4 to 12.5 | 60 |
| 7 (SWIR) | 2.09 to 2.35 | 30 |
| Pan (VIS, NIR) | 0.52 to 0.90 | 15 |

Table 6-3: *Spectral characteristics of the ETM instrument.*

The ETM instrument has an 8 bit radiometric resolution and is designed to achieve a radiometric data calibration with a 5 % degree of uncertainty. The ETM channels have both low and high gain setting. The low gain sensor setting measures a greater radiance with decreased sensitivity, while high gain measures a lesser radiance range with an increased sensitivity. The thermal infrared channel 6 has two gain settings, a high and a low gain setting. For other channels the instrument registers image data in one of two possible gain settings depending on the solar conditions during data acquisition.

The Landsat 7 ETM is an operational satellite system, i.e. the capacities of the satellite, instrument and ground stations are sufficient to allow continuous acquisition. The ETM instrument is supported by a ground network that receives ETM data, via direct downlink, at the primary receiving station at the USGS in South Dakota, and throughout a world wide network of receiving stations. The data sets are made available on-line via the EROS Data Center. On request systematically corrected level 1b products (i.e. corrected for scan direction and band alignment as well as radiometric and geometric corrected) are generated and distributed to users.

A mechanical failure of the ETM instrument's scan line corrector on the 31st May 2003 has made later data sets unusable for scientific applications. The scan line corrector normally compensates for the significant geometric image distortion, resulting from the satellite's rapid forward motion.

6.2.2 Sensitivity study

The two ETM SWIR channels and the TIR channel were investigated in this study. Figures 6-1 to 6-6 show different fire sizes and temperatures plotted against simulated ETM SWIR and TIR spectral at-sensor radiances. The SWIR fire scenarios are plotted for background conditions R I to V, while the TIR fire scenarios are plotted for background conditions Th I to IV (background conditions: see section 6.1.1). Tables 6-4 and 6-5 summarize the lower (LD) and upper coal fire registration limits (UD) derived from figures 6-1 to 6-6. The upper coal fire registration limits (UD) in tables 6-4 and 6-5 and figures 6-1 to 6-6 reflect the saturation limit of the corresponding ETM low gain channel.

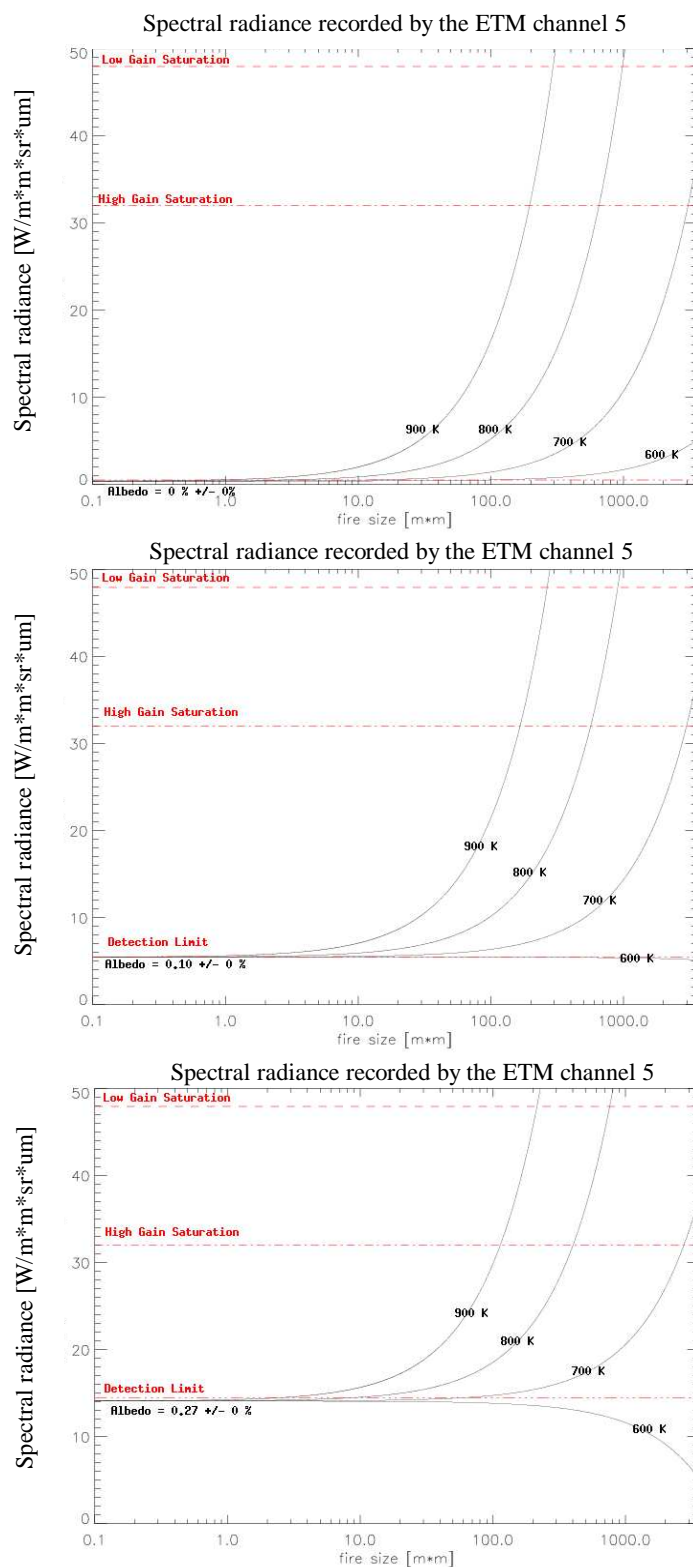


Figure 6-1: Spectral radiance of an image pixel-correspondent ground segment, containing a sub-pixel fire component at various fire temperatures, fire areas and background conditions, recorded by the ETM channel 5. The dotted lines mark the lower and upper detection limits. Top) night-time: no reflectance (R I); middle) daytime homogeneous coal surface: 10 % reflectance (R II); bottom) daytime homogeneous sandstone surface: 27 % reflectance (R III).

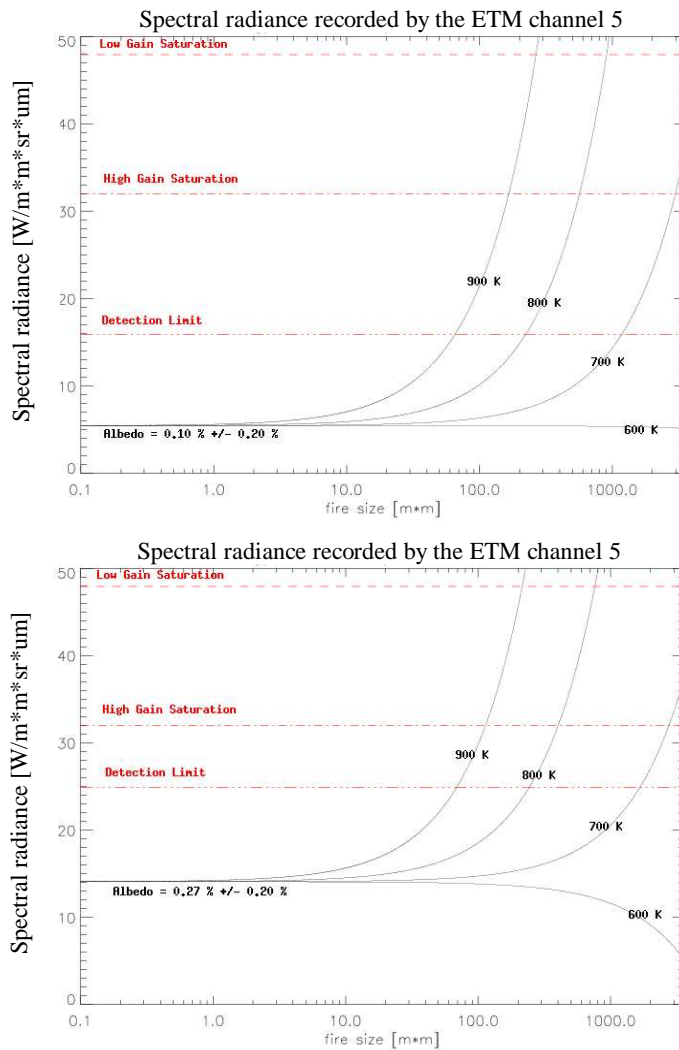


Figure 6-2: Spectral radiance of an image pixel-correspondent ground segment, containing a sub-pixel fire component at various fire temperatures, fire areas and background conditions, recorded by the ETM channel 5. The dotted lines mark the lower and upper detection limits. Top) daytime heterogeneous coal surface: 10 % reflectance, max. variation 20 % reflectance (R IV); bottom) daytime heterogeneous sandstone surface: 27 % reflectance, max. variation 20 % reflectance (R V).

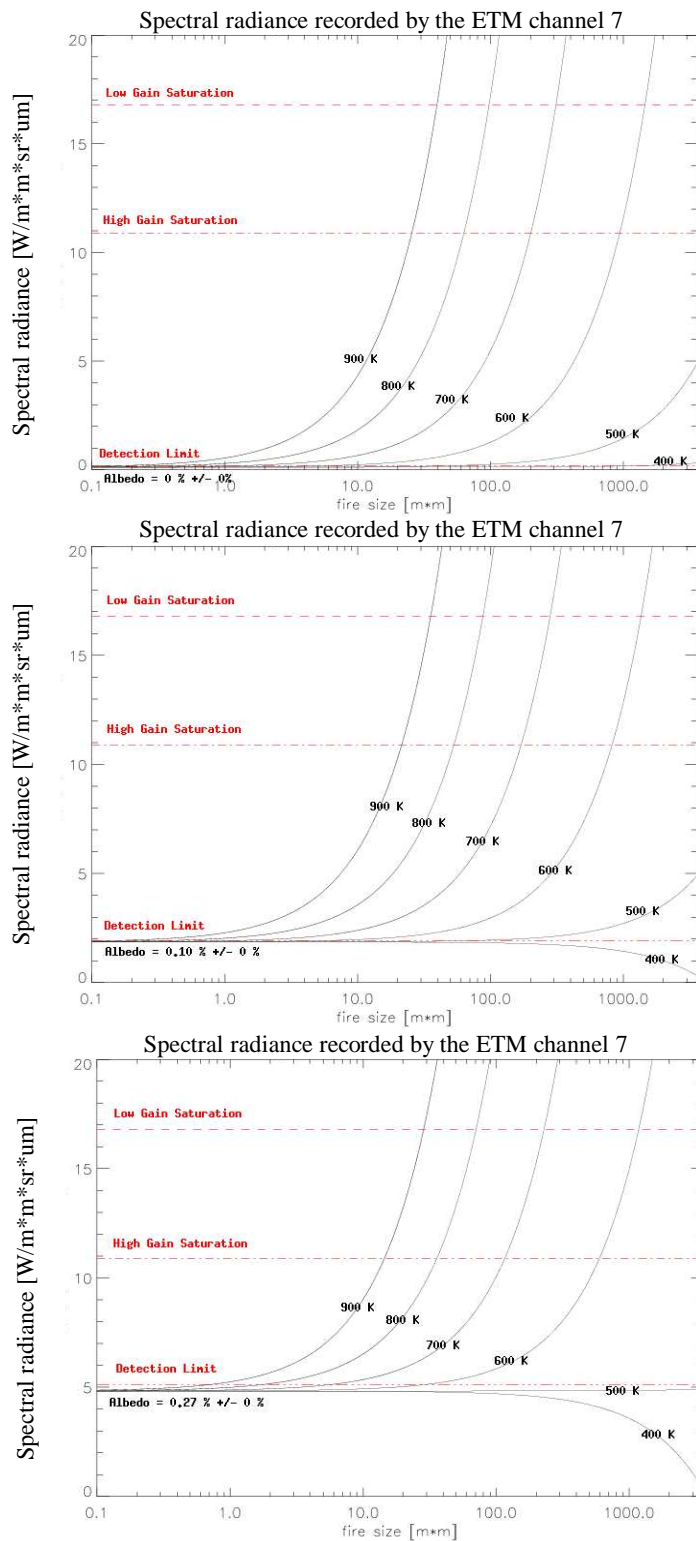


Figure 6-3: Spectral radiance of an image pixel-correspondent ground segment, containing a sub-pixel fire component at various fire temperatures, fire areas and background conditions, recorded by the ETM channel 7. The dotted lines mark the lower and upper detection limits. Top) night-time: no reflectance (R I); middle) daytime homogeneous coal surface: 10 % reflectance (R II); bottom) daytime homogeneous sandstone surface: 27 % reflectance (R III).

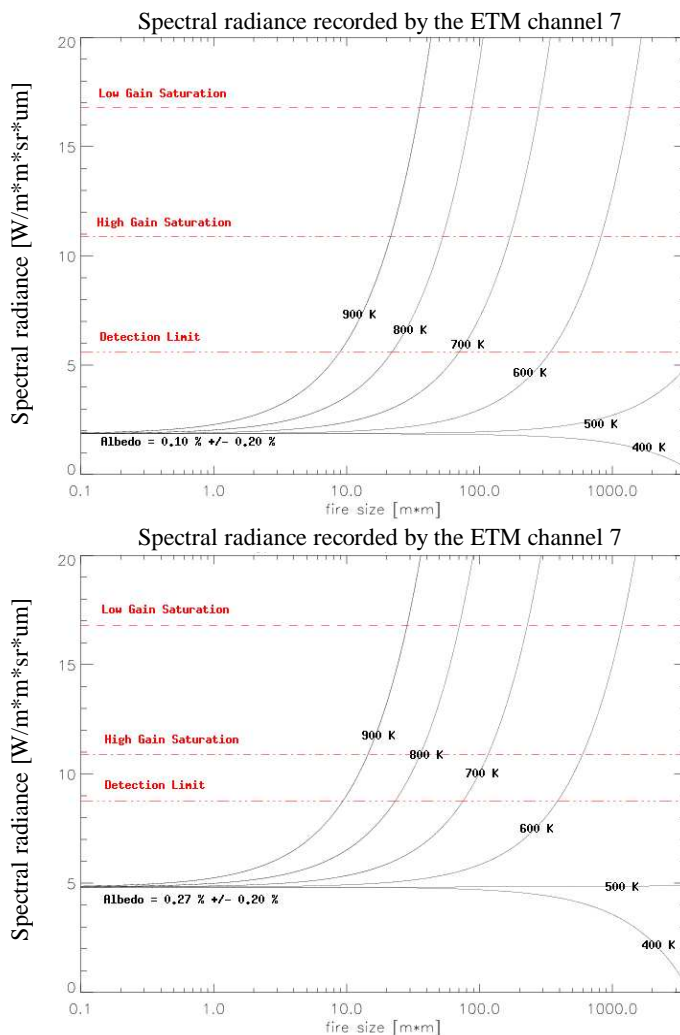


Figure 6-4: Spectral radiance of an image pixel-correspondent ground segment, containing a sub-pixel fire component at various fire temperatures, fire ares and background conditions, recorded by the ETM channel 7. The dotted lines mark the lower and upper detection limits. Top) daytime heterogeneous coal surface: 10 % reflectance, max. variation 20 % reflectance (R IV); bottom) daytime homogeneous sandstone surface: 27 % reflectance, max. variation 20 % reflectance (R V).

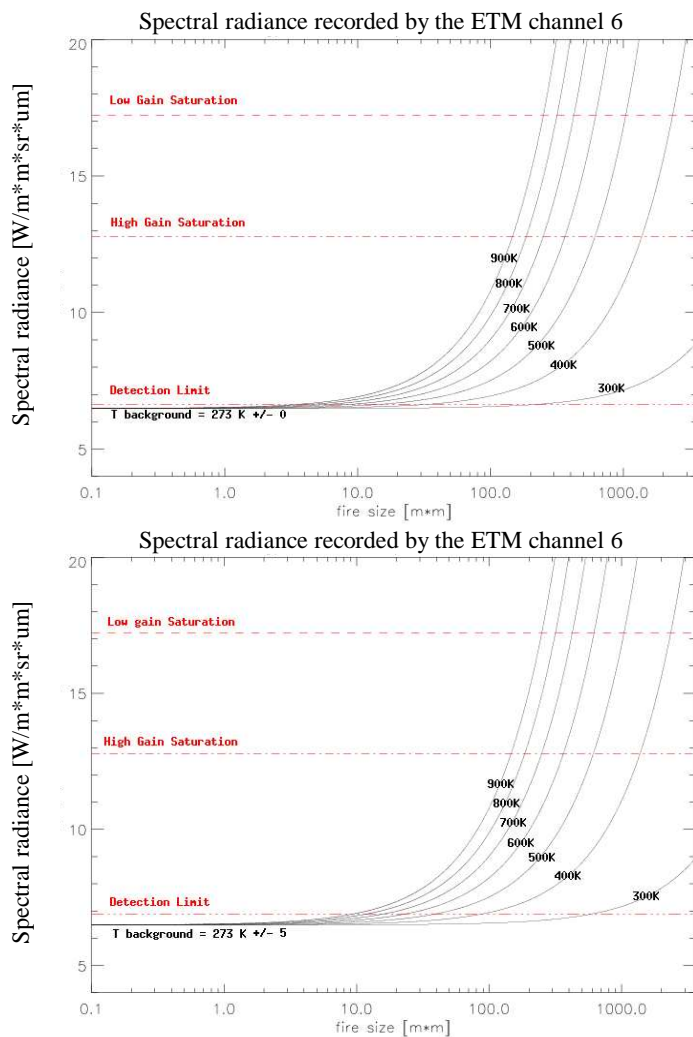


Figure 6-5: Spectral radiance of an image pixel-correspondent ground segment, containing a sub-pixel fire component at various fire temperatures, fire areas and background conditions, recorded by the ETM channel 6. The dotted lines mark the lower and upper detection limits. Top) winter homogeneous background: background temperature 273 K (Th I); bottom) winter background: background temperature 273 K, max. background variation 5 K (Th III).

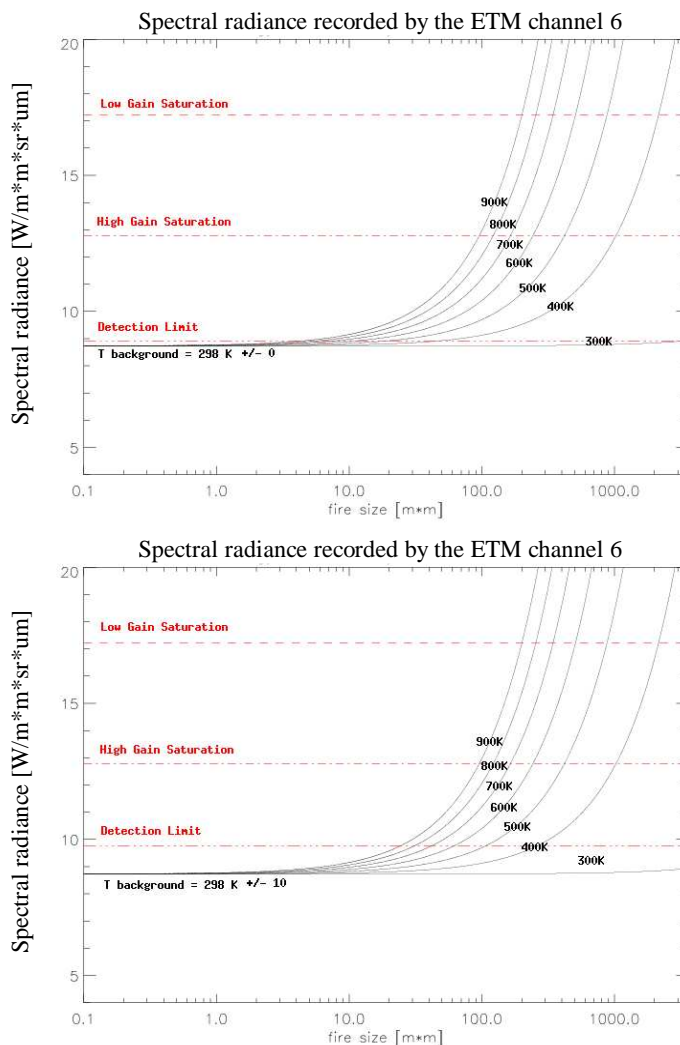


Figure 6-6: Spectral radiance of an image pixel-correspondent ground segment, containing a sub-pixel fire component at various fire temperatures, fire area and background conditions, recorded by the ETM channel 6. The ground segment corresponds with an image pixel and contains a sub-pixel fire component at various fire temperatures, fire area and background conditions. The dotted lines mark the lower and upper detection limits. Top) summer homogeneous background: background temperature 298 K (Th II); bottom) summer background: background temperature 298 K, max. background variation 10 K (Th IV).

6 The potential of the ETM, ASTER and BIRD instrument to register spectral coal fire radiances

| background scenario | channel 5 fire area [m ²] | | | channel 7 fire area [m ²] | | |
|--|---------------------------------------|--------------------|--------------------|---------------------------------------|--------------------|--------------------|
| | T fire 600 K | T fire 500 K | T fire 400 K | T fire 600 K | T fire 500 K | T fire 400 K |
| R I (night-time, no reflectance) | LD 300 UD 3600 | - | - | LD 9 UD 1000 | LD 100 UD 3600 | - |
| R II (daytime, homogeneous coal surface) | - | - | - | LD 10 UD 1000 | LD 100 UD 3600 | - |
| R III (daytime, homogeneous sandstone surface) | - | - | - | LD 30 UD 1000 | - | - |
| R IV (daytime, heterogeneous coal surface) | - | - | - | LD 200 UD 1000 | - | - |
| R V (daytime heterogeneous sandstone surface) | - | - | - | LD 300 UD 900 | - | - |

Table 6-4: Minimum and maximum coal fire size that can be registered by the ETM channels 5 and 7 at certain fire temperatures and background conditions. LD = lower detection limit, UD = upper registration limit low gain. The different background scenarios are described in detail in section 6.1.1. A 600 K coal fire, for example, can only be registered under night-time conditions (R I) by the ETM channel 5, when the fire size, within a ground segment corresponding image pixel, ranges between 300 m² and 3600 m².

| background scenario | channel 6 fire area [m ²] | | |
|--|---------------------------------------|--------------------|--------------------|
| | T fire 600 K | T fire 500 K | T fire 400 K |
| Th I (winter, homogeneous background) | LD 10 UD 600 | LD 20 UD 1000 | LD 30 UD 2100 |
| Th II (summer, homogeneous background) | LD 10 UD 500 | LD 20 UD 900 | LD 70 UD 2050 |
| Th III (winter, heterogeneous background) | LD 20 UD 600 | LD 40 UD 1000 | LD 100 UD 2100 |
| Th IV (summer, heterogeneous background) | LD 60 UD 500 | LD 100 UD 900 | LD 200 UD 2050 |

Table 6-5: Minimum and maximum coal fire sizes that can be registered by the ETM channel 6 at a certain fire temperature and background condition. LD = lower registration limit, UD = upper registration limit low gain. The different background scenarios are described in detail, in section 6.1.1. A 600 K coal fire, for example, can be registered in winter, on a homogeneous background (Th I) by the ETM channel 6, provided that the fire size, within an image pixel-correspondent ground segment, ranges between 10 m² and 600 m².

6 The potential of the ETM, ASTER and BIRD instrument to register spectral coal fire radiances

Table 6-4 and figures 6-1 to 6-2 clearly indicate that the capacity of the ETM 5 channel to register spectral fire radiances is restricted to fires with high temperatures and / or large sizes. 600 K fires can only be registered during night-time if the fire size exceeds 300 m². Fires with temperatures of around 500 K or lower cannot be registered by the ETM 5 channel under the assumed background conditions. Investigated CFSA in the study areas are relatively cold, with average temperatures ranging between 339 K and 459 K (description in chapter 5, section 5.2). Consequently the majority of coal fires that were investigated cannot be detected by the ETM channel 5.

During field observations coal fire related, surface hot spots were observed, with temperatures exceeding 600 K. These were locally very limited, with a maximum size of 15 m² in a ground segment corresponding with an ETM pixel (description in chapter 5, section 5.2). Figure 6-1 demonstrates that 700 K to 800 K hot spots, with sizes of about 15 m², are close to the lower detection limit of the ETM channel 5, under absolutely homogeneous background conditions. Thus, under optimal conditions (e.g. night-time) these exceptionally hot surface, or near surface coal fire spots could produce very weak signals in the ETM channel 5.

Although the ETM channel 7 can register significantly smaller and / or colder fires, in comparison with the ETM channel 5, the majority of investigated CFSA cannot be detected. 600 K fires can be registered by the ETM channel 7 under all modelled background conditions, but, due to the relatively low saturation limit, the maximum fire size is restricted to about 1000 m² (table 6-4, figures 6-3 to 6-4). 500 K fires can only be registered if the background surface shows no radiance variations and if the fire size exceeds 100 m². Fires with temperatures of 400 K or less cannot be recorded by the ETM 7 channel. Uppermost average surface temperatures (~ 450 K) of coal fires in the studied coalfields are thus at the registration limit of the ETM channel 7. Geological strata in the coalfields consist of closely alternating layers, with different surface reflectances (e.g. sandstone and coal layers) and the occurrence of large homogeneous surfaces is thus not likely. Consequently, the capability of the ETM 7 channel to record spectral coal fire radiances is restricted to coal fires with exceptional hot surface temperatures during night-time.

The ETM 6 channel has a high potential to register CFSA (table 6-5, figures 6-5 to 6-6). Spectral radiances of fires with average temperature of 600 K can be recorded from a minimum size of about 10 m² (winter, homogeneous background) up to 60 m² onward (summer, heterogeneous background). Nevertheless, the low saturation limit of this channel restricts the registration of 600 K fires to a maximum size of 600 m². A 500 K fire can be registered up to a size of 1000 m², in winter on a homogeneous background, while the minimum detectable fire size of a 500 K fire is about 20 m². On a heterogeneous summer background a 500 K fire can be registered if the fire size ranges between 100 m² and 900 m². CFSA with average temperatures of about 400 K can be recorded by the ETM 6

6 The potential of the ETM, ASTER and BIRD instrument to register spectral coal fire radiances

channel for fire sizes ranging between 30 m² and 2100 m² (homogeneous winter background) and 200 m² to 2000 m² (heterogeneous summer background). Average temperatures of CFSA in the study areas range between 339 K and 459 K, while the maximum fire size in an ETM corresponding ground segment is smaller than 1000 m². Spectral radiances of the overall majority of CFSA in the study areas can thus be recorded by the ETM 6 channel, at least during night-time (homogeneous background).

According to tables 6-4 and 6-5 and figures 6-1 to 6-6, increased and unsaturated pixel values in two ETM channels are very unlikely to be found for the investigated coal fires. A 400 K fire does not produce increased signals in two channels under the assumed background conditions. 600 K or 500 K fires can produce unsaturated signals in two channels, if the fire size ranges between 10 m² and 1000 m² or 100 m² to 1000 m², respectively. Nevertheless, average temperatures of observed CFSA are lower than 500 K and it is thus very unlikely that any investigated coal fire zone in the Wuda, Gulaben and Ruqigou coalfield would reveal increased and unsaturated pixels in two ETM channels.

6.2.3 Conclusions

According to this sensitivity study the ETM channel 6 has a high potential to register spectral coal fire radiances, while the capability of the two ETM SWIR channels to record spectral coal fire radiances is very limited.

A bi-spectral fire quantification (Dozier, 1981) needs increased and unsaturated pixel values in at least two, well-separated input channels (description in chapter 3, section 3.3.1). The ETM SWIR and TIR channels are spectrally well-separated, but anomalous and unsaturated pixel values in two channels are, according to this study, very unlikely. Prakash et al. (1997) and Zhang et al. (1997) report increased and unsaturated pixel values in two TM SWIR channels from surface coal fires in northern China and India. The two TM SWIR channels have a lower spatial resolution, but approximately the same spectral resolution as the ETM SWIR channels, and have therefore, a lower capacity to register coal fire related spectral radiances. Nevertheless, the number of coal fire induced, increased SWIR pixels is very limited in both studies. The bi-spectral technique is considered here as a tool that can be applied to quantify exceptionally large or hot surface coal fires, but which is not applicable to generally quantify coal fires.

Alternative fire quantification techniques (MIR and MODIS methods: described in chapter 3, section 3.3.2 and 3.3.3) derive CFRE from only one input channel. The optimal ETM channel for such a fire quantification concept is, according to this study, definitively the ETM TIR channel. Nevertheless, existing approaches are based on MIR pixel radiances, fail for fire temperatures below 600 K, and cannot, therefore, be directly applied to an ETM band based coal fire quantification.

6.3 ASTER sensitivity study

6.3.1 Satellite and instrument characteristics

The Advanced Spaceborne Thermal Emission and Reflection Radiometer (ASTER) was launched on NASA's Earth Observing System (EOS) Terra satellite in December 1999. The ASTER program is managed in cooperation between the NASA, Japan's Ministry of Economy, Trade and Industry (METI) and the U.S. Earth Remote Sensing Data Analysis Center (ERSDAC).

The Terra satellite is flying on a 705 km sun-synchronous orbit with a 10:30 am equatorial crossing. The ASTER instrument includes three different sub-systems: The Visible and Near Infrared (VNIR), the Shortwave Infrared (SWIR) and the Thermal Infrared (TIR) sub-system. The VNIR sub-system, with 15 m pixel resolution, has three channels ranging from 0.52 μm to 0.86 μm . The SWIR sub-system has a 30 m spatial resolution and records spectral radiances from 1.60 μm to 2.43 μm , while the TIR sub-system registers radiances from 8.125 μm to 11.65 μm with a 90 m IFOV. In contrast to the ETM, ASTER has five different TIR and six different SWIR channels. The ASTER TIR channels have, however, a 50% lower spatial resolution when compared with the ETM TIR channel. The different TIR and SWIR channels were primary-designed for geological applications, and are located at carbonate, hydrogen and silicate absorption bands. The characteristics of the ASTER instrument are summarized in table 6-6.

| characteristic | VNIR | SWIR | TIR |
|-----------------------|---|-------------------------------------|--------------------------------------|
| spectral range | band 1: 0.52 - 0.60 μm | band 4: 1.600 - 1.700 μm | band 10: 8.125 - 8.475 μm |
| | band 2: 0.63 - 0.69 μm | band 5: 2.145 - 2.185 μm | band 11: 8.475 - 8.825 μm |
| | band 3: 0.76 - 0.86 μm (nadir and background observation) | band 6: 2.185 - 2.225 μm | band 12: 8.925 - 9.275 μm |
| | | band 7: 2.235 - 2.285 μm | band 13: 10.25 - 10.95 μm |
| | | band 8: 2.295 - 2.365 μm | band 14: 10.95 - 11.65 μm |
| | | band 9: 2.360 - 2.430 μm | |
| ground resolution [m] | 15 | 30 | 90 |
| swath width [km] | 60 | 60 | 60 |
| quantization [bits] | 8 | 8 | 12 |

Table 6-6: ASTER instrument characteristics.

6 The potential of the ETM, ASTER and BIRD instrument to register spectral coal fire radiances

The backward looking band 3 provides stereo data allowing the generation of digital elevation models. The swath width of the ASTER instrument is 60 km x 60 km. The ASTER TIR sub-system registers spectral radiances with a 12 bit radiometric resolution, higher than the ETM TIR channel.

The ASTER is an experimental, on-demand instrument, i.e. ASTER data is only acquired in response to a user-submitted, acquisition request. The Earth Remote Sensing Data Analysis Center (ERSDAC) is the body responsible for the processing and distribution of ASTER data. The ERSDAC can process a wide variety of products, ranging from level 1a (raw data format) to level 4 data (end product). High level products include spectral radiances and reflectance of the Earth' s surface, surface temperatures and emissivities, digital elevation maps, surface composition and vegetation maps, as well as cloud, sea, ice, and polar ice products.

6.3.2 Sensitivity study

The spectral range of the ASTER SWIR channels is very close to the spectral range of the ETM SWIR channels, and as both instrument channels also share an identical spatial resolution, the ASTER SWIR channels were not included in this study. The ETM channel 6 covers more or less the entire ASTER TIR spectral range, but has, in contrast to the ASTER TIR channels, a higher spatial resolution. In order to analyse the effect of the lower spatial resolution of the ASTER system, two ASTER TIR channels (channels 10 and 14) were investigated regarding their potential to register spectral fire radiances. The spectral range of the two channels reflects both the upper and lower limit of the ASTER TIR spectral range. The results of the ASTER sensitivity study are summarised in table 6-7 and 6-8. The sensitivity plots are presented in figures 6-7 to 6-10.

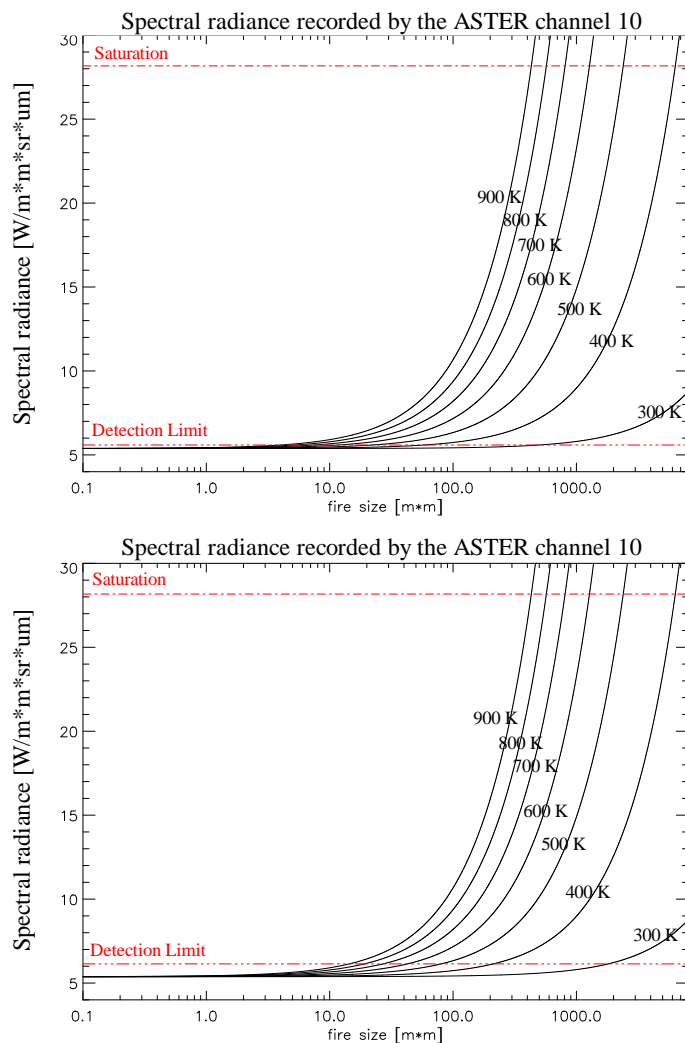


Figure 6-7: Spectral radiance of an image pixel-correspondent ground segment, containing a sub-pixel fire component at various fire temperatures, fire areas and background conditions, recorded by the ASTER channel 10. The dotted lines mark the lower and upper detection limits. Top) winter homogeneous background: background temperature 273 K (Th I); bottom) winter background: background temperature 273 K, max. background variation 5 K (Th III).

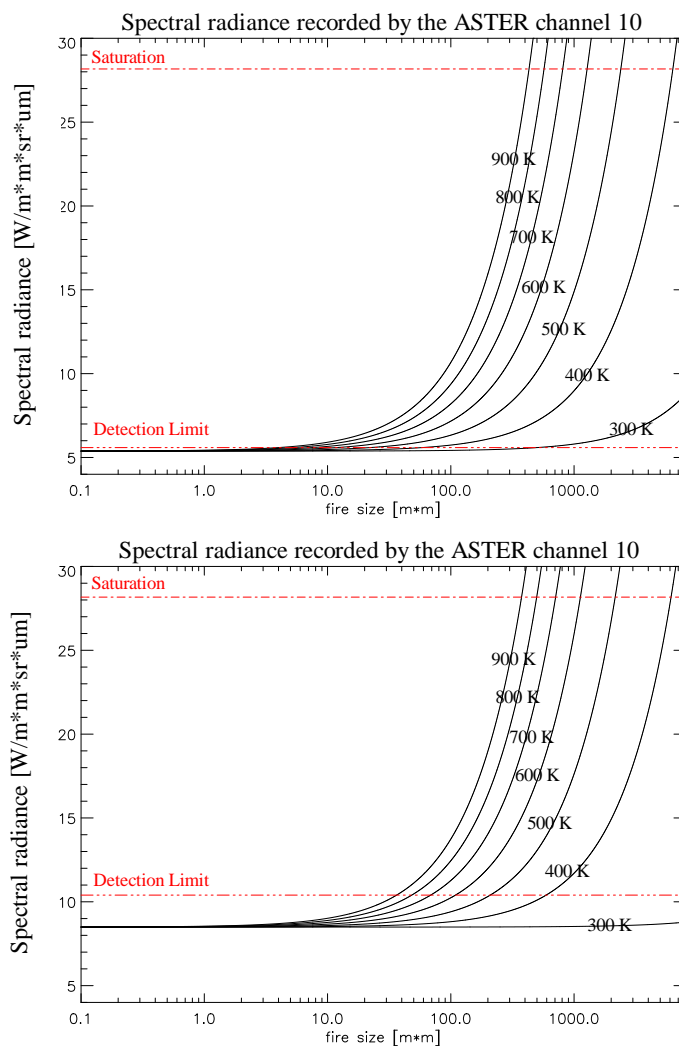


Figure 6-8: Spectral radiance of an image pixel-correspondent ground segment, containing a sub-pixel fire component at various fire temperatures, fire areas and background conditions, recorded by the ASTER channel 10. The dotted lines mark the lower and upper detection limits. Top) summer homogeneous background: background temperature 298 K (Th I); bottom) summer background: background temperature 298 K, max. background variation 10 K (Th III).

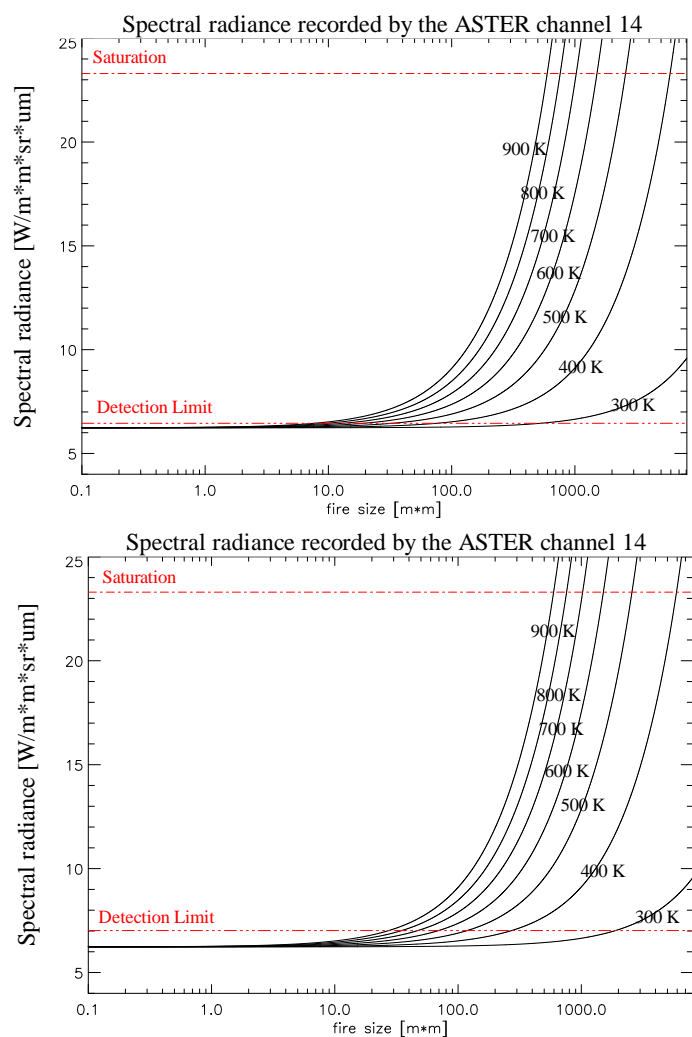


Figure 6-9: Spectral radiance of an image pixel-correspondent ground segment, containing a sub-pixel fire component at various fire temperatures, fire areas and background conditions, recorded by the ASTER channel 14. The dotted lines mark the lower and upper detection limits. Top) winter homogeneous background: background temperature 273 K (Th I); bottom) winter background: background temperature 273 K, max. background variation 5 K (Th III).

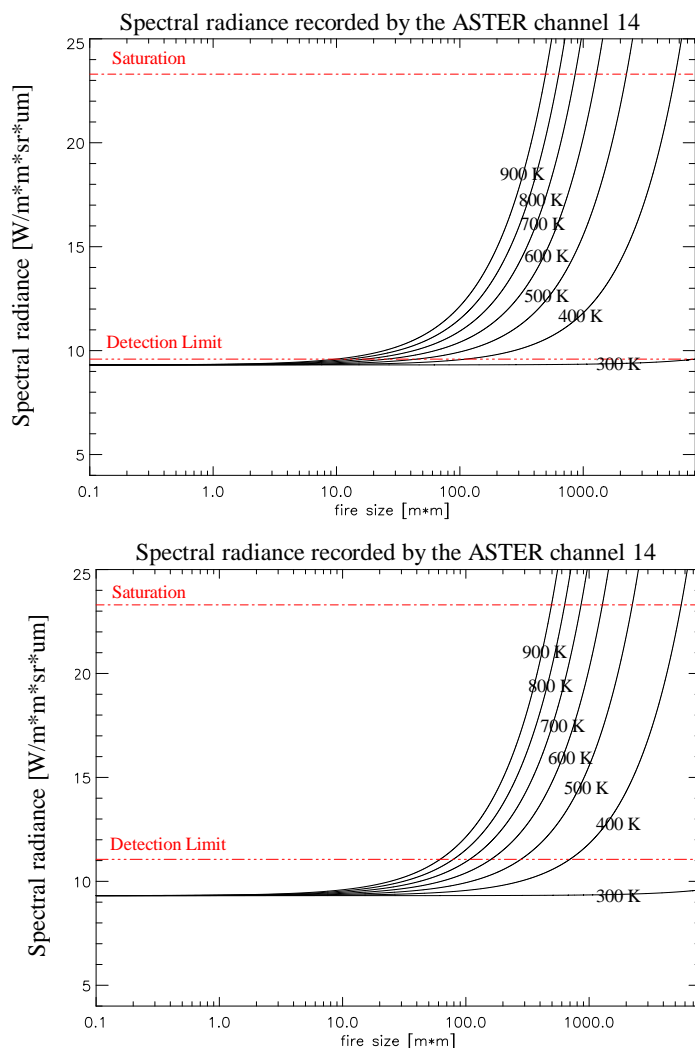


Figure 6-10: Spectral radiance of an image pixel-correspondent ground segment, containing a sub-pixel fire component at various fire temperatures, fire areas and background conditions, recorded by the ASTER channel 14. The dotted lines mark the lower and upper detection limits. Top) summer homogeneous background: background temperature 298 K (Th I); bottom) summer background: background temperature 298 K, max. background variation 10 K (Th III).

6 The potential of the ETM, ASTER and BIRD instrument to register spectral coal fire radiances

| background scenario | ASTER channel 10 fire area [m ²] | | |
|--|--|--------------------|--------------------|
| | T fire 600 K | T fire 500 K | T fire 400 K |
| Th I (winter, homogeneous background) | LD 8 UD 1100 | LD 18 UD 2300 | LD 60 UD 6000 |
| Th II (summer, homogeneous background) | LD 9 UD 900 | LD 30 UD 1900 | LD 90 UD 5700 |
| Th III (winter, heterogeneous background) | LD 45 UD 1100 | LD 80 UD 2300 | LD 200 UD 6000 |
| Th IV (summer, heterogeneous background) | LD 100 UD 900 | LD 130 UD 1900 | LD 600 UD 5700 |

Table 6-7: Minimum and maximum coal fire size that can be registered by the ASTER channel 10, at certain fire temperatures and background conditions. LD = lower registration limit, UD = upper registration limit low gain. The different background scenarios are described in detail in section 6.1.1.

| background scenario | ASTER channel 14 fire area [m ²] | | |
|--|--|--------------------|--------------------|
| | T fire 600 K | T fire 500 K | T fire 400 K |
| Th I (winter, homogeneous background) | LD 23 UD 1050 | LD 37 UD 2400 | LD 60 UD 5700 |
| Th II (summer, homogeneous background) | LD 25 UD 1100 | LD 40 UD 2100 | LD 100 UD 5000 |
| Th III (winter, heterogeneous background) | LD 70 UD 1050 | LD 110 UD 2400 | LD 260 UD 5700 |
| Th IV (summer, heterogeneous background) | LD 150 UD 1100 | LD 250 UD 2100 | LD 700 UD 5000 |

Table 6-8: Minimum and maximum coal fire size which can be registered by the ASTER channel 14 at certain fire temperatures and background conditions. LD = lower registration limit, UD = upper registration limit low gain. The different background scenarios are described in detail in section 6.1.1.

6 The potential of the ETM, ASTER and BIRD instrument to register spectral coal fire radiances

Figures 6-7 to 6-10, and tables 6-7 and 6-8, illustrate that the two investigated ASTER TIR channels have a very similar sensitivity to the registration of spectral coal fire radiances. This reflects the very narrow spectral range of the ASTER TIR channels. In general, the ASTER channel 10 has a slightly higher sensitivity to register spectral coal fire radiance than the ASTER channel 14.

Due to the spatial resolution of the ASTER TIR sub-system, the investigated ASTER TIR channels have a generally higher minimum detection limit than the ETM TIR channel (tables 6-5, 6-7 and 6-8, 6-9). However, the minimum detectable fires size under homogeneous background conditions, for the ASTER 10 channel, is only max. 30 m² higher compared to the ETM TIR channel. Under heterogeneous background conditions the minimum detection limit of the ASTER TIR channel 10 is with max. 400 m² significantly higher.

The ASTER TIR sub-system performs 5 thermal infrared measurements at different spectral ranges, although the spectral range of the individual bands is very narrow. The bi-spectral method (Dozier, 1981) builds on radiance differences induced by the hot portion within an image pixel at two different spectral ranges (description in chapter 3, section 3.3.1). In figure 6-11 band-integrated Planck functions for different temperatures are plotted against spectral radiances observed by the different ASTER TIR bands. This figure clearly illustrates that the radiance difference observed by the different ASTER TIR channels is very low in the temperature range that can be expected for CFSA. In addition, the two analysed ASTER TIR channels have shown a very similar sensitivity to the registration of spectral coal fire radiances, indicating that the coal fire-induced, ASTER TIR radiance differences are very small. Consequently, it is not expected here that the bi-spectral technique can be applied to ASTER TIR input data in order to derive stable coal fire estimates.

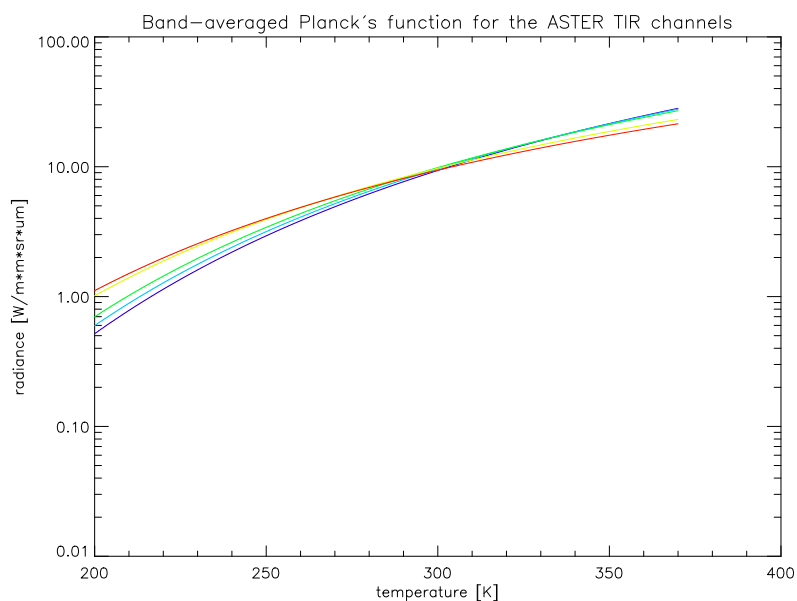


Figure 6-11: Band-averaged Planck's function for the ASTER TIR channels. Due to the fact that the ASTER TIR channels have an upper saturation limit, the band-averaged Planck's function is only given in the sensitivity range of the corresponding TIR bands. The plot indicates that the radiance difference observed by the different TIR sensors is very low in the temperature range expected CFSA. [$T > 300\text{K}$]. Red = channel 10, yellow = channel 11, green = channel 12, light blue = channel 13, blue = channel 14.

6.3.3 Conclusions

This theoretical analysis has demonstrated that the ASTER TIR channels have a high potential to register spectral coal fire radiances. The lower spatial resolution of the ASTER TIR channels, when compared to the ETM TIR channels, is not critical under homogeneous background conditions (e.g. night-time), but might, under daytime conditions, prevent the detection of some of the low radiative fire components. This study has revealed that the ASTER channel 10 has a slightly higher sensitivity to the registration of spectral coal fire radiance than the ASTER channel 14.

Although the ASTER sensor performs spectral measurements at different TIR spectral ranges, this study has shown that the bi-spectral technique can not be applied to retrieve stable coal fire estimates. Consequently, any ASTER coal fire quantification approach must be based on a single-band TIR approach.

6.4 BIRD sensitivity study

6.4.1 Satellite and instrument characteristics

The DLR small satellite BIRD is a technology demonstrating mission of new infrared pushbroom channels, specifically designed to support the detection and quantification of hot spots on the earth's surface. The BIRD satellite was launched into a sun-synchronous orbit in October 2001 (Briess et al., 2003).

The satellite carries two imaging instruments, the Hot Spot Recognition System (HSRS) and a Wide-Angle Optoelectronic Stereo Scanner (WAOSS-B). The HSRS has two well-separated thermal channels, a mid infrared band, centred at 3.8 μm (MIR channel), and a thermal infrared band, centred at 8.9 μm (TIR channel). The WAOSS-B instrument possesses a nadir-looking, near-infrared band, centred at 0.87 μm (NIR channel), and two off-nadir channels. The off-nadir channels are centred at 0.635 μm and 0.87 μm , respectively. The technical characteristics of the two BIRD imaging instruments are summarised in table 6.7.

| | HSRS | WAOSS-B |
|-------------------|--|--|
| spectral bands | MIR: 3.4 μm to 4.2 μm TIR: 8.5 μm to 9.3 μm | VIS: 0.60 μm to 0.67 μm NIR: 0.84 to 0.90 μm |
| field of view | 19° | 50° |
| ground pixel size | 370 m | 185 m |
| sampling step | 185 m | 185 m |
| swath width | 190 km | 533 km |

Table 6-9: Technical characteristics of the two BIRD imaging instruments.

BIRD HSRS data are over-sampled by a factor of two, along both x and y axes, resulting in a sampling step of 185 m. The sampling step coincides with the resolution of the WAOSS-B. A unique feature of the HSRS MIR and TIR channels is a real-time adjustment of their integration time (Skrbek and Lorenz, 1998). If on-board processing of HSRS data indicates that detector elements are saturated, or close to saturation, in the first exposure, then a second exposure is performed within the same sampling interval, with a reduced integration time. This eliminates detector saturation over high temperature targets, but preserves a 0.1 - 0.2 K radiometric resolution for pixels at normal temperatures (Lorenz and Skrbek, 2001). This high radiometric resolution, combined with the fact that the HSRS does not have an upper saturation limit, is a major advantage for fire quantification studies, when compared with ETM and ASTER data. According to Wooster et al. (2003) this high level of radiometric resolution is required for an accurate application of the bi-spectral method.

6 The potential of the ETM, ASTER and BIRD instrument to register spectral coal fire radiances

The BIRD HSRS and WAOSS-B is not an operational satellite system. BIRD data are downloaded by the DLR at the ground station in Oberpfaffenhofen (Germany) only on request. The data sets are made available for scientific applications as systematically corrected products. A detailed description of the BIRD instrument can be found in Skrbek and Lorenz (1998).

6.4.2 Sensitivity study

The BIRD MIR and TIR channels were analysed in order to ascertain BIRD's potential to register spectral coal fire radiances. Although the HSRS system has a sampling step of 185 m, the IFOV is 370 m, and thus a spatial resolution of 370 m was assumed for the theoretical investigations. The results of the BIRD sensitivity study are shown in figures 6-12 to 6-15 and summarised in tables 6-10 and 6-11. As stated in section 6.1, BIRD MIR simulations do not include sun reflectance, and are thus only fully representative for night-time observations. Due to the fact that the BIRD HSRS system does not saturate, only a lower detection limit is given in figures 6-12 to 6-15 and tables 6-10 and 6-11.

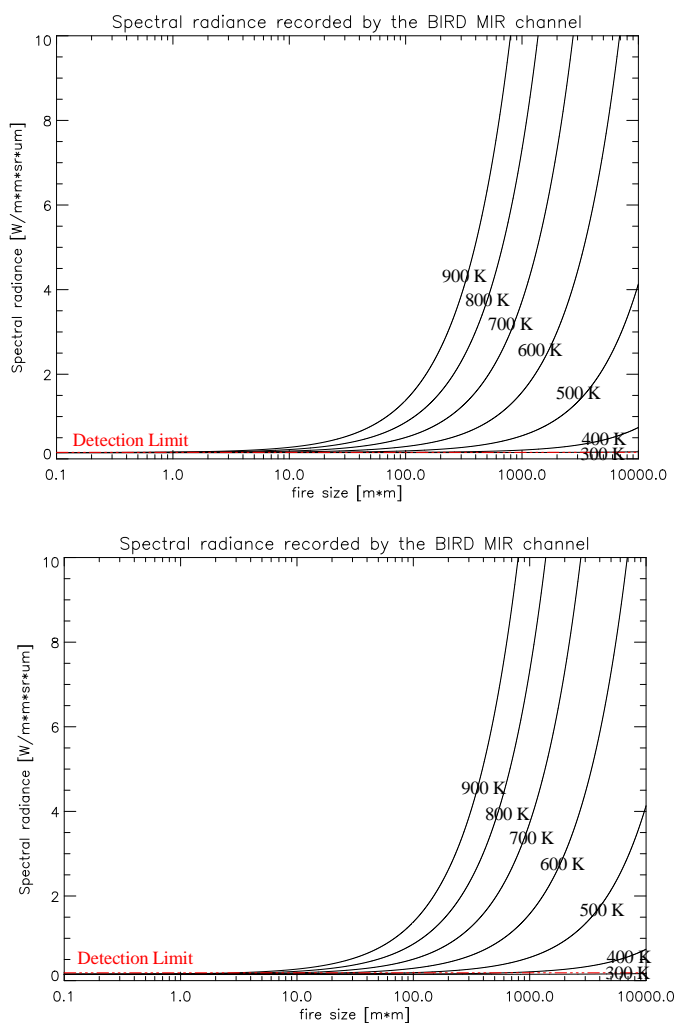


Figure 6-12: Spectral radiance of an image pixel-correspondent ground segment, containing a sub-pixel fire component at various fire temperatures, fire areas and background conditions, recorded by the BIRD MIR channel. The dotted lines mark the lower detection limits. Top) winter homogeneous night-time background: background temperature 273 K (Th I); bottom) winter night-time background: background temperature 273 K, max. background variation 5 K (Th III).

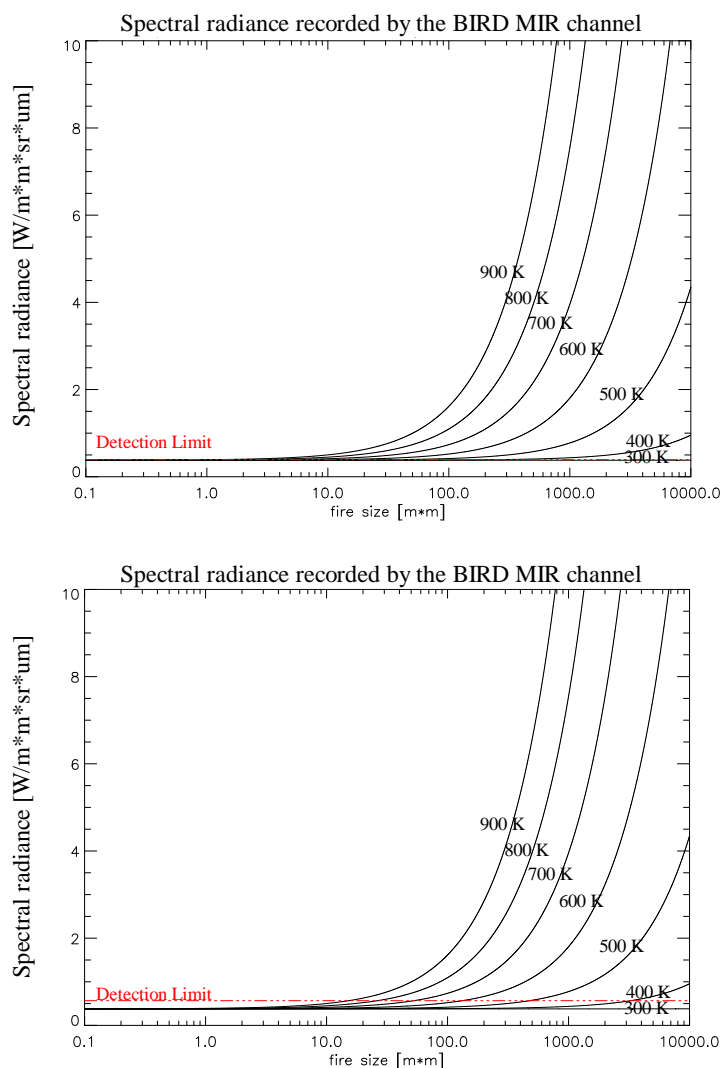


Figure 6-13: Spectral radiance of an image pixel-correspondent ground segment, containing a sub-pixel fire component at various fire temperatures, fire areas and background conditions, recorded by the BIRD MIR channel. The dotted lines mark the lower detection limits. Top) summer homogeneous night-time background: background temperature 298 K (Th I); bottom) summer night-time background: background temperature 298 K, max. background variation 10 K (Th III).

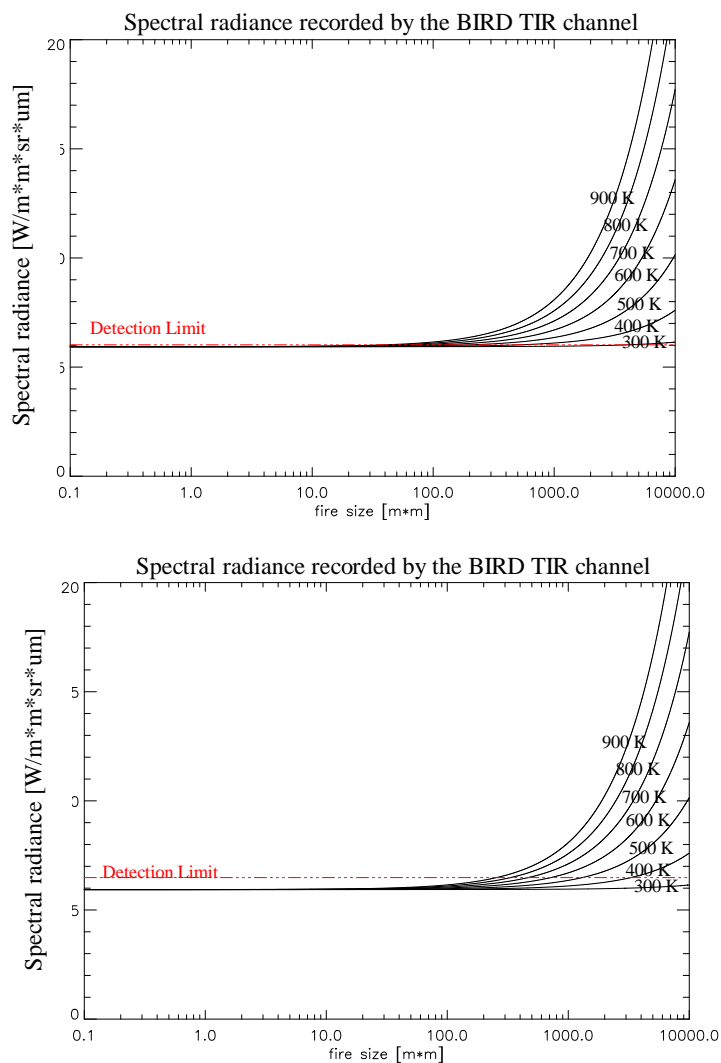


Figure 6-14: Spectral radiance of an image pixel-correspondent ground segment, containing a sub-pixel fire component at various fire temperatures, fire areas and background conditions, recorded by the BIRD TIR channel. The dotted lines mark the lower detection limits. Top) winter homogeneous background: background temperature 273 K (Th I); bottom) winter background: background temperature 273 K, max. background variation 5 K (Th III).

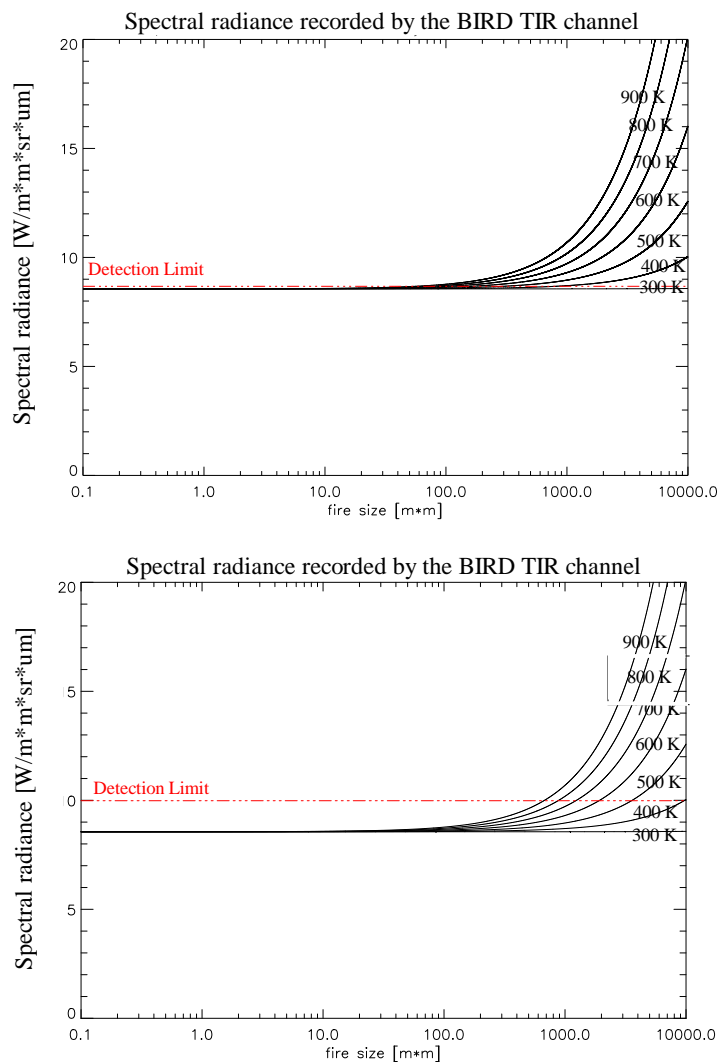


Figure 6-15: Spectral radiance of an image pixel-correspondent ground segment, containing a sub-pixel fire component at various fire temperatures, fire areas and background conditions, recorded by the BIRD TIR channel. The dotted lines mark the lower detection limits. Top) summer homogeneous background: background temperature 298 K (Th I); bottom) summer background: background temperature 298 K, max. background variation 10 K (Th III).

6 The potential of the ETM, ASTER and BIRD instrument to register spectral coal fire radiances

| background scenario | BIRD HSRS MIR channel fire area[m ²] | | |
|--|--|--------------------|--------------------|
| | T fire 600 K | T fire 500 K | T fire 400 K |
| Th I (winter, homogeneous background) | LD 11 | LD 15 | LD 400 |
| Th II (summer, homogeneous background) | LD 11 | LD 80 | LD 500 |
| Th III (winter, heterogeneous background) | LD 12 | LD 110 | LD 620 |
| Th IV (summer, heterogeneous background) | LD 120 | LD 500 | LD 3000 |

Table 6-10: Minimum coal fire size that can be registered by the BIRD MIR channel under particular fire temperature and background conditions. LD = lower registration limit. The different background scenarios are described in detail in section 6.1.1.

| background scenario | BIRD HSRS TIR channel fire area [m ²] | | |
|--|---|--------------------|--------------------|
| | T fire 600 K | T fire 500 K | T fire 400 K |
| Th I (winter, homogeneous background) | LD 120 | LD 270 | LD 700 |
| Th II (summer, homogeneous background) | LD 180 | LD 370 | LD 900 |
| Th III (winter, heterogeneous background) | LD 700 | LD 1200 | LD 3100 |
| Th IV (summer, heterogeneous background) | LD 1400 | LD 2100 | LD 10000 |

Table 6-11: Minimum coal fire size that can be registered by the BIRD TIR channel under particular fire temperature and background conditions. LD = lower registration limit. The different background scenarios are described in detail in section 6.1.1.

6 The potential of the ETM, ASTER and BIRD instrument to register spectral coal fire radiances

The BIRD MIR channel is highly effective in registering relatively hot CFSA (figures 6-12 and 6-13, table 6-10). Although the spatial resolution of the BIRD MIR channel is about a factor six smaller than the spatial resolution of the ETM TIR channel, 500 K to 600 K coal fire components can be detected, from a size of approximately 15 m² onward, against an absolute homogeneous night-time winter background. On a heterogeneous summer night-time background a 500 K fire component can still be detected from a size of approximately 500 m² onward. However, the potential of the BIRD MIR channel to detect 400 K CFSA is significantly lower. A 400 K fire can only be detected if the fire size is larger than approximately 400 m², under homogeneous night-time winter conditions, while the fire size has to be larger than 3000 m², against a warm summer daytime-time background which has significant background temperature variations. It is important to note, in figures 6-12 and 6-13, that background temperature variations in the MIR range have a significantly lower effect on the overall detection limit, as compared with the ETM TIR range (e.g. figure 6-6).

The BIRD TIR channel covers approximately the same spectral range as the ASTER channel 10, but when compared to the ASTER TIR system, has a significantly lower spatial resolution. This leads to markedly higher minimum detection limits (figures 6-7, 6-8, 6-14, 6-15). Under absolutely homogeneous, winter night-time background conditions, 600 K coal fires can only be registered from a size of 120 m² onward. Under similar background conditions, a 400 K fire component has to be larger than approximately 700 m² to be registered by the BIRD TIR sensor. In contrast to the BIRD MIR channel, TIR spectral background-radiance variations have a significant impact on the lower detection limit. Against a heterogeneous summer background, the fire size of a 600 K and a 400 K fire component has to be larger than 1400 m² and 10000 m², respectively. Consequently, only very large CFSA can be recognised by the BIRD TIR channel.

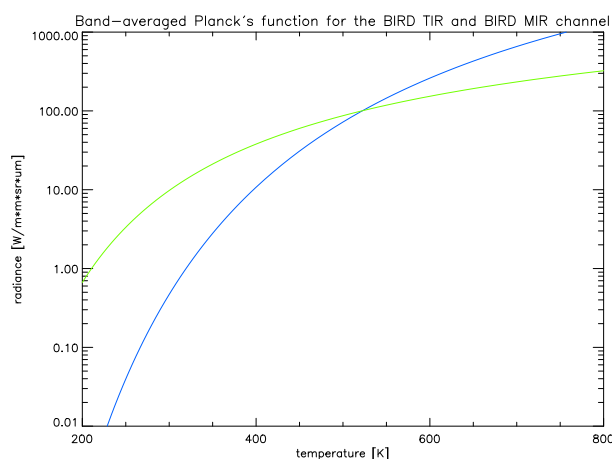


Figure 6-16: Band-averaged Planck's function for the BIRD MIR (blue) and TIR (green) channel.

The BIRD MIR and TIR channels are designed for an optimal use of the bi-spectral technique (Wooster et al., 2003). Due to the fact that the BIRD MIR and TIR channel do not saturate, relatively

6 The potential of the ETM, ASTER and BIRD instrument to register spectral coal fire radiance

large and hot CFSA produce a signal in both the BIRD TIR and MIR channels (table 6-10 and 6-11). The band integrated Planck function in figure 6-16 clearly demonstrates that the radiance difference observed by the BIRD MIR and TIR channel is significant in the temperature range expected for coal fire corresponding CFSA. Thus, the bi-spectral technique can be applied on BIRD data to quantify relatively large and / or hot CFSA.

Wooster et al. (2003) have investigated the BIRD MIR data with regard to there potential to derive FRE via a single band concept. This study has demonstrated that BIRD MIR based, single band fire quantification approaches are ineffective for fire temperatures below 600 K. This is because the relationship between MIR spectral radiances and the total coal fire related, radiative energy release is distinctly non linear, for fire temperatures below 600 K. Consequently, BIRD MIR data can not be used to estimate CFRE via a single band concept.

6.4.3 Conclusions

The theoretical BIRD analysis has demonstrated that the MIR spectral range is very sensitive to coal fire related, radiative emissions. However, this does not compensate for the lower spatial resolution, which is considerably inferior to that of the ETM TIR data. This means that only relatively hot, CFSA can be registered by the BIRD MIR channel. The low spatial resolution of the BIRD TIR channel results in a significantly reduced overall capacity to register coal fire related, spectral radiances, when compared with the ASTER or ETM TIR channels.

7 CONCEPTUAL APPROACH: THE DERIVATION OF COAL FIRE RADIATIVE ENERGY VIA TIR RADIANCES

This chapter presents a new approach to the derivation of coal fire radiative energy (CFRE) via the analysis of coal fire pixel radiance, in the thermal infrared spectral region. In contrast to existing, one channel based, FRE retrieval methods (MIR and MODIS method, described in chapter 3, section 3.3), this new approach is adapted to fire temperatures below 600 K. The theoretical evaluations in chapter 6 demonstrate that ASTER and ETM TIR data have a significantly greater potential than BIRD TIR data to register spectral coal fire radiances. The following evaluations were, therefore, performed only for the ASTER and ETM TIR channels.

7.1 Methods

The existing MODIS and MIR approaches compute the total FRE of surface anomalies via recorded fire pixel and background pixel radiances or temperatures in the MIR spectral region (description in chapter 3, section 3.3). In this study a similar concept to the MODIS and MIR method is analysed, but, in contrast to the two existing techniques, TIR pixel radiances are used to compute the total CFRE. Fire temperatures for both MODIS and MIR method simulations represent typical temperatures of vegetation fires (description in chapter 3, section 3.3). Here, fire temperature and size simulations are adapted to typical coal fire surface scenarios observed during the two field campaigns.

In order to analyse the relationship between TIR spectral fire radiances and the total CFRE release, an approach akin to the MIR method (MIR method, described in chapter 3, section 3.3.3), was used for the ASTER and ETM TIR data. This was done by plotting fire temperatures against the ratio of the true CFRE emitted from a unit area surface to its TIR spectral radiances. The TIR spectral range analysed in this study includes the spectral range of the ETM channel 6 (figure 7-1), the ASTER channel 10, channel 12 and the ASTER channel 14 (figure 7-3). The band-integrated TIR spectral radiances were computed via equation 3-2 and equation 3-4 (band integrated Planck function), by considering the spectral response functions of the different TIR instrument channels. The true CFRE was calculated via equation 3-10 assuming a ground surface emissivity of 0.98.

In addition, an investigation was made, using a technique similar to the MODIS method (MODIS method: described in chapter 3, section 3.3.2), by simulating data from 1000 coal fire scenarios. In contrast to the MODIS method, ETM and ASTER TIR spectral radiances are plotted against total CFRE (figure 7-2 and 7-4). Plotted data represents 1000 simulated fire scenarios, each containing a random fire temperature, at a random size, with a maximum fire size of 1000 m², superimposed on a random background temperature. Modelled fire temperatures range from 350 K to 600 K, while background temperatures range from 273 K to 300 K. The maximum fire size reflects the maximum

7 Conceptual approach: Derivation of coal fire radiative energy via TIR radiances

size of CFSA observed in the study areas within an ETM pixel corresponding ground segment. Maximum fire temperatures clearly overestimate average coal fire temperatures of CFSA in the study area. TIR spectral radiances were computed in a similar manner to the theoretical analyses in chapter 6, using a sub-pixel concept (equation 3-11, see also chapter 6, section 6.1.3).

7.2 Derivation of CFRE via ASTER and ETM TIR radiances

7.2.1 ETM channel 6

The ratio of the true fire release radiative energy emitted from a unit area surface to the ETM channel 6 spectral radiance does not show a strong temperature sensitivity if the temperature of the emitter increases from 350 K to 600 K. It is seen in figure 7 that this ratio varies between 48 to 82 sr μm from 350 K to 600 K.

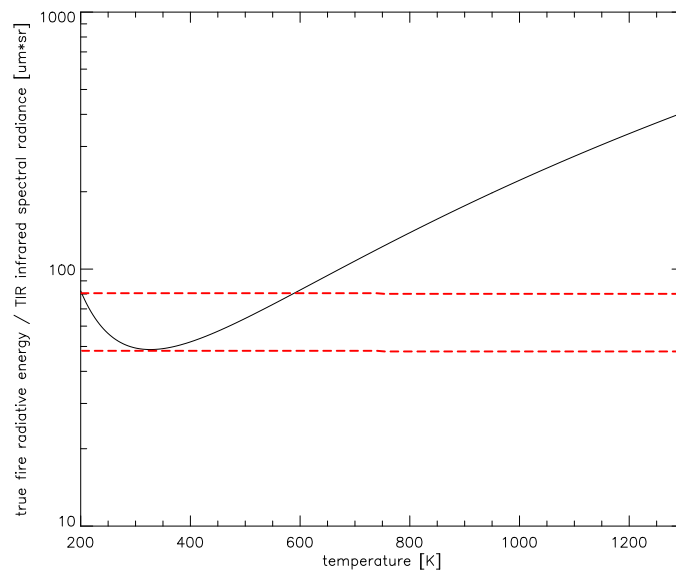


Figure 7-1: Surface temperature is here plotted against the ratio of the total fire radiative energy, emitted by a unit area surface to its corresponding spectral radiance, recorded in the spectral range of the ETM band 6. The red lines mark ratio values in the temperature range 350 K to 600 K.

A simulation of 1000 sub-pixel fire scenarios (figure 7-2) reveals good correlation between the ETM 6 spectral coal fire radiance and the total CFRE. If this relationship is approximated linearly (not displayed in figure 7-2) the linear correlation (R^2) is 0.98 within the limits of both the ETM high and low gain saturation.

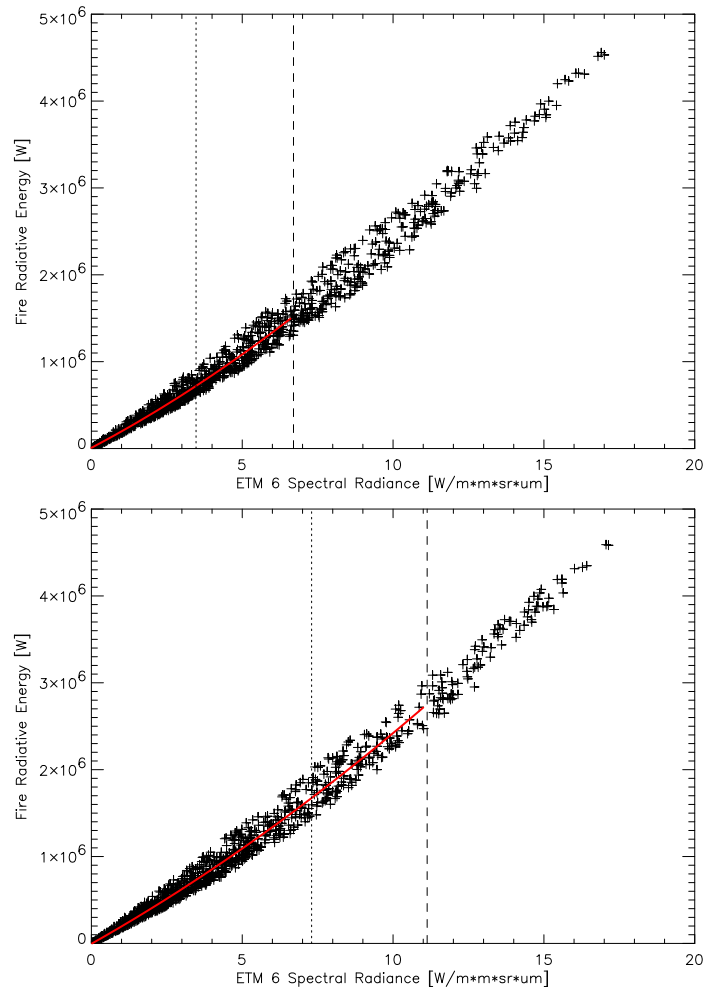


Figure 7-2: Relationship between spectral radiance, observed by the ETM TIR sensor, and the total radiative surface energy release from the coal fire. Data are from 1000 modelled fire scenarios with a fire area ranging between 1 m² and 1000 m², a fire temperature ranging between 350 K and 600 K and a background temperature ranging between 273 K and 300 K. A polynomial best-fit relationship, overlain as a red line, gives a good correlation with the modelled data, within the limits of the TIR band saturation. (Dashed line = saturation at a background temperature of 273K, dotted line = saturation at a background temperature at 298 K). Top) ETM band 6 high gain; bottom) ETM band 6 low gain.

Consequently, ETM 6 fire pixel radiances can be directly used to calculate total CFRE. A polynomial best-fit relationship such as shown in figure 7-2 leads to:

$$CFRE_{ETM} = 6300 + 185500 (L_{ETM,P} - L_{ETM,BG}) + 5700 (L_{ETM,P} - L_{ETM,BG})^2 \text{ [W]} \quad (7-1)$$

where:

- $L_{ETM,P}$ = atmospherically-corrected ETM band 6 radiance of a potential coal fire pixel [$W m^{-2} sr^{-1} \mu m^{-1}$],
- $L_{ETM,BG}$ = mean atmospherically-corrected ETM band 6 radiance of

surrounding background pixels [$\text{W m}^{-2} \text{sr}^{-1} \mu\text{m}^{-1}$].

7.2.2 ASTER channel 10, ASTER channel 12, ASTER channel 14

Figure 7-3 indicates that the ratio between the total CFRE, emitted from a unit area surface to its corresponding ASTER TIR spectral radiances does not strongly depend on the temperature for 350 K to 600 K emitters. The ratio is very stable for the ASTER channel 10 with values ranging from 37 to 43 $\mu\text{m sr}$, while it becomes less stable for ASTER channels with a spectral range at longer wavelengths. The ASTER channels 12 and 14 reveal a ratio ranging from 39 to 50 $\mu\text{m sr}$ and 49 to 86 $\mu\text{m sr}$, respectively.

Composite-fire radiances recorded in the ASTER TIR channels show good correlation to the total CFRE (figure 7-4). If we approximated the relationship between simulated fire radiance and CFRE linearly (not shown in figure 7-4), the correlation (R^2) is 0.99 for the ASTER band 10. The linear correlation for the simulated fire scenarios decreases with the increase in wavelength in the ASTER TIR bands 10 to 14.

The theoretical studies described in chapter 6, section 6.3 demonstrate that the short wave TIR range is very sensitive to the registration of spectral coal fire radiances. The modelled coal fire scenarios show an excellent linear correlation between ASTER 10 spectral radiance and total CFRE and the ASTER band 10. Thus it is here considered that the ASTER channel 10 is the most suitable of all ASTER TIR bands to derive CFRE via the TIR method. A polynomial best-fit relationship for the ASTER channel 10 such as shown in figure 7-4 leads to:

$$\text{CFRE}_{\text{ASTER}} = 1070 + 262500 (L_{\text{ASTER,P}} - L_{\text{TIR,BG}}) + 2600 (L_{\text{TIR,P}} - L_{\text{TIR,BG}})^2 \text{ [W]} \quad (7-2)$$

where:

- $L_{\text{ASTER,P}}$ = atmospherically-corrected ASTER band 10 TIR radiance of a potential coal fire pixel [$\text{W m}^{-2} \text{sr}^{-1} \mu\text{m}^{-1}$]
- $L_{\text{ASTER,BG}}$ = mean atmospherically-corrected ASTER band TIR radiance of surrounding background pixels [$\text{W m}^{-2} \text{sr}^{-1} \mu\text{m}^{-1}$].

7 Conceptual approach: Derivation of coal fire radiative energy via TIR radiances

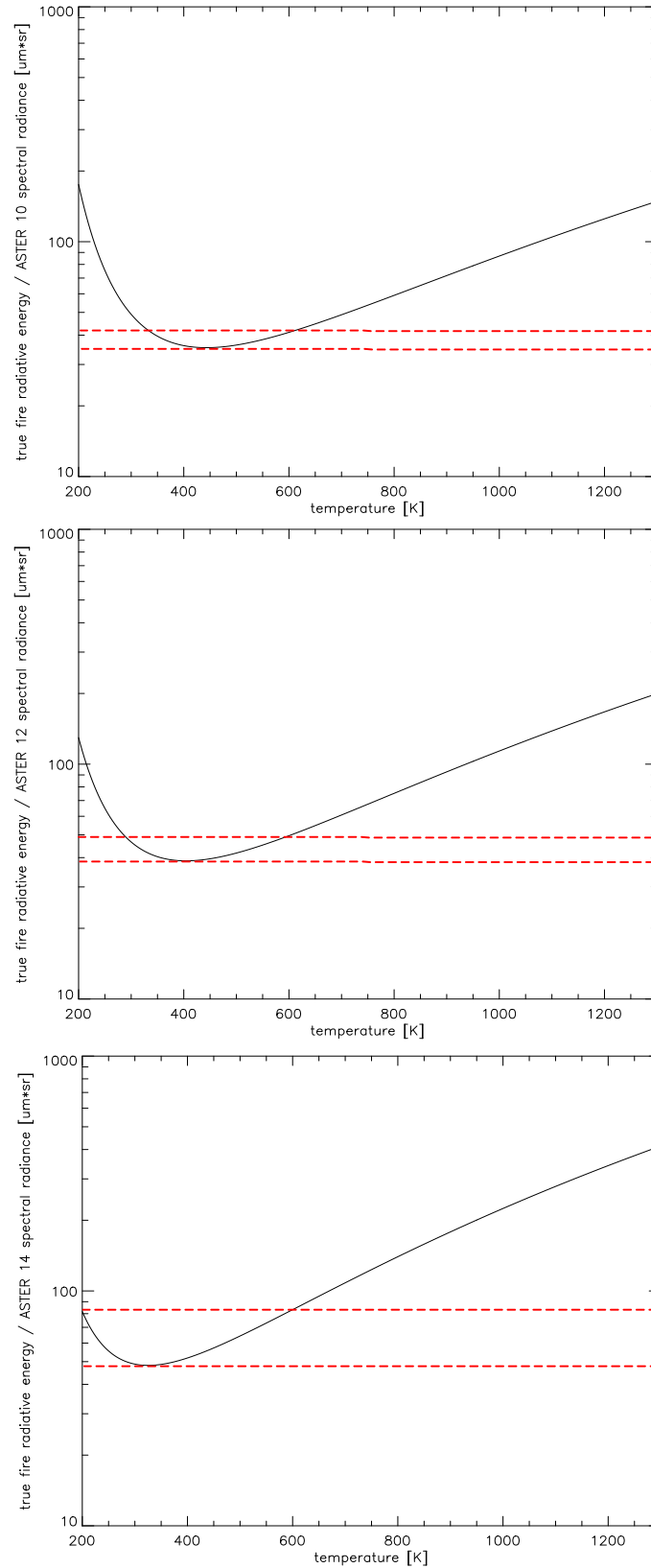


Figure 7-3: Surface temperature, plotted against the ratio of the total fire radiative energy, emitted by a unit area surface to its corresponding spectral radiance, recorded in the spectral range of top) the ASTER band 10, middle) the ASTER band 12 and bottom) the ASTER band 14. The red lines mark ratio values in the temperature range 350 K to 600 K.

7 Conceptual approach: Derivation of coal fire radiative energy via TIR radiances

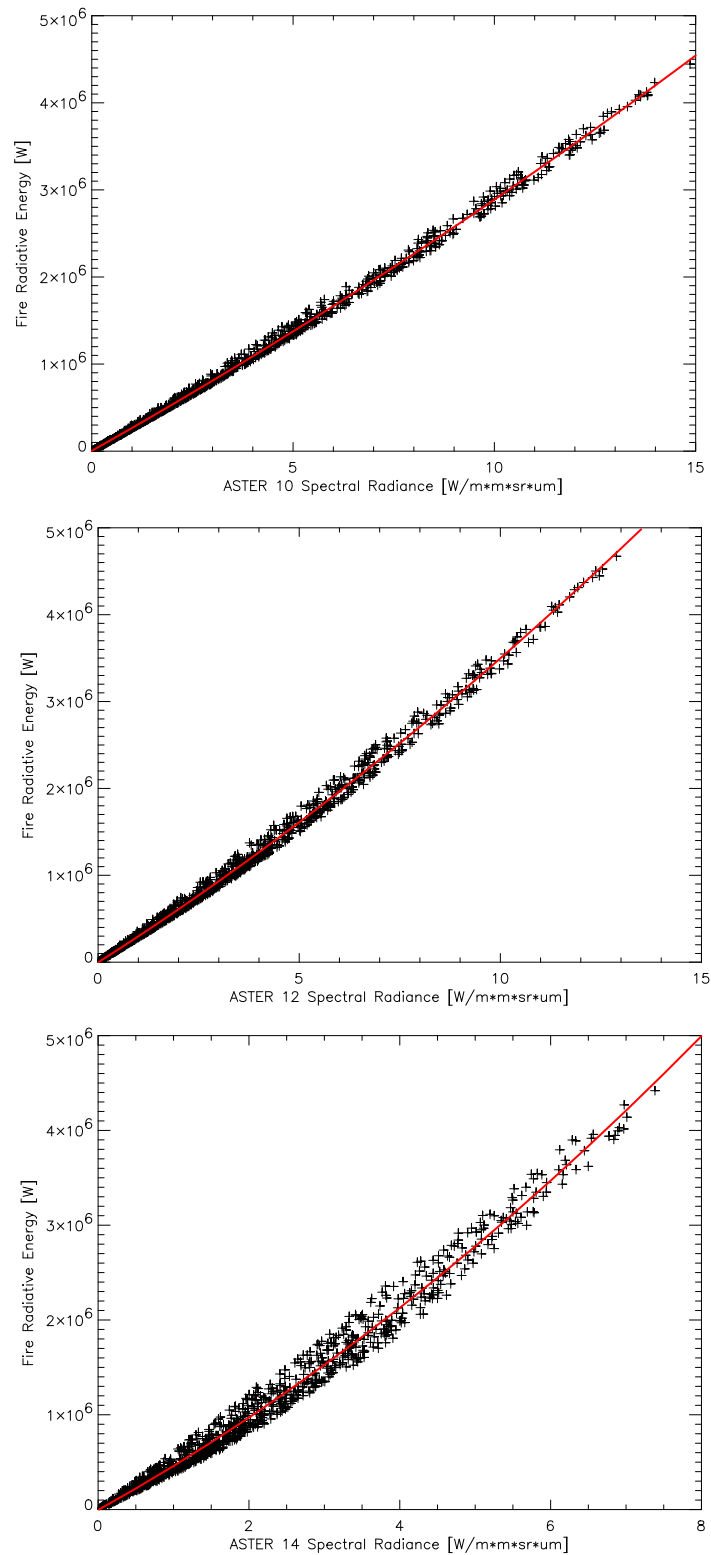


Figure 7-4: Relationship between the spectral radiance, observed by the ASTER TIR sensor, and the coal fire's total radiative surface energy release. Data is from 1000 modelled fire scenarios, with a fire area ranging from 1 m^2 to 1000 m^2 , a fire temperature ranging from 350 K to 600 K and a background temperature ranging from 273 K to 300 K. All modelled fire scenarios are below the saturation limit of the ASTER TIR sensors. Top) ASTER band 10; middle) ASTER band 12; bottom) ASTER band 13. A polynomial best-fit relationship overlain as red line is in close correlation with the modelled data. The best linear correlation can be observed for the ASTER band 10.

7.3 Discussion of limitations of the TIR approach

The above described TIR band based coal fire quantification concept has several limitations. First of all, there are limitations which are introduced by the TIR method itself:

- The above described TIR method is adapted to coal fire temperatures ranging between 350 K and 600 K. The total CFRE release of hotter fires will therefore, be significantly underestimated. Nevertheless, large coal fires with significantly higher temperatures were not observed during the field investigations (description in chapter 5, section 5.2). According to Goerlich (2004, pers. communication), the overall majority of the coal fires investigated in the framework of the German GTZ project in Xinjiang have surface temperatures below 600 K (description in chapter 2, section 2.3). Therefore this method can be applied without major concerns in the present project. The theoretical evaluation in this chapter has demonstrated that CFRE from this low range of temperatures of CFSA can be reasonably estimated via the TIR method.
- The accuracy of the TIR method strongly depends on the accuracy of the estimated TIR background signal. The theoretical evaluations in chapter 6 have demonstrated that the TIR spectral range is very sensitive to background temperature variations. Coal fire areas consist of surfaces with different thermal properties in the TIR range (alternating sandstone, shale and coal layers) and are thus prone to show high variations in the TIR background signal. Errors induced by background temperature variations can be reduced by applying the sub-pixel fire quantification concept to hot pixel clusters rather than to individual single pixels (description in chapter 3, section 3.3.1). Nonetheless, the total CFRE can only be estimated, via the TIR method, within the expected error range of the TIR background signal. A detailed analysis of the TIR background variations, in the direct vicinity of the coal fire clusters, is therefore crucial for the accuracy of the TIR method-based coal fire quantification.
- Furthermore, the TIR method presented in this chapter is based on a semi-empirical relationship between the spectral TIR coal fire radiance and the total CFRE. Due to the fact that both the ASTER and TIR spectral fire radiances do not have an absolute linear correspondence with the total CFRE, computed CFRE can differ from real CFRE – even if we assume an absolutely homogeneous background in the direct vicinity of CFSA. Nevertheless, the derivations of the CFRE, computed via the presented relationship in equations 7-1 and 7-2, and the real CFRE, computed for modelled fire scenarios, are relatively small, with approximately +/- 30 % of the total calculated CFRE for the ETM channel 6 and approximately +/- 10 % of the total calculated CFRE for the ASTER channel 10.

7 Conceptual approach: Derivation of coal fire radiative energy via TIR radiances

It also has to be taken into consideration that the TIR method based satellite data analysis can only estimate coal fire related radiative surface energy releases at the time of the satellite acquisition, which leads to the following limitations:

- In the context of coal fires, the coal combustion energy is lost by a variety of processes in addition to radiation, such as e.g. conduction into the ground. Consequently, satellite based CFRE estimates include only one part of the totally released coal fire combustion energy and can thus not be used directly to estimate total coal combustion rates. However, satellite derived CFRE can be regarded as a valuable physical coal fire parameter supporting the tools used for estimation of the coal fire induced losses and damages, to the environment, by local fire fighting authorities. Given numbers of coal combustion computed via satellite CFRE estimates reflect a minimum energy loss caused by the fires at the time of data take and can thus outline the minimum dimension of the coal fire induced coal loss of a particular coal fire zone.
- Satellite observations can only measure CFRE at the moment of the satellite acquisition. According to the field observation, a CFSA can vary significantly due to different meteorological conditions (e.g. wind, air circulation and moisture content). Thus satellite data CFRE retrievals have to be regarded as a snapshot at one particular time, which does not necessarily reflect a long-term fire activity.

When considering all the above obstructions the precision of the methods tested in this thesis might appear of insufficient accuracy. However, in the view of the difficulty to estimate the extend of the observed processes in nature and of continuous monitoring of the waste area of coal fires, without a possibility of depth control of the fires, the here discussed methods of remote sensing are a crucial tool in grasping at least some reliable, quantitative information on the coal fires.

CASE STUDIES

8 CASE STUDY I: THE ESTIMATION OF COAL FIRE RELATED, SURFACE-RADIATIVE ENERGY RELEASES IN THE RUQIGOU, GULABEN AND WUDA COALFIELDS, USING ETM, ASTER AND BIRD DATA

In this case study, coal fire related, surface-radiative energy releases (CFRE) are computed for the Wuda, Ruqigou and Gulaben coalfields, using ASTER, ETM and BIRD data. Here, the newly-developed TIR method (described in chapter 7) is applied to multi-temporal ETM and ASTER data, and then the resultant calculated CFRE values are compared to CFRE retrievals computed from BIRD data, via the existing bi-spectral method. The case study also explores the potential of the investigated satellite instrument data to compute CFRE on a regional scale. In addition to this BIRD-derived, equivalent coal fire temperatures and sizes are compared with in-situ coal fire measurements, carried out during the field campaigns in 2002 and 2003.

8.1 Analysis of ETM data

8.1.1 Methods

An analysis was made of data taken from the study coalfields, consisting of summer daytime Landsat ETM data, from 21st September 2002, winter daytime ETM data from 12th February 2003 and summer night-time ETM data from 28th September 2002. The daytime scenes include ETM, SWIR and TIR data, while the night-time data consists only of the TIR band. The two scenes from September 2002 were recorded synchronously with the field campaigns.

The scenes were geometrically corrected using a nearest-neighbour approach, and using ground control points taken with a GPS device during the field campaign. DN-values of ETM level 1b, TIR data were transformed into spectral radiance values using equation 3-6. The spectral radiances at the maximum and minimum digital number ($L_{\min, \lambda}$ and $L_{\max, \lambda}$ in equation 3-6) used for this calculation are listed in chapter 10, table 10-1.

Atmospheric correction was performed for the ETM TIR bands, using the ATCOR model (Richter and Schlaepfer, 2002), based on look-up tables calculated via the MODTRAN code (Berk et al., 1989). The look-up tables contain parameterised values for path radiance, atmospheric ground-to-sensor transmittance and for downwelling atmospheric flux for different height levels. The applied atmospheric parameters are listed in chapter 10, table 10-3. The ground pixel radiances are calculated via equation 3-7. Image pixel-corresponding height levels were provided, via a digital elevation model

8 Case study I: Estimation of coal fire related, surface-radiative energy releases

(DEM).⁸⁻¹⁾ Since all study areas have a dry-desert climate the MODTRAN dry-desert model was applied, with an atmospheric water column of 0.41 cm at sea level. Surface temperatures of the Yellow River, measured during satellite overpasses (see chapter 5, section 5.4), coincide with corresponding ETM TIR water temperatures within 1.3 K.

Coal fire correspondent, anomaly pixels in the ETM TIR band were first visually detected, before the CFRE were computed. In order to distinguish coal fire related, anomaly pixels from background pixels, an adaptive threshold was set, within a visually defined window, around each corresponding coal fire area, mapped during the field campaign in September 2002. It is important to note here that only coal seam fires were included for this study, i.e., burning coal stock piles, which are widespread, for example, in the northern and eastern part of the Wuda syncline, were not considered.

CFRE were computed from ETM channel 6 data, via the TIR method using equation 7-1. Prior to this computation, neighbouring fire pixels were grouped into individual image clusters in order to reduce errors introduced by background signal variations. Background radiance ($L_{\text{ETM, BG}}$ in equation 7-1) was calculated as mean radiance from ten background pixels surrounding each fire cluster. Directly neighbouring background pixels bordering the fire pixels, were however excluded from the computation, because these pixels can be directly influenced by the fire signal and are thus not necessarily representative for background radiation. In order to check the stability of the derived energy releases against background errors, CFRE estimations were performed for three values of the TIR background signal (see table 8-1, 8-2):

- mean background value corresponding to the mean CFRE ('mean' in table 8-1, 8-2).
- mean background value minus one standard deviation corresponding to the maximum CFRE ('mean-SD' in table 8-1, 8-2).
- mean background value plus one standard deviation corresponding to the minimum CFRE ('mean+SD' in table 8-1, 8-2).

8.1.2 Interpretations

Figure 8-1 shows SWIR bands from the two ETM daytime scenes of the Ruqigou and Gulaben coalfields. The coal fire related, surface anomalies (CFSA) in the Gulaben coalfield, investigated during the field observations of September 2002, revealed the highest surface temperatures, and should thus, according to the ETM sensitivity study in chapter 6, section 6.2, have the greatest potential to be

⁸⁻¹⁾ The DEM used in this study was provided by the DLR radar team, and is an ERS (ESA Remote Sensing Satellite) DEM sub-sampled to the spatial resolution of the ETM TIR data.

8 Case study I: Estimation of coal fire related, surface-radiative energy releases

registered by one of the ETM SWIR channels. Nevertheless, figure 8-1 clearly indicates that none of the mapped coal fire zones of the Gulaben coalfield shows significant raised DN values in a daytime SWIR channel. This confirms the theoretical ETM analysis in chapter 6, section 6.2 suggesting that the SWIR spectral range is in general not suitable to register spectral coal fire radiances.

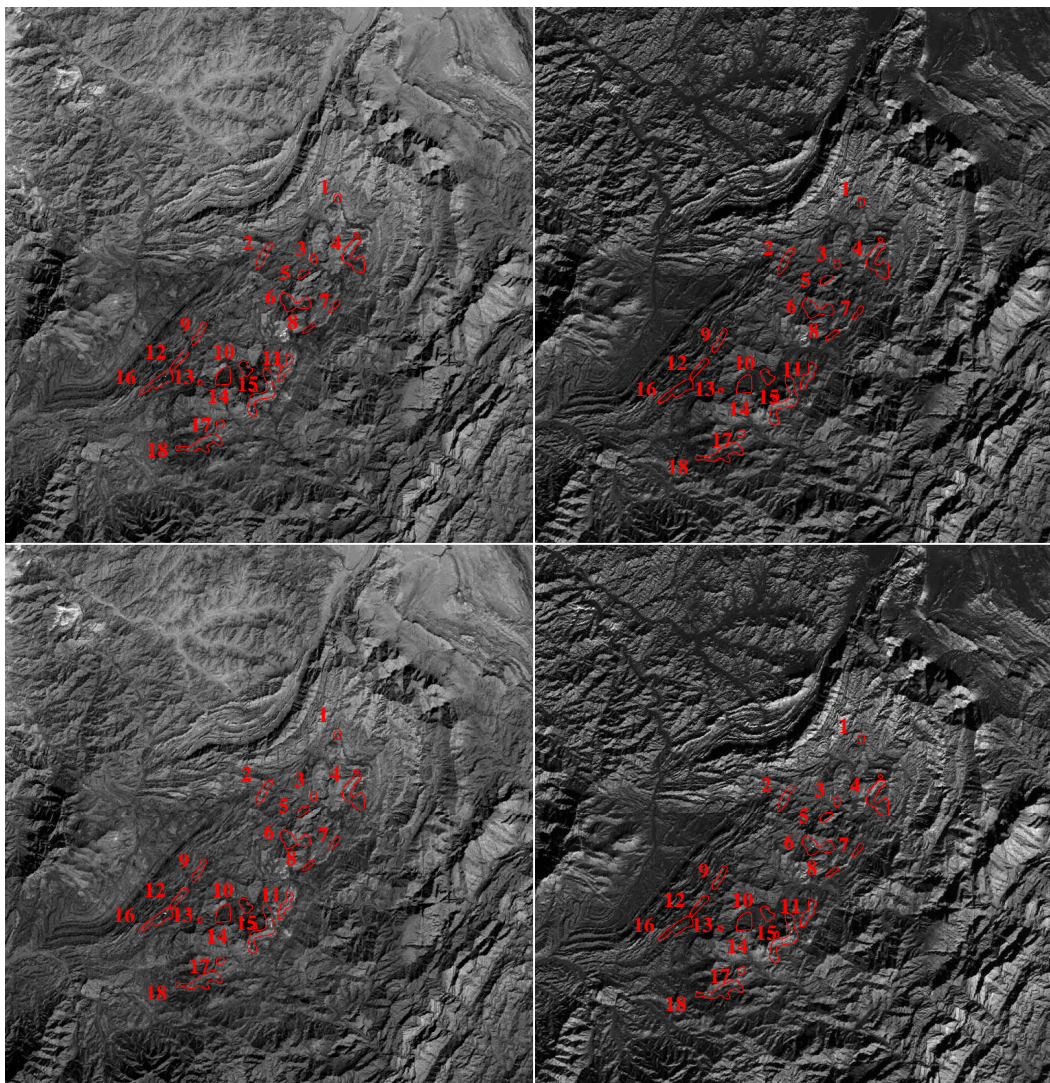


Figure 8-1: ETM SWIR and TIR channels with superimposed coal fire related, surface anomalies (CFSA, red outlines). The CFSA were mapped during the field campaign in September 2002. Upper left) ETM Band 5, 12.02.2003; upper right) ETM channel 5, 21.09.2002; lower left) ETM channel 7, 12.02.2003; lower right) ETM channel 7, 21.09.2002.

ETM TIR data (figures 8-2 and 8-3) can, in contrast to the ETM SWIR data, be used to detect coal fire zones from the Wuda, Gulaben and Ruqigou coalfields. None of the detected fire pixels is saturated in the ETM 6 high gain data that were investigated, reflecting the low temperatures and / or small sizes of the CFSA in the study areas.

With the summer daytime ETM TIR data only individual hot pixels or small pixel clusters can be outlined for certain fire zones (figures 8-2 and 8-3) and the real extent of the corresponding CFSA zone

8 Case study I: Estimation of coal fire related, surface-radiative energy releases

is very significantly underestimated when compared with the actual field observations. The summer daytime TIR data reveal radiant temperature differences of more than 20 K for some coal and sandstone-related image pixels, a fact that distinctly limits the potential of summer daytime ETM TIR channel to detect coal fires. The background variation of more than 20 K is higher than the assumed background variation for the heterogeneous summer background model in chapter 6.

Due to the relatively lower background variations in the winter daytime ETM TIR band, significantly more coal fire pixels can be identified in this band than in the summer daytime ETM band (figures 8-2 and 8-3). This background temperature variation is, at approximately +/- 8 K, slightly higher than the assumed background variation, in the heterogeneous winter background model in chapter 6.

Significantly more continuous fire clusters can be detected with night-time ETM TIR data (figures 8-2 and 8-3). All investigated coal fire zones in the Ruqigou and Gulaben study area, and twelve out of seventeen fire areas in the Wuda coalfield, could be clearly identified. This reflects the low night-time, background temperature variations ($\Delta T < 6$ K), and confirms the theoretical analysis in chapter 6, section 6.2, i.e., that ETM TIR data have a high potential to register spectral coal fire radiances.

Figures 8-2 and 8-3 show colour-coded CFRE images of the study areas. Indicated CFRE correspond to mean CFRE values, calculated via the TIR technique. In tables 8-1 and 8-2 the mean, minimum and maximum computed CFRE are given for detected coal fire zones in the Ruqigou, Gulaben and Wuda coalfields. A summative value is provided in the case where a mapped CFSA comprises more than one anomaly cluster. A dash indicates that no CFSA is detectable within the investigated fire zone.

CFRE values, derived from detected summer daytime, ETM anomaly-pixel data, have a high degree of uncertainty, with an estimated average uncertainty of approx. +/-70 % of the CFRE retrievals⁸⁻²⁾ for the Ruqigou, Gulaben and Wuda coalfields (tables 8-1 and 8-2). This high level of uncertainty, in the CFRE retrievals, results from high background variations in the summer daytime ETM band. Consequently, summer daytime ETM data are considered unsuitable for the quantification of CFSA

CFRE, computed from winter daytime ETM imagery, are more stable than summer daytime ETM-CFRE values, allowing CFRE to be estimated with an estimated average uncertainty of +/- 55 % of the CFRE retrievals for the Ruqigou, Gulaben and Wuda coalfields. This is due to relatively lower background variations in winter than in summer, allowing for a more exact determination of the CFRE.

⁸⁻²⁾ The estimated uncertainty range in the retrieved CFRE values refers to the maximum calculated CFRE variation due to variations in the TIR background signal. The TIR background radiance is varied according to the descriptions in chapter 8.1.1 around the standard deviation of the TIR radiance of the background pixels surrounding each fire cluster.

8 Case study I: Estimation of coal fire related, surface-radiative energy releases

Nevertheless, CFRE retrievals derived from winter daytime ETM data are, in general, lower than corresponding night-time ETM CFRE values (see tables 8-1 and 8-2). This is due to the fact that the detected fire clusters are often spatially more extended in night-time winter ETM data, than in winter daytime ETM data (figures 8-2). In a few cases (e.g. Ruqigou / Gulaben fire 16, Ruqigou / Gulaben 4, Ruqigou / Gulaben 14, table 8-2 and figure 8-3) the spatial extent of the detected fire clusters is significantly lower in winter daytime ETM data than in the summer night-time ETM data, resulting in a drastic underestimation of corresponding CFRE. When winter daytime ETM data cover approximately the same area (e.g. Wuda fire 1, Ruqigou / Gulaben fire 15, table 8-1 and 8-2), the winter day- and night-time ETM-derived CFRE estimates differ by relatively small amounts.

The investigated summer night-time ETM data allow CFRE to be estimated within an estimated average uncertainty of approx. +/- 35 % of the CFRE retrievals (tables 8-1 and 8-2). It appears therefore to be effective for the deviation of CFRE. As discussed previously, this indicated low uncertainty is due primarily to low night-time background variations. Total computed mean CFRE, derived from night-time ETM imagery, are estimated to be 115 MW for the Ruqigou / Gulaben coalfields, and 34 MW for the Wuda coalfield. Computed mean CFRE from winter daytime ETM imagery are 18 MW for the Wuda coalfield and 44 MW for the Ruqigou / Gulaben coalfields.

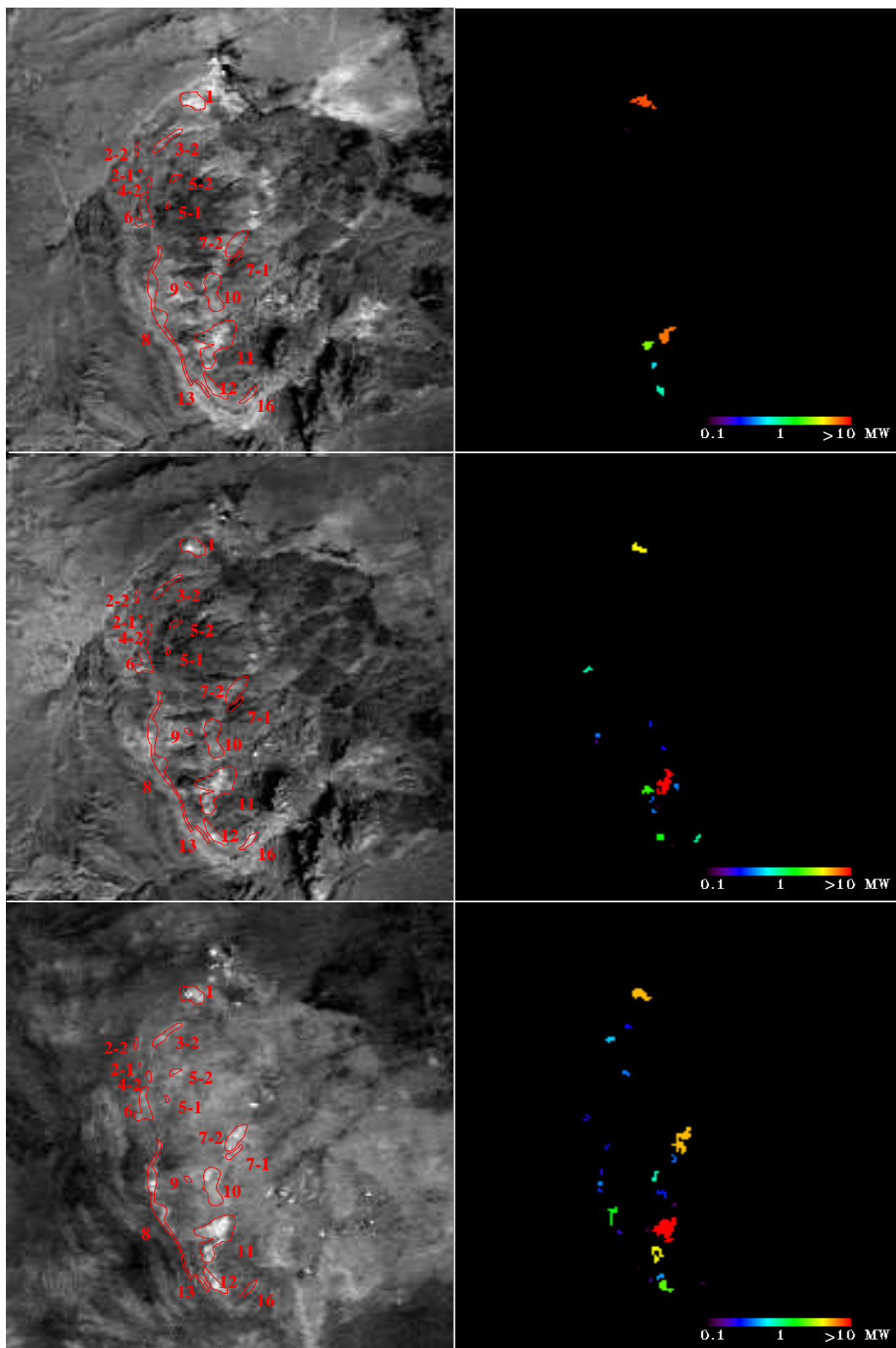


Figure 8-2: ETM TIR bands with superimposed CFSA (red outlines) in the Wuda coalfield (left) and corresponding radiative energy release images of detected coal fire clusters (right). The CFSA were mapped during the field campaign in September 2002. Upper left) ETM TIR Band, 21.09.02 (daytime summer); upper right) Radiative energy release of detected coal fire pixels, 21.09.02 (daytime summer); middle left) ETM TIR Band, 12.02.03 (daytime winter); middle right) Radiative energy release of detected coal fire pixels, 12.02.03 (daytime winter); lower left) ETM TIR Band, 28.09.02 (night-time summer); lower right) Radiative energy release of detected coal fire pixels, 28.09.02 (night-time summer).

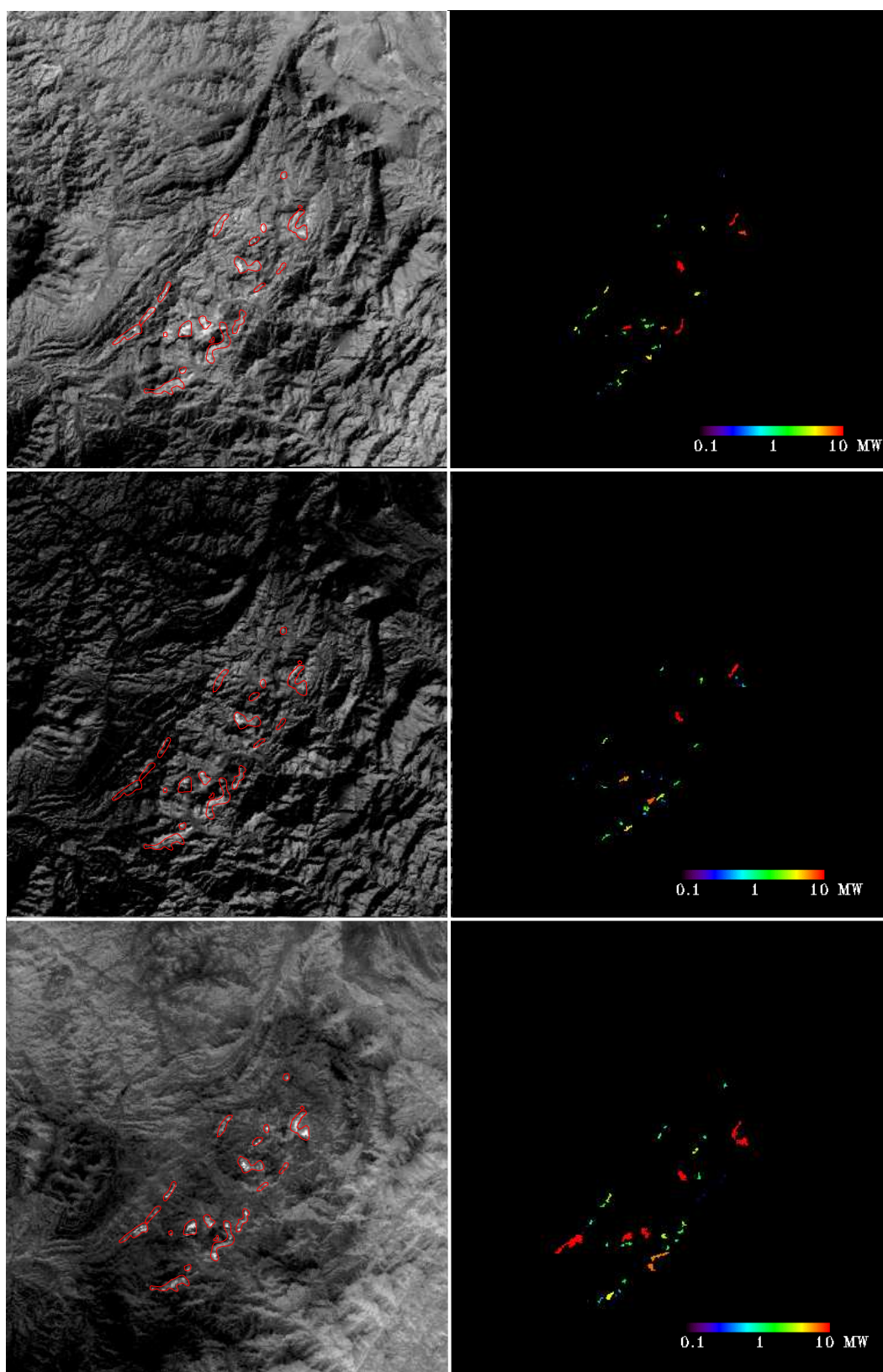


Figure 8-3: ETM TIR bands with superimposed CFSA (red outlines) of the Ruqigou / Gulaben coalfields (left) and corresponding radiative energy release images of detected coal fire clusters (right). The CFSA were mapped during the field campaign in September 2002. Upper left) ETM TIR Band, 21.09.02 (daytime summer); upper right) Radiative energy release of detected coal fire pixels, 21.09.02 (daytime summer); middle left) ETM TIR Band, 12.02.03 (daytime winter); middle right) Radiative energy release of detected coal fire pixels, 12.02.03 (daytime winter); lower left) ETM TIR Band, 28.09.02 (night-time summer); lower right) Radiative energy release of detected coal fire pixels, 28.09.02 (night-time summer).

8 Case study I: Estimation of coal fire related, surface-radiative energy releases

| coal fire Wuda | TIR background | energy release [MW] | | |
|----------------|----------------|----------------------------------|----------------------------------|--------------------------------|
| | | ETM daytime summer 21.09.2002 | ETM daytime winter 12.02.2003 | ETM night summer 28.09.2002 |
| 1 | mean | 5.5 | 3.1 | 3.9 |
| | mean + SD | 1.7 | 2.1 | 1.9 |
| | mean - SD | 10.7 | 4.9 | 6.4 |
| 3-2 | mean | - | - | 0.8 |
| | mean + SD | - | - | 0.5 |
| | mean - SD | - | - | 1.0 |
| 5-2 | mean | - | - | 0.4 |
| | mean + SD | - | - | 0.3 |
| | mean - SD | - | - | 0.5 |
| 6 | mean | - | 0.8 | 0.4 |
| | mean + SD | - | 0.6 | 0.3 |
| | mean - SD | - | 1.0 | 0.5 |
| 7-1+7-2 | mean | - | - | 4.2 |
| | mean + SD | - | - | 2.6 |
| | mean - SD | - | - | 6.0 |
| 8 | mean | - | 0.6 | 2.7 |
| | mean + SD | - | 0.3 | 2.0 |
| | mean - SD | - | 0.9 | 3.7 |
| 10 | mean | - | 0.6 | 1.2 |
| | mean + SD | - | 0.4 | 0.8 |
| | mean - SD | - | 0.7 | 1.9 |
| 11 | mean | 7.5 | 10.3 | 17.2 |
| | mean + SD | 3.3 | 5.4 | 11.5 |
| | mean - SD | 12.8 | 16.8 | 23.9 |
| 12 | mean | 0.8 | 1.4 | 2.4 |
| | mean + SD | 0.2 | 1.0 | 1.5 |
| | mean - SD | 1.5 | 1.8 | 3.1 |
| 13 | mean | - | - | 0.2 |
| | mean + SD | - | - | 0.1 |
| | mean - SD | - | - | 0.2 |
| 16 | mean | - | 0.9 | 0.1 |
| | mean + SD | - | 0.5 | 0.1 |
| | mean - SD | - | 1.3 | 0.2 |
| sum mean | | 13.8 | 17.7 | 33.5 |
| sun mean - SD | | 5.2 | 10.3 | 21.6 |
| sum mean+ SD | | 25.0 | 27.4 | 47.4 |

Table 8-1: Coal fire relate, surface radiative energy releases (CFRE) derived from recognised anomaly pixels in the ETM TIR bands, for mapped CFSA of the Wuda coalfield. Mean energy values are indicated as 'mean', minimum values as 'mean + SD' and maximum values as 'mean - SD'. In case a mapped CFSA includes more than one detected fire cluster, a summative value is provided. A dash indicates that no CFSA could be detected within the corresponding fire zone.

8 Case study I: Estimation of coal fire related, surface-radiative energy releases

| coal fire Ruqigou/ Gulaben | TIR background | energy release [MW] | | |
|----------------------------------|-------------------|-------------------------------------|-------------------------------------|--|
| | | ETM daytime summer 21.09.2002 | ETM daytime winter 12.02.2003 | ETM night-time summer 28.09.2002 |
| 1 | mean | 0.4 | 0.1 | 1.0 |
| | mean + SD | 0.2 | 0.1 | 0.8 |
| | mean - SD | 0.6 | 0.1 | 1.2 |
| 2 | mean | 2.5 | 0.7 | 1.4 |
| | mean + SD | 1.5 | 0.5 | 1.0 |
| | mean - SD | 3.6 | 1.1 | 2.0 |
| 3 | mean | 2.5 | 1.6 | 1.0 |
| | mean + SD | 1.4 | 1.1 | 0.7 |
| | mean - SD | 3.7 | 2.3 | 1.3 |
| 4 | mean | 12.6 | 8.3 | 20.6 |
| | mean + SD | 8.0 | 4.6 | 14.2 |
| | mean - SD | 18.4 | 12.4 | 28.1 |
| 5 | mean | - | - | 2.4 |
| | mean + SD | - | - | 2.2 |
| | mean - SD | - | - | 2.6 |
| 6 | mean | 21.6 | 7.7 | 10.6 |
| | mean + SD | 10.7 | 4.7 | 6.4 |
| | mean - SD | 36.0 | 11.2 | 15.8 |
| 7 | mean | - | - | 0.5 |
| | mean + SD | - | - | 0.4 |
| | mean - SD | - | - | 0.6 |
| 8 | mean | 2.5 | 1.2 | 0.5 |
| | mean + SD | 0.9 | 0.7 | 0.4 |
| | mean - SD | 4.3 | 1.7 | 0.6 |
| 9 | mean | 3.5 | 2.1 | 3.5 |
| | mean + SD | 1.8 | 1.7 | 2.8 |
| | mean - SD | 5.6 | 2.8 | 4.1 |
| 10 | mean | 4.0 | 0.8 | 7.5 |
| | mean + SD | 1.2 | 0.6 | 5.9 |
| | mean - SD | 8.0 | 1.2 | 9.1 |
| 11 | mean | 7.9 | 1.3 | 3.9 |
| | mean + SD | 3.3 | 0.7 | 3.3 |
| | mean - SD | 14.1 | 2.1 | 5.7 |
| 12 | mean | 3.6 | 0.5 | 1.1 |
| | mean + SD | 1.5 | 0.4 | 0.9 |
| | mean - SD | 5.9 | 0.8 | 1.2 |
| 13 | mean | 0.5 | 0.8 | 0.7 |
| | mean + SD | 0.3 | 0.5 | 0.6 |
| | mean - SD | 0.7 | 1.2 | 0.8 |
| 14 | mean | 9.2 | 4.7 | 14.4 |
| | mean + SD | 4.1 | 2.6 | 9.3 |
| | mean - SD | 15.5 | 7.2 | 20.5 |
| 15 | mean | 9.4 | 11.0 | 12.6 |
| | mean + SD | 6.3 | 4.3 | 8.2 |
| | mean - SD | 17.3 | 19.3 | 17.8 |
| 16 | mean | 3.8 | 1.0 | 26.6 |
| | mean + SD | 2.6 | 0.7 | 19.3 |
| | mean - SD | 4.5 | 1.1 | 35.2 |
| 17 | mean | 2.6 | 0.9 | 1.2 |
| | mean + SD | 1.6 | 0.5 | 1.0 |
| | mean - SD | 3.7 | 1.3 | 1.4 |
| 18 | mean | 2.9 | 1.5 | 5.1 |
| | mean + SD | 1.2 | 0.6 | 3.6 |
| | mean - SD | 4.9 | 2.9 | 6.8 |
| | sum mean | 89.5 | 44.2 | 114.6 |
| | summean + SD | 46.6 | 24.3 | 81.0 |
| | sum mean - SD | 146.8 | 68.7 | 154.8 |

Table 8-2: CFRE derived from recognised anomaly pixels in the ETM TIR bands for mapped CFSA of the Ruqigou / Gulaben coalfield. Mean energy values are indicated as ‘mean’, minimum values as ‘mean + SD’ and maximum values as ‘mean - SD’. In cases where a mapped CFSA includes more than one detected fire cluster, a summative value is provided. A dash indicates that no CFSA could be detected within the corresponding fire zone.

8.1.3 Conclusions

This study has demonstrated that summer daytime ETM data are unsuitable for use in the detection and quantification of coal fires, due to excessive background variations. Nevertheless, ETM winter daytime data can be used to quantify coal fires, although the total CFRE release, computed for an entire coalfield, is still approximately a factor two smaller, when compared with total ETM night-time CFRE retrievals.

If we assume that the calorific value of the coal of the Ruqigou / Gulaben coalfield is 31.0 MJ / kg (for average calorific values of Ruqigou and Gulaben coal, see table 3-2) and that the calorific value of the coal of the Wuda coalfield is 21 MJ / kg (for Wuda coal calorific values, see table 3-4), then the total CFRE, computed from night-time ETM data, corresponds to approximately 117000 t annual burned coal in the Ruqigou / Gulaben coalfield, and approximately 51000 t annual burned coal in the Wuda coalfield.

The Wuda mining company estimates the annual coal fire induced coal loss to be approximately 200000 t. According to Goerlich (2004, pers. communication) this number is realistic for a coalfield of the size of the Wuda coalfield, however it has to be regarded as a rough estimate by the local mining authorities. ETM TIR-derived CFRE estimates correspond to a lower coal combustion rate. In general, this underestimation is expected, and most probably due to the fact that during coal combustion energy is lost by a variety of processes in addition to radiation, such as for example, by conduction into the ground (description in chapter 2, section 2.3). However, the ETM derived CFRE values only reflect a 'snapshot' of the present coal fire situation, which is not necessarily representative for an annual estimate of the coal combustion rate. In addition, coal loss estimated from night-time ETM data clearly outlines the overall dimension of the coal fire problem at the Wuda coalfield.

Unfortunately, there are no annual, coal fire induced, coal loss estimations available for the Ruqigou and Gulaben coalfields. According to Goerlich (2004, pers. communication) the presented calculated figure of 117000 t annual coal loss is too small for coalfields the size of the Ruqigou and Gulaben coalfields, but is however within overall expected dimensions.

It is important to note that the relationship between CFRE and combusted coal is not yet fully understood and, in fact, could be critical to establish, in the context of sub-surface coal fires. Nonetheless, potential coal losses, computed through CFRE derived from night-time ETM TIR data, have similar dimensions to reported / expected annual, coal fire induced, coal losses. Therefore, CFRE derived from night-time ETM TIR data is here considered as an important tool to grasp at least some reliable, quantitative information on the coal fires.

8.2 Analysis of BIRD data

8.2.1 Methods

BIRD day- and night-time imaging of both the Ruqigou / Gulaben and Wuda coalfields was performed on the 21st September 2002, the 4th February 2002 and on the 16th January 2003.

The BIRD datasets were atmospherically corrected using the MODTRAN, dry desert model (Berk et al., 1989) with an atmospheric water column of 0.41 cm at sea level. The BIRD data was first geometrically corrected, prior to atmospheric correction. For this study an atmospheric correction model was programmed for BIRD MIR and TIR data, using equation 3-7, and the atmospheric parameters listed in table 8-3. Due to the fact that in the MIR spectral range the path radiance consists, during daytime, of a reflective and a thermal part (description in chapter 3, section 3.2.2), different atmospheric correction parameters were applied for four different sun zenith classes. As with the ETM TIR atmospheric correction, a sub-sampled ERS DEM was used to account for different high levels.

| | high level [km] | L_{path} [mW / m ² sr μm] | T | F [mW / m ² μm] |
|-----------------------------------|--------------------|---|--------|-------------------------------|
| BIRD TIR | 0.0 | 2427.2 | 0.6615 | 6890.1 |
| | 0.5 | 2129.5 | 0.6863 | 6008.6 |
| | 1.0 | 1854.1 | 0.7107 | 5206.4 |
| | 2.0 | 1598.1 | 0.7351 | 4474.6 |
| | 1.5 | 1365.6 | 0.7593 | 3810.9 |
| | 2.5 | 1164.2 | 0.7833 | 3224.8 |
| BIRD MIR (sun zenith >0° to 30°) | 0.0 | 56.3 | 0.7091 | 501.4 |
| | 0.5 | 47.4 | 0.7272 | 430.5 |
| | 1.0 | 40.7 | 0.7445 | 369.3 |
| | 1.5 | 34.6 | 0.7612 | 314.1 |
| | 2.0 | 29.3 | 0.7773 | 271.7 |
| | 2.5 | 24.8 | 0.7927 | 235.9 |
| BIRD MIR (sun zenith >30° to 50°) | 0.0 | 56.0 | 0.7091 | 499.1 |
| | 0.5 | 47.2 | 0.7272 | 428.4 |
| | 1.0 | 40.4 | 0.7445 | 367.5 |
| | 1.5 | 34.4 | 0.7612 | 314.9 |
| | 2.0 | 29.1 | 0.7773 | 270.3 |
| | 2.5 | 24.7 | 0.7927 | 234.7 |
| BIRD MIR (sun zenith >50°) | 0.0 | 53.2 | 0.7099 | 483.7 |
| | 0.5 | 46.5 | 0.7272 | 423.3 |
| | 1.0 | 39.8 | 0.7445 | 362.9 |
| | 1.5 | 33.9 | 0.7612 | 310.8 |
| | 2.0 | 28.7 | 0.7773 | 266.8 |
| | 2.5 | 24.3 | 0.7927 | 231.6 |
| BIRD MIR (no reflectance) | 0.0 | 46.9 | 0.7091 | 428.4 |
| | 0.5 | 38.9 | 0.7272 | 361.6 |
| | 1.0 | 32.4 | 0.7445 | 304.9 |
| | 1.5 | 26.9 | 0.7612 | 256.9 |
| | 2.0 | 22.2 | 0.7773 | 217.3 |
| | 2.5 | 18.4 | 0.7927 | 186.8 |

Table 8-3: Path radiance (L_{path}), atmospheric ground-to-sensor transmittance (T) and downwelling flux of atmosphere (F) used for atmospheric corrections of the BIRD MIR and TIR data.

8 Case study I: Estimation of coal fire related, surface-radiative energy releases

The coal fire detection was performed in a manner similar to the above described coal fire detection using ETM data, but because the MIR spectral range is much more sensitive to coal fires than the TIR spectral range (description in chapter 6, section 6.4.2), BIRD MIR data, and not BIRD TIR data was used to outline potential coal fire pixels. To account for possible co-registration errors of the TIR and MIR channel, and to reduce errors introduced through variations in the background signal (description in chapter 3, section 3.3.1), continuous fire pixels were clustered, as in the case of the ETM analysis in this chapter. The CFRE, the equivalent surface coal fire area and the equivalent surface coal fire temperature were estimated for each individual fire cluster by applying the bi-spectral technique (description in chapter 3, section 3.3.1) to detected fire pixels in the BIRD MIR and TIR band. The transformation of spectral radiance to temperature was performed numerically using spectral radiances / temperature look-up tables.

Background MIR and TIR radiance were derived from ten background pixels surrounding each fire cluster, whilst direct neighbours were again not considered. In order to check the stability of the bi-spectral retrievals coal fire estimations were performed for the following TIR background values (see tables 8-4 and 8-5):

- the mean value of the TIR radiance for the neighbouring background pixels ('mean' in tables 8-4 and 8-5), corresponding to an estimation of the mean equivalent surface fire temperature, the mean equivalent surface fire area and the mean radiative energy release.
- the mean value minus one standard deviation of the TIR radiance for the neighbouring background pixels ('mean-SD' in tables 8-4 and 8-5), corresponding to an estimation of the lower limit of the fire temperature, the upper limit for the fire area and the upper limit of the radiative energy release.
- the mean value plus one standard deviation of the TIR radiance for the neighbouring background pixels ('mean+SD' in tables 8-4 and 8-5), corresponding to an estimation of the upper limit of fire temperature, the lower limit for the fire area and the lower limit of the radiative energy release.

In addition, quantitative coal fire estimations are marked with brackets in tables 8-4 and 8-5 where the cluster-averaged TIR signal exceeded the estimated background level by less than 1 K, since in this case, the bi-spectral retrievals are according to Wooster et al. (2003) not reliable.

8.2.2 Interpretations

BIRD MIR bands, with superimposed CFSA, mapped during the field campaign in September 2002, and corresponding colour-coded CFRE release images are shown in figures 8-4 and 8-5. In most cases the given energy releases correspond to the mean computed CFRE (mean TIR background value) for the potential coal fire cluster. In cases in which the TIR radiance of the detected fire cluster did not exceed the mean TIR background value, but did exceed the minimum computed TIR background value ('mean-SD'), the corresponding upper limit of the estimated CFRE is given.

A visual coal fire detection of summer daytime BIRD MIR data resulted in two outlined coal fire areas in the Wuda coalfield and ten outlined fire areas in the Ruqigou / Gulaben coalfield. Despite the overall observation interval of nearly five months, most of the detected summer anomalies are reproduced in the MIR channel of the winter daytime BIRD data, and two more coal fire related pixel clusters were outlined in the Wuda coalfield. Nevertheless, fewer coal fire areas can be visually detected on winter daytime BIRD MIR data than on winter daytime ETM TIR data. Thus, the greater sensitivity to fire temperature of the BIRD MIR spectral range, over that of the ETM TIR range, cannot totally compensate for the fact that BIRD data have a factor six lower spatial resolution than ETM data. This result confirms the theoretical evaluations in chapter 6, section 6.4.2.

On night-time BIRD data, five out of seventeen coal fire areas in the Wuda coalfield, and fourteen out of eighteen coal fire areas of the Ruqigou / Gulaben coalfield, can be outlined. As discussed previously, this relatively high night-time detectability is caused by low, background temperature variations. Most of the anomaly clusters detected in the BIRD MIR channel can also be recognised in the BIRD TIR channel, allowing a computation of the equivalent fire temperature, equivalent fire area and the radiative energy release of detected clusters, via the bi-spectral technique. Nevertheless, in a number of cases the upper limit, and, in a few cases, the mean value of the derived coal fire parameters was uncertain (see figures in brackets, tables 8-5 and 8-6) or could not be computed (marked as a hyphen '-', tables 8-4 and 8-5).

The equivalent BIRD-derived, mean temperatures range between 300 K and 600 K. This is in good agreement with the field observations. CFRE estimates derived from BIRD data are unstable⁸⁻³⁾ for the Wuda coalfield, but relatively certain for the Ruqigou / Gulaben coalfield. In general, CFRE can be retrieved from BIRD data with an estimated average uncertainty of approx. + / - 75 % of the CFRE retrievals for BIRD daytime and an estimated average uncertainty of approx. + / - 40 % of the CFRE retrievals for BIRD night-time data. Night-time BIRD CFRE estimates, computed for the entire

⁸⁻³⁾ The term unstable refers to those cases where the cluster-averaged TIR signal exceeded the estimated background signal by less than 1 K

mapped fire zones of the Ruqigou / Gulaben coalfields, are, in general, smaller than night-time ETM CFRE retrievals. Nevertheless, despite two exceptions (fire zones 15 and 16) there are good correlations for CFRE, computed for entire fire zones from the winter daytime ETM, and winter night-time BIRD data (table 8-5 and table 8-2). It seems that the comparatively lower spatial resolution of the BIRD data is compensated for by a higher sensitivity to fire temperature in the MIR spectral range and under night-time conditions. The good correlation between CFRE retrievals, from winter daytime ETM data, and night-time BIRD data proves that despite the high background variations in the TIR range, physically meaningful CFRE can be derived via the TIR method.

8.2.3 *Conclusions*

The total mean energy releases derived from summer daytime BIRD data, winter daytime BIRD data and night-time BIRD data are relatively constant, ranging between 22 MW and 36 MW for the Ruqigou / Gulaben coalfields. Compared to ETM night-time data, the total CFRE derived from BIRD night-time data is a factor three smaller. Thus, we can consider BIRD data to be useful in the quantification of larger, CFSA. In general though, the spatial resolution of the BIRD MIR and TIR channels at 370 m is insufficient for the quantification of coal fires on a regional scale. The BIRD sensor is a technical demonstrator, and this study has outlined that a future operational system that included both MIR and TIR spectral channels, at a high spatial resolution, would definitely have a very high potential to quantify coal fires.

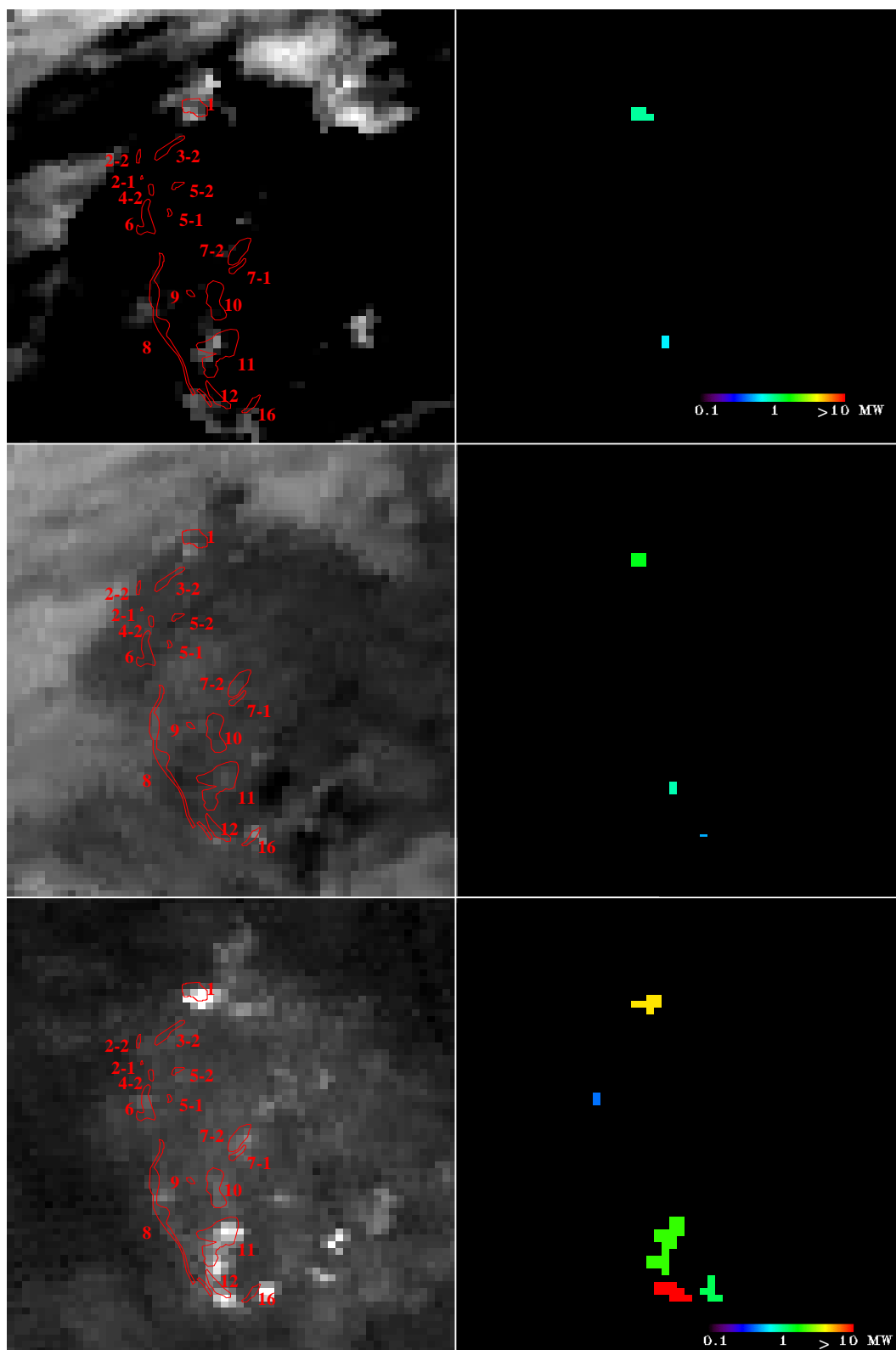


Figure 8-4: BIRD MIR bands with superimposed CFSA (red outlines) of the Wuda coalfield (left) and corresponding radiative energy release images of detected coal fire clusters (right). The CFSA were mapped during the field campaign in September 2002. Upper left) BIRD MIR band, 21.09.02 (daytime summer); upper right) Radiative energy release of detected coal fire pixels, 21.09.02 (daytime summer); middle left) BIRD MIR band, 04.02.02 (daytime winter); middle right) Radiative energy release of detected coal fire pixels, 04.02.02 (daytime winter); lower left) BIRD MIR band, 16.01.03 (night-time winter), lower right) Radiative energy release of detected coal fire pixels, 16.01.03 (night-time winter).

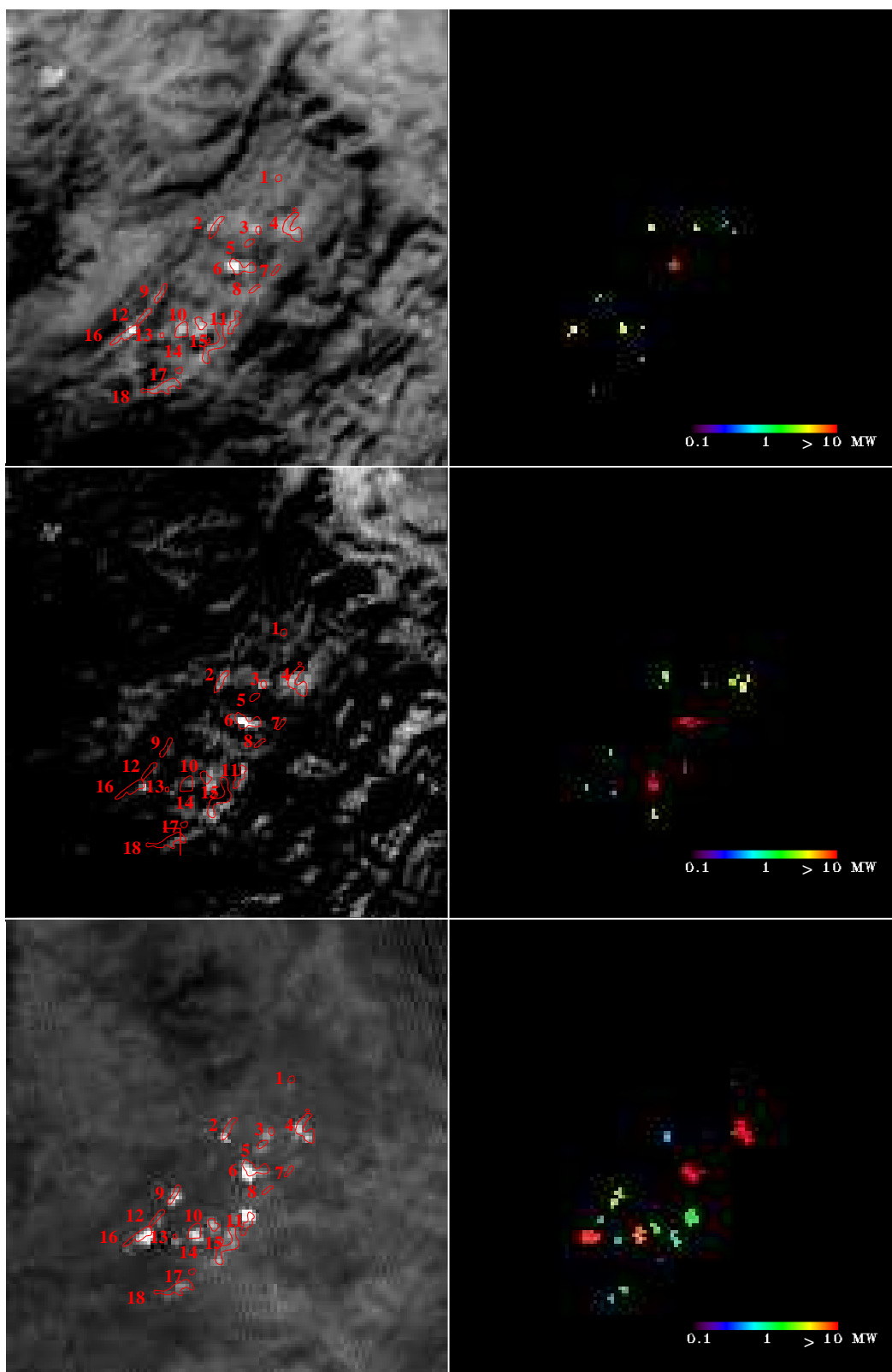


Figure 8-5: BIRD MIR bands with overlain CFSA (red outlines) of the Ruqigou / Gulaben coalfields (left) and corresponding radiative energy release images of detected coal fire clusters (right). The CFSA were mapped during the field campaign in September 2002. Upper left) BIRD MIR band, 21.09.02 (daytime summer); upper right) Radiative energy release of detected coal fire pixels, 21.09.02 (daytime summer); middle left) BIRD MIR band, 04.02.02 (daytime winter) middle right) Radiative energy release of detected coal fire pixels, 04.02.02 (daytime winter); lower left) BIRD MIR band, 16.01.03 (night-time winter); lower right) Radiative energy release of detected coal fire pixels, 16.01.03 (night-time winter).

8 Case study I: Estimation of coal fire related, surface-radiative energy releases

| coal fire Wuda | TIR background | eq. T | eq. A | energy release | eq. T | eq. A | energy release | eq. T | eq. A | energy release |
|-------------------|----------------|-----------------------------------|-------------------|----------------|-----------------------------------|-------------------|----------------|--------------------------------------|-------------------|----------------|
| | | [K] | [m ²] | [MW] | [K] | [m ²] | [MW] | [K] | [m ²] | [MW] |
| | | BIRD daytime summer 21.09.2002 | | | BIRD daytime winter 04.02.2002 | | | BIRD night-time winter 16.01.2003 | | |
| 1 | mean | - | - | - | 393 | 1279 | 1.3 | - | - | - |
| | mean + SD | - | - | - | (420) | (432) | (0.6) | - | - | - |
| | mean - SD | 362 | 2341 | 0.8 | 382 | 2255 | 1.9 | 323 | 15152 | 4.1 |
| 8 | mean | - | - | - | - | - | - | - | - | - |
| | mean + SD | - | - | - | - | - | - | - | - | - |
| | mean - SD | - | - | - | - | - | - | 309 | 2284 | 0.4 |
| 11 | mean | - | - | - | 331 | 2359 | 0.8 | 405 | 898 | 1.0 |
| | mean + SD | - | - | - | (337) | (1318) | (0.5) | - | - | - |
| | mean - SD | 347 | 2667 | 0.6 | 310 | 3342 | 1.2 | 371 | 3230 | 2.4 |
| 12 | mean | - | - | - | - | - | - | - | - | - |
| | mean + SD | - | - | - | - | - | - | - | - | - |
| | mean - SD | - | - | - | - | - | - | 340 | 5818 | 2.4 |
| 13 | mean | - | - | - | 402 | 229 | 0.3 | - | - | - |
| | mean + SD | - | - | - | - | - | - | - | - | - |
| | mean - SD | - | - | - | 360 | 878 | 0.5 | - | - | - |
| 16 | mean | - | - | - | (510) | (136) | (0.5) | 355 | 2932 | 1.6 |
| | mean + SD | - | - | - | - | - | - | - | - | - |
| | mean - SD | - | - | - | 433 | 616 | 1.0 | 320 | 26101 | 6.8 |
| sum mean | | | | | - | 2.9 | | (2.6) | | |
| summean + SD | | | | | - | (1.1) | | - | | |
| sum mean - SD | | | | | 1.4 | 4.6 | | 16.1 | | |

Table 8-4: CFRE, equivalent fire temperatures and equivalent fire sizes, derived from recognised anomaly pixels in the BIRD MIR bands, for each mapped CFSA of the Wuda coalfield. Mean energy values are indicated as ‘mean’, minimum values as ‘mean + SD’ and maximum values as ‘mean - SD’. In cases where a mapped CFSA includes more than one detected fire cluster, a summative value is provided. A dash indicates that no CFSA could be detected within the corresponding fire zone.

8 Case study I: Estimation of coal fire related, surface-radiative energy releases

| coal fire Ruqigou | TIR background | eq. T | eq. A | energy release | eq. T | eq. A | energy release | eq. T | eq. A | energy release |
|----------------------|-------------------|--------------------------------------|-------------------|-------------------|--------------------------------------|-------------------|-------------------|---|-------------------|-------------------|
| | | [K] | [m ²] | [MW] | [K] | [m ²] | [MW] | [K] | [m ²] | [MW] |
| | | BIRD daytime summer 21.09.2002 | | | BIRD daytime winter 04.02.2002 | | | BIRD night-time winter 16.01.2003 | | |
| 1 | mean | - | - | - | - | - | - | - | - | - |
| | mean + SD | - | - | - | - | - | - | - | - | - |
| | mean - SD | - | - | - | - | - | - | 398 | 4.6 | 0.1 |
| 2 | mean | 373 | 1235 | 2.5 | 363 / 396 | 3501 / 542 | 2.6 | (443) | (256) | (0.5) |
| | mean + SD | 425 | 693 | 0.9 | (405) / (336) | (663) / (1.5) | 0.8 | - | - | - |
| | mean - SD | 357 | 11041 | 4.4 | 351 / 365 | 7245 / 1571 | 4.8 | 392 | 905 | 1.0 |
| 3 | mean | 357 | 5803 | 2.3 | 339 | 2462 | 1.0 | (344) | (548) | (0.3) |
| | mean + SD | 386 | 1656 | 1.2 | (347) | (1330) | (0.6) | (478) | (17.3) | (0.1) |
| | mean - SD | 343 | 13842 | 3.6 | 334 | 3756 | 1.3 | 320 | 1727 | 0.5 |
| 4 | mean | 383 / 347 | 1234 / 2268 | 1.4 | 362 / 327 | 3409 / 11658 | 5.2 | 306 | 35318 | 7.3 |
| | mean + SD | (-) / (340) | (-) / (1647) | 0.3 | (555) / (311) | (35) / (9231) | 1.6 | 323 | 14165 | 4.6 |
| | mean - SD | 348 / 349 | 6230 / 3041 | 2.8 | 348 / 332 | 8918 / 15914 | 7.3 | 298 | 67757 | 10.4 |
| 6 | mean | 433 | 4276 | 6.3 | 373 | 14712 | 11.0 | 348 | 14712 | 8.0 |
| | mean + SD | 531 | 666 | 2.7 | (422) | (3153) | (4.6) | 371 | 6665 | 5.2 |
| | mean - SD | 399 | 11949 | 10.3 | 355 | 32278 | 18.5 | 335 | 25986 | 10.7 |
| 9 | mean | 396 | 1135 | 1.0 | 352 | 2542 | 1.4 | 362 | 2983 | 2.1 |
| | mean + SD | 440 | 273 | 0.4 | 350 | 1728 | 0.9 | 383 | 1518 | 1.4 |
| | mean - SD | 381 | 2321 | 1.6 | 353 | 3383 | 1.9 | 348 | 4882 | 2.7 |
| 10 | mean | 342 | 3482 | 0.8 | 336 | 30253 | 11.3 | 324 | 5173 | 1.7 |
| | mean + SD | (360) | (1028) | (0.4) | (423) | (1218) | (1.8) | (352) | (1817) | (1.0) |
| | mean - SD | 329 | 10818 | 1.3 | 324 | 84162 | 24.9 | 309 | 10930 | 2.5 |
| 11 | mean | - | - | - | - | - | - | 600 | 216 | 1.5 |
| | mean + SD | - | - | - | (467) | (402) | (1.0) | (841) | (32) | (0.9) |
| | mean - SD | - | - | - | - | - | - | 529 | 526 | 2.2 |
| 12 | mean | - | - | - | - | - | - | 325 | 1514 | 0.5 |
| | mean + SD | - | - | - | - | - | - | 334 | 862 | 0.4 |
| | mean - SD | - | - | - | - | - | - | 320 | 2247 | 0.7 |
| 13 | mean | - | - | - | 365 | 1056 | 0.7 | 347 | 921 | 0.5 |
| | mean + SD | - | - | - | (437) | (115) | (0.2) | (390) | (224) | (0.2) |
| | mean - SD | - | - | - | 348 | 2565 | 1.3 | 330 | 1978 | 0.8 |
| 14 | mean | 386 | 4042 | 2.9 | - | - | - | 317 | 17568 | 4.9 |
| | mean + SD | (521) | (184) | (0.7) | - | - | - | (332) | (8626) | (3.4) |
| | mean - SD | 358 | 13665 | 5.6 | - | - | - | 306 | 30366 | 6.6 |
| 15 | mean | 370 | 1336 | 0.6 | 357 | 4264 | 2.4 | 351 / 336 | 1749 / 818 | 1.4 |
| | mean + SD | (414) | (222) | (0.3) | (422) | (373) | (0.5) | 405 / 437 | 326 / 43 | 0.5 |
| | mean - SD | 354 | 2984 | 1.1 | 345 | 9914 | 4.4 | 332 / 313 | 4109 / 2599 | 2.2 |
| 16 | mean | 463 | 1598 | 3.3 | 434 | 474 | 0.8 | 368 | 7854 | 5.9 |
| | mean + SD | (494) | (525) | (1.9) | (565) | (46) | (0.3) | 389 | 4113 | 4.7 |
| | mean - SD | 435 | 3158 | 4.8 | 404 | 1156 | 1.4 | 354 | 12643 | 7.8 |
| 18 | mean | 366 | 1840 | 0.9 | - | - | - | 313 / 316 | 4930 / 1790 | 1.8 |
| | mean + SD | (403) | (372) | (0.4) | - | - | - | 310 / - | 387 / - | 0.3 |
| | mean - SD | 354 | 4133 | 1.6 | - | - | - | 295 / 299 | 15753 / 6191 | 3.5 |
| | sum mean | | 22 | | | 36.4 | | | 36.4 | |
| | sum mean +SD | | 9.2 | | | 12.3 | | | 22.7 | |
| | sum mean - SD | | 37.1 | | | 65.3 | | | 51.7 | |

Table 8-5: CFRE, equivalent fire temperatures and equivalent fire sizes, derived from recognised anomaly pixels in the BIRD MIR bands, for each mapped anomaly zone of the Wuda coalfield. Mean energy values are indicated as ‘mean’, minimum values as ‘mean + SD’ and maximum values as ‘mean - SD’. In the case where a mapped, CFSA includes more than one detected fire cluster, a summative value is provided. A dash indicates that no coal fire related anomaly could be detected within the corresponding fire zone.

8.3 Analysis of ASTER DATA

8.3.1 Methods

For this case study an investigation was made of a night-time ASTER scene, acquired synchronously with the field campaign in September 2002, covering the Wuda coalfield, taken on the 21st September 2002. CFRE retrievals were then directly compared to CFRE estimations derived from the near-simultaneous night-time ETM scene from the 28th September 2002.

Night-time data from ASTER channels 10 and 14 were geometrically corrected and the digital numbers were transformed to radiances using the calibration constants listed in chapter 10, table 10-2. The atmospheric correction was performed in a manner similar to the ETM TIR data processing, using equation 3-7 and look-up tables for path radiances, atmospheric ground to sensor transmittance and downwelling atmospheric flux, calculated via the MODTRAN code (Berk et al. 1989). The parameters that were applied for the atmospheric correction are listed in chapter 10, table 10-4. Temperatures of the Yellow River, measured at one location during satellite overpasses, coincide with corresponding ASTER brightness temperatures within 1.6 K.

CFSA were visually detected, using the ASTER band 10, in a similar manner to the ETM and BIRD coal fire detection, by setting an adaptive threshold within a visually defined window around each coal fire area that was mapped during the field campaign, in September 2002. Having identified the anomaly pixels, neighbouring fire pixels were grouped into individual clusters. The TIR method was applied to ASTER band 10 data in order to retrieve CFRE for each detected fire cluster. The ASTER band 10 was chosen as input channel because it has the highest capability of all ASTER TIR bands to derive accurate CFRE values via the TIR method, according to the theoretical evaluations in chapter 7, section 7.2.2. In addition, effective fire temperature and fire areas were computed via the bi-spectral technique (equations 3-11 and 3-12) for each fire cluster, using ASTER bands 10 and 14 as input sources. As with the BIRD approach, equation 3-13 was applied in order to compute CFRE from bi-spectral fire size and temperature estimations.

For both the TIR and the bi-spectral method, background radiances were computed from ten neighbouring pixels around each cluster, excluding direct neighbours. As with the BIRD and ETM data analysis, the stability of derived CFRE to background uncertainties was tested. CFRE was computed for the mean background value (“mean” in table 8-6), the mean background value minus one standard deviation (“mean-SD” in table 8-6) and the mean background value plus one standard deviation (“mean+SD” in table 8-6) when applying both the TIR and the bi-spectral method.

8.3.2 Interpretations

Although ASTER band 10 has a 50 % lower spatial resolution than the ETM TIR band, a significant difference could not be observed in the capacity of ASTER band 10 to detect coal fires. With one exception, all coal fire areas mapped in September 2002, that were visually detected on night-time ETM TIR band data could be as well identified on night-time ASTER TIR band 10 data (see figure 8-6 and 8-2). The coal fire cluster that could not be delineated on night-time ASTER band 10 is, according to the field observations, a sub-surface coal fire with a weak CFSA.

CFRE derived from ASTER TIR data, via the bi-spectral technique and the TIR method, are listed in table 8-6. In addition, table 8-6 details CFRE derived from near-simultaneous night-time ETM TIR band data, so that a direct comparison can be made between ASTER and ETM CFRE retrievals. Mean CFRE estimates derived from ASTER and night-time ETM data are illustrated in figure 8-6.

Night-time ASTER CFRE estimates, derived via the TIR method, are relatively dependable with regard to background variations, with an estimated average uncertainty of approx. +/- 25 % of the CFRE retrievals. The uncertainty is, therefore, slightly lower compared to the uncertainty level of night-time data, at +/- 35 % ETM. The CFRE derived from ETM and ASTER data for the different coal fire areas show good correlations. Nevertheless, table 8-6 clearly indicates that ASTER TIR derived CFRE is in general lower than ETM derived values. The lower spatial resolution of the ASTER scene seems to prevent the recording of some of the less radiative fire components, resulting in a 27 % lower total CFRE when compared with ETM night-time retrievals.

As expected from the sensitivity study in chapter 6, section 6.3.2 the ASTER bi-spectral retrievals are absolutely undependable due to variations of the background signal. For some coal fire clusters the mean CFRE could not be determined and for many fire clusters, the upper and / or lower limit of CFRE retrievals could not be determined either (indicated by a hyphen '-', table 8-6). Table 8-6 shows that mean CFRE energy releases computed for mapped coal fire zones are not in good agreement with ETM computed values. This mirrors the very narrow spectral range of the ASTER TIR channels, and outlines the fact that the bi-spectral technique applied cannot be applied to the quantification of coal fires via ASTER TIR data.

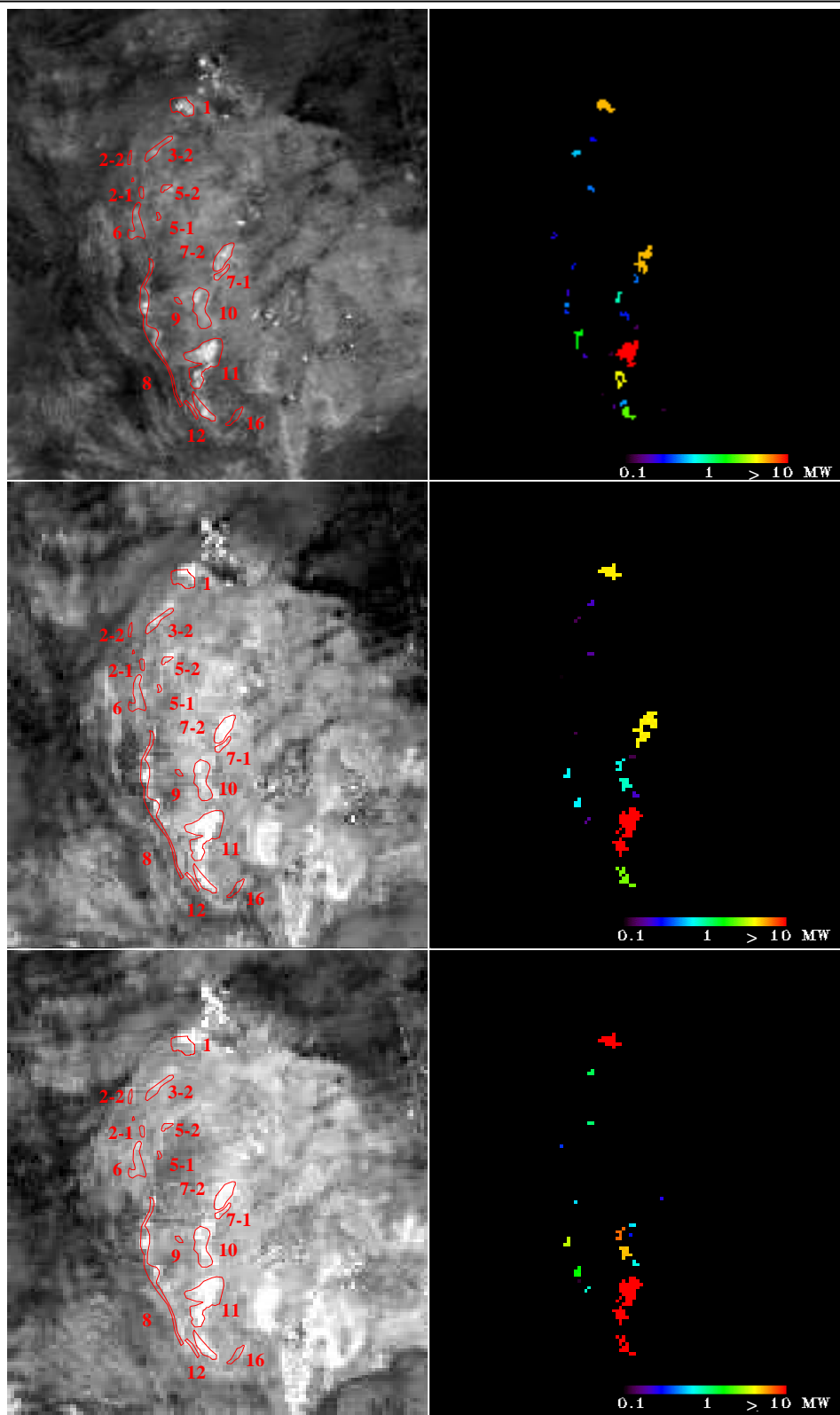


Figure 8-6: ASTER and ETM TIR bands with superimposed coal fire related, surface anomalies (red outlines) of the Wuda coalfield (left) and radiative energy release images of detected coal fire clusters (right). The surface anomaly zones were mapped during the field campaign in September 2002. Upper left) ETM TIR Band, 28.09.02 (night-time); upper right) radiative energy release of detected coal fire pixels (TIR method), 28.09.02 (night-time); middle left) ASTER TIR Band 10, 21.09.02 (night-time); middle right) radiative energy release of detected coal fire pixels (TIR method), 21.09.02 (night-time); lower left) ASTER TIR Band 14, 21.09.02 (night-time); lower right) radiative energy release of detected coal fire pixels (Dozier method band 10 and band 14, 21.09.02 (night-time)).

8 Case study I: Estimation of coal fire related, surface-radiative energy releases

| coal fire Wuda | TIR background | energy release [MW] | | | T [K] | area [m ²] |
|-------------------|-------------------|---|--|--|----------|---------------------------|
| | | ETM night 28.09.2002 band 6 TIR method | ASTER night 21.09.2002 band 10 TIR method | ASTER night 28.09.2002 band 10 / band 14 bi-spectral method (fire detection band 10) | | |
| 1 | mean | 3.9 | 3.3 | 13.2 | 485 | 4754 |
| | mean + SD | 1.9 | 2.5 | - | - | - |
| | mean - SD | 6.4 | 4.2 | 15.9 | 324 | 56991 |
| 3-2 | mean | 0.8 | 0.3 | 0.8 | 360 | 1394 |
| | mean + SD | 0.5 | 0.2 | 1.0 | 797 | 46 |
| | mean - SD | 1.0 | 0.5 | - | - | - |
| 5-2 | mean | 0.4 | 0.2 | - | - | - |
| | mean + SD | 0.3 | 0.1 | - | - | - |
| | mean - SD | 0.5 | 0.2 | 1.0 | 294 | 13953 |
| 6 | mean | 0.4 | 0.1 | 0.4 | 323 | 1703 |
| | mean + SD | 0.3 | 0.1 | 0.3 | 368 | 488 |
| | mean - SD | 0.5 | 0.1 | - | - | - |
| 7-1+7-2 | mean | 4.2 | 3.3 | 0.2 | - | - |
| | mean + SD | 2.6 | 2.5 | 0.1 | 357 | 428 |
| | mean - SD | 6.0 | 4.1 | 0.3 | 377 | 184 |
| 8 | mean | 2.7 | 1.6 | 4 | 349 | 704 |
| | mean + SD | 2.0 | 1.1 | 3.7 | 331 | 1640 |
| | mean - SD | 3.7 | 2.1 | 4.5 | 334 | 7315 |
| 10 | mean | 1.2 | 1.9 | 5.7 | 344 | 1616 |
| | mean + SD | 0.8 | 1.2 | 0.6 | 347 | 1438 |
| | mean - SD | 1.9 | 2.5 | 5.7 | 347 | 10419 |
| 11 | mean | 17.2 | 11.8 | 36.8 | 298 | 3965 |
| | mean + SD | 11.5 | 9.7 | 31.5 | 329 | 1936 |
| | mean - SD | 23.9 | 14.0 | 43.3 | 393 | 5529 |
| 12 | mean | 2.4 | 2.0 | 7.9 | 323 | 115 |
| | mean + SD | 1.5 | 1.7 | 6.6 | 398 | 55 |
| | mean - SD | 3.1 | 2.4 | 9.3 | 705 | - |
| 13 | mean | 0.2 | - | - | 349 | 1916 |
| | mean + SD | 0.1 | - | - | 384 | 515 |
| | mean - SD | 0.2 | - | - | 439 | 2427 |
| sum | sum mean | 33.5 | 24.5 | 69.0 | 489 | 232 |
| | sum mean -SD | 21.6 | 19.0 | 44.5 | 315 | 2773 |
| | sum mean+ SD | 47.4 | 30.1 | 80.0 | 610 | 40 |

Table 8-6: CFRE, derived from recognised anomaly pixels in the ETM and ASTER TIR bands, for mapped CFSA of the Wuda coalfield. Mean energy values are indicated as 'mean', minimum values as 'mean + SD' and maximum values as 'mean - SD'. In cases where a mapped, CFSA includes more than one detected fire cluster, a summative value is provided. A dash indicates that no CFSA could be detected within the corresponding fire zone.

8.3.3 Conclusions

The results of this case study confirm the theoretical evaluations in chapter 6, which indicate that ASTER data have an approximately similar capacity to ETM data to detect coal fires. The lower spatial resolution of the ASTER data prevents some of the less radiative fire components from being recorded, and thus, the lower spatial resolution of ASTER data is a disadvantage for coal fire quantification studies, when compared with ETM data. However, the total energy release, computed via the TIR method, still outlines the dimension of the coal fire problem in the Wuda coalfield, and consequently night-time ASTER data are here considered to be effective in the quantification of coal fires on a regional scale.

This case study indicates that the five ASTER TIR bands are spectrally too close to each other to derive stable CFRE values via the bi-spectral technique. This confirms the theoretical analysis in chapter 6, section 6.3.2. Due to the fact that the SWIR spectral range is generally not sufficiently sensitive to the general registration of spectral coal fire radiance (description in chapter 6, section 6.3.2 and chapter 8, section 8.1.2), the developed TIR method is the only method that can be applied to ASTER data in order to quantify coal fires.

8.4 General conclusions

With regard to a coal fire analysis, this case study has clearly demonstrated that physically meaningful CFRE values can be derived from high resolution TIR satellite data. CFRE retrievals from ASTER and ETM data, calculated via the presented TIR approach, are in the same order of magnitude as CFRE retrievals from BIRD data that have been calculated via the commonly used bi-spectral technique. In addition, TIR CFRE retrievals made by two different instruments from near-synchronous TIR satellite observations are in good correlation with one another, indicating the robustness of the TIR method.

Nevertheless, TIR channel satellite data can only measure coal fire related surface radiative energy emission and can thus only provide an estimate of the minimum amount of coal which is lost due to coal fires. The fact that total coal loss estimates derived from calculations of radiative surface energy emissions correlate well with coal loss estimates from local mining companies is promising and indicates that thermal satellite data can in fact be used to estimate the overall dimension of the coal fire problem. Existing estimates of annual, coal fire induced CO₂ emission for China vary considerably, and differ by about the factor of 20 from each other (description in chapter 2, section 2.4). A satellite-based coal fire inventory in China could thus provide an estimate of the minimum amount of coal fire induced coal loss in China, and thereby increase the precision of such estimates.

9 CASE STUDY II: THE POTENTIAL OF ETM AND BIRD DATA TO QUANTIFY MOVEMENTS AND ACTIVITY CHANGES IN COAL FIRE RELATED, SURFACE ANOMALIES

This chapter is concerned with analysing the potential of satellite data to quantify particular coal fires. Here detailed field maps of a sub-surface and a near-surface coal fire from the Wuda coalfield are compared with ETM thermal data. In addition, coal fire energy release (CFRE), computed via the TIR method or the bi-spectral technique, from multi-temporal BIRD and ETM night-time data, is analysed with the aim to evaluate whether or not multi-temporal thermal satellite data can be used to register movement or activity changes in coal fire related surface anomalies (CFSA).

9.1 Comparison of ETM brightness temperatures and field observations

In this section ETM night- and daytime data, acquired during the field campaign in September 2002, are compared with detailed field maps and temperature measurements of Wuda coal fires 7 and 8 (field descriptions see chapter 5, section 5.3).

9.1.1 Methods

ETM sensor imaging was performed on the 21st September 2002 under daytime conditions, and on the 28th September 2002 during night-time conditions. The two data sets were geometrically corrected via a nearest-neighbour approach, using ground control points, taken with a GPS device during the field campaign in September 2002. Although more than thirty ground control points were used for the geometric correction, both night-time and daytime data still evidenced a slight geometric distortion of about one ETM pixel (~ 50 m). The digital numbers (DN) of the ETM data were converted to brightness temperatures to allow a direct comparison between pixel-integrated brightness temperatures and field brightness temperature measurements. Both the transformation of DN to radiances and the atmospheric correction were performed in a similar manner to the preparation of ETM data, described in chapter 8, section 8.1.1. In addition, radiance values were converted to brightness temperatures by means of radiance / brightness temperature look-up tables. The look-up tables were computed via equations 3-2 and 3-4, using the ETM channel 6 sensor response function.

The field temperature measurements were undertaken in a time window of about one hour around the satellite overpass. Ground temperature data are missing for coal fire 8 night-time observation, as this coal fire could not be accessed during night-time. The temperature patterns of the two investigated coal fire areas are very complex (description in chapter 5, section 5.3) and a statistically significant quantity of temperature data for the entire area could not be measured during satellite overpasses. The ground temperatures were measured along two profiles, which do not necessarily reflect the temperature pattern of the entire fire zone. Consequently, the overpass synchronous ground temperatures could not

9 Case study II: The potential of ETM and BIRD data to quantify movements and activity ...

be used to compute corresponding ETM pixel brightness temperatures. Nevertheless, the measured ground temperatures can be regarded as an indicator for the temperature variations of both the background and the CFSA. Both, the temperature profiles and the fire maps were geometrically located using a GPS handheld receiver. A comparison of GPS measurements and geographic coordinates of three triangulation points in the Wuda coalfield revealed a maximal dislocation of the GPS measurements of about 15 m.

For this study both detailed field maps of Wuda coalfield coal fire numbers 7 (sub-surface coal fire) and 8 (near-surface coal fire)⁹⁻¹⁾ and temperature profiles measured during the satellite overpasses, were directly superimposed on the processed ETM data (figures 9-1 to 9-4). The satellite data was stretched non-linearly, so that the visualisation would show a maximum contrast between background and fire pixels. The pixel brightness temperatures indicated by green numbers in figures 9-1 to 9-4, and the grey scales of the displayed satellite images, can thus not be directly linked to each other.

⁹⁻¹⁾ The term near-surface coal fire is used here to describe a coal fire that is only partly exposed at the surface.

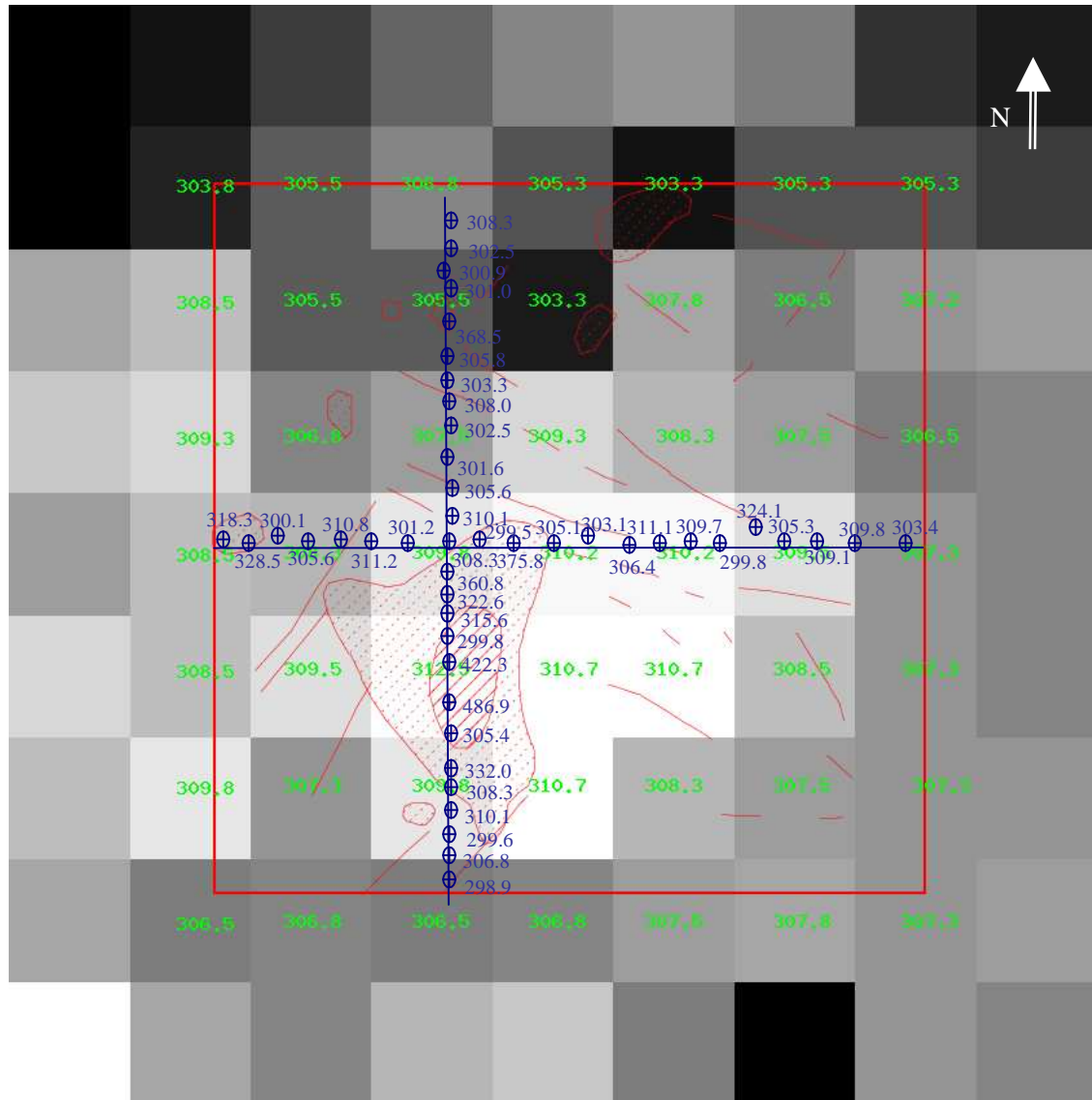


Figure 9-1: ETM channel 6 (daytime, 21.09.02) brightness temperatures, superimposed on a detailed surface map of the sub-surface coal fire 7 of the Wuda coalfield. The field mapping was performed during the first field campaign in September 2002 (details see chapter 5, section 5.3). Red lines = coal fire cracks with a maximum width of 1 m, red dotted area = strongly collapsed bedrock with a week coal fire activity, red dashed area = strongly collapsed zone with intensive coal fire activity, green numbers = ETM pixel brightness temperature [K], blue crosses = location of ground temperature measurements, blue numbers = ground brightness temperature [K] measured in a time window of about one hour around the satellite overpass.

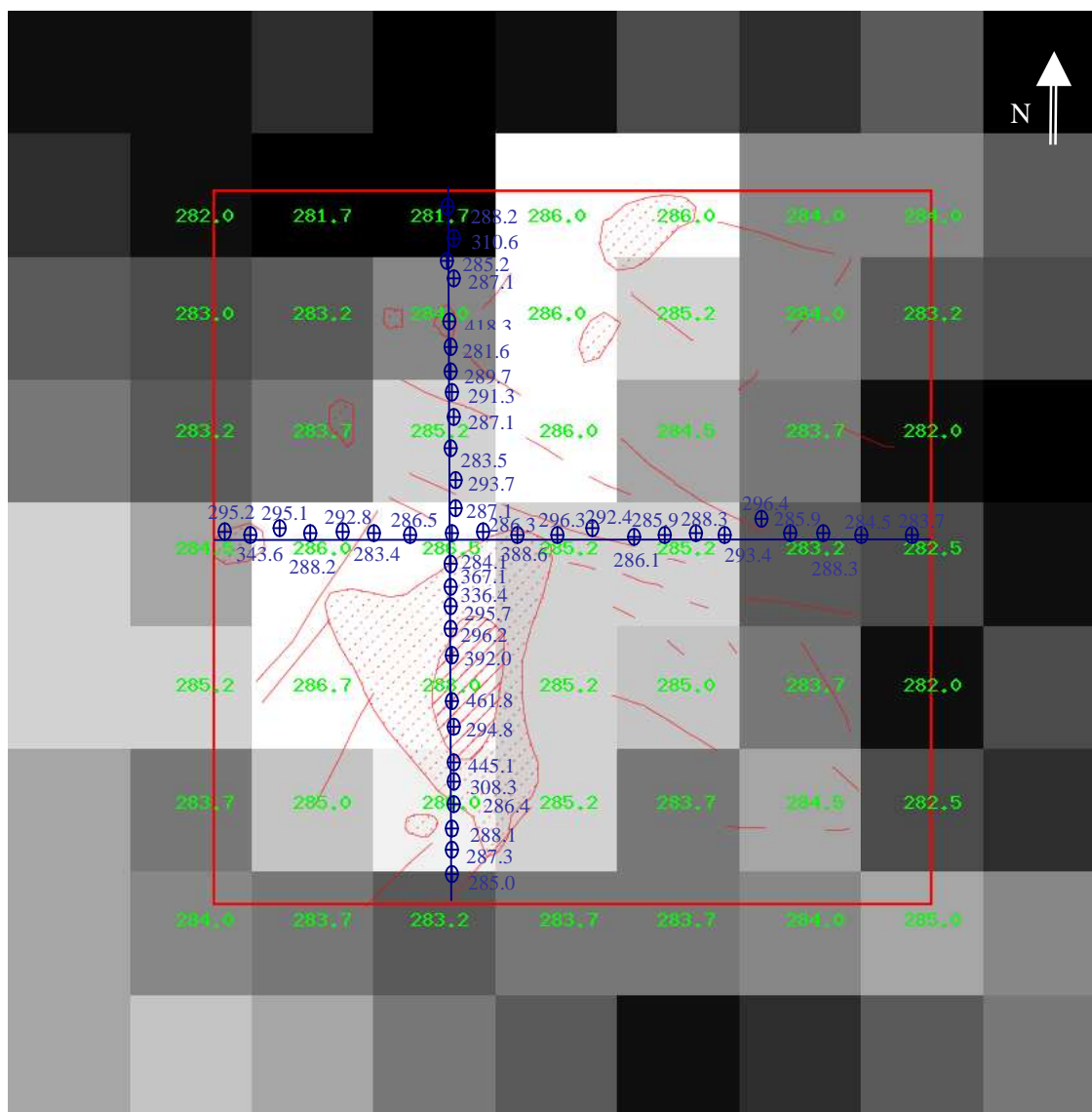


Figure 9-2: ETM channel 6 (night-time, 28.09.02) brightness temperatures, superimposed on a detailed surface map of the sub-surface coal fire 7 of the Wuda coalfield. The field mapping was performed during the first field campaign in September 2002 (details see chapter 5, section 5.3). Red lines = coal fire cracks with a maximum width of 1 m, red dotted area = strongly collapsed bedrock with a week coal fire activity, red dashed area = strongly collapsed zone with intensive coal fire activity, green numbers = ETM pixel brightness temperature [K], blue crosses = location of ground temperature measurements, blue numbers = ground brightness temperature [K] measured in a time window of about one hour around the satellite overpass.

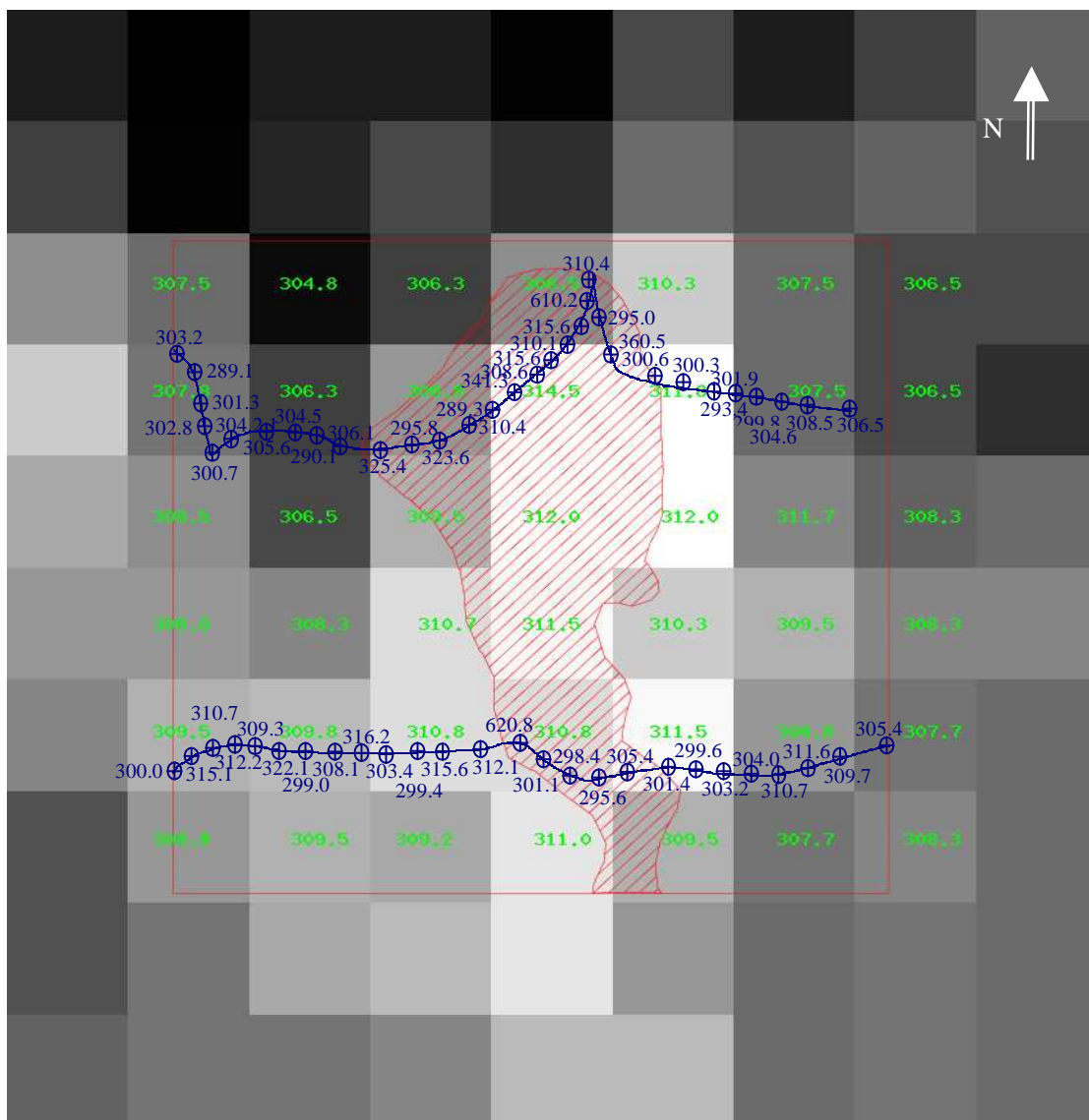


Figure 9-3: ETM channel 6 brightness temperatures (daytime, 21.09.02), superimposed on a detailed surface map of the near-surface coal fire 8 of the Wuda coalfield. The field mapping was performed during the first field campaign in September 2002 (details see chapter 5, section 5.3). Red dashed area = zone with CFSA, green numbers = ETM pixel brightness temperature [K], blue crosses = location of ground temperature measurements, blue numbers = ground brightness temperature [K] measured in a time window of about one hour around the satellite overpass.

closely with measured, background temperatures along the two profiles, indicating that the ETM thermal data are well calibrated.

The night-time ETM channel 6 data can be clearly correlated with sub-surface coal fire 7 (figure 9-2). The ETM data and the field map have a geometrical offset of about half an image pixel, which is probably the outcome of a combination of the GPS error and a slight image misregistration. Nine image pixels within the CFSA show high pixel values, but the maximum temperature rise is, at approximately 4 K, rather small. The maximum on-ground temperature, measured during the satellite overpass, is at 462 K, significantly higher than the pixel-integrated ETM temperatures (T max. 288 K), indicating that coal fire related hot spots are locally very limited. It is important to note here that the temperature rise is relatively similar for all anomaly pixels, although the strongly collapsed fire zone in the southern part of the investigated coal fire area definitely showed the highest surface temperatures. This is most probably due to background temperature variations, which are large, averaging approx. 1.5 K, when compared with the relatively low, coal fire induced, ETM brightness temperature rise. Consequently, the ETM night-time data cannot be used to analyse differences in the surface temperature pattern of this sub-surface coal fire. In addition, it is important to note that the coal fire related cracks in the south eastern and north western part of the investigated fire zone do not lead to higher pixel values. These cracks are too locally limited to produce a significant signal. Therefore, the ETM night-time data can only be used to locate major CFSA in the investigated sub-surface coal fire.

The ETM daytime data for the near-surface coal fire 8 show slightly higher pixel values in the northern part of the CFSA (figure 9-3). For at least one anomaly pixel the brightness temperature difference between fire and background pixels is large, at approximately 6 K. Assuming that the geometric offset is about 50 m, this significantly hotter image pixel can be related to exceptionally hot, near-surface CFSA at the northern edge of the investigated area. Nevertheless, the temperature variations of the neighbouring background pixels are large, with an average of 3 K. The maximum temperature observed along the northern profile of the CFSA is at 610 K significantly higher than the corresponding, pixel-integrated ETM temperature (max. 315 K), which once again outlines the very limited size of the coal fire related, surface hot spots. Background temperatures, measured along the northern profile of the near-surface coal fire 8 during daytime, are lower than corresponding pixel brightness temperatures, while the background temperatures measured along southern profile approximately match the corresponding pixel brightness temperatures (figure 9-3). The northern temperature profile was measured about thirty minutes prior to the southern profile, which could explain the observed temperature differences, if we assume a similar strength of sun heating as was present during the intraday measurements referred to in chapter 5 (figure 5-7).

In contrast to the daytime observation, the near-surface coal fire 8 can easily be detected on ETM night-time data (figure 9-4), and the CFSA in the northern and southern part of the anomaly zone can be clearly located. Nevertheless, the CFSA in the central part of the anomaly zone are too small to generate a clear signal, and as with the sub-surface coal fire, only major anomaly zones can be outlined. The maximum brightness temperature rise, at approximately 6 K, is relatively similar to the brightness temperature rise recorded during daytime observations, yet the surface coal fire and temperature variations of nearby image pixels are, at approx. 1.5 K, rather high.

9.1.3 Conclusions

Similar to the results of the regional study in chapter 8, this study outlines, once again, the low potential of the ETM summer data to quantify coal fires. The investigated CFSA of a sub-surface coal fire could not be delineated, and only exceptionally hot CFSA of the investigated near-surface coal fire produced detectable signals in daytime data.

However, this study has demonstrated, in the case of both the near-surface and sub-surface coal fires under investigation, that major CFSA can be clearly located on geometrically corrected, ETM night-time data. This result is encouraging and indicates that at least ETM night-time data can be used for detailed, satellite-based, coal fire studies. However, weak CFSA of the investigated near-surface and sub-surface coal fires could not be detected, and thus the total extend of the CFSA cannot be fully outlined on ETM night-time data. Additionally, it is to be noted that due to low, coal fire related, pixel-temperature rises, in combination with significant background variations, ETM night-time data cannot be used to analyse detailed temperature patterns of CFSA.

9.2 Analysis of multi-temporal BIRD and ETM night-time data

In this section CFRE and / or fire temperature and sizes, computed from two ETM and BIRD night-time data takes, are directly compared to each other in order to analyse the potential of thermal satellite data to register movement and activity changes in specified coal fire zones. The ETM channel 6 has the highest spatial resolution of all operationally available, thermal satellite systems and was therefore chosen for this study. BIRD data has in fact a significantly lower spatial resolution than ETM data. Yet, as both the theoretical evaluations in chapter 6 and the case study in chapter 8 have demonstrated, BIRD MIR channel background radiance variations are significantly lower than those of the ETM TIR channel. So in order to study the effect of the low MIR background radiance variations for a multi-temporal coal fire study, a temporal series of BIRD derived data was additionally analysed.

9.2.1 *Methods*

The data under analysis included ETM night-time acquisitions from 28th September 2002 and 25th September 2001 over the Wuda coalfield and BIRD night-time images of the Ruqigou and Gulaben coalfields on 16th January and the 27th September 2003. Night-time data was chosen in contrast to daytime data, because both ETM and BIRD night-time data have proven to have a significantly higher potential to detect and quantify CFSA (description in chapter 8, sections 8.1, 8.2 and chapter 9, section 9.1).

Field observations coinciding with satellite overpasses were only performed for the September 2002 ETM Wuda acquisition. Consequently, the multi-temporal analysis of both ETM and BIRD data cannot be directly linked to synchronous field observations. Nevertheless, the Wuda coal fires were frequently monitored during recent years by the Wuda Mining Bureau, and indications of shifts and activity changes of CFSA were available from Y. Jia, the chief engineer of the Wuda coal fire-fighting team. Since only a very limited number of hot spots could be detected on the BIRD night-time data over Wuda (see chapter 8, figure 8-4), the multi-temporal BIRD study focused on the Ruqigou and Gulaben coalfields, where several CFSA could be detected. Detailed coal fire observations from the local fire fighting teams of the Ruqigou and Gulaben coalfields were unavailable for this study.

The CFRE and / or fire temperatures and sizes were derived via the bi-spectral or TIR method, according to a similar method to that used for the ETM and BIRD data processing, described in chapter 8, sections 8.1 and 8.2. The data sets used in this study, i.e., ETM data from September 2002 and the BIRD data from January 2003 (figures 9-5 and 9-6), are identical to the data sets used in the regional study in chapter 8, sections 8.1 and 8.2 (figures 8-5 and 8-2). The ETM September 2001 and BIRD September 2003 data, however, were added, and processed for this study.

Although the aim of the study is the analysis of temporal shifts and activity changes within particular fire zones, only one CFRE and / or one coal fire temperature and size estimation is given for entire fire clusters in a particular fire zone. This is in line with the study of Wooster et. al. (2003, description in chapter 3, section 3.3.1) indicating that CFRE retrievals of entire fire cluster are significantly more stable than CFRE retrievals of one pixel. As with the regional study described in chapter 8, different CFRE estimations were performed for three values of the TIR background signal: mean background radiance, mean background value minus one standard derivation and mean background value plus one standard derivation (tables 9-1 and 9-2, for details see chapter 8, section 8.1.1).

9.2.2 *Interpretations and conclusions of the multi-temporal ETM analysis*

The ETM channel 6 data, presented in figure 9-5, clearly indicate that background radiance variations in the Wuda area were significantly lower during the acquisition of the ETM 2001 data than during the acquisition of the ETM 2002 data. The red arrow in figure 9-5 points towards a small calcareous mountain ridge that indicates the different topography-induced, radiance variations in both data sets. An additional indication for the differing background variations is the error range given for the CFRE retrievals in table 9-1. The 2001 CFRE retrievals vary slightly, due to low background variations, but only by approx. +/- 20 % on average, while the 2002 retrievals are significantly less stable, with an average estimated uncertainty of approx. +/- 35 %.

This difference in background radiance variation is surprising, because both data sets were acquired during similar seasons. The difference could be explained by different, specific weather conditions. Due to these considerable differences in background radiance variations, the coal fires of the Wuda coalfield can be more easily detected on the ETM 2001 data than on the ETM 2002 data (figure 9-5).

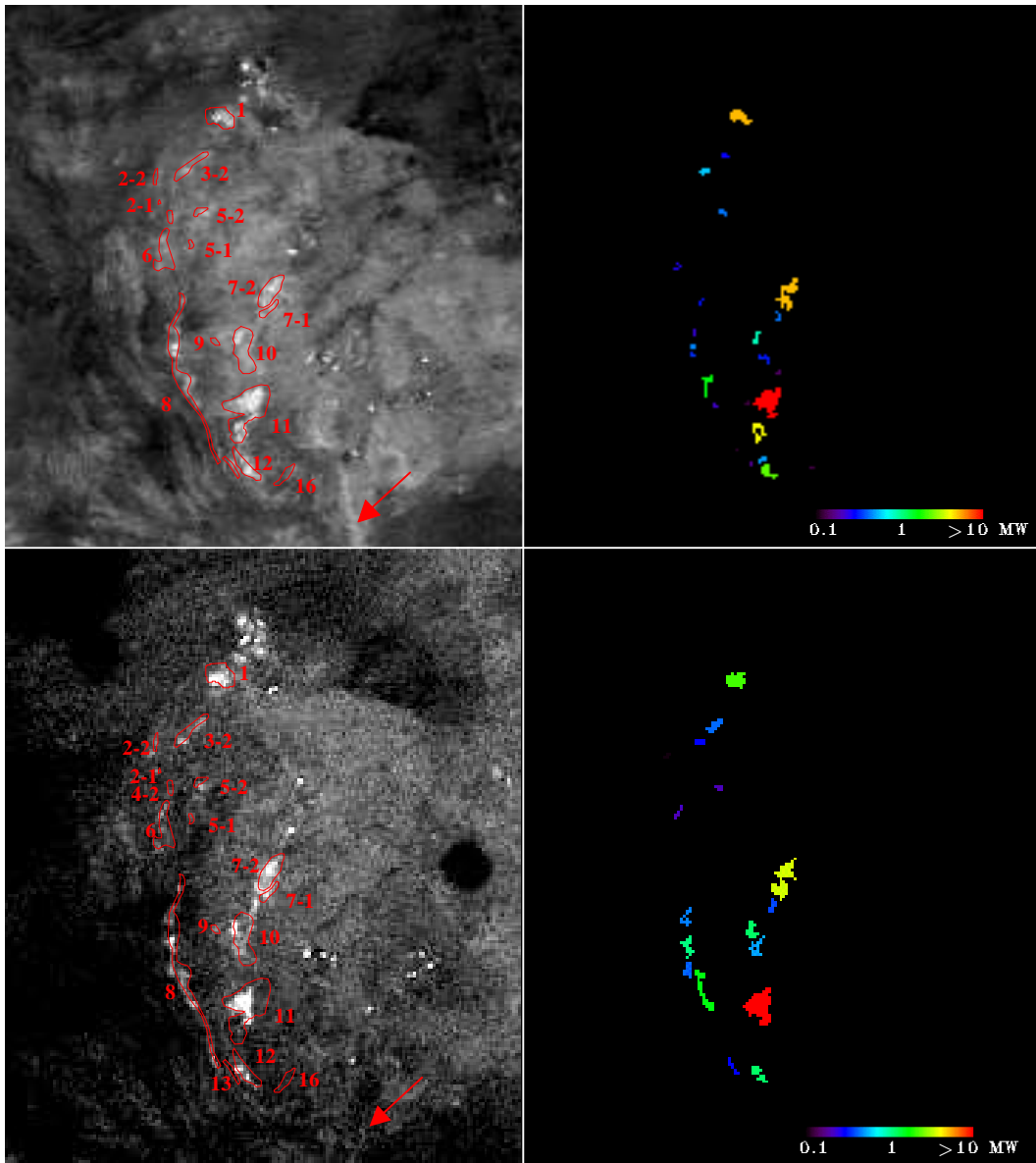


Figure 9-5: ETM night-time TIR channels of the Wuda coalfield with corresponding CFRE images. The CFRE images were computed via the TIR method. The red outlines mark CFSA mapped during the field campaign in September 2002. The red arrow points towards a mountain ridge indicating that the topography induced background temperature variations are significant lower in the 2001 data. Upper left) ETM TIR channel 28.09.02 (night-time); upper right) CFRE image 28.09.02 (night-time); lower left) ETM TIR channel 25.09.01 (night-time); lower right) CFRE image 25.09.01 (night-time).

Figure 9-5 clearly indicates that due to the different background radiance variations, it is difficult to observe detailed, local, temporal shifts in coal fires 3-2, 7, 10 and 8.⁹⁻²⁾ CFRE computed for these coal fires, from both data sets, is relatively constant (see table 9-1), although a significantly larger, fire-related pixel area can be visually detected in the 2001 ETM data (figure 9-5). According to Jia (2003, pers. communication) no significant changes of coal fire activity in the 3-2, 7, 10 and 8 coal fires were

⁹⁻²⁾ The field observations in September 2002 and September 2003 indicate, that CFSA can shift significantly within one year. Measured annual shifts exceeded more than 100 m at some locations.

observed, from September 2001 to September 2002. This indicates that the calculated CFRE accurately reflects the relatively stable coal fire situation. The anomaly pixels that were additionally detected on the 2001 data seem to have rather low CFRE, and thus the radiative energy contribution of these pixels to the total radiative energy budget of the entire coal fire zone is rather small.

| coal fire Wuda | TIR background | energy release [MW] | |
|----------------|----------------|---------------------------|---------------------------|
| | | ETM night-time 25.09.2001 | ETM night-time 28.09.2002 |
| 1 | mean | 1.7 | 3.9 |
| | mean + SD | 1.2 | 1.9 |
| | mean - SD | 2.3 | 6.4 |
| 3-2 | mean | 0.7 | 0.8 |
| | mean + SD | 0.5 | 0.5 |
| | mean - SD | 0.8 | 1.0 |
| 5-2 | mean | 0.2 | 0.4 |
| | mean + SD | 0.2 | 0.3 |
| | mean - SD | 0.2 | 0.5 |
| 6 | mean | 0.2 | 0.4 |
| | mean + SD | 0.2 | 0.3 |
| | mean - SD | 0.3 | 0.5 |
| 7-1+7-2 | mean | 3.2 | 4.2 |
| | mean + SD | 2.4 | 2.6 |
| | mean - SD | 3.9 | 6.0 |
| 8 | mean | 3.1 | 2.7 |
| | mean + SD | 2.1 | 2.0 |
| | mean - SD | 4.1 | 3.7 |
| 10 | mean | 1.5 | 1.2 |
| | mean + SD | 1.1 | 0.8 |
| | mean - SD | 1.9 | 1.9 |
| 11 | mean | 8.2 | 17.2 |
| | mean + SD | 6.7 | 11.5 |
| | mean - SD | 9.7 | 23.9 |
| 12 | mean | 1.0 | 2.4 |
| | mean + SD | 0.8 | 1.5 |
| | mean - SD | 0.6 | 3.1 |
| 13 | mean | 0.1 | 0.2 |
| | mean + SD | 0.1 | 0.1 |
| | mean - SD | 0.2 | 0.2 |
| 16 | mean | - | 0.1 |
| | mean + SD | - | 0.1 |
| | mean - SD | - | 0.2 |
| | • mean | 19.9 | 33.5 |
| | • mean - SD | 15.3 | 21.6 |
| | • mean+ SD | 24.0 | 47.4 |

Table 9-1: Coal fire related, surface energy releases (CFSA) derived from two ETM channel 6 night-time data sets at different temporal settings. The term 'mean' refers to CFRE retrievals computed using the mean background radiances of neighbouring image pixels, the term 'mean + SD' refers to CFRE retrievals calculated via the mean background radiances plus one standard derivation and the term 'mean - SD' refers to CFRE retrievals calculated via the mean background radiances minus one standard derivation. In the case where a mapped, CFSA includes more than one detected fire cluster, a summative value is provided. A dash indicates that no CFSA could be detected within the corresponding fire zone.

In contrast to the coal fires 3-2, 7, 10 and 8 the number of the detected fire pixels from both data sets for coal fire zones 13 and 16 is rather small. CFRE retrievals, computed from small fire clusters are, due to background variations, very undependable (Wooster, 2003), and are thus also unreliable for any direct comparison. The coal fires 5-2 and 6 show slightly more anomaly pixels than coal fire zones 13 and 16 in both data sets. According to Jia (2003, pers. communication) the coal fire activity in fire

number 6 remained relatively constant from September 2001 to 2002, while coal fire 5-2 was almost entirely covered by a clay layer during this period, and should thus reveal significantly weaker CFSA in September 2002. As a consequence the calculated CFRE rise in coal fires 5-2 and 6 (see table 9-1) does not reflect the real coal fire situation or the fire fighting activity at fire 6 was not successful at all.

Despite the different background radiance variations in both data sets a new coal fire zone in the southern part of the coal fire number 11 can be clearly detected on the ETM 2002 data (figure 9-5). Jia (2003, pers. communication) confirmed the development of this new zone. The CFRE release rise from September 2001 to September 2002 is very high, at approximately 9 MW, and indicates a significant change of the fire activity in coal fire 11.

The analysis of the two ETM thermal data sets has demonstrated that ETM night-time data can be used to register movement in relatively large, CFSA. Although the analysed data sets revealed significantly different background radiance variations, a major new CFSA could be clearly located in the Wuda coalfield. Nevertheless, the background radiance variations of the two data sets were too dissimilar to allow for a visual analysis of detailed spatial shifts, or for the observation of an overall trend in CFSA found in the Wuda coalfield. ETM night-time data sets, acquired during winter, could reveal more stable background conditions than the two investigated ETM summer night-time data sets, and might thus allow a more detailed mapping of movements and shifts of coal fire zones.

The CFRE computed for relatively large CFSA in the Wuda coalfield clearly reflects very well the activity of the CFSA, despite the different background radiance variations. Thus, CFRE computed for large fire clusters is reliable, even under different night-time TIR background conditions. However, the CFRE, computed for small fire clusters, was not representative for the observed CFSA, and has therefore to be regarded as unreliable for satellite based, multi-temporal coal fire analysis.

9.2.3 Interpretation and conclusion regarding a multi-temporal BIRD data analysis

The two BIRD data sets were acquired with an offset of about 9 months, and thus reflect distinctive seasonal factors. Nevertheless, the background temperature variations in the summer BIRD MIR night-time data sets are only slightly higher than the background variations found in the winter BIRD MIR night-time data in the direct vicinity of the coal fires, and in fact some CFSA can be clearly outlined in both data sets (figure 9-6).

Coal fire clusters of coal fires 1, 3, 5, 12 and 13 are relatively small and bi-spectral retrievals derived from the two BIRD data sets are either rather low or possibly unstable (table 9-2). Consequently, these coal fires were excluded from the multi-temporal comparison.

The bi-spectral retrievals, computed from the January 2003 data for fire zone 2 of the Ruqigou coalfield, were found to be unstable (table 9-2). However, in addition to the increased coal fire related pixel values in the southern part, summer 2003 data show significantly higher MIR radiances in the northern part of coal fire 2 (figure 9-6). This suggests a hotter or larger CFSA in the northern part of the coal fire zone 2.

The bi-spectral retrievals for coal fire number 4, computed from both data sets, are stable and indicate a significant change in fire activity between January 2003 and September 2003 (table 9-2). However, the position of the major CFSA of coal fire number 4 remained, according to the visually detected fire pixels, relatively constant (figure 9-6).

CFRE estimates for coal fire number 6 are stable and relatively constant. In general, the temperature of the CFSA seems to be slightly higher in September 2003 than was the case in January 2003. However, the high level of uncertainty in bi-spectral retrievals for low temperatures and small fire sizes (description in chapter 3, section 3.3.1) allows only a rough estimate. The detected coal fire pixels in both data sets (figure 9-6) indicate stronger CFSA in the eastern part of coal fire 6.

The relatively stable CFRE estimates of coal fire 9 (table 9-2) suggest weaker and / or smaller CFSA in September 2003, compared to January of the same year. According to the location of the visually detected coal fire pixels the location of major CFSA seems to have slightly shifted.

Both the location of the detected coal fire pixels and the computed energy releases indicate a relatively constant surface fire activity for coal fire 14, in both January and September 2003 (figure 9-6, table 9-2). The CFRE estimates for coal fire 15 indicate a slight increase in surface coal fire activities between January and September 2003. Slightly more coal fire related, anomalous pixel values can be observed in the southern part of the fire zone in September 2003 data, compared to January 2003 data. This indicates an enlargement of the CFSA in this zone.

According to BIRD observations, the CFSA of coal fire 16 are relatively constant. Both the bi-spectral retrievals and the location of the detected coal fire pixels indicate relatively stable CFSA. BIRD observations also show CFRE retrievals from coal fire 18 to be approx. constant.

Although BIRD thermal data has a significantly lower spatial resolution than ETM thermal data, clear indications of shifts or activity changes could be observed for eight coal fire zones of the Ruqigou and Gulaben coalfields. This was achieved either by interpreting bi-spectral retrievals, or the location of detected coal fire clusters. Field observations, coinciding with the satellite overpass, could not be carried out for the two investigated BIRD acquisitions, although the observed shifts and activity

changes are clearly identifiable and probably do reflect real changes of corresponding CFSA. Thus the low night-time background radiance variations of the MIR channel show BIRD data sets to be very effective for the observation of major movements in CFSA.

However, as with the ETM data analysis, only relatively large fire clusters could be meaningfully quantified. The majority of observed coal fires in the Wuda coalfield did not produce increased pixel values in the BIRD January 2003 night-time data (see figure 8-4) and thus a multi-temporal, BIRD data based, coal fire study is definitely restricted to fire zones with relatively hot and / or large, CFSA anomalies.

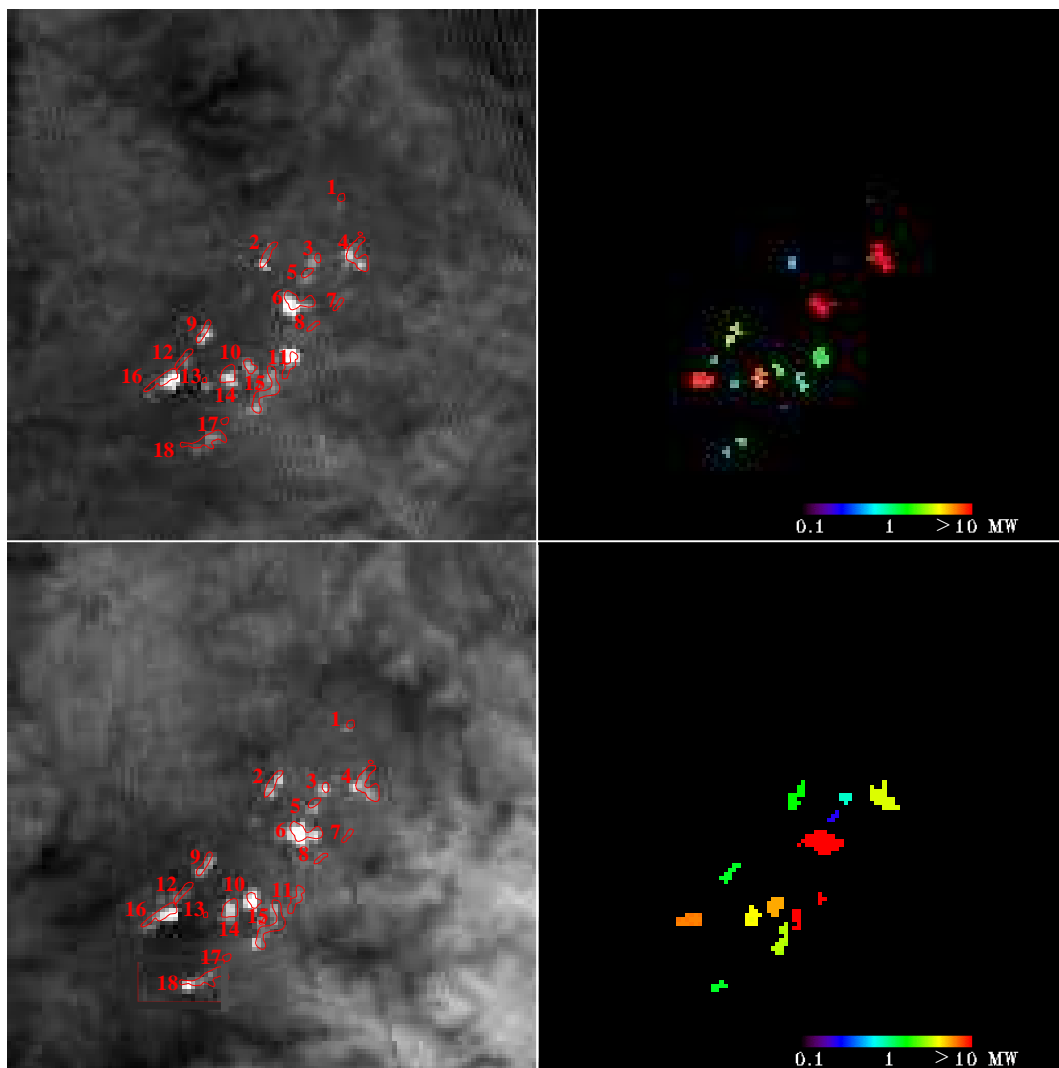


Figure 9-6: BIRD night-time MIR channels of the Ruqigou coalfield with corresponding CFRE images. The CFRE images were computed via the bi-spectral technique using BIRD MIR and TIR channel as input data. The red outlines mark CFSA, mapped during the field campaign in September 2002. Upper left) BIRD MIR channel 16.01.03 (night-time); upper right) CFRE images 16.01.03 (night-time); lower left) BIRD MIR channel 27.09.03 (night-time); lower right) CFRE images 27.09.03 (night-time).

| coal fire Ruqigou | TIR background | BIRD night-time 16.01.03 | | | BIRD night-time 27.09.03 | | |
|----------------------|-------------------|--------------------------|----------------------------|------------------------|--------------------------|----------------------------|------------------------|
| | | eq. T [K] | eq. A [m ²] | energy release [MW] | eq. T [K] | eq. A [m ²] | energy release [MW] |
| 1 | mean | - | - | - | 690 | 22 | 0.1 |
| | mean + SD | - | - | - | - | - | - |
| | mean - SD | 398 | 4.6 | 0.1 | 440 | 60 | 0.1 |
| 2 | mean | (443) | (256) | (0.5) | 420 | 1014 | 1.4 |
| | mean + SD | - | - | - | 714 | 20.0 | 0.3 |
| | mean - SD | 392 | 905 | 1.0 | 377 | 3330 | 2.6 |
| 3 | mean | (344) | (548) | (0.3) | 405 | 642 | 0.8 |
| | mean + SD | (478) | (17.3) | (0.1) | 454 | 213 | 0.4 |
| | mean - SD | 320 | 1727 | 0.5 | 379 | 1326 | 1.0 |
| 4 | mean | 306 | 35318 | 7.3 | 375 | 3719 | 2.8 |
| | mean + SD | 323 | 14165 | 4.6 | 468 | 426 | 1.0 |
| | mean - SD | 298 | 67757 | 10.4 | 343 | 11133 | 4.7 |
| 5 | mean | - | - | - | 129 | 446 | 0.2 |
| | mean + SD | - | - | - | - | - | - |
| | mean - SD | - | - | - | 540 | 389 | 0.5 |
| 6 | mean | 348 | 14712 | 8.0 | 413 | 8909 | 11.5 |
| | mean + SD | 371 | 6665 | 5.2 | 435 | 5262 | 8.8 |
| | mean - SD | 335 | 25986 | 10.7 | 397 | 13585 | 14.3 |
| 8 | mean | - | - | - | - | - | - |
| | mean + SD | - | - | - | - | - | - |
| | mean - SD | - | - | - | - | - | - |
| 9 | mean | 362 | 2983 | 2.1 | 395 | 1200 | 1.2 |
| | mean + SD | 383 | 1518 | 1.4 | (447) | (363) | (0.7) |
| | mean - SD | 348 | 4882 | 2.7 | 370 | 2545 | 1.8 |
| 10 | mean | 324 | 5173 | 1.7 | 380 | 5029 | 4.1 |
| | mean + SD | (352) | (1817) | (1.0) | 430 | 1412 | 2.2 |
| | mean - SD | 309 | 10930 | 2.5 | 354 | 11393 | 6.1 |
| 11 | mean | 600 | 216 | 1.5 | - | - | - |
| | mean + SD | (841) | (32) | (0.9) | - | - | - |
| | mean - SD | 529 | 526 | 2.2 | 500 | 30 | 0.1 |
| 12 | mean | 325 | 1514 | 0.5 | (427) | (327) | (0.1) |
| | mean + SD | 334 | 862 | 0.4 | - | - | - |
| | mean - SD | 320 | 2247 | 0.7 | 396 | 1319 | 0.1 |
| 13 | mean | 347 | 921 | 0.5 | - | - | - |
| | mean + SD | (390) | (224) | (0.2) | - | - | - |
| | mean - SD | 330 | 1978 | 0.8 | - | - | - |
| 14 | mean | 317 | 17568 | 4.9 | 356 | 5607 | 3.1 |
| | mean + SD | (332) | (8626) | (3.4) | 370 | 3181 | 2.2 |
| | mean - SD | 306 | 30366 | 6.6 | 346 | 8646 | 4.0 |
| 15 | mean | 351 / 336 | 1749 / 818 | 1.4 | 349 / - | 5095 / - | 2.4 / - |
| | mean + SD | 405 / 437 | 326 / 43 | 0.5 | 446 / - | 333 / - | 0.6 |
| | mean - SD | 332 / 313 | 4109 / 2599 | 2.2 | 323 / 424 | 17148 / 401 | 5.1 |
| 16 | mean | 368 | 7854 | 5.9 | 376 / 436 | 6860 / 29 | 4.7 |
| | mean + SD | 389 | 4113 | 4.7 | 369 / - | 2611 / - | 2.7 |
| | mean - SD | 354 | 12643 | 7.8 | 353 / 394 | 1267 / 1031 | 6.8 |
| 18 | mean | 313 / 316 | 4930 / 1790 | 1.8 | 394 | 1246 | 1.2 |
| | mean + SD | 310 / - | 387 / - | 0.3 | 416 | 638 | 0.9 |
| | mean - SD | 295 / 286 | 15753 / 6191 | 3.5 | 381 | 1973 | 1.7 |
| | | 299 / 285 | | | | | |
| | • mean | | | 36.4 | | | 33.6 |
| | • mean + SD | | | 22.7 | | | 19.8 |
| | • mean - SD | | | 51.7 | | | 48.8 |

Table 9-2: Coal fire related, surface radiative energy releases (CFRE), equivalent fire temperatures and equivalent fire sizes, derived from two BIRD data sets (MIR + TIR channels) at different temporal settings. Mean energy values are indicated as ‘mean’, minimum values as ‘mean + SD’ and maximum values as ‘mean - SD’. In the case where a mapped, CFSA includes more than one detected fire cluster, a summative value is provided. A dash indicates that no CFSA could be detected within the corresponding fire zone. Brackets indicate unstable bi-spectral estimates.

9.3 General conclusions

The comparison of satellite data with detailed field observations, made in conjunction with satellite overpasses, has outlined the fact that BIRD and ETM data can be used to locate major CFSA with a degree of accuracy of somewhat less than 100 m. Using these data it was possible to clearly locate a sub-surface coal fire area below a highly collapsed bedrock and a major CFSA of a surface coal fires with temperatures exceeding locally 500 K. This study contains the first systematic comparison between, on the one hand, detailed field measurements of coal fire temperatures, and on the other hand, synchronous satellite data. The field temperature measurements were performed along two profiles, which however, are not necessarily representative for the entire satellite corresponding ground segment. An important suggestion for any future field campaign, targeted at validating satellite coal fire temperature retrievals, is that such a study should be performed along a dense grid.

The results of this first satellite-based, multi-temporal coal fire study indicate that a satellite-based, coal fire monitoring system, is capable of detecting major shifts or activity changes in relatively large and hot CFSA. High background-radiance variations in the ETM TIR channel make a direct comparison of visually-detected coal fire pixels, derived from two different ETM scenes, rather difficult. However, CFRE retrieved from relatively large ETM pixel clusters seems to be reliable, even under varying night-time, background situations, and is therefore suitable for multi-temporal, coal fire monitoring. Significant lower background radiance variations in the BIRD MIR channel allow the observation of major shifts of CFSA, even though the BIRD sensor has a significantly lower spatial resolution compared to the ETM sensor. A newly developed CFSA, with a total area of more than 50000 m²⁹⁻³⁾ could be clearly located on multi-temporal ETM night-time data. In addition, CFRE retrieved from four major CFSA in the Wuda coalfield via multi-temporal ETM night-time data (total area extend > 30000 m²) clearly indicates stable coal fire conditions. However, a satellite-based coal fire monitoring system cannot replace field observations in the case of small and relatively cool, CFSA.

The satellite observations in this multi-temporal case study could only be partially verified by field observations, and the results of the case study can therefore only be regarded as primary results which form a basis for future studies. In order to verify these primary results it is necessary to make further detailed field observations at a variety of temporal settings, and in conjunction with satellite overpasses. Future studies should also include an effective and systematic long-term field monitoring campaign. A major focus of this future field campaign has the observations of short-term coal fire activity changes, including observations at different times of the day (i.e. effect of solar heating on CFSA) and different meteorological conditions (i.e. effect of wind and rain on CFSA). The importance

⁹⁻³⁾ The total area refers to the area of the detected coal fire cluster.

of this focus lies in the need to ascertain whether or not the ‘snapshots’ available from polar orbiting satellite observations can form a basis for general conclusions regarding coal fire activity.

The major limitation of the ETM system for coal fire monitoring is the missing MIR channel, while the major limitation of the BIRD system is its low spatial resolution. A future sensor system, combining both the high resolution of the ETM TIR channel and the bi-spectral capability of the BIRD system, could be a valuable tool for a detailed, satellite data based, coal fire monitoring system.

COAL FIRE QUANTIFICATION ALGORITHM

10 AN ASTER AND ETM SATELLITE DATA BASED, AUTOMATED, COAL FIRE QUANTIFICATION (CFQ) ALGORITHM

In this chapter a satellite data based, automated, coal fire quantification (CFQ) algorithm is presented and discussed. The algorithm is restricted to ASTER and ETM data and is not designed to work on BIRD data. The reason for this is, as discussed in the previous chapters, there are already established fire quantification approaches for BIRD data (bi-spectral technique; Dozier, 1981). An example of this can be found in the BIRD hotspot detection and quantification algorithm, recently presented by Zhukov and Oertel (2001).

10.1 The aim of the CFQ algorithm

The ASTER / ETM CFQ algorithm is designed to compute coal fire, radiative energy releases (CFRE), from potential coal fire pixels of respective satellite image data. The coal fire quantification is performed via the TIR method (description in chapter 7), using ETM band 6 or ASTER band 10 respectively. The CFQ algorithm does not include a coal fire detection element and may thus be seen as a post-processing step to an ASTER and ETM data based coal fire detection procedure.

Zhang (2004) recently presented the first non-interactive TIR satellite data based, coal fire detection algorithm. The coal fire detection is performed here via a statistical method, using a moving window technique to extract thermal anomalies in large areas. For each window a set of statistical tests is performed including, e.g., histogram-based, dynamic threshold tests to identify potential coal fire related thermal anomalies.

Based on the fact that coal fires often occur on, or in the vicinity of coal-bearing strata and coal surfaces like coal storage and coal waste piles, Kuenzer (personal communication, 2004) is developing an automated, coal fire area demarcation algorithm. The algorithm mainly aims at the automated extraction of coal surfaces from multi-spectral ETM and Aster daytime data, applying a knowledge-based test sequence and partial unmixing techniques to calibrated and atmospherically corrected data. The extracted coal surfaces are then buffered to define a zone in which the occurrence of coal fires is likely. These demarcated regions are further modified taking vegetation density and the occurrence of pyrometamorphic rocks into account. A first application of the statistically based thermal anomaly detection method, combined with coal fire area demarcation on ETM data from two previously non-studied areas, has demonstrated that coal fires can be reliably detected using this approach (Zhang et al., submitted).

10 An ASTER and ETM satellite data based, automated coal fire quantification algorithm

At the DLR, the algorithms of Zhang (2004) and Kuenzer (personal communication, 2004), and the presented CFQ algorithm are currently being combined into an automated, coal fire detection and quantification algorithm, suitable to detect and quantify coal fires in northern China on a routine basis.

10.2 CFQ algorithm description

10.2.1 Algorithm outline

The CFQ algorithm presented here mainly performs the different processing steps described in detail in chapter 8, sections 8.1.1 (ETM data processing) and 8.3.1 (ASTER data processing). The CFQ algorithm requires ASTER channel band 10 data or ETM channel band 6 data, and a coal fire mask (= binary file including detected coal fire pixels) as input. The output includes two different CFRE images as well as an ASCII file containing the computed CFRE values and a quality assessment.

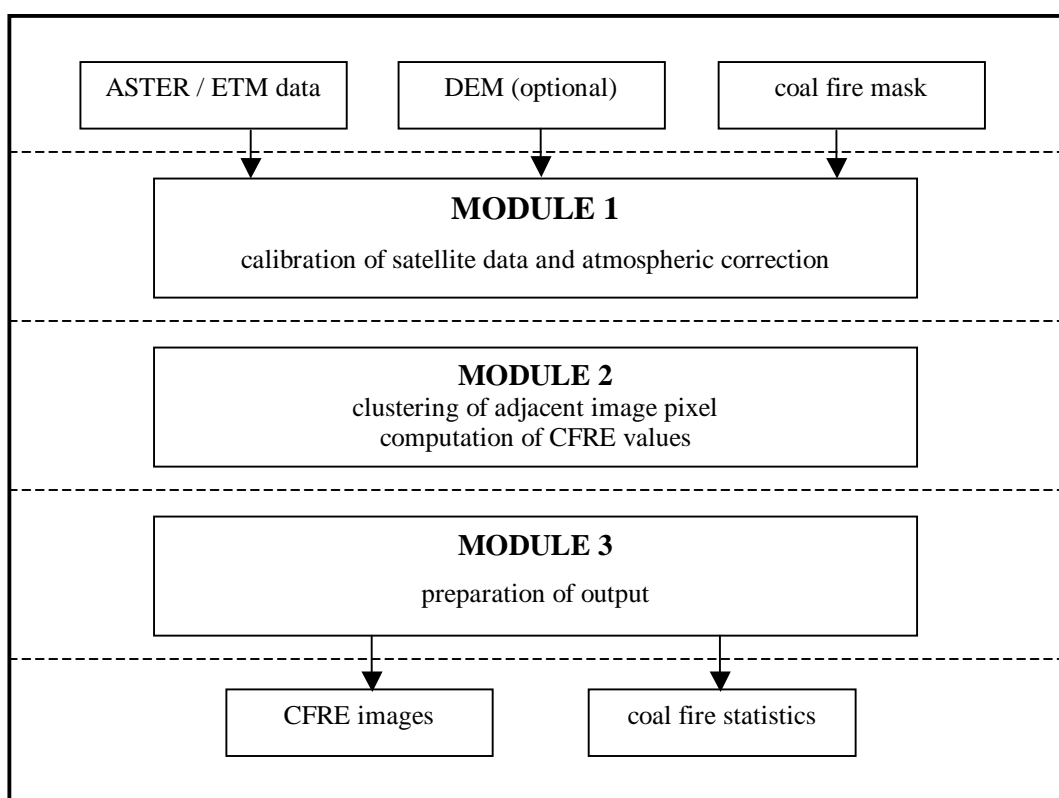


Figure 10-1: Outline of QFC algorithm.

In a first processing step the input data sets are calibrated and atmospherically corrected. The atmospheric correction is adapted to dry-desert climatic conditions, which are considered to be suitable for the semi-arid to arid regions in northern China. Following the results of the theoretical study (chapter 6) and the two case studies (chapters 8 and 9), neighbouring fire pixels are then grouped together to form continuous fire clusters, in order to minimise computation errors, induced by background signal variations. The TIR method (description in chapter 7) is applied to each individual coal fire cluster to calculate the respective CFRE. Prior to the preparation of the output data, a quality assessment is performed for each computed CFRE value.

10 An ASTER and ETM satellite data based, automated coal fire quantification algorithm

The ASTER / ETM CFQ algorithm can be logically divided into three main modules (figure 10-1). The first module performs the calibration and atmospheric correction of the ASTER and ETM data sets. The second module clusters adjacent coal fire pixels into coal fire clusters and computes respective CFRE for each coal fire cluster via the TIR method, while the last module creates the output CFRE images and the tabulated results including the computed CFRE values and a quality assessment.

10.2.2 Module 1: Calibration and atmospheric correction

This module includes the calibration and atmospheric correction of the ASTER and ETM data. The calibration of the ASTER and ETM TIR data is performed via equation 3-6 and the calibration parameters listed in tables 10-1 and 10-2. Different calibration parameters are applied for ASTER band 10, ETM channel 6, high-gain data and ETM channel 6 low-gain data. Due to the fact that a bias of $0.31 \text{ W / m}^2 \text{ sr } \mu\text{m}$ was found in the pre-launch calibration of the ETM band 6 data that was processed before the 20th December 2000, ETM data sets processed before this date are corrected for this bias. The configuration parameters are stored in a respective file and can be adapted by the user if required.

| Low Gain | | High Gain | |
|--|--|--|--|
| L_{\min} [W / m ² sr μm] | L_{\max} [W / m ² sr μm] | L_{\min} [W / m ² sr μm] | L_{\max} [W / m ² sr μm] |
| 0.0 | 17.04 | 3.2 | 12.65 |

Table 10-1: Radiances at the maximum and minimum digital number of the ETM TIR channel, used to transform ETM level 1b DN values to spectral radiances (*Landsat 7 Science Data Users Handbook: http://ftpwww.gsfc.nasa.gov/IAS/handbook/handbook_toc.html*)

| L_{\min} [W / m ² sr μm] | L_{\max} [W / m ² sr μm] |
|--|--|
| 0.0 | 32.7 |

Table 10-2: Radiances at the maximum and minimum digital number of the ASTER TIR channel, used to transform ETM level 1b DN values to spectral radiances (<http://asterweb.jpl.nasa.gov/>).

The atmospheric correction of the ASTER and ETM data was optimised to dry desert conditions. The atmospheric correction parameters are calculated via the MODTRAN code (Berk et al., 1989), as with the data processing described in chapter 8, sections 8.1.1 and 8.3.1. The atmospheric correction is performed via equation 3-7 and the atmospheric parameters are listed in tables 10-3 and 10-4. In cases where the user provides a digital elevation model (DEM), an atmospheric correction is performed for each image pixel in order to account to the changes in atmospheric thickness due to actual topographic

10 An ASTER and ETM satellite data based, automated coal fire quantification algorithm

elevation. If no DEM is available, all pixel values are corrected using atmospheric parameters corresponding to a user-defined, mean terrain elevation. The parameterised atmospheric constants are stored in external look-up tables, which can be modified by the user.

| high level [km] | Lpath [mW / m ² sr μm] | trans | Flux [mW / m ² μm] |
|-----------------|-----------------------------------|--------|-------------------------------|
| 0.0 | 2445.3 | 0.7080 | 6803.7 |
| 0.5 | 2159.1 | 0.7320 | 5932.5 |
| 1.0 | 1891.7 | 0.7557 | 5141.4 |
| 1.5 | 1640.8 | 0.7793 | 4423.7 |
| 2.0 | 1408.9 | 0.8028 | 3768.7 |
| 2.5 | 1201.3 | 0.8262 | 3176.3 |

Table 10-3: Path radiance (L_{path}), atmospheric ground-to-sensor transmittance (T) and downwelling flux of atmosphere (F) used for the atmospheric correction of the ETM channel 6.

| high level [km] | Lpath [mW / m ² sr μm] | trans | Flux [mW / m ² μm] |
|-----------------|-----------------------------------|--------|-------------------------------|
| 0.0 | 1267.2 | 0.7814 | 5817.4 |
| 0.5 | 1118.9 | 0.8079 | 5072.5 |
| 1.0 | 980.3 | 0.8341 | 4396.1 |
| 2.0 | 850.3 | 0.8602 | 3782.4 |
| 1.5 | 730.1 | 0.8861 | 3222.4 |
| 2.5 | 622.5 | 0.9119 | 2715.9 |

Table 10-4: Path radiance (L_{path}), atmospheric ground-to-sensor transmittance (T) and downwelling flux of atmosphere (F) used for the atmospheric correction of the ASTER channel 10.

10.2.3 Module 2: Clustering of adjacent coal fire pixels and computation of CFRE

In module 2 adjacent fire clusters are aggregated into continuous fire clusters. After the clustering, a two-dimensional distance map is calculated, which contains the distance to the nearest background pixel for each coal fire cluster. Each element in this distance map is assigned a distance corresponding to the number of pixels to be visited when travelling from the current fire cluster to the neighbouring background pixel. Based on this distance map, the ten closest neighbours to the fire cluster are selected in order to compute the mean background radiance, as well as the respective standard deviation of the background radiance. Based on the computed background radiances, CFRE values are computed in a next processing step for each coal fire cluster using equations 7-1 (ETM data) and 7-2 (ASTER data).

10.2.4 Module 3: Preparation of output

In this module a colour-coded CFRE image is created that includes the mean CFRE value for each coal fire cluster. Furthermore, a tabulated output file is generated containing the CFRE estimates and the quality measures for each cluster. This allows visual assessment of the results as well as the use in further processing steps.

10.3 Quality assessment

The accuracy of the TIR-derived CFRE estimate strongly depends on the accuracy of the estimated background signal, as evaluated in chapter 7. Therefore, the quality of the computed CFRE value is assessed by calculating CFRE estimates for three different values of the TIR background signal. This is done in a similar manner to the ETM and ASTER data analysis in chapter 8, sections 8.1.1 and 8.3.1:

- mean background value (corresponds to the mean CFRE)
- mean background value minus one standard deviation (corresponds to the maximum CFRE)
- mean background value plus one standard deviation (corresponds to the minimum CFRE)

This information can be used directly as a quality indicator for the derived, mean CFRE value. Substantial differences between minimum and maximum CFRE values suggest high background variations, and thus indicate unreliable mean CFRE estimates.

10.4 Description of required input for the CFQ algorithm, and its output products

10.4.1 Inputs to the CFQ algorithm

Satellite data

The CFQ algorithm has been developed especially for ASTER channel 10 and ETM channel 6 data. It has been implemented in such a way that it automatically handles both ETM channel 6 high-gain data and ETM channel 6 low-gain data. The ETM and ASTER data, being ingested into the algorithm, are sensor-calibrated and geometrically corrected level 1b data sets, with pixel values in digital numbers (DN).

Digital elevation model

A digital elevation model (DEM) can be optionally provided to the algorithm. The DEM has to have the same spatial resolution as the corresponding satellite data and must also cover a similar area. DEM pixel values have to be assigned in meters above sea level. In the case where no DEM is available, the user can specify a mean sea level height that can then be used as a reference height for the atmospheric correction.

Coal fire pixel mask

A coal fire pixel mask is mandatory for the CFQ algorithm. The mask must be derived from the ETM or ASTER satellite data, prior to running the quantification algorithm. This can be done either by using

10 An ASTER and ETM satellite data based, automated coal fire quantification algorithm

an automated, coal fire detection algorithm (e.g. Zhang, 2004), or by visually interpreting the thermal anomalies of the corresponding satellite scene. The coal fire mask has to be stored as a binary array, with coal fire values set to one (1) and no coal fire values set to zero (0).

10.4.2 CFQ algorithm output products

The output of the coal fire quantification algorithm consists of four data sets, described below:

Main output

The main output consists of two TIFF files containing a visualisation of the computed mean CFRE values. The first file includes colour-coded, mean CFRE values for each fire clusters, scaled logarithmically from 0.1 to 10 MW and 0.1 MW to 100 MW, respectively. The different scaling is performed, on the one hand to highlight energy variations of fire clusters with low corresponding CFRE values, and on the other, to avoid saturation of fire clusters with high corresponding CFRE values. An example of the main output from the CFQ algorithm is displayed in figure 10-2.

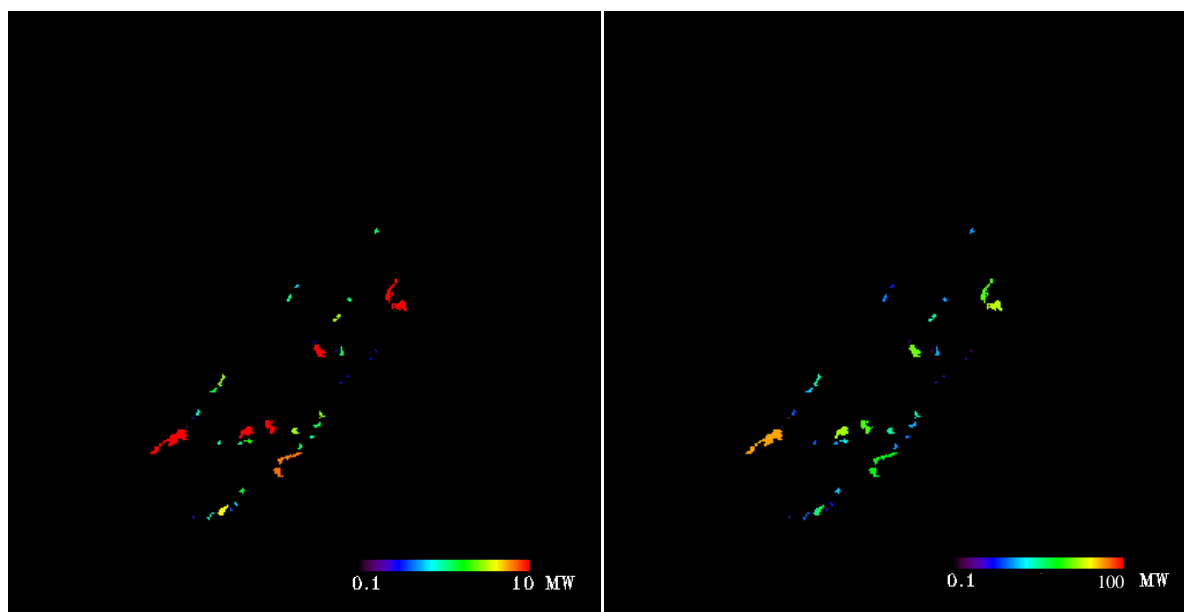


Figure 10-2: An example of the CFQ algorithm main output: CFRE images from the Ruqigou and Gulaben coalfields, derived from ETM night-time TIR data. The output includes two CFRE images representing mean, computed CFRE estimates for entire fire clusters, scaled logarithmically, left) from 0.1 to 10 MW and right) from 0.1 to 100 MW.

Tabulated output (ASCII file)

Beside the main output, an ASCII file is provided, which contains a fire identifier/cluster number (in the first column), the upper left x and y coordinates of each fire cluster (second and third column), the total size of the fire cluster (fourth column), the computed mean CFRE value of each fire cluster (fifth column), the computed maximum CFRE value (sixth column) and the computed minimum CFRE value (seventh column). Table 10-5 includes an example of the CFQ output ASCII file.

10 An ASTER and ETM satellite data based, automated coal fire quantification algorithm

| cluster number | UL x | UL y | cluster size | mean CFRE | max CFRE | min CFRE |
|----------------|------|------|--------------|-----------|------------|-----------|
| 1 | 238 | 141 | 25200 | 1.0003818 | 1.2221395 | 0.7880989 |
| 2 | 245 | 174 | 136800 | 7.7151241 | 10.9264536 | 4.9836359 |
| 3 | 186 | 178 | 14400 | 0.5775985 | 0.6897060 | 0.4684574 |
| 4 | 181 | 184 | 32400 | 0.8871909 | 1.3476485 | 0.4675472 |
| 5 | 22 | 186 | 21600 | 0.9915951 | 1.3235970 | 0.6804683 |
| ... | ... | ... | ... | ... | ... | ... |

Table 10-5: An example of the CFQ output ASCII file.

The upper left x and y coordinates refer to pixel positions and not to geographical coordinates. The cluster size is given in m^2 and refers to the area coverage of the detected coal fire cluster. Due to the fact that a coal fire pixel always contains both fire and background information, as described in chapter 5, the cluster size does not refer to the actual size of the coal fire surface anomaly. The mean, maximum and minimum CFRE values for each fire cluster are given in $MW / m^2 sr \mu m$. The computation of the mean, max and min CFRE is explained in section 10.3 (quality assessment).

10.5 Limitations and transferability of the CFQ algorithm

The atmospheric correction included in the CFQ algorithm is adapted to dry-desert atmospheric conditions. In the TIR spectral range, the ground-to-sensor signal is strongly influenced by atmospheric water vapour content. The dry desert model used here assumes a very low atmospheric water vapour content, limiting the application of the current CFQ algorithm to arid and semi-arid regions. The CFQ algorithm can however easily be adapted by the user to other atmospheric conditions, simply by replacing the respective look-up tables.

A major limitation of the CFQ algorithm that occurs as a result of the implemented TIR band based, coal fire quantification approach is, as described in chapter 7, that the TIR method cannot be applied to large and hot CFSA anomalies. ‘Hot’ in this case refers to average surface temperatures of more than 600 K. Nevertheless CFSA in the three coalfields are in average significantly cooler than 600 K, and similarly low, coal fire related, surface temperatures have been reported from other coalfields in northern China (see chapter 2, section 2.3). As this algorithm, however, was only tested in three coalfields yet, it will be subject of further work to verify the wider applicability of the CFQ algorithm for general quantification of coal fires in northern China.

An additional limitation of the TIR method is its high sensitivity to background temperature variations (description in chapter 7). The CFQ main output (CFRE images) should thus only be interpreted in combination with the quality assessment figures along with the tabulated output.

10 An ASTER and ETM satellite data based, automated coal fire quantification algorithm

Despite the limitations induced by the atmospheric correction and the TIR method, the accuracy of the CFRE determination strongly depends on the accuracy of the input coal fire pixel mask. As mentioned in the introduction to this chapter, the research of Zhang et al. (submitted) and Zhang (2004) has outlined that coal fires can be detected, in previously unknown areas, using ETM data. However, an additional, visual interpretation of the automatically detected anomaly pixels, achieved by combing geological field information, and the knowledge of local coal fire experts, will definitely improve coal fire detection. Additional input information should therefore be considered whenever it is available.

As discussed before, the CFQ algorithm here presented is specifically developed for ASTER and ETM TIR band data. It can however, be easily adapted to other high-resolution TIR data (for example to high-resolution airborne TIR data) by changing the atmospheric lookup tables and the calibration parameters in the configuration file. Thus, the presented algorithm can, in cases where the coal fire surface temperatures are lower than 600 K, be regarded as a robust tool for a remote coal fire analysis task.

CONCLUSIONS AND REFERENCES

11 CONCLUSIONS

Kaufman et al. (1996) first proposed the remote measurement of fire radiative energy (FRE) as a new approach to providing quantitative information on forest and grassland fires. Until recently however, this concept has not been tested towards its applicability to coal seam fires. The results from this study demonstrate that the ASTER, ETM and BIRD satellite sensors possess the necessary spectral and radiometric characteristics to measure coal fire radiative energy (CFRE).

Field observations clearly demonstrate that coal fire related surface anomalies (CFSA) are significantly colder than grassland and forest fires. In addition, the same observations outline that coal fire related surface anomalies are generally rather small. As in the case of forest and grassland fires, a satellite data based, coal fire quantification approach needs also to be based on a sub-pixel concept. However, in contrast to vegetation fires, a coal fire quantification approach has to target 'warm spots' rather than 'hot spots'.

The performed coal fire simulations indicate that the TIR and MIR spectral range is significantly more sensitive in registration of coal fire related 'warm spots' than the SWIR spectral range. In addition, theoretical analysis indicates that amongst existing FRE approaches, only the commonly used bi-spectral fire quantification approach can be applied to quantify relatively large and warm CFSA, via BIRD satellite data. For ASTER and ETM data, existing FRE retrieval methods including the bi-spectral technique cannot be applied for the analysis coal fires. In this study an alternative CFRE retrieval method is illustrated for ASTER and ETM data, which is based on TIR spectral radiances. For CFSA with averages temperatures below 600 K and relatively stable TIR background temperature conditions, the use of this newly developed TIR method is recommended.

The two case studies presented here outlined the possibilities and limitations of a satellite data based CFRE retrieval approach. ASTER, ETM and BIRD night-time data appear to be effective in retrieving CFRE, allowing CFRE to be estimated within an average of +/- 25 % (ASTER), of +/- 35 % (ETM) and of +/- 40 % (BIRD) accuracy. However, the low spatial resolution of the BIRD data prevents some of the low radiative coal fire components from being detected and therefore total computed CFRE energy releases are on average significantly lower than estimates based on ETM and ASTER data. Summer daytime conditions provide the most difficult situation for reliable CFRE estimates, on account of TIR background temperature variations. Thus, night-time conditions have to be regarded as optimal for satellite data based CFRE studies. The good agreement reported for derived CFRE values, using satellite data from different instruments, indicates that physically meaningful values of CFRE can be derived via the investigated satellite instruments.

11 Conclusions

Although coal fire energy is lost not only by radiation but is also lost by various processes such as for example conduction into the ground, the potential coal losses computed via ETM night-time derived CFRE values do approximate the overall dimension of the coal fire problem in the investigated coalfields. This result provides confidence in the ability of spaceborne sensors to obtain reliable, quantitative information on the coal fires. It is once again important to mention here that CFRE computed via satellite data only reflects part of the energy lost by coal combustion. Consequently, satellite based CFRE retrievals can only be used to provide an estimate of minimum coal combustion rates.

One key point that remains to be addressed in the future is the extent of potential CFRE underestimation due to undetected, cool CFSA components. This may be examined by means of a comparisons between, on the one hand, high-resolution thermal airborne data and, on the other hand, satellite data. A further point is that, whilst the presented TIR coal fire quantification technique is only applicable for CFSA temperatures below 600 K, more detailed field observations are needed in order to justify the application of the presented approach on a regional scale. Furthermore, it is necessary to determine to what extent the 'snapshots' available from ETM, ASTER or BIRD data are able to characterise temporal variations of CFSA. The first multi-temporal comparison of BIRD and ETM CFRE values, presented here indicates that only major shifts or activity changes of CFSA can be monitored. Especially in case of small and cooler coal fire related surface anomalies satellite observations cannot replace a thorough ground monitoring. In order to verify these results, future remote sensing studies should include further, more detailed field observations.

The coal fire quantification algorithm presented here can be regarded as a robust tool to derive CFRE estimates via ASTER and ETM data. The present author is well aware of that the previously operational ETM instrument is not longer functioning. This study has demonstrated that the experimental ASTER data can replace ETM data for coal fire analyses. The quality of the coal fire quantification strongly depends on the quality of the coal fire detection. Zhang et al. (submitted) and Kuenzer (pers. Communication, 2004) have demonstrated that coal fires can be automatically detected on thermal night-time satellite data. However, a visual interpretation of the automatically detected thermal anomalies, combined with geological field information and expertise from local mining authorities will undoubtedly improve the results of the coal fire detection and quantification.

Finally, the results of this study indicate that the BIRD MIR spectral band is much more radiometrically sensitive to coal fires than the ETM TIR spectral band. However, the factor 6 higher spatial resolution of ETM allows it to perform better than BIRD under night-time and winter daytime conditions. In summer daytime conditions coal fires cannot be reliably recognised in ETM TIR data due to large background temperature variations. The European Space Agency (ESA) is currently

11 Conclusions

exploiting a complex satellite constellation, the Global Monitoring for Environment and Security Earth Observation Component (GMES OC). The GMES OC preparatory activities began in June 2004. An activity will include definition studies for infra-red fire detection sensors which are being considered for inclusion in the payload of several satellites (European Space Agency Earth Observation Programme Board, 2004). It is recommended that such a prospective satellite sensor, dedicated to the problem of coal seam fire detection and analysis under both daytime and night-time conditions, should have a non-saturating MIR and a TIR channel with a spatial resolution of at least 100 m.

12 REFERENCES

- ACKERSBERG, R., 2003, Understanding self-ignition of coal, Internal unpublished project report, German Montan Technology and Federal Institute for Materials Research and Testing, Germany.
- BERK, A., BERNSTEIN, L. S., and REBERTSON, D. C., 1998, MODTRAN: a moderate resolution model for LOWTRAN 7. Final Report GL-TR-89-0122, U.S. Air Force Systems Command, USA.
- BRIESS, K., JAHN, H., LORENZ, E., OERTEL, D., SKRBEEK, W., and ZHUKOV, B., 2003, Fire recognition potential of the Bi-spectral InfraRed Detection (BIRD) satellite. *International Journal of Remote Sensing*, 24, 865-872.
- BUSTIN, R. M., and MATHEWS, W. H., 1985, In situ gasification of coal, a natural example: additional data on the Aldridge Creek coal fire, south-eastern British Columbia. *Canadian Journal of Earth Science*, 22, 1858-1864.
- CASSELLS, C. J. S., and van GENDEREN, J. L., 1995, Thermal modelling of underground coal fires in Northern China. 21st Annual Conference of The Remote Sensing Society, 11-14 September 1995 (Southampton), pp. 544-551.
- CASSELLS, C. J. S., van GENDEREN, J. L. and ZHANG X. M., 1996, Detection and measuring underground coal fires by remote sensing. 8th Australian Remote Sensing Conference, 28 March 1996 (Canberra), pp 90-101.
- CHEN, W., 1992, Digital image processing application for coal fire remote sensing investigation. *Remote Sensing for Land and Resources*, 12, 21-24.
- CHEN, W., 1997, Subsidence Assessment in the Ruqigou coalfield, Ningxia, China, using a Geomorphological Approach. Master Thesis, ITC Netherlands.
- DAI, S., REN, D., TANG, Y., SHAO, L., and LI, S., 2002, Distribution, isotopic variation and origin of sulfur in coals in the Wuda coalfield, Inner Mongolia, China. *International Journal of Coal Geology*, 51, 237– 250.
- DIAZ, C. M., WAGNER, R. H., WINKLER PRINS, C. F., and GRANADOS, L. F., 1983, The Carboniferous of the World, Volume 1: china, Korea, Japan and SE Asia. In IUGS Publ. No. 16 (España: Empresa Nacional ADARO de Investigaciones Mineras S.A.), pp.11-177.
- DMT, 2001, Visit of Wuda, Gulaben and Ruqigou coalfield – Field Report. Internal unpublished project report, German Montan Technology, Germany.
- DOZIER, J., 1981, A method of satellite identification of surface temperature fields of sub-pixel resolution. *Remote Sensing of Environment*, 11, 221-229.
- EUROPEAN SPACE AGENCY EARTH OBSERVATION PROGRAMME BOARD, 2004, GMES Earth Observation Component: Proposal of preparatory activities. ESA/PB-EO(2004)48, European Space Agency, France.
-

12 References

- FENG, K. K., CHAKRAVORTY, R. N., and COCHRANE, T. S., 1973, Spontaneous combustion - A coal mining hazard. *CIM Bulletin*, 66, 75-84.
- FLANNIGAN, M. D., and VONDER HAAR, T. H., 1986, Forest fire monitoring using NOAA satellite AVHRR. *Canadian Journal of Forest Research*, 16, 975-982.
- GIELISCH, H., 2002, Statusbericht zum GTZ-Project: Löschung von Kohlebränden in der VR China. Internal unpublished report, German Montan Technology, Germany.
- GIELISCH, H., and KAHLEN, E., 2003, Geology of the Helan Shan – Field Report. Internal unpublished project report, German Montan Technology, Germany.
- GIGLIO, L., and KENDALL, J. D., 2001, Application of the Dozier retrieval to wildfire characterisation-a sensitivity analysis. *Remote Sensing of Environment*, 77, 34-49.
- GUAN, H. Y., van GENDEREN, J. L., and SCHALKE, H. J. W. G., 1996, Study and survey on the geological hazards of coal fires in north China. 30th International Geological Congress Abstracts, 4-14 August 1996 (Beijing, China), pp 458.
- GUAN, H. Y., and van GENDEREN, J. L., 1997, Report on environment monitoring of spontaneous combustion in the coal fields of north China (in Chinese). International Institute for Aerospace Survey and Earth Sciences, Netherlands.
- HALIK, U., BANDELOW, F.K., SCHULZ, J., 2003, Land-use and socio-economic aspects of the Helan Shan in Ningxia and Inner Mongolia, China. Internal unpublished project report, German Montan Technology, Germany.
- JONES, P. J., 1995, Carboniferous Timescales 5. Record 1995/34, Austr. Geol. Org., Australia.
- KAUFMAN, Y. J., TUCKER, C. J., and FUNG, I., 1990, Remote sensing of biomass burning in the tropics. *Journal of Geophysical Research*, 95, 9927 - 9939.
- KAUFMAN, Y., REMER, L., OTTMAR, R., WARD, D., RONG, R. L., KLEIDMAN, R., FRASER, R., FLYNN, L., MCDUGAL, D., and SHELTON, G., 1996, Relationship between remotely sensed fire intensity and rate of emission of smoke: SCAR-C experiment in Global biomass burning, edited by In. J. Levine (MA: MIT Press), pp. 685-696.
- KAUFMAN, Y. J., JUSTICE, C. O. , FLYNN, L. P. , KENDALL, J. D., PRINS, E. M., GIGLIO, L., WARD, D. E., MENZEL, W. P., and SETZER, A. W., 1998, Potential global fire monitoring from EOS-MODIS. *Journal of Geophysical Research*, 103, 32215-32238.
- KRAUSE, U., 2003, Status Report on the activities for the Chinese German Mutual Project. Internal unpublished project report, Federal Institute for Materials Research and Testing, Germany.
- KUENZER, C., ZHANG, J., TETZLAFF, A., VOIGT, S., VAN DIJK, P., WAGNER, W., and MEHL, H., submitted, Uncontrolled coal fires and their environmental impacts: Investigating two arid mining environments in north-central China. *International Journal of Applied Geography*.
- LEE, T. F., and TAG, P. M., 1990, Improved detection of hotspots using the AVHRR 3.7 μm channel. *Bulletin of the American Meteorological Society*, 71, 1722-1730.
-

12 References

- LILLESAND, T. M., and KIEFER, R. W., 1994, Remote Sensing and Image Interpretation, 3rd edn (New York: John Wiley & Sons).
- LORENZ, E., and SKRBK, W., 2001, Calibration of a Bi-spectral Infrared Push-Broom Imager. Infrared Spaceborne Remote Sensing IX, 29 July - 3 August 2001 (San Diego, USA), 4486, pp.90-103.
- MANSOR S. B., CRACKNELL A. P., SHILIN B. V., and GORNYI, V. I., 1994, Monitoring of underground coal fires using thermal infrared data. *International Journal of Remote Sensing*, 15, 1675-1685.
- MATSON, M., and DOZIER, J., 1981, Identification of subresolution high temperature sources using a thermal IR sensor. *Photo. Engr. and Remote Sensing*, 47, 1311-1318.
- MATSON, M. and HOLBEN, B., 1987, Satellite detection of tropical burning in Brazil. *International Journal of Remote Sensing*, 8, 509-516.
- PRAKASH, A., SARAF, A. K., GUPTA, R. P., DUTTA, M., and SUNDARAM, R. M., 1995, Surface thermal anomalies with underground fires in Jhahra coal mine, India. *International Journal of Remote Sensing*, 16, 2105-2109.
- PRAKASH, A., GUPTA, R. P., and SARAF, A. K., 1997, A Landsat TM based comparative study of surface and sub-surface fires in the Jharia coalfield, India. *International Journal of Remote Sensing*, 18, 2463-2469.
- PRAKASH, A., and GUPTA, R. P., 1999, Surface fires in the Jharia coalfield, India-their distribution and estimation of area and temperature from TM data. *International Journal of Remote Sensing*, 20, 1935-1946.
- PRINS, E. M., FELTZ, J. M., MENZEL, W. P., and WARD, D. E., 1998, An overview of GOES-8 diurnal fire and smoke results for SCAR-B and 1995 fire season in South America. *Journal of Geophysical Research*, 103, 31821-31835.
- PRINS, E. P., and MENZEL, W. P., 1994, Trends in south American biomass burning detected with the GOES-VAS from 1983-1991. *Journal of Geophysical Research-Atmospheres*, 99, 16719-16735.
- REN, D., ZHAO, F., WANG, Y., YANG, S., 1999, Distributions of minor and trace elements in Chinese coals. *International Journal of Coal Geology*, 40, 109-118.
- RICHTER and SCHLAEPFER, 2002, Geoatmospheric processing of airborne imaging spectrometer data, Part 2: atmospheric/topographic correction. *Int. J. Remote Sensing*, 23, 2631-2649.
- ROBINSON, J. M., 1991, Fire from space: global fire evaluation using infrared remote sensing. *International Journal of Remote Sensing*, 12, 3-24.
- ROSEMA, A., GUAN, H., VEKERDY, Z., TEN KATEN, A. M. and PRAKASH, A., 1999, Manual of coal fire detection and monitoring. NITG 99-221-C, Netherlands Institute of Applied Geoscience, Netherlands.
-

12 References

- SARAF, A.K., PRAKASH, A., SENGUPTA, S., and GUPTA, P., 1995, Landsat-TM data for estimating ground temperature and depth of sub-surface coal fire in the Jharia coal field, India. *International Journal of Remote Sensing*, 16, 2111-2124.
- SETZER, A. W. and PEREIRA, M. C., 1991, Amazonia biomass burnings in 1987 and an estimate of their tropospheric emissions, *Ambio*, 20, 19-22.
- SKRBEEK, W., and LORENZ, E., 1998, HSRC-an infrared sensor for hot spot detection. *Infrared Spaceborne Remote Sensing IV* (Denver, US), pp.167-176.
- Van GENDEREN, J.L., and GUAN, H., 1997, Environmental monitoring of spontaneous combustion in the north China coalfields. Final report to European Commission under contract No. C11*-CT93-0008 (DG-HSMV), Netherlands Institute of Applied Geoscience, Netherlands.
- VEKERDY, Z., PRAKASH, A., and GENS, R., 1999, Data integration for the study and visualization of sub-surface coal fires. 13th International Conference on applied Remote Sensing, 1-3 March 1999 (Vancouver, Canada), pp.150-151.
- VOIGT, S., TETZLAFF, A., ZHANG, J., KUENZER, C., ZHUKOV, B., STRUNZ, G., OERTEL, D., ROTH, A., VAN DIJK, P. and MEHL, H., 2004, Integrating Satellite Remote Sensing Techniques for Detection and Analysis of Uncontrolled Coal Seam Fires in North China. *International Journal of Coal Geology*, 59, 121-136.
- WALKER, S., 1999, Uncontrolled fires in coal and coal wastes. International Energy Agency, IEA on coal Research, UK.
- WOOSTER, M. J., 2002, Long-term infrared surveillance of Lascar Volcano: contrasting activity cycles and cooling pyroclastics. *Geophysical Research Letters*, 28, 847-850.
- WOOSTER, M. J., ZHUKOV, B., and OERTEL, D., 2003, Fire radiative energy for quantitative study of biomass burning: derivation from the BIRD experimental satellite and comparison to MODIS fire products. *Remote Sensing of Environment*, 86, 83-107.
- YANG, H., 1995, Detection of areas of spontaneous combustion of coal by using airborne and TM data in Xinjian, China. MSc Thesis at the International Institute for Aerospace Survey and Earth Sciences, Netherlands.
- ZHANG, J., 2004, Spatial and Statistical Analysis of Thermal Satellite Imagery for Extraction of Coal Fire Related Anomalies. PhD thesis at the Technical university of Vienna, Austria.
- ZHANG, J., WAGNER, W., PRAKASH, A., MEHL, H., AND VOIGT, S., 2004, Detecting Coal Fire Using Remote Sensing Techniques. *International Journal of Remote Sensing*, 25, 3193-3220.
- ZHANG, J. , KUENZER, C., HIRNER, A., TETZLAFF, A., WAGNER, W., MEHL, H. and VOIGT, S., submitted, Detecting unknown coal fires in a previously non-studied area using Landsat-7 ETM+ data. *International Journal of Remote Sensing*.
- ZHANG, X., van GENDEREN, J. L. and KROONENBERG, S. B., 1997, A method to evaluate the capability of landsat-5 TM band 6 data for sub-pixel coal fire detection. *International Journal of Remote Sensing*, 18, 3279-3288.
-

12 References

ZHANG, X., 1998, Coal fires in northwest of China, Detection, monitoring, and prediction using remote sensing data. Ph.D. thesis at the ITC Enschede, Netherlands.

Curriculum Vitae

Tetzlaff Anke

| | |
|------------------------------------|---|
| | Date of Birth: 21 st October 1974 |
| | Gender: female |
| | Nationality: German |
| September 1981 to February 1990 | Polytechnische Oberschule, Erfurt, Germany, Grundschule (primary-school) |
| March 1990 to June 1995 | Ernst-Mach-Gymnasium, Haar, Germany: Gymnasium (secondary-school). |
| September 1998 to October 2000 | Scholarship Studienstiftung des Deutschen Volkes: German National Academic Foundation. |
| August 1999 to February 2000 | University of Pretoria, South Africa: Exchange term. |
| November 1995 to April 2001 | Ludwig-Maximilians University of Munich, Germany: Study of Geology. Main subjects: Remote Sensing and Geophysics. |
| April 2001 to August 2001 | Sakosta EuroConsult, Munich, Germany: Freelancer Geology. |
| August 2001 to March 2004 | German Aerospace Center (DLR), German Remote Sensing Data Center, Oberpfaffenhofen, Germany: PhD position. |
| Since April 2004 | Swedish Meteorological and Hydrological Institute (SMHI), Norrköping, Sweden: Project Scientist. |